Ray-wave correspondence and extended ray dynamics in optical microcavities

Dissertation
zur Erlangung des akademischen Grades

doctor rerum naturalium
(Dr. rer. nat.)

genehmigt durch die Fakultät für Naturwissenschaften
der Otto-von-Guericke-Universität Magdeburg

von Diplom-Physikerin Julia Unterhinninghofen
geb. am 15.02.1982 in Frankfurt am Main

Gutachter: Prof. Dr. Jan Wiersig
Prof. Dr. Roland Ketzmerick

eingereicht am: 24.09.2010
verteidigt am: 24.01.2011

Contents

Abstract

In this work, the correspondence between ray (based on geometric optics) and wave (based on solutions of Maxwell's equations) descriptions in a particular type of optical microcavities, deformed microdisk cavities, is studied both in cases where it can be successfully applied and in cases where it fails. For many applications of microcavities, such as laser resonators, optical modes which have directed far field emission and long life-times are desirable. Unfortunately, it is in general difficult to achieve both these goals simultaneously.

A special deformed microdisk shape that supports long-lived modes with directional emission is presented in this work. It is a microdisk with an elliptical cross-section and a wavelength-scale "notch" at the boundary. The fact that long-lived modes with directional emission exist here can be understood with a ray model: rays which travel along the boundary for a long time (corresponding to so-called "whispering gallery" modes) eventually are scattered by the notch and reflected to the opposite cavity boundary, which acts like a lens and collimates the rays in the far field. The predictions of this ray model agree well with the far field of the optical modes. Elliptical microdisk cavities with a notch have been fabricated experimentally by our collaborators in Prof. Dr. Federico Capasso's group at Harvard, who used them as resonators for quantum cascade lasers; the ray and wave simulations of the far field are compared to the measured far fields, and good agreement is found as well.

Ray models can be expected to fail if the wavelength of cavity modes approaches the cavity length scale; examples for this failure of ray-wave correspondence are given in this work. One solution for this problem, which allows one to retain the simplicity of a ray model, is to extend the ray description by introducing corrections to it which are based on the wave description; these corrections are the Goos-Hänchen shift (GHS) and the Fresnel filtering effect. The calculation of such corrections and their inclusion in the ray description of deformed microdisk cavities is a main point of this work; the results of this extended ray dynamics are compared to wave calculations and applied to experimentally measurable quantities such as far field patterns.

As the results of the extended ray model scale with the ratio of the wavelength corresponding to cavity modes, it can not only be investigated in optical microcavities, but in microwave cavities as well. This is convenient, because while the electric field inside a microcavity can not be measured accurately with current techniques, this can easily be done in microwave cavities. Such measurements of the GHS in microwave cavities, which have been performed during a visit to Prof. Dr. Hans-Jürgen Stöckmann's group at the University of Marburg, are presented in this work. Beams with different incoming angles are generated by superposition of the plane waves produced by microwave antennas; the resulting beams are then reflected at the cavity boundary and the GHS can be measured. The results agree well with numerical calculations.

1. Introduction

Optical microcavities confine light in three dimensions and have sizes ranging from below 1 μm to several hundreds of μm. Light confinement can be achieved by two basic mechanisms. The first one is total internal reflection at the cavity walls; this is used in three-dimensional (e.g., microspheres [CLB+93] and -toroids [IGYM01]) as well as quasi-two-dimensional (e.g., microcrystals [BIL+00] or microdisks [MLS+92]) structures. As microdisk cavities are studied in this thesis, their properties will be reviewed in more detail in chapter 2. The second confinement mechanism is based on multiple Bragg-reflections which create a photonic band gap. This mechanism is used in photonic crystal defect cavities [PLS+99] and vertical-cavity surface-emitting lasers (VCSELs) [IKK88, GBM+96].

Optical microcavities have a variety of applications. They easily can be fabricated by semiconductor technologies in many different shapes and sizes. Microlasers, which use them as resonators, have advantages over conventional lasers: because the cavity size is relatively small, the spacing between its optical modes is large, and thus single-mode lasing can be achieved easily. Furthermore, the rate of spontaneous emission into the lasing mode to the rate of spontaneous emission into all modes, the so-called β factor [DJ88, RC94], is modified by the presence of a microcavity, so that it can be near one [UGA+07]. In this case, only a small excitation suffices to start lasing, which makes such devices efficient. Other applications of optical microcavities are sensors [AKF+05], filters [SHKC02], and single-photon devices [MIM+00] which may be used for quantum computing applications or quantum cryptography [CCF+10]. Optical microcavities also offer potential for basic research, such as the study of light-matter interaction in cavities, the so-called "cavity quantum electrodynamics" [RSL+04, WGJ+09]. One successful type of optical microcavities are deformed microdisks, quasi-two-dimensional cavities with non-circular cross-sections which confine light by total internal reflection.

One drawback is that for most applications, not only long mode lifetimes (which optical microcavities generally can provide), but also directed light output from the cavity is desirable. Achieving this in microdisks in combination with long life times is still a goal which is actively researched. In order to optimize both directional output and mode life times, and, perhaps more importantly, in order to gain physical insight into how these goals are achieved in a particular cavity design, ray-dynamical simulations have been very successful. In the regime where the mode wavelengths λ are small compared to the cavity length scale R, one is in the geometric optics limit of wave optics, and can study the scattering of light rays and the light output because of refraction, which can predict the output directionality of optical microcavities accurately in many cases (i.e., [NS97, WH08, WYY+10]). However, as optical microcavities are fabricated with scales R comparable to the wavelength [SGS+10], it is clear that one is far away from the limit

of geometric optics and ray models are expected to fail. In fact, deviations from ray predictions have been reported in the past. As one does not want to lose the simplicity and physical insight of ray models completely, it suggests itself to improve ray models by introducing corrections derived from the wave description.

The dynamics of light rays trapped by total internal reflection inside a microdisk is equivalent to the dynamics of a classical particle moving in a two-dimensional area bound by hard walls; such a system is called a "billiard" in nonlinear dynamics. Billiards often show a phenomenon called *chaos*, which manifests itself in a sensitive dependence on initial conditions. The ray dynamics in a microcavity thus also often is chaotic, and can be studied using methods from nonlinear dynamics. The mode equation describing optical modes in microdisk cavities, on the other hand, is equivalent to the time-independent Schrödinger equation describing the quantum dynamics inside a billiard, which means that the optical modes of a microdisk cavity may be studied using methods from the field of *quantum chaos* [Stö00, Haa10] (which studies the quantum dynamics of systems with chaotic classical dynamics) and on the other hand provide systems in which predictions from quantum chaos may be tested experimentally. This is not unimportant, as model systems for quantum chaos have been relatively scarce for a long time. One important question in quantum chaos is the one of "quantum-classical correspondence", i.e., the question of how features of the classical dynamics are reflected in the quantum properties of a system. This corresponds directly to what is called "ray-wave correspondence" in optical microcavities and is often studied in the so-called *semiclassical limit*, which corresponds to the limit of small λ/R in microcavities. With the possibility of fabricating cavities in many sizes down to the scale of the wavelength, the merits and limits of semiclassical approximations can be directly investigated. Because optical microcavities, as opposed to billiards, are inherently *open* systems, they also provide model systems for the study of quantum chaos in open systems.

In this thesis, ray-wave correspondence in cavities is investigated both in cases where it is successful and in cases where it fails. It is the basis of a mechanism for combining long mode life-times and directional light output in notched elliptical microcavities; there, the output directionality can be understood well using a ray model, and ray, wave, and experimental results all agree well. On the other hand, the limits of ray models are investigated as well; better agreement with wave results is possible farther into the wave limit if one used an extended ray dynamics including wave corrections. The application of such an extended ray model to deformed microdisk cavities is the main result of this thesis. While the predictions of this extended ray model can only be tested indirectly (for example by looking at far field emission patterns) in experiments using optical microcavities, they can be tested in *microwave* cavities. Such microwave experiments are presented as well.

Structure of this thesis

This thesis is structured as follows. Chapter 2 introduces deformed microdisk cavities. The ray dynamics in such systems is equivalent to the dynamics of a classical particle in

an (open) billiard; the properties of such billiard systems and important results on them from nonlinear dynamics are reviewed in chapter 3. Optical modes in microcavities are solutions of a mode equation, the so-called Helmholtz equation, which is discussed in chapter 4. Chapter 4 also reviews the relation to the field of quantum chaos and the relation of wave solutions to the ray description.

Chapter 5 introduces a cavity boundary shape which supports modes with high quality factors and unidirectional emission. These features are explained by using a ray model, which shows that the directionality arises from a combination of scattering and a collimation process similar to the one a lens performs. In chapter 6, the conventional ray dynamics is extended, so that it includes first-order wave corrections. These corrections are shown to improve the agreement with wave solutions: they can explain wave localization (section 6.4), phase-space shifts of periodic orbit positions (section 6.5) and the formation of periodic orbits which are different for clockwise and counterclockwise propagating rays (section 6.6.1). Measurements of the wave corrections in a microwave cavity are presented in chapter 7 and shown to agree well with numerical calculations.

2. Deformed microdisk cavities

In microdisk resonators, light confinement is achieved by utilizing *total internal reflection* (TIR) at a dielectric interface – light hitting this interface with an angle larger than the critical angle for total internal reflection will be confined inside the dielectric material, whereas light hitting the interface with a lower angle will be refracted out. Such resonators are often realized as planar microdisk resonators (not necessarily with a circular cross-section) and are discussed in the following. The light is confined both vertically and in the disk plane, as sketched in Fig. 2.1; emission mainly takes place in the disk plane. Light confined by TIR can only leak out of the cavity evanescently, which leads to long life-times of optical modes.

Microdisk resonators can be fabricated as semiconductor nanostructures [MLS+92, GCN+98, KKPV06] (with semiconductor quantum wells or quantum dots as a gain medium for laser applications), as cavities made of polymers with dyes as a gain medium [KJD+95, FSVY97, LLHZ06], or as liquid jets of ethanol which are ejected from a non-circular hole [YML+06] (which are not very practical for applications but nice as model systems as the deformation can be precisely tuned). Semiconductor microdisks are typically fabricated by lithographic techniques, which allow for precise control of both the boundary shape and the cavity size. Figure 2.2 shows a typical example of a deformed microdisk in both a top-view (showing the deformed boundary shape) and a side-view (showing the pedestal on which the cavity stands). This cavity is described in [SFL+09]. The radius is $\approx 2\,\mu$m, and the vertical extension is about $0.2\,\mu$m – the cavity can thus be approximated as a two-dimensional object (the validity of this assumption is discussed in section 4.1). Refractive indices for semiconductor materials are ≈ 3 (i.e. 3.3 for GaAs); polymers have refractive indices around 1.5, and the value for ethanol used in liquid jets is around 1.3.

If the boundary shape of a dielectric microdisk is given, the refractive index of the material inside it defines the optical properties. While it is assumed to be piecewise constant, it may depend on the mode wavelength; light amplification (gain) can be described by introducing a complex refractive index. Its imaginary part then describes gain (or losses, if it is positive). Recently, modes for cavities with *negative refraction* [Ves68] have been calculated as well [WUS+10a]. Throughout this thesis, positive refraction without gain or loss (i.e. a real, positive refractive index) will usually be assumed.

The frequencies ω of optical modes are complex numbers (see section 4.1). The wavelength λ is then given by $\lambda = 2\pi c/\mathrm{Re}\,\omega$ (this is the *vacuum wavelength*; the wavelength in the cavity material is given by $\lambda' = \lambda/n$ if n is the refractive index). Instead, the wave vector $k = \omega/c$ (also a complex number) can be used. The imaginary part of ω is related to the life-time τ of a mode by $\tau = -1/\mathrm{Im}\,\omega/2$. Both the wavelength λ and the wave number k are often scaled to a typical cavity length scale R (i.e. the radius

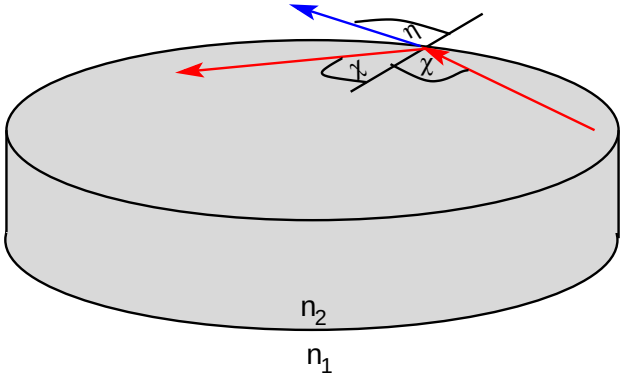

Figure 2.1.: Light confinement in a microdisk resonator with refractive index n_2. If the light is not confined by TIR, part of it can be refracted out to the region with refractive index $n_1 < n_2$.

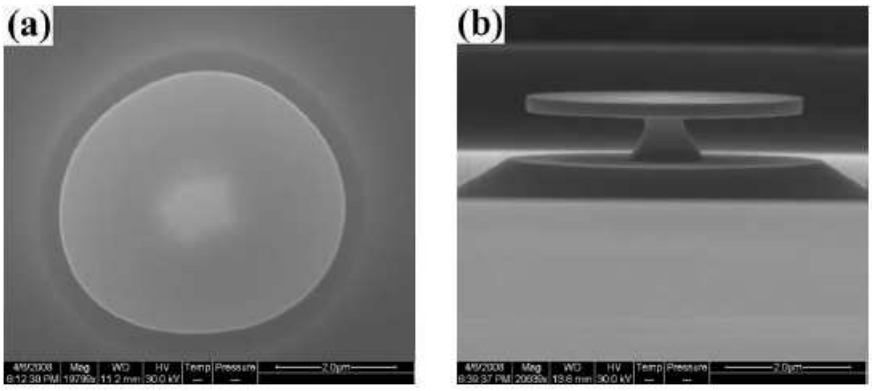

Figure 2.2.: Example of a semiconductor deformed microdisk (made of GaAs). (a) Top view. (b) Side view. The scale bar is 2 μm in both cases (Picture courtesy of H. Cao).

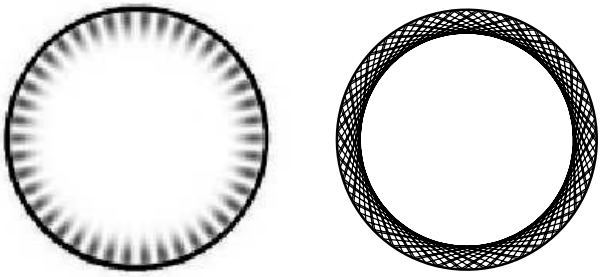

Figure 2.3.: Left panel: example of a whispering-gallery mode in a microdisk with circular cross-section. Right panel: corresponding light ray.

of a circular cavity). This use of λ/R or the so-called "size parameter" kR allows for comparison between the properties of cavities with different sizes. Here, mostly kR will be used to characterize modes, but in chapter 7, the frequency $\nu = \omega/2\pi$ will be used as well.

One important parameter for a cavity mode is the so-called *quality factor* (or Q factor) Q. Q is defined as the ratio between the light intensity inside the cavity and the energy flow out of the cavity, multiplied by the mode frequency. One finds

$$Q = \mathrm{Re}\,\omega\tau = -\frac{\mathrm{Re}\,\omega}{2\,\mathrm{Im}\,\omega} = -\frac{\mathrm{Re}\,kR}{2\,\mathrm{Im}\,kR}. \tag{2.1}$$

The life-time τ of a mode is inversely proportional to the mode line-width $\Delta\omega = -2\mathrm{Im}\,\omega$; one can thus also write $Q = \omega/\Delta\omega$. Another parameter is the *free spectral range*, the spacing between mode frequencies; usually, this spacing is not constant, but depends on the frequency range one considers. The free spectral range is large for small cavities, which is desirable because it makes single-mode lasing easy to achieve.

In one wants to use a microdisk as a resonator for a laser, one needs a cavity which supports modes with high Q factors. On the other hand, most laser applications require *directed* light output; thus, an optical microdisk is most useful for applications if is supports high-Q modes which have directional emission. Unfortunately, in many cases there is a trade-off between the two properties: if one enhances the output directionality of a disk by variation of some parameter, the Q-factor degrades significantly. This trade-off between Q factor and output directionality is quite general and affects other types of microcavities as well; it is known as "Q-spoiling" [NSC94].

Microdisk resonators with circular cross-section support so-called *whispering-gallery modes* (WGMs; an example is shown in Fig. 2.3). They correspond to light rays which travel along the cavity boundary; this phenomenon is named after the "whispering gallery" in St. Paul's cathedral in London, where acoustic waves travel around a gallery. The first mathematical description (for waves in elastic solids and water waves) is due to Lord Rayleigh [Ray85]. WGMs have large Q-factors, but usually emit light uniformly in

all directions. They also exist in deformed microdisks with non-circular cross-sections; examples in such cavities are given in chapters 5 and 6.

Several ways of achieving both high-Q modes and directional output have been proposed and are reviewed in [BBSN06b], [XZL+10], and [WUS+10b]. They range from mode-coupling between high-Q, low directionality and low-Q, high directionality mode [WH06] to the placement of obstacles within disks [DMSW08, DMSW09] and the tailoring of the cavity boundary shape. The most successful shapes seem to be quadrupoles [NS97, GCN+98] and spirals [CTS+03, HK09]; limaçons [WH08, YWD+09, SHW+09, SFL+09, YKK09] are also becoming popular. Many of the proposed designs suffer from the fact that only some of the cavity modes emit light directionally, which can be a problem in applications because precisely the right modes have to be excited. The limaçon cavity does not have this problem: there are many modes have the same far field and thus output directionality. Another boundary shape with this feature, which also illustrates a new mechanism for achieving output directionality, is introduced in chapter 5.

3. Ray dynamics in microcavities: billiards

In this chapter, some basic results for the nonlinear dynamics of so-called billiard systems are reviewed. Mathematical results are only sketched and not proved; for a more detailed overlook see, e.g., [Gas98, TG06, Haa10] and the references of this chapter. The numerical calculation of the billiard dynamics is described in appendix A.

3.1. Definition and coordinates

In nonlinear dynamics, systems with hard boundaries which reflect particles specularly are called billiards, because they are obviously similar to a billiard table. Two-dimensional billiards with hard walls can, in polar coordinates r, ϕ, be described by the Hamiltonian

$$H = \frac{1}{2m}\left(p_r^2 + \frac{p_\phi^2}{r^2}\right) + V(r,\phi), \tag{3.1}$$

with the potential

$$V(r,\phi) = \begin{cases} \infty, & r,\phi \text{ on boundary} \\ 0, & \text{elsewhere} \end{cases}. \tag{3.2}$$

The motion between reflections at the boundary is force-free (the potential (3.2) only has a non-vanishing derivative at the boundary), the particle moves on straight lines between bounces; two parameters are thus sufficient to describe the dynamics completely: an initial value on the boundary and an initial outgoing angle (see Fig. 3.1) – with these, the straight line connecting this initial position to the next reflection point on the boundary can be found. While the phase space of a billiard is in principle four-dimensional, and the motion takes place on three-dimensional subspaces with conserved total energy E, the dynamics, one can describe the dynamics in the so-called *Poincaré surface of section* (Poincaré SOS). It is spanned by the Birkhoff coordinates [Bir27]. They are given by the arc length s along the billiard boundary and the sine of the angle of incidence p. The angle of incidence χ is given as the angle between the particle momentum $\mathbf{P}$ and the local normal vector $\boldsymbol{\nu}$ at the bounce point; it fulfills $P\sin\chi = \mathbf{P}\cdot\boldsymbol{\tau}$ with the local tangent vector $\boldsymbol{\tau}$. $P\sin\chi$ is thus the tangential momentum of the particle and $p = \sin\chi$ the normalized tangential momentum. One can distinguish clockwise and counter-clockwise motion by the sign of χ (and thus p); here, the convention is adopted that positive χ values correspond to *counter-clockwise* motion. s and p are conjugate variables [Ber81]. In the following, s will usually be normalized to the circumference $s_{\max}$ of the billiard.

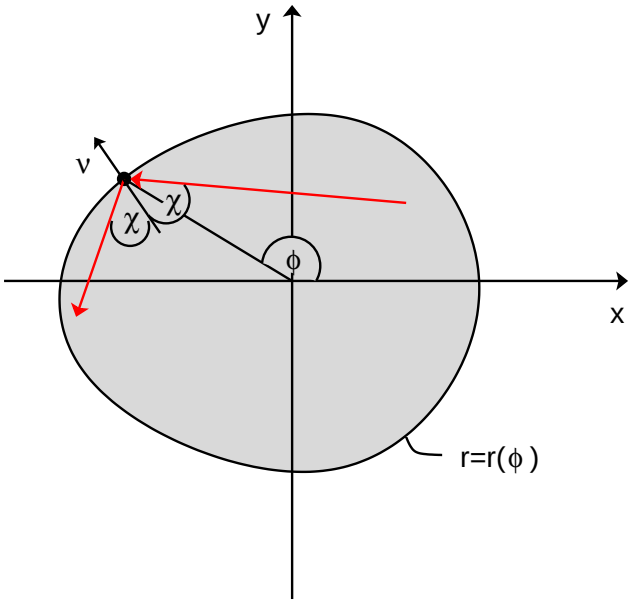

Figure 3.1.: Definition and choice of coordinates in a billiard.

Billiards with other wall potentials are also investigated in the literature (billiards with non-hard boundaries, so-called "soft-wall" billiards, and billiards with openings); an optical microcavity can thus be seen as an open billiard. However, as the billiards without openness describe the light intensity confined to the cavity well, only hard-wall billiards will be considered in the following.

3.2. Dynamics in billiard systems

In the Birkhoff coordinates, the motion in the billiard can be described by a map B which maps one bounce point (s_j, p_j) to the next one (s_{j+1}, p_{j+1}). In general, such maps can not be written down analytically; an example of a system where this is indeed possible is given in section 3.3.1. The Jacobian $\hat{J}_B$ defines the linearized map (or tangent map; sometimes also called monodromy matrix):

$$\hat{J}_B = \begin{pmatrix} \frac{\partial s_{j+1}}{\partial s_j} & \frac{\partial s_{j+1}}{\partial p_j} \\ \frac{\partial p_{j+1}}{\partial s_j} & \frac{\partial p_{j+1}}{\partial p_j} \end{pmatrix}. \tag{3.3}$$

In the Birkhoff coordinates, the map B is area-preserving if the system is Hamiltonian, which implies $\det \hat{J}_B = 1$. An example of a billiard map which is not area-preserving is given in chapter 6.

Different types of motion are distinguished by their stability with respect to small changes in the initial conditions and by the behaviour of the dynamics in phase space. If the difference between trajectories corresponding to slightly different initial conditions grows exponentially, and a trajectory fills the whole (apart from a set of measure zero)

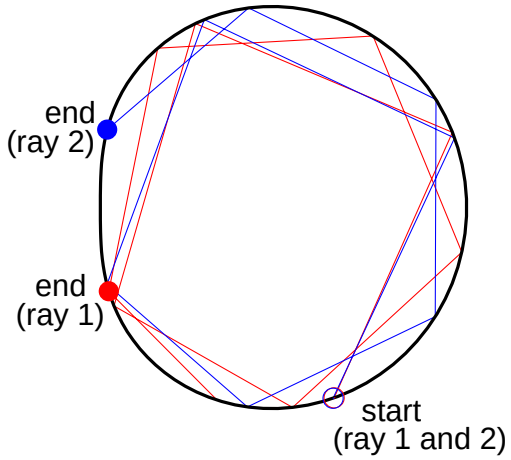

Figure 3.2.: Two trajectories performing chaotic motion in a billiard. Their initial conditions (open dots) differ by 0.1 %; after 10 bounces (end positions marked by filled dots), they have become uncorrelated and their dynamics is completely different.

phase space as time goes to infinity, the motion is called *chaotic*. In a chaotic billiard, a trajectory fills a (two-dimensional) area in the Poincaré SOS if the dynamics if followed infinitely. If the growth of the difference between trajectories is slower than exponential, and trajectories stay restricted to certain phase-space regions, the motion is called *regular*. In the Poincaré SOS of a billiard, points of the trajectory lie on a (one-dimensional) line or closed curve; because such lines or curves are mapped onto themselves by the billiard map $\hat{B}$, they are called "invariant lines" (or invariant curves). Because the Poincaré SOS with $s = 0$ and $s = s_{\max}$ identified has the topology of a cylinder, and and invariant line winds around that cylinder as tori, invariant lines are also called invariant tori.

Figure 3.2 shows the sensitivity of chaotic motion: the initial conditions differ by 0.1 % (both in s and in p), and the trajectories are uncorrelated after the boundary has been hit only 10 times. Phase space examples of regular and chaotic motion are shown in Fig. 3.3. Systems which show regular motion for all initial conditions are called "integrable"; billiard examples are studied in section 3.3.1. Systems which show chaotic motion for all but a few initial conditions (which fill a set of measure zero in phase space) are called "chaotic". Typically, both regular and chaotic motion is possible in a system depending on the initial conditions; such systems are called "mixed". Examples are discussed in section 3.3.2.

Fixed points (s^*, p^*) of the map B fulfill $(s^*, p^*) = B(s^*, p^*)$, they are not changed by the mapping. They are important for the dynamics because periodic orbits, which close themselves after m bounces, are fixed points of B^m. The motion near such a fixed point

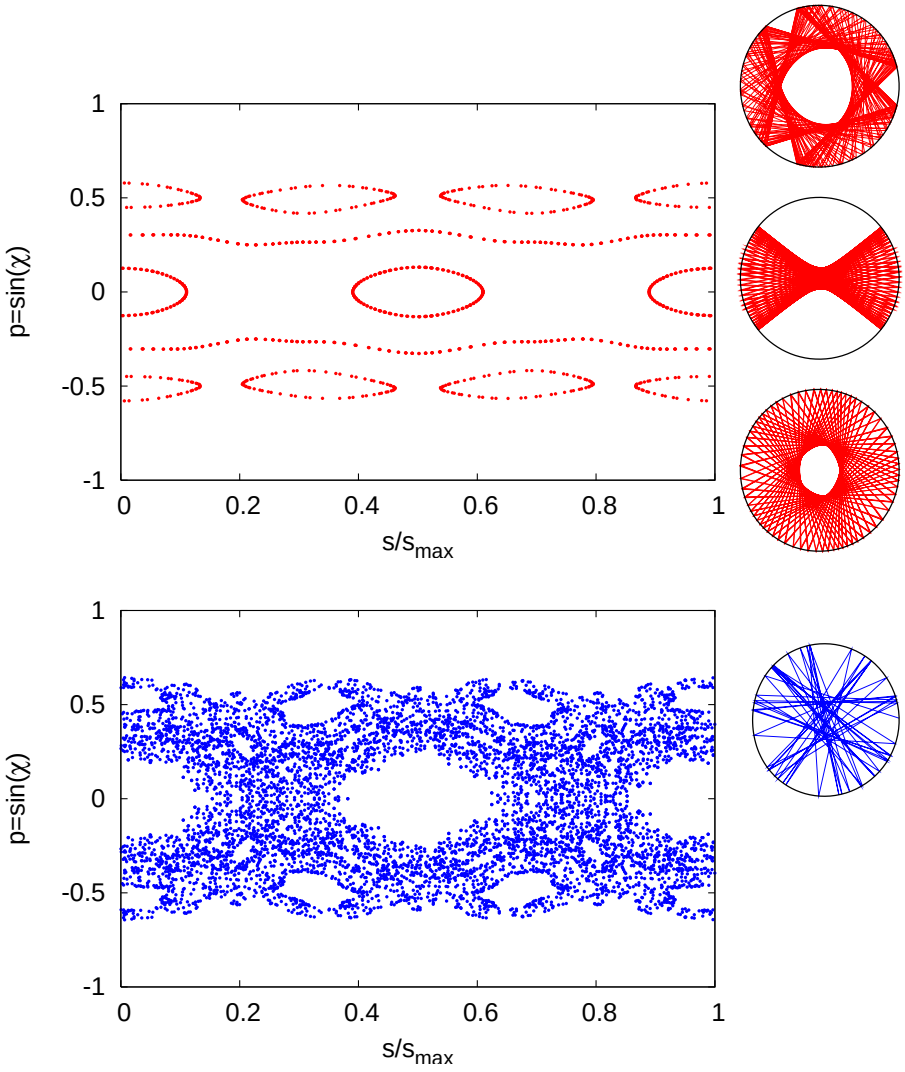

Figure 3.3.: Examples for regular (red dots, top panel) and chaotic (blue dots, bottom panel) motion in a billiard with a mixed phase space. The dynamics is shown both in the Poincaré SOS (main panel) and in real space (on the right).

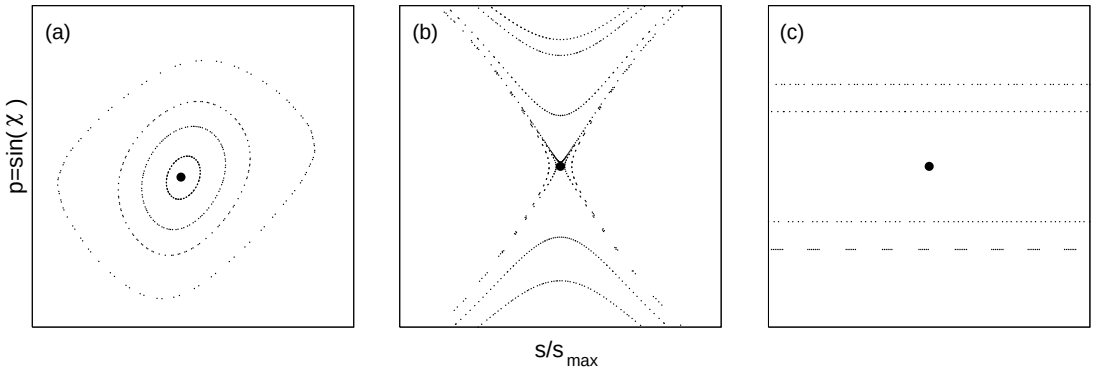

Figure 3.4.: The three different types of fixed points (black dots). (a) Stable (elliptic) fixed point; points nearby the fixed point move around it on ellipses. (b) Unstable (hyperbolic) fixed point; points nearby the fixed point move on hyperbolas. (c) Marginally stable (parabolic) fixed point. Points nearby it move on straight lines.

is described by the eigenvalues of $\hat{M} \equiv \hat{J}_B^m$. They are given by

$$\lambda_\pm = \frac{\operatorname{tr}\hat{M}}{2} \pm \frac{1}{2}\sqrt{\left(\operatorname{tr}\hat{M}\right)^2 - 4}. \tag{3.4}$$

The following three cases can be distinguished and are illustrated in Fig. 3.4.

1. $\lambda_\pm$ complex with $\lambda_\pm = e^{\pm i\phi}$ (corresponding to $\operatorname{tr}\hat{M} < 2$): points nearby the fixed point oscillate around it; the fixed point is called *stable* or *elliptic*, because points near the fixed point move around it on ellipses.

2. $\lambda_\pm$ real with $\lambda_+ = 1/\lambda_-$ (corresponding to $\operatorname{tr}\hat{M} > 2$): points which lie in the direction of the eigenvector ("unstable direction") corresponding to the eigenvalue larger than one move away from the fixed point at an exponential rate, while points in the direction of the other eigenvector move towards the fixed point at an exponential rate. The fixed point is *unstable* or *hyperbolic*, as points nearby it move on hyperbolas.

3. $\lambda_+ = \lambda_- = \lambda$ (implies $\lambda = \pm 1$, corresponding to the case $\operatorname{tr}\hat{M} = 2$): this degenerate case describes a *marginally stable* (also called *marginally unstable*) fixed point. Points nearby the fixed point move towards or away from it at a linear rate. Such fixed points are also called *parabolic*.

3.3. Examples of billiard systems

3.3.1. Integrable systems

In integrable systems with two degrees of freedom, another constant of motion apart from the energy E exists, so that the motion in the Poincaré SOS takes place on one-

dimensional subspaces (lines). Two examples are reviewed: the circle and the ellipse, which is the only smooth and convex deformation of the circle which remains integrable [Ami97].

Circle

In polar coordinates (r, ϕ), the circular billiard is given by the boundary curve $r(\phi) = R$, where R is the radius of the circle. Because of the rotational symmetry in the (x, y) plane, the conjugated momentum to ϕ, $p_\phi = mr^2\dot{\phi}$, is conserved in addition to the energy E. The circular billiard is thus an integrable billiard. The angle of incidence χ, which fulfills $\sin\chi = p_\phi/(RP)$, is conserved in this case, as p_ϕ, R and P are all conserved quantities (the modulus of the momentum, P, is conserved because it is related to the conserved energy by $P = \sqrt{2mE}$). In a circular billiard, the angle of incidence thus does not change in the course of the motion; in the Poincaré SOS, this means that the motion takes place on lines $p = \sin\chi = \text{const}$.

Two types of motion can be distinguished: periodic orbits, where the orbits close after a number of bounces, and orbits which never close. In order for an orbit to be periodic, the angle of incidence has to be a rational multiple of 2π. Figure 3.5 shows examples of both periodic and non-periodic motion in the circular billiard. The two types of motion can be described by the winding number w, which is defined as

$$w = \frac{1}{s_{\max}} \lim_{j\to\infty} \left(\frac{s_j - s_1}{j} \right), \tag{3.5}$$

where s_j is the arc length at the j-th bounce, *not* taken modulo $s_{\max}$: it grows as the orbit winds around the boundary many times. If w is irrational, the orbit never closes; if $w = \ell/k$ is a rational number, the orbit closes after k bounces, having wound around the billiard center ℓ times.

Because of the simple geometry, it is possible to write down the map for the circular billiard explicitly. As the angle of incidence is conserved, one directly finds $p_{j+1} = p_j$. From Fig. 3.6, one can find $s_{j+1} = s_j + R\alpha$, with $\alpha = \pi - 2\chi$. Application of trigonometric identities yields

$$\begin{aligned} p_{j+1} &= p_j, \\ s_{j+1} &= s_j + 2R \arccos p_j. \end{aligned} \tag{3.6}$$

Using Eq. (3.6), the linearized map can be easily calculated:

$$\hat{J}_B = \begin{pmatrix} 1 & \frac{2R}{\sqrt{1-p_j^2}} \\ 0 & 1 \end{pmatrix}. \tag{3.7}$$

For all fixed points, one finds $\operatorname{tr} \hat{J}_B = 2$; in the circle, all periodic orbits are marginally stable.

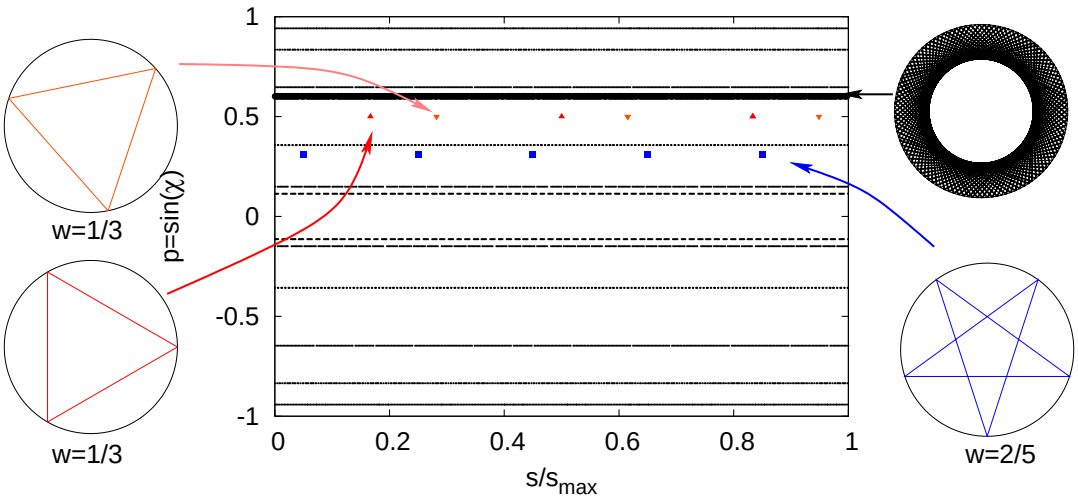

Figure 3.5.: Examples of orbits in the circular billiard. The main panel shows the Poincaré SOS, and on the left and right, the orbits are depicted in real space. In the case of the periodic orbits, the winding number w is noted below the real-space representation.

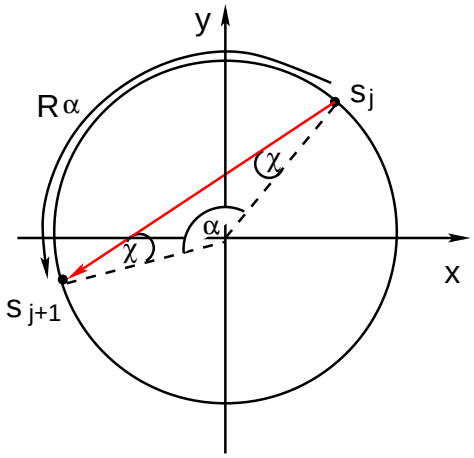

Figure 3.6.: Definition of the circle billiard map.

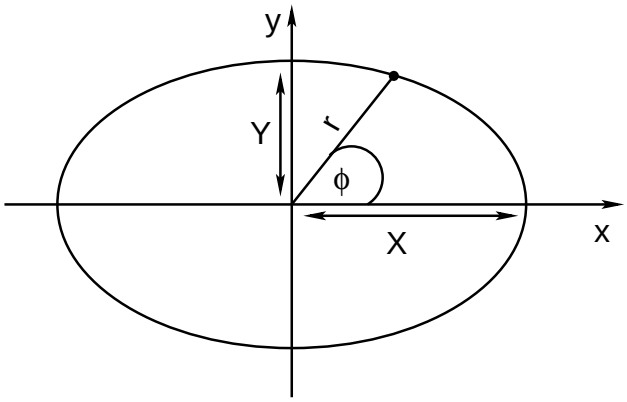

Figure 3.7.: Elliptical billiard shape.

Ellipse

The ellipse is usually defined in Cartesian coordinates as

$$\frac{x^2}{X^2} + \frac{y^2}{Y^2} = 1 \tag{3.8}$$

(see Fig. 3.7). Introducing polar coordinates, $x = r(\phi)\cos\phi$, $y = r(\phi)\sin\phi$, the boundary curve can also be written as

$$r(\phi) = \frac{1}{\sqrt{\frac{\cos^2\phi}{X^2} + \frac{\sin^2\phi}{Y^2}}}. \tag{3.9}$$

Often, ellipses with normalized area $A = \pi XY = \pi$ are considered, which implies $Y = 1/X$. In this case, the ellipse can be characterized by two parameters, i.e. the half-axis length X and the half-axes ratio $\epsilon = X/Y$ (this is used in chapter 5) or X and the eccentricity $e = \sqrt{X^2 - Y^2}/X$ (this is used in chapter 6).

The ellipse has no obvious symmetries which lead to additional constants of motion as in the case of the circle. However, there is such a quantity, which is given by be product of the angular momenta with respect to the two ellipse foci. The existence of this constant of motion will be derived in the following. Figure 3.8 illustrates the geometrical relations that will be used.

Let F_1 and F_2 be the two ellipse foci, with positions $x \pm c$, where $c = \sqrt{X^2 - Y^2}$ is the distance from the foci to the origin. The normalized vectors pointing from them to a point $O = (x, y)$ on the ellipse are denoted $\mathbf{r}_1$ and $\mathbf{r}_2$. The local normal vector $\boldsymbol{\nu}$ at the point O is given by

$$\boldsymbol{\nu} = \frac{1}{\sqrt{x^2/X^4 + y^2/Y^4}} \begin{pmatrix} x/X^2 \\ y/Y^2 \end{pmatrix}, \tag{3.10}$$

$\mathbf{r}_1$ and $\mathbf{r}_2$ are given by

$$\mathbf{r}_1 = \frac{1}{\sqrt{(x-c)^2 + y^2}} \begin{pmatrix} x-c \\ y \end{pmatrix}, \mathbf{r}_2 = \frac{1}{\sqrt{(x+c)^2 + y^2}} \begin{pmatrix} x+c \\ y \end{pmatrix}. \tag{3.11}$$

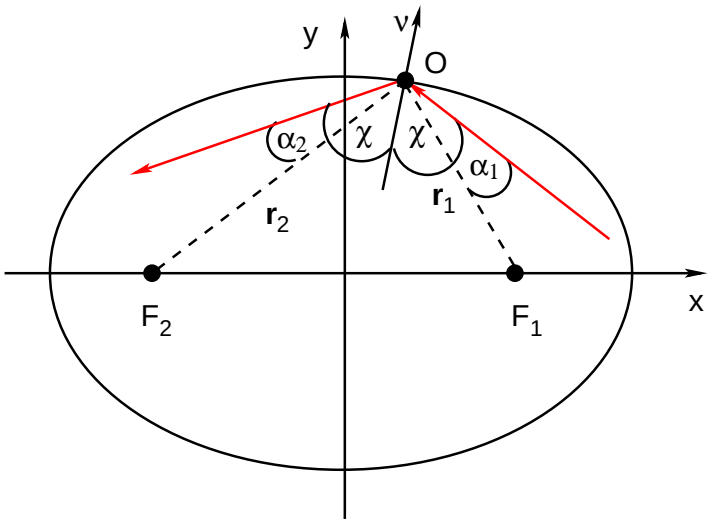

Figure 3.8.: Geometrical relations with respect to the foci F_1 and F_2 of the ellipse.

The angles α_1 and α_2 fulfill $\cos\alpha_i = \mathbf{r}_i \cdot \boldsymbol{\nu}$. By elimination of y with the ellipse definition (3.8), one can find [Nöc97]

$$\frac{\mathbf{r}_1 \cdot \boldsymbol{\nu}}{\mathbf{r}_2 \cdot \boldsymbol{\nu}} = 1, \tag{3.12}$$

which implies $\alpha_1 = \alpha_2$.

The angular momenta $L_{1,2}$ with respect to the foci $F_{1,2}$ can now be calculated. For the incoming ray, one finds

$$\begin{aligned} L_{1,\text{inc}} &= |\mathbf{P} \times \mathbf{r}_1| = P r_1 \sin\alpha, \\ L_{2,\text{inc}} &= |\mathbf{P} \times \mathbf{r}_2| = P r_2 \sin(2\chi - \alpha). \end{aligned} \tag{3.13}$$

For the outgoing ray, one finds $L_{1,\text{out}} = P r_1 \sin(2\chi - \alpha)$ and $L_{2,\text{out}} = P r_2 \sin\alpha$. The product $L_{12} = L_1 L_2$ is thus unchanged by the collision with the boundary, as it is the same for the incoming and the outgoing ray. As the angular momenta L_1 and L_2 are also conserved *between* collision with the boundary, L_{12} is a constant of motion.

The types of motion in the elliptical billiard can be classified by the sign of L_{12}. Orbits with $L_{12} > 0$ are of whispering-gallery type, while orbits with $L_{12} < 0$ travel between the top and bottom part of the boundary; such orbits are called "bouncing-ball" orbits. In the Poincaré SOS, both types of motion are separated by a separatrix with $L_{12} = 0$; it corresponds to an unstable periodic orbit going from the left to the right. Apart from one stable (bouncing-ball from the top to the bottom) and one unstable (corresponding to the separatrix) orbit, all orbits in the ellipse are marginally stable.

Figure 3.9 shows the Poincaré SOS of an elliptical billiard; a whispering-gallery orbit and a bouncing-ball orbit are shown in real space as well.

It is interesting to note that while the quantum version of the elliptical billiard is, of course, still integrable, the *open* elliptical quantum billiard is not. The implications for ray-wave correspondence in elliptical dielectric cavities are discussed in section 6.4.

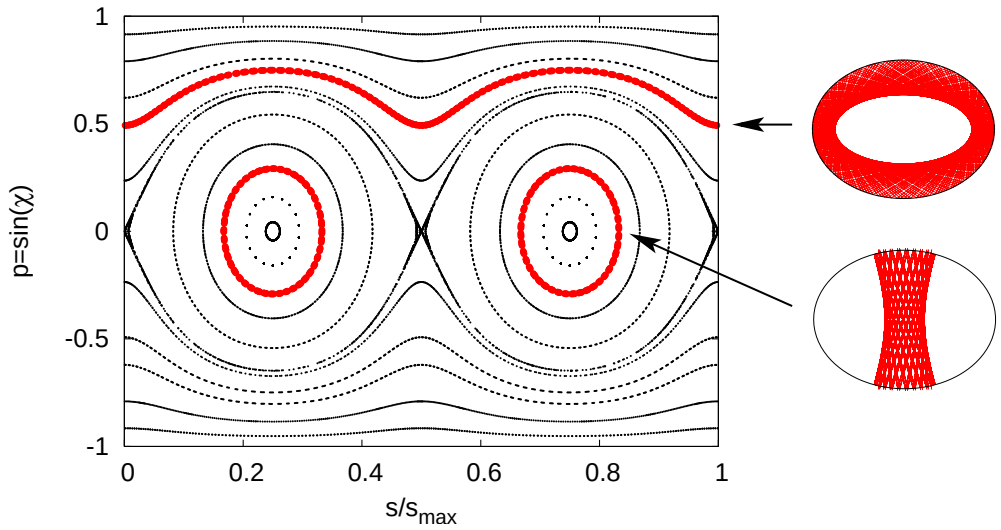

Figure 3.9.: Poincaré SOS of an elliptical billiard with area π and eccentricity $e = 0.645$. On the right, both a whispering-gallery- and a bouncing-ball orbit are depicted in real space.

3.3.2. Systems with a mixed phase space

As an example for a system with a mixed phase space, the family of limaçon billiards, defined by the boundary curve $r(\phi) = R(1 + \epsilon \cos\phi)$, are considered. They can be seen as deformations of the circle ($\epsilon = 0$); as $\epsilon \cos\phi$ is the first ("dipole") term in a multipole expansion of any given boundary, such shapes arise quite naturally and have indeed been studied intensively both theoretically and experimentally. It should be noted that the limaçon boundary shape is not the same as the shape of the family of billiards introduced by Robnik [Rob83]. The Robnik billiards can be described by the boundary curve $r(\phi) = R\sqrt{1 + \delta \cos\phi}$ with a deformation parameter δ; their boundary is thus given by the square root of the limaçon boundary.

In two limiting cases the dynamics in the limaçon is the same for all initial conditions. For $\epsilon = 0$, the integrable circle is recovered. For $\epsilon = 1$, the shape of the billiard is knows as the cardioid, and the dynamics is proved to be fully chaotic [Woj86, Szá92, Mar93, DB01]. In between these two cases, the phase space becomes mixed, with both chaotic and regular regions. This transition from regular to chaotic behavior with mixed dynamics in between upon change of one or more parameters is common in Hamiltonian systems. It is illustrated in Fig. 3.10, where Poincaré SOS's for different ϵ values are shown. In Fig. 3.10 (a), the deformation parameter is $\epsilon = 0.1$. The system still is almost integrable, and most invariant lines are still present, even if slightly deformed from the straight lines of the circle. Some have, however, vanished; instead, stable and unstable fixed points are present as well as islands surrounding the stable fixed points.

This replacement of invariant lines with stable islands and unstable periodic orbits goes on in in Fig. 3.10 (b) at $\epsilon = 0.2$. More invariant lines have disappeared and are replaced by stable and unstable fixed points. In addition, in the region where the

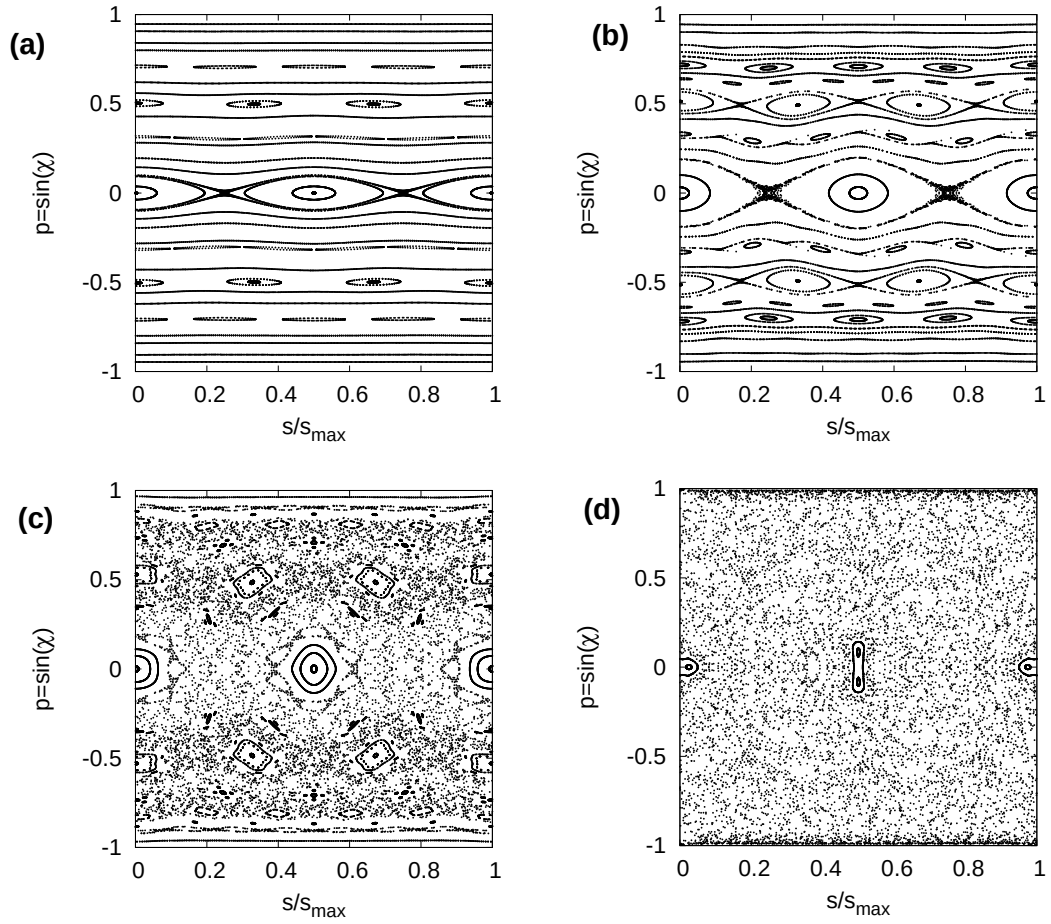

Figure 3.10.: Phase space of the limaçon billiard for (a) $\epsilon = 0.1$, (b) $\epsilon = 0.2$, (c) $\epsilon = 0.3$, and (d) $\epsilon = 0.43$.

separatrix corresponding to the unstable period-2 orbit has been at $\epsilon = 0.1$, a region of *chaotic* motion is present: trajectories started there fill an area in phase space, instead of lying on a line.

At $\epsilon = 0.3$, as shown in Fig. 3.10 (c), the chaotic region has grown and now fills a larger part of the SOS. Some stable islands remain, but they have a more complicated structure than before, with small islands corresponding to periodic orbits with winding numbers ℓ/k with large k surrounding larger ones. At high p, invariant lines are still present as well.

Most stable islands have vanished at $\epsilon = 0.43$ in Fig. 3.10 (d). The largest one corresponds to the period-2 orbit; but there are smaller ones present as well. The chaotic regions of phase space haven grown even more, but still some invariant lines remain close to $|p| = 1$. For even higher ϵ values, this scenario continues: the chaotic parts grow even further. At $\epsilon = 0.5$, no whispering-gallery-like orbits (invariant lines near $|p| = 1$) exist anymore. However, the dynamics still is not fully chaotic: it is known that stable periodic orbits exist at even higher ϵ values [DB01]. Only at $\epsilon = 1$, the limaçon is proved to be fully chaotic.

Three theorems which are important in nonlinear dynamics can be illustrated in this system and are discussed in the following.

Poincaré-Birkhoff theorem

The first theorem, the *Poincaré-Birkhoff theorem* [Poi12, Bir13, Bir26], describes what happens to invariant lines upon a small perturbation. An example is shown in Fig. 3.11: on the left, an invariant line corresponding to the marginally stable period-3 orbits in the circle billiard is shown. On the right, the circle has been perturbed, so that is boundary has now the shape of the limaçon with $\epsilon = 0.2$. The invariant line no longer exists; instead, a stable fixed point (with an island around it) and an unstable fixed point, both corresponding to the only period-3 orbits now possible in the system, have formed. The Poincaré-Birkhoff theorem states that this result is quite general: upon perturbation, invariant lines break up into pairs of stable and unstable periodic orbits.

KAM theorem

The second important theorem, the *Kolmogorov-Arnol'd-Moser (KAM) theorem* [Kol54, Arn63, Mos66], is concerned with the question *when*, i.e. for which perturbation strength, this breakup of an invariant torus happens. It is clear from Fig. 3.10 that not all invariant lines are broken right away; some are broken before the others. If an integrable Hamiltonian H_0 is perturbed so that the Hamiltonian of the perturbed system reads $H = H_0 + \epsilon H_1$ with a perturbation strength ϵ, orbits with winding numbers w which fulfill

$$\left| w - \frac{r}{s} \right| \geq \frac{K(\epsilon)}{s^{2.5}} \tag{3.14}$$

with integer numbers r and s and a constant $K(\epsilon)$ which only depends on the perturbation strength remain unbroken. Equation (3.14) is fulfilled for orbits with sufficiently

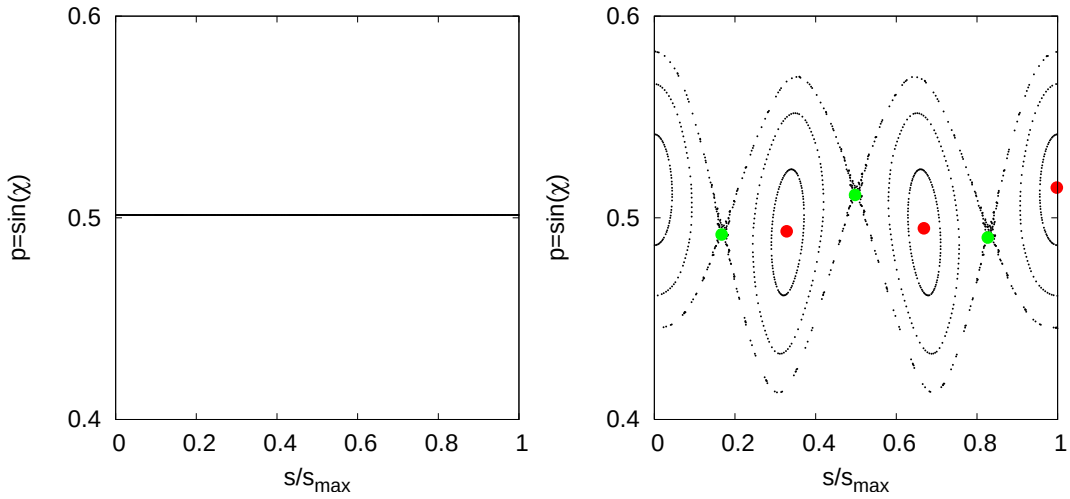

Figure 3.11.: Left panel: invariant line at $p = 0.5$ in the circle. It corresponds to the period-3 orbits. Right panel: stable (red dots) and unstable (green dots) period-3 orbits in the $\epsilon = 0.2$ limaçon. The motion near the fixed points is shown as well.

irrational winding numbers, i.e. orbits whose winding numbers can not be approximated well by a rational number r/s. Periodic orbits with small periodicity are thus most affected by a perturbation, which may be expected as the deviations because of the perturbation accumulate as the orbit visits similar positions many times. Orbits with irrational winding number never visit exactly the same spot again, and small perturbations might average out. The "most irrational" number, whose continued fraction expansion converges slowest, is the golden mean

$$\gamma = \frac{1+\sqrt{5}}{2} = \frac{1}{1+\frac{1}{1+\ldots}} \approx 1.6180\ldots \tag{3.15}$$

γ does not appear as a winding number in billiards (as winding numbers there are always smaller than one), but $1/\gamma$, which also has a slowly converging continued fraction expansion, can. For sufficiently high perturbation strengths ϵ, no invariant tori remain intact.

Lazutkin's theorem

The third theorem, *Lazutkin's theorem* [Laz73], answers the question why some invariant lines persist up to high perturbations, even if they have winding numbers which are "more rational" than, i.e., $1/\gamma$. The reason is that in a billiard, the perturbation which is introduced by deforming the boundary is not uniform: it influences orbits near the boundary less than orbits which venture deep inside the billiard. This is intuitively clear, because orbits near the boundary travel only short lengths between bounces, so that the deviations from the circular boundary they experience are small. Lazutkin's theorem

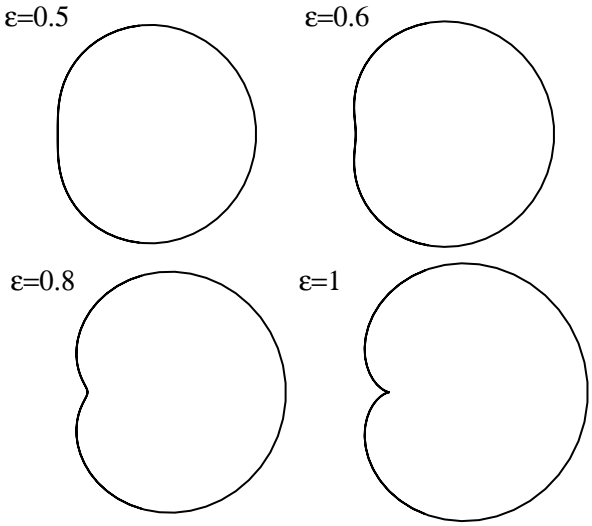

Figure 3.12.: Limaçon billiards for $\epsilon = 0.5$ (still convex), $\epsilon = 0.6$, $\epsilon = 0.8$ and $\epsilon = 1$ (no longer convex). At $\epsilon = 1$, the boundary is no longer smooth as well.

states that a region of invariant lines fills a small but non-zero phase space area near $|p| = 1$ as long as the billiard stays convex. Applied to the limaçon billiard this means that invariant tori persist up to $\epsilon \leq 0.5$, as the limaçon ceases to be convex at $\epsilon > 0.5$ (see Fig. 3.12). Latzutkin's theorem is important for applications because it ensures that whispering-gallery modes exist in limaçon-shaped cavities up to deformations where the ray dynamics is predominantly chaotic, which in turn leads to long-lived WG modes escaping the cavity by means of chaotic transport, leading to long-lived modes with directional emission [YWD$^+$09].

In conclusion, one finds the following generic scenario when perturbing an integrable system: first, invariant lines are destroyed and, by the Poincaré-Birkhoff theorem, replaced by stable fixed points (with stable islands around them) and unstable fixed points (with separatrices near them). Perturbing the system even further, chaotic regions form near the separatrices, while stable fixed points cease to be stable. The invariant lines are broken up according to their winding numbers, and the chaotic regions grow. By Lazutkin's theorem, however, a region of invariant lines fills a small but non-zero phase space area near $|p| = 1$ as long as the billiard stays convex.

3.4. Dielectric cavities as open billiards

If light rays in a cavity are studied, one also has to consider that the cavity is *open* for some light rays: light can be refracted out of the open billiard according to Snell's law

$$n_1 \sin \chi = n_2 \sin \eta, \tag{3.16}$$

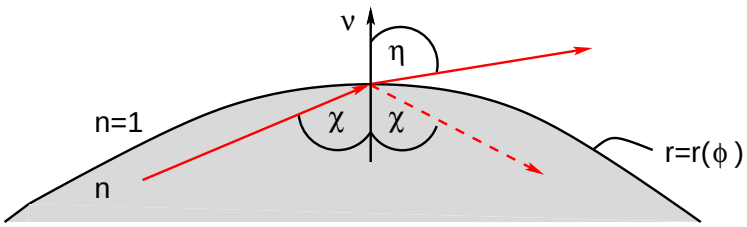

Figure 3.13.: Refraction and reflection according to Snell's law.

if the incoming angle is below the critical angle χ_{cr} for total internal reflection (TIR) (see Fig. 3.13)

$$|\sin \chi_{\mathrm{cr}}| = \frac{n_2}{n_1} = \frac{1}{n}, \tag{3.17}$$

if the refractive index in the cavity is n and the refractive index outside is one. In a Poincaré SOS, the condition (3.17) means that rays with momenta $|p| \leq 1/n$ leak out of the cavity; the region $|p| \leq 1/n$ is thus often called the "leaky region" and the transport of rays from above/below the critical lines $|p| = 1/n$ to the leaky region determines the life-time of light rays in the cavity as well as its emission properties (how emission is calculated ray-dynamically is discussed in sections 5.3 and A.2).

In the circle, it is clear from the Poincaré SOS that the life-time of light inside the cavity is very high: because the invariant lines are straight lines, rays started above the critical line for TIR always stay above it, and the only way light can get out of such a cavity is because of surface roughness (i.e., the circle is not perfectly circular) or because of evanescent leakage, which is a wave effect (the quantum equivalent is tunneling). Figure 3.14 (a) shows the Poincaré SOS for a circular billiard with the leaky region indicated for $n = 3.3$. One could guess that fully chaotic billiards would also make bad cavities, as almost any ray started outside the leaky region would be transported to it after some time, because chaotic trajectories fill the whole phase space – and the light would only be in the cavity for a short time. However, this is not true if one considers *waves*: in this case, interference can lead to long life-times of the rays. These effects are briefly discussed in section 4.2.3. In systems with a mixed phase space, it can take a long time for chaotic trajectories to reach the leaky region, an example (for the $\epsilon = 0.3$ limaçon) is shown in Fig. 3.14 (b). This slow diffusion is due to dynamical barriers in phase space.

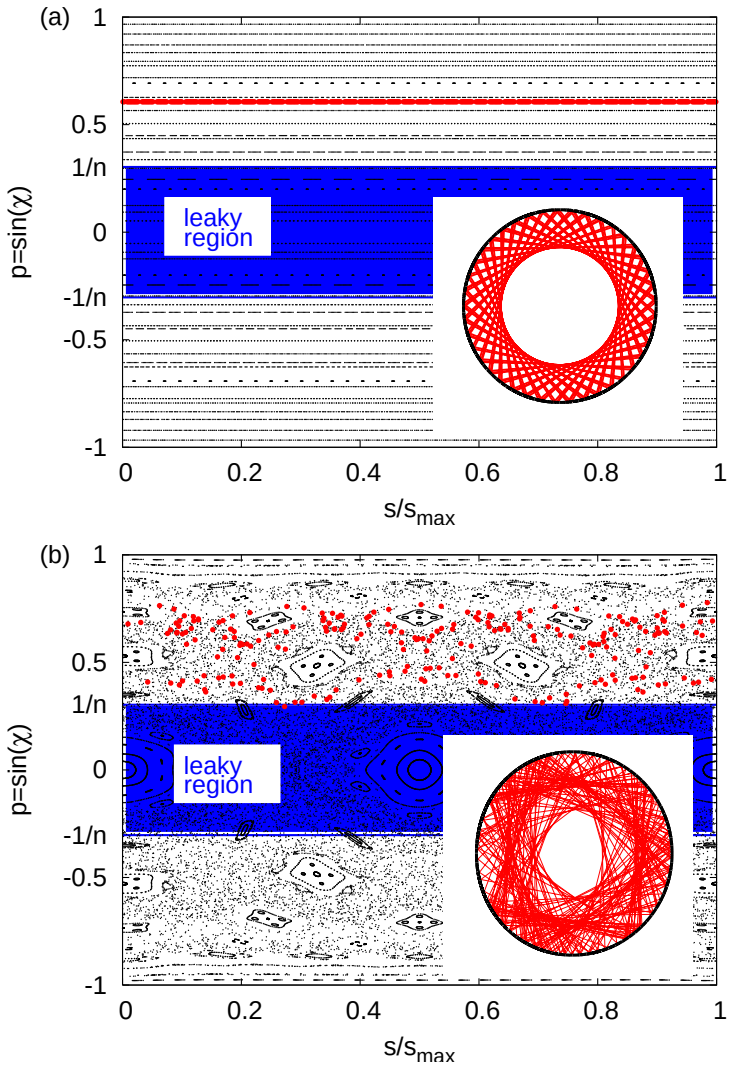

Figure 3.14.: Poincaré SOS with the leaky region (blue region) for (a) the circle, (b) the $\epsilon = 0.3$ limaçon. The insets show the trajectories indicated by the red dots in real space. The refractive index is $n = 3.3$.

4. Wave equation for microdisk cavities

In this chapter, the wave equation for microdisks is derived and methods for its numerical solution are reviewed. In section 4.2 the subject of "ray-wave correspondence", the relation between the wave and ray-dynamical description of such systems, is discussed.

4.1. Helmholtz equation

In the quasi-two-dimensional (quasi-2d) geometry of a microdisk cavity with piecewise constant index of refraction as shown in Fig. 4.1, Maxwell's equations can be reduced to scalar wave equations for the fields $E_z(x, y)$ and $H_z(x, y)$, which determine the other field components; the derivation is discussed in appendix B.

Of course, microdisks as introduced in chapter 2 are not really two-dimensional; treating them as such is an approximation. The validity of this approximation has been tested carefully in [BDM+09] for circular microwave resonators. The authors of [BDM+09] found systematic deviations of their experimental data from two-dimensional calculations. If one is only interested in modes at fixed frequency or over a small frequency range, these deviations can be accounted for by introducing a new effective refractive index [GNP+08, WYD+09, YWD+09]. In semiconductors, refractive indices are typically not known more precisely than within 1 %; the systematic deviations are well below that value. The two-dimensional approximation can thus be considered valid for microdisk resonators. Similar results were also obtained in [Mic09], where two-dimensional and three-dimensional solutions of Maxwell's equations for a disk geometry were compared.

Typically, only solutions with either $H_z = 0$ for all x, y (so-called *transverse magnetic* (TM) modes) or $E_z = 0$ (transverse electric (TE) modes) are considered in microcavities. Figure 4.2 shows how TM and TE polarizations are related to the s and p polarizations usually considered when calculating reflection coefficients. The Helmholtz equation is then a scalar equation for $\psi = E_z$ (TM case) or $\psi = H_z$ (TE case):

$$\left(\Delta + n(x, y)^2 k^2\right) \psi(x, y) = 0, \tag{4.1}$$

with the refractive index n and the wave number k. Δ is the Laplacian in the (x, y) plane. Equation (4.1) is equivalent to the time-independent Schrödinger equation. However, while Dirichlet boundary conditions ($\psi = 0$ on the boundary) are usually used in quantum mechanics, the boundary conditions in the optical case with positive refraction

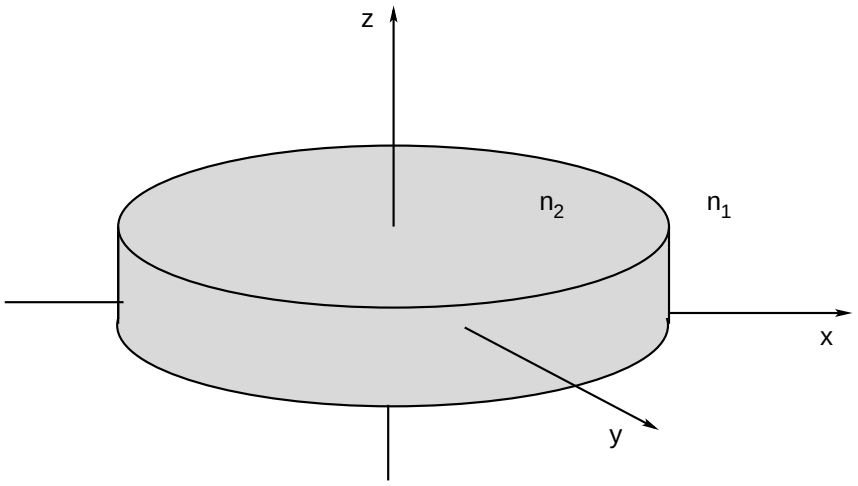

Figure 4.1.: Quasi-2d geometry. The disk plane is the (x, y)-plane and the z components of the fields determine the optical modes.

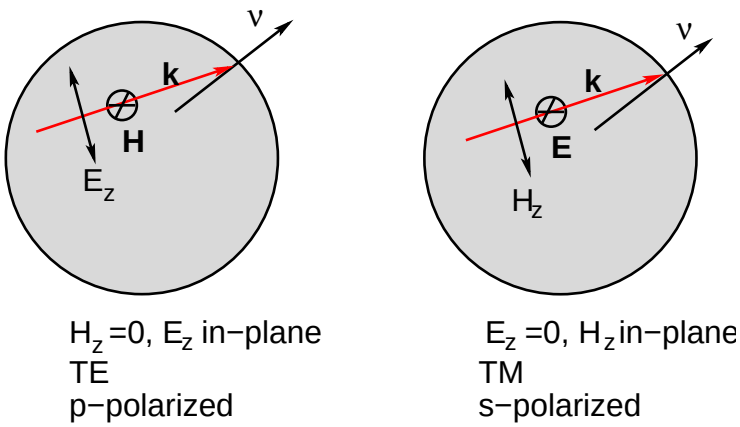

Figure 4.2.: Relation between TM and TE polarization and s and p polarization in microdisks.

read

$$\begin{aligned} \psi_1 = \psi_2,\ \partial_\nu \psi_1 = \partial_\nu \psi_2 \ (\mathrm{TM}), \\ \psi_1 = \psi_2,\ \frac{\partial_\nu \psi_1}{n_1^2} = \frac{\partial_\nu \psi_2}{n_2^2} \ (\mathrm{TE}), \end{aligned} \tag{4.2}$$

where $\boldsymbol{\nu}$ is a normal vector on the cavity boundary and $\partial_\nu = \boldsymbol{\nu} \cdot \nabla$. Often, the refractive index n_1 outside the cavity is one (vacuum). At infinity, outgoing-wave conditions are assumed, which is reasonable for the description of lasers (light is created in the cavity and can only leak out, but not come back):

$$\psi(r \to \infty) \sim h(\theta, k) \frac{e^{ikr}}{\sqrt{r}}. \tag{4.3}$$

Outgoing-wave conditions explicitly break the time-reversal invariance which the Maxwell equations still has.

Optical microcavities described by Eq. (4.1) can be seen as *open quantum billiards*, just as the ray description of such a cavity is equivalent to the dynamics of a classical particle in an open billiard. They are described by the same wave equation as quantum billiards, but different boundary conditions apply, which leads to the possibility of light leaking out of the cavity. They are thus a model system not just for quantum chaos, but for the study of quantum chaos in *open* systems. Because of this openness, the cavity modes ψ are quasi-bound states with a complex wave vector k – with the real part related to the frequency of the mode via $\omega = c \operatorname{Re} k$ and the imaginary part related to the life-time of the mode as discussed in chapter 2.

When studying microcavities, the first step is to find the optical modes of the cavity – the solutions of the Helmholtz equation with the appropriate boundary conditions. Often, they can be directly related to the lasing modes.

4.1.1. Methods for solving the Helmholtz equation

Analytical solution of the Helmholtz equation (4.1) with the boundary conditions (4.2) is only possible for a circular cross-section, where the Helmholtz equation is separable in polar coordinates. Even for an ellipse, where the Helmholtz equation separates for Dirichlet boundary conditions, an analytical solution is not possible [Nöc97] for dielectric boundary conditions. Therefore, numerical methods have to be employed; the ones which are most commonly used are briefly discussed in the following.

Wave-matching

The main idea for *wave-matching* solutions [NS95] is to expand the wave function as a series of Bessel functions inside the cavity and Hankel functions outside. Application of the continuity conditions leads to relation between the coefficients in this series, and these "matching equations" can then be numerically solved. An advantage of the method is that it is numerically quite cheap; a significant drawback, however, is that

the assumption that such as expansion is always possible (also known as the "Rayleigh hypothesis" [Ray07]) is not valid for too large deformations from the circle [vF80]. Wave-matching is thus only useful for microcavities with small deformations. Furthermore, a piecewise constant index of refraction (which may be complex) is assumed.

Finite-difference time domain methods

Finite-difference time domain (FDTD) methods [Yee66, TH00] solve Maxwell's equations by "brute force" on a spatial and temporal grid. While this method is numerically expensive especially for small wavelengths (fine discretization needed) and high-Q (long time-integration needed as one waits for the mode to decay) cavities, it has many advantages: spatial dependence of the refractive index can be included as well as nonlinearity, i.e. a dependence of the refractive index on the light intensity. FDTD codes are available commercially and can be easily adapted to various geometries.

Boundary element method

A boundary element method (BEM) [Wie03] has been used for the mode calculations in this thesis and is discussed in detail in appendix C. The basic idea it to map the Helmholtz equation to an integral equation defined on the cavity boundary and then solve this integral equation numerically. This method is numerically relatively inexpensive. The refractive index, however, has to be piecewise constant. As in the wave-matching and FDTD cases, it may be complex.

4.1.2. Simulation of lasing

All methods described so far consider interaction with the cavity material only via the refractive index. A cavity used for lasing needs a *gain medium* which amplifies light. This can be included by using a complex refractive index whose imaginary part corresponds to gain (or loss) in the medium. This, of course, is a very simple material model which completely ignores the microscopic nature of the gain medium; it also neglects nonlinear interaction between the modes, which modifies the lasing frequencies. The method described in the following tries to improve on this by introducing a very simple microscopic model and coupling it to the electromagnetic field in a cavity.

In the Maxwell-Bloch equations approach (described for microcavities in [HSI05]), a quantum two-level system is coupled to the classical electromagnetic field, and the resulting equations are solved. Using this approach, mode interaction can be studied and the lasing frequencies can be predicted more accurately. For high pumping power, the numerical solution of the Maxwell-Bloch equations is numerically expensive; sometimes, it is enough to just consider the *slowly varying* parts on the field amplitudes. In this case, the Maxwell-Bloch equations reduce to the Schrödinger-Bloch equations, which are also nonlinear (the name comes from the fact that the equation for the fields is formally equivalent to a Schödinger equation with an potential depending on the wave function).

Self-consistent laser theory

An interesting way of solving the Maxwell-Bloch equations in the steady state, the so-called *self-consistent ab initio laser theory* (SALT) [TSC06, TSG07, TSG+09] uses the fact that in the steady state, the Maxwell-Bloch equations can be integrated using a Green's function approach. In this formalism, multimode lasing and mode competition are described well; the method can be applied to a variety of geometries and random lasers as well.

A problem with methods based on the Maxwell-Bloch equations is that the material model is too simple. Investigations in semiconductor physics have shown (see, e.g., [GWLJ07] for an example using quantum dots as a gain medium) that the dynamics in semiconductors is far more complex than the one in a two-level system and that this fact leads to modifications in the emission properties of semiconductor lasers.

4.2. Ray-wave correspondence

As discussed in the previous section, optical microcavities can be seen as open quantum billiards (with boundary conditions different from the ones usually encountered in quantum systems), and because of the analogy between the Helmholtz equation and the time-independent Schrödinger equation, methods from the field of quantum chaos can be applied to them. One important question in quantum chaos is the relation between the quantum and the classical properties of a system; this is known as "quantum-classical correspondence" in the quantum chaos field, where the corresponding relation between the ray and the wave description of a cavity is called "ray-wave correspondence". While it is clear that such a correspondence has to exist – after all, the ray description is found from the wave description in the limit $kR \to \infty$ ($\lambda/R \to 0$), where R is a typical cavity length scale, and the classical dynamics follows from quantum mechanics in the limit $\hbar \to 0$ –, the details are less clear, in particular in the case of systems with chaotic ray dynamics. It is shown in section 4.2.2 that the standard way of deriving the ray limit of the Helmholtz equation in general fails for systems with chaotic dynamics.

Chaos in quantum systems can not be defined as the exponential divergence of trajectories, because there are no trajectories and the time evolution is linear. Instead, it often is defined via the *statistics* of energy levels (mode frequencies in the cavity case) [Haa10, Stö00], which is distinctively different for regular and chaotic dynamics. However, it is also possible to relate mode lifetimes and other properties to the ray dynamics in a cavity (examples are discussed in section 4.2.3), and modes can be projected onto the Poincaré SOS for comparisons with the ray dynamics (this is discussed in section 4.2.1).

If one considers quantum systems near the classical limit (corresponding to cavities with $kR \gg 1$, i.e. the wavelength λ is small compared to the system size R), one can try to express quantities like the density of states as a series in $\hbar$ (or, correspondingly, λ/R). Considering only the first terms in such an expansion is called *semiclassical approximation*; an important result is the so-called Gutzwiller trace formula [Gut71], which links the quantum mechanical density of states to a sum over the periodic orbits

of a system. For optical microcavities, a similar trace formula (which takes into account the reflection coefficient and the phases a ray acquires when scattered at the boundary) has been developed [BDS08] and tested experimentally for a microwave cavity [BBD+10]. Periodic orbits in chaotic mesoscopic systems often can be directly related to measurable quantities, like magneto-resistance oscillations [WRM+93]. Pairs of trajectories (the so-called "Sieber-Richter-pairs") [RS02] with small action differences can be used to calculate quantum corrections to conductivities in mesoscopic systems as well. Another way to do semiclassics is not to come from the wave (quantum) limit and expand in λ/R ($\hbar$), but to come from the ray (classical) limit and introduce corrections proportional to λ/R ($\hbar$). One way to do this is described in detail in chapter 6.

4.2.1. Husimi distribution

One important tool for the study of ray-wave correspondence is the so-called Husimi distribution, which was introduced by Husimi [Hus40], adapted for quantum billiards by Crespi *et al.* [CPC93], and has been generalized to dielectric cavities in [HSS03]. The basic idea is to *project* the wave function on the cavity boundary to the Poincaré SOS. In the Poincaré SOS, a ray's position at the boundary and momentum are noted. The probability of light intensity to be found at the phase space position (s, p) is given by the overlap of ψ and a coherent state localized at (s, p); such a coherent state most closely resembles the classical ray. The calculation of Husimi distributions in dielectric cavities is discussed in section C.3.

It is clear that calculating Husimi distributions only makes sense if the wavelength λ is not too large compared to the typical cavity length scale R (i.e. for $kR \gg 1$). If $\lambda \approx R$, the widths of the coherent states become large, and there is no good correspondence between the projection and the Poincaré SOS. The Husimi distribution itself is a semiclassical approximation. However, it seem that even for small kR, Husimi distributions yield sensible results especially when compared not to the conventional, but an extended ray dynamics which includes wave corrections (see chapter 6). Figure 4.3 shows an example for the correspondence of Husimi distributions to the Poincaré SOS.

4.2.2. Eikonal approximation

Ray dynamics, which has been discussed in chapter 3, is a limiting case of wave dynamics in the limit $\lambda/R \to 0$ (or $kR \to \infty$). In this section, it is shown how ray dynamics can be derived from wave dynamics by means of the so-called *Eikonal ansatz*; it is formally equivalent to the derivation of the classical Hamilton-Jacobi equation from the Schrödinger equation (see, e.g., [Nol08]). The discussion here follows [TSS05]; a similar argument has already been proposed by Einstein [Ein17]. It will be shown that Eikonal theory usually fails for systems with chaotic dynamics.

The ansatz in Eikonal theory is to write the wave function $\psi(\mathbf{r})$ as

$$\psi(\mathbf{r}) = A(\mathbf{r})e^{ikS(\mathbf{r})}; \tag{4.4}$$

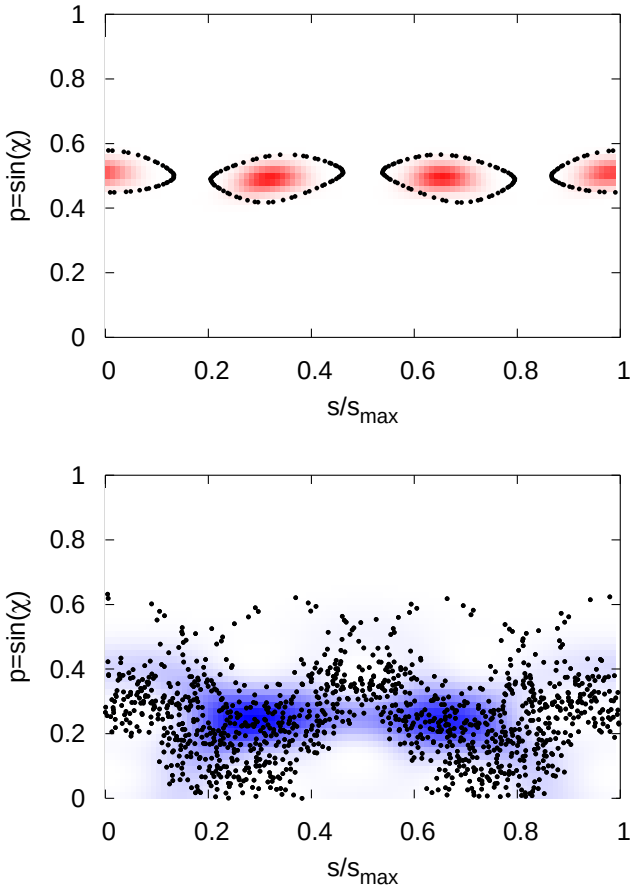

Figure 4.3.: Husimi distributions for (top panel) a "regular" state (in the $\epsilon = 0.2$ limaçon cavity) and (bottom panel) a "chaotic" state (in the $\epsilon = 0.3$ limaçon cavity). The dots indicate the corresponding ray dynamics.

this can be seen as the first term of an expansion

$$\psi(\mathbf{r}) = e^{ikS(\mathbf{r})} \sum_{j=0}^{\infty} \frac{A_j(\mathbf{r})}{k^j} \tag{4.5}$$

in $1/k \sim \lambda$. The function $S(\mathbf{r})$ is called the "Eikonal" (from the Greek word for "image") in geometric optics; it corresponds to the action function in Hamilton-Jacobi theory. Inserting the ansatz (4.4) into the Helmholtz equation (4.1) yields

$$\begin{aligned} \Delta\psi &= ik\psi\Delta S + 2ike^{ikS}\nabla S \cdot \nabla A + e^{ikS}\Delta A - k^2\psi\nabla S \cdot \nabla S \\ &= -k^2 n^2 \psi, \end{aligned} \tag{4.6}$$

which can be written as the Eikonal equation

$$(\nabla S(\mathbf{r}))^2 = n^2(\mathbf{r}) \tag{4.7}$$

and the so-called "transport equation"

$$2\nabla S \cdot \nabla A + A\Delta S = 0 \tag{4.8}$$

if A only varies weakly with $\mathbf{r}$, so that $\Delta A \approx 0$ can be assumed. A wave solution ψ thus defines a family of light rays described by the vector field ∇S, which defines the propagation direction; the lines of constant S can be interpreted as wave fronts. The Eikonal ansatz is justified if the wave function ψ does not vary significantly on scales smaller than the wavelength λ. Only in this case one can define wave fronts which are straight lines on scales longer than a wavelength. The assumption that wave fronts exist, and thus that an Eikonal ansatz can be made, is usually valid for system with integrable dynamics. It is, however, usually *not* valid for systems with chaotic dynamics; there, the wave function varies on the scale of the wavelength. An example is shown in Fig. 4.4.

In general, one Eikonal as in Eq. (4.4) is not sufficient to fulfill the dielectric boundary conditions, and the ansatz has to be improved by superimposing many Eikonal wavefunctions,

$$\psi(\mathbf{r}) = \sum_j A_j(\mathbf{r}) e^{ikS_j(\mathbf{r})}. \tag{4.9}$$

If a ray defined by a momentum ∇S_j from the expansion (4.9) collides with the boundary, it ceases to exist and another ray defined by $\nabla S_{j'}$ from the expansion takes its place, travelling in a different direction. It is sufficient to take into account a finite number of terms in Eq. (4.9) if a ray coming from a point $\mathbf{r}_0$ with a momentum ∇S_j can re-enter the vicinity of $\mathbf{r}_0$ only with a finite number of possible momenta $\nabla S_{j'}$. This is trivially the case for periodic orbits: there, the return momentum is fixed. It is also more generally the case for regular motion also on non-periodic orbits. If one, however, has a system with *chaotic* ray dynamics, it is no longer the case, as the number of possible return momenta grows infinitely as time goes to infinity because of the phase-space filling property of chaotic trajectories. Thus, no Eikonal ansatz with a finite number of Eikonals exists for chaotic systems. An *infinite* sum in Eq. (4.9) is used in the so-called

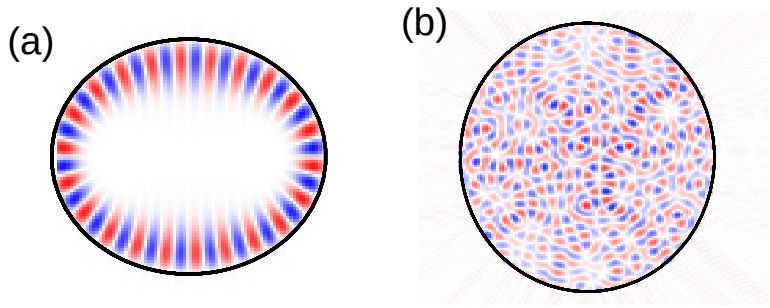

Figure 4.4.: Wave functions $\mathrm{Re}\,\psi$ in (a) a regular state (in the ellipse) and (b) a chaotic state (in the limaçon). Wave fronts can only be defined if the wavefunction does not vary significantly on scales smaller than the wavelength; this is not fulfilled in (b).

"random superposition of plane waves" models [Ber77] for chaotic wave functions, which are used to predict statistical properties of chaotic systems. However, when the Eikonal ansatz is considered, the amplitudes in the infinite sum in Eq. (4.9) are not random, but fixed by the transport equation (4.8), and the sum would in general diverge, because the amplitudes A_j can not get arbitrarily small. One can thus conclude that the Eikonal ansatz does not work in chaotic systems; while an ansatz similar to the Eikonal one can be used when considering statistical properties, it is not useful to construct the ray dynamics from the wave function as it can be done in systems with regular dynamics. How ray and wave properties can be linked in chaotic systems is discussed in the next section.

4.2.3. Wave localization and tunneling

In the following, different mechanisms leading to the localization of the wave function ψ in certain parts of phase space are discussed as well as mechanisms which lead to *delocalization* and the leaking of intensity out of a cavity. Such delocalization mechanisms are related to the quantum mechanical effect of *tunneling*; an in-depth discussion can be found, e.g., in [Löc09]. Evanescent leakage, the electromagnetic analog of quantum tunneling, has been directly observed in microcavities, as described in [TKJVC09]. There, both the light inside a cavity and the emitted light outside have been measured, and a "gap" region of small intensity right outside the cavity boundary was found, providing direct evidence that the light indeed "tunnels" out of the cavity.

Both wave localization and "tunneling" are directly related to properties of optical

microcavities: wave localization above the critical line for TIR ensures high Q factors, and tunneling rates into the leaky region or to chaotic parts of the phase space influence both the Q factor and the output directionality.

Localization on stable islands

The *semiclassical eigenfunction hypothesis* [Per73, Ber77] states that although chaos and regularity in quantum chaos are defined on the basis of the statistics of many quantum states, individual wave functions belonging to regular and chaotic states can well be distinguished by their localization on corresponding phase space structures – "regular" states localize on regular phase space structures, i.e. islands or tori, and "chaotic" states localize on chaotic parts of phase space (Fig. 4.3 shows an example for this behaviour). While this hypothesis is valid in many cases, there are examples where it is wrong: in [HKOS02], which considers a kicked system, states with contributions both in regular and chaotic parts of phase space are found. This phenomenon is known as "flooding of regular islands" [BKM05, BKM07] and the corresponding states are sometimes called "amphibious states".

Scarring

Scarring [Hel84] is a wave interference effect which leads to the localization of states along unstable periodic ray trajectories. Scarred modes have been observed in optical microcavities both theoretically and experimentally [RTS$^+$02, LLC$^+$02, LRR$^+$04, FYC05]; they are important for applications because while they can have high Q factors, they still can be subject to chaotic transport, which can lead to desirable output properties [WH08]. Scarring has been observed not only in microcavities; scarred modes have, i.e., been discovered in optical fibers as well [DLMM01].

Dynamical localization

Another wave interference effect is *dynamical localization* [FGP82]. Here, destructive interference leads to a reduction of diffusion through chaotic regions of phase space, which in turn can lead to higher life-times of light in a cavity. Dynamical localization has been observed in optical microcavities with rough boundaries [FS97, FCPN05]; it is closely related to Anderson localization [And58] known from solid state physics.

Dynamical tunneling

In quantum mechanics, tunneling refers to the passing on an *energy barrier* which can not be passed classically. Dynamical tunneling [DH81] means the passing of a barrier in *phase space*, which also is classically not possible: for example, invariant lines are followed for all times and can not be left classically, but as wave functions are always delocalized in phase space, this is not true quantum mechanically, and the transfer from an invariant line to another part of phase space is possible. Dynamical tunneling has been investigated not only for quantum systems, but also for optical microcavities

[HN97]; dynamical tunneling rates have been related to Q factors of a microdisk in the case of the Annular microcavity [BKL$^+$09].

Chaos-assisted tunneling

Chaos-assisted tunneling [TU94] refers to the tunneling between regular parts of a mixed phase space not directly, but via an intermediate step into a chaotic part of phase space. Because transport in the chaotic regions is fast, chaos-assisted tunneling can dominate over dynamical tunneling even though it is a two-step process. Chaos-assisted tunneling has been observed in microwave cavities [DGH$^+$00] as well as optical microcavities [PN05], where it can lead to directional emission [SHF$^+$10].

5. Directional emission from elliptical resonators with a notch

5.1. Resonators with notches and point scatterers

As discussed in chapter 2, finding resonator shapes which allow for modes with high Q factors and directional light output is interesting for applications. Combination of these two features can be achieved in many different ways [WUS+10b, XZL+10]. One of them is structuring the circular boundary on a wavelenght-size scale, i.e. by cutting one or many notches in it; the Q factors and directionalities resulting from such deformations are studied in [BBSN06a] in microdisk resonators. Another way is placing an obstacle inside a circular resonator. This obstacle can be an air hole (so-called annular cavity [HR02, WH06]; investigated experimentally in [TV07]) or a small region with a high refractive index, which acts as a point scatterer [AR04, DMSW08, DMSW09]. Both deformations of the circle lead to the development of modes with high Q factors and directional emission.

In this chapter, an elliptical microcavity (which, like the circle, has high-Q modes, but no directional emission) with a wavelenght-size notch at the boundary is studied and shown to have highly directional emission. The notch acts like a point scatterer; the unidirectional emission, however, is achieved because of the elliptical boundary shape, which is shown to collimate light scattered by the notch in the far field. This notched elliptical resonator has high-Q modes, unidirectional emission with very low beam divergence (≈ 5 degrees). Moreover, the far field is universal (all even parity modes have the same far field pattern) and the directionality can be achieved for both TM and TE polarization.

5.2. The Gaussian-notched elliptical resonator

In Cartesian coordinates, the boundary shape of a notched elliptical resonator can be written as

$$\begin{aligned} x &= \left[\epsilon - \delta \exp\left(\frac{-2(\phi-\pi)^2}{\vartheta^2}\right)\right]\cos\phi, \\ y &= \sin\phi. \end{aligned} \tag{5.1}$$

with the major and minor axes Y and X and $\epsilon = X/Y$. This describes an ellipse with a notch at $\phi = \pi$. The notch depth is controlled by the parameter δ, the notch opening

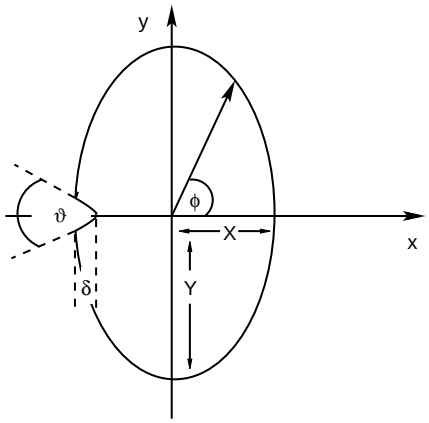

Figure 5.1.: Parameters describing the notched ellipse. $\epsilon = X/Y$ is the ratio of the half-axes, δ and ϑ control the notch depth and width, respectively.

angle (notch width) is controlled by the parameter ϑ (see Fig. 5.1). Equation (5.1) yields a Gaussian-shaped notch; while other shapes are possible, the results are quite independent on the precise form, as will be shown later. The Gaussian shape is here chosen mostly for numerical convenience, as no piecewise defined boundary curve has to be used. In section 5.5, other notch shapes are studied as well.

Figure 5.2 shows a Poincaré surface of section for the notched ellipse. The "notching" is a perturbation applied to an integrable system (the elliptical billiard, see section 3.3.1). Upon applying this perturbation, the system dynamics becomes mixed; there are large chaotic regions as well as stable islands, as indicated in Fig. 5.2. The feature which will prove to be most important for the understanding of directional emission from the notched elliptical resonator is the existence of rays like the one marked green in Fig. 5.2. Such rays travel along the boundary, like whispering-gallery rays, for many bounces; but at some point, they hit the notch and get reflected into a bouncing-ball like motion (the opposite, bouncing-balls getting reflected into whispering-galleries by the notch, also happens, of course). As any non-periodic whispering-gallery ray will hit the notch at some point, this type of motion is very common in this system.

5.3. Far field emission patterns

5.3.1. Calculating far field emission from ray dynamics

Far field emission patterns can be calculated using the Fresnel-weighted unstable manifold of the chaotic repeller [LRK+04, SH07, WH08]. The chaotic repeller is the set of phase space points that never visits the leaky region both in forward and backward time evolution; its unstable manifold is the set of points that converges to it in backward time evolution. In open, chaotic systems, the unstable manifold controls the escape routes out of the system. Consider a ray starting on a phase space point on the unstable manifold in the leaky region. In forward time evolution, it will refract out of the cavity

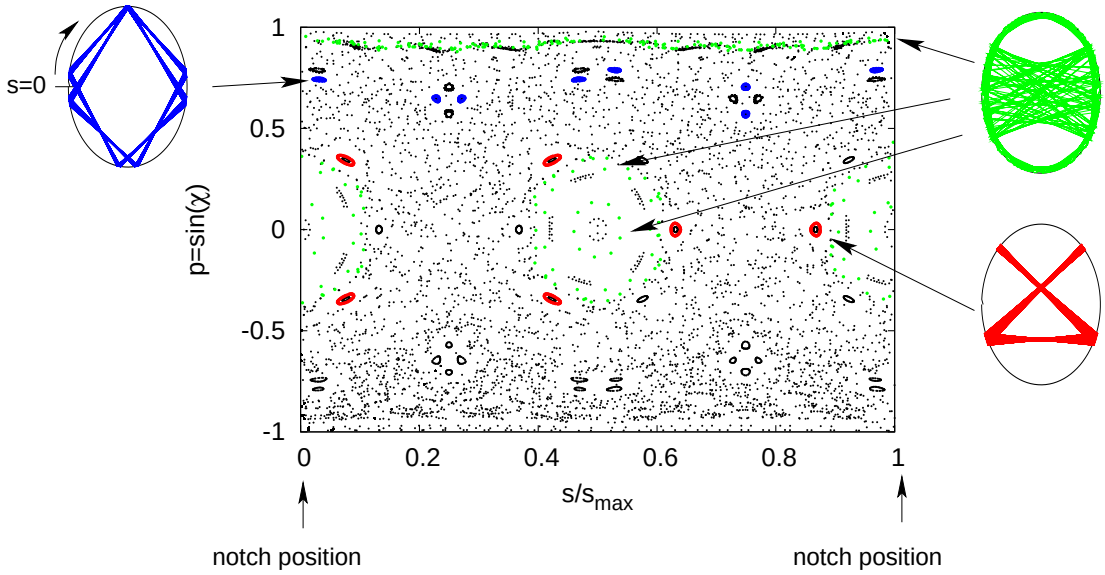

Figure 5.2.: Poincaré surface of section for an ellipse with $\epsilon = 0.83$ with a Gaussian notch with $\delta = 2/96$ and $\vartheta = 3/96$. Some stable islands ("bowtie" (red) and a period-8 island (blue) which avoids the notch) are indicated as well as a ray (green) following a whispering-gallery structure for a long time until hitting the notch which is located at $s/s_{\max} = 0 \equiv 1$.

soon because it starts below the critical angle for total internal reflection. In backward time evolution, it will stay in the cavity basically forever, because the time evolution of the point converges to the chaotic repeller and never visits the leaky region. Thus, the overlap region of the unstable manifold with the leaky region consists of long-lived rays refracting out of the cavity eventually. Even though the concept of escape along the unstable manifold was developed for chaotic systems, Altmann [Alt09] has only recently shown that it can be applied to systems with a mixed phase space as well.

The unstable manifold can be calculated as a survival probability [LRK+04]. One starts with an ensemble of rays uniformly distributed in phase space with equal intensity (set to one). They are then subjected to the time evolution of the system; at each bounce, the intensity I of each ray is changed according to the Fresnel laws: $|r(\chi)|^2 I$ for the reflected ray staying inside the cavity and $|t(\chi)|^2 I$ for the transmitted ray, which gets refracted out (see Fig. 5.3). r and t are the complex Fresnel reflection and transmission coefficients; they fulfill $|r|^2 + |t|^2 = 1$. The outgoing angle η can be calculated using Snell's law: if the incoming ray hits the boundary under the angle χ, then $\sin\eta = n \sin\chi$ with the refractive index n of the cavity (assuming $n = 1$ outside). From η, the far field emission angle θ can be calculated as the angle between the emission direction and the positive x axis (see Appendix A for details). Here, θ is taken between $-\pi$ and 0 (-180 degrees and 0 degrees) for emission into the $y < 0$ half-space, and $0 \leq \theta \leq \pi$ (0 degrees $\leq \theta \leq$ 180 degrees) otherwise. Adding up the contributions of all rays in the initial ensemble to the intensity outside the cavity, one finds the far field pattern. Figure 5.4

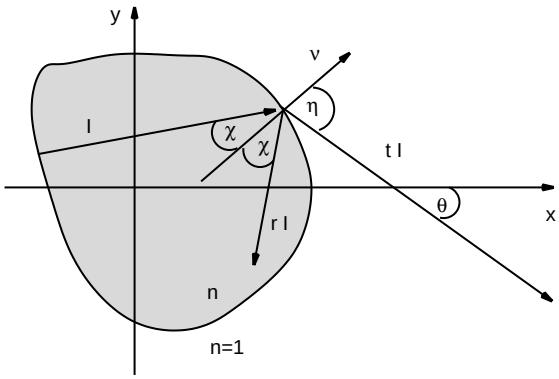

Figure 5.3.: Calculating far field emission from ray dynamics. A ray with intensity I is reflected at the boundary; the reflected parts gets the updated intensity $|r|^2 I$ with the Fresnel coefficient $r = r(\chi)$, the outgoing part the intensity $|t|^2 I$. The outgoing angle η can be calculated using Snell's law. The far field emission angle θ is then the angle between the emission direction and the x axis.

shows an exemplary far field pattern for the notched ellipse as well as a Fresnel-weighted unstable manifold, both generated by starting 1000 uniformly distributed rays. This system shows highly directional emission.

5.3.2. Far field of the notched ellipse

How is the highly directional emission from the notched elliptical cavity archived? It is not obvious from the unstable manifold alone (Fig. 5.4); while the unstable manifold only has small tails into the leaky region ($s/s_{\max} = 1$ and $0.0 \leq s/s_{\max} \leq 0.6$), this overlap region contains many different angles χ, which in turn could be naively thought to lead to various far field angles θ.

One part of the answer can be found if one studies *where* the outgoing rays *come from*. Starting again with a uniform distribution of rays, they are followed until they get refracted out of the cavity (i.e., until $|\sin\chi| \leq 1/n$), and the position they are coming from is noted. Most interesting are *long-lived* rays escaping the cavity. Figure 5.5 shows where long-lived rays escaping the cavity come from in phase space (top panel) and around the cavity boundary (bottom panel). The areas right above the critical line and around $p = 0.5$, where some long-lived rays come from, are connected to the bowtie- and period-8 stable islands indicated in Fig. 5.2. The long, narrow structure around $s/s_{\max} \approx 0.7$ comes from the unstable period-3 orbit, two bounce points of which are right below the critical line. But these different structures are not responsible for the majority of the escaping rays, as can be seen from the bottom panel of Fig. 5.5. The majority of escaping rays comes from $s/s_{\max} = 0 \equiv s/s_{\max} = 1$: the notch position. The notch thus acts like a *point scatterer*: rays hit it, get scattered to the other side of the cavity with some new angle of incidence, and then can get refracted out. When this

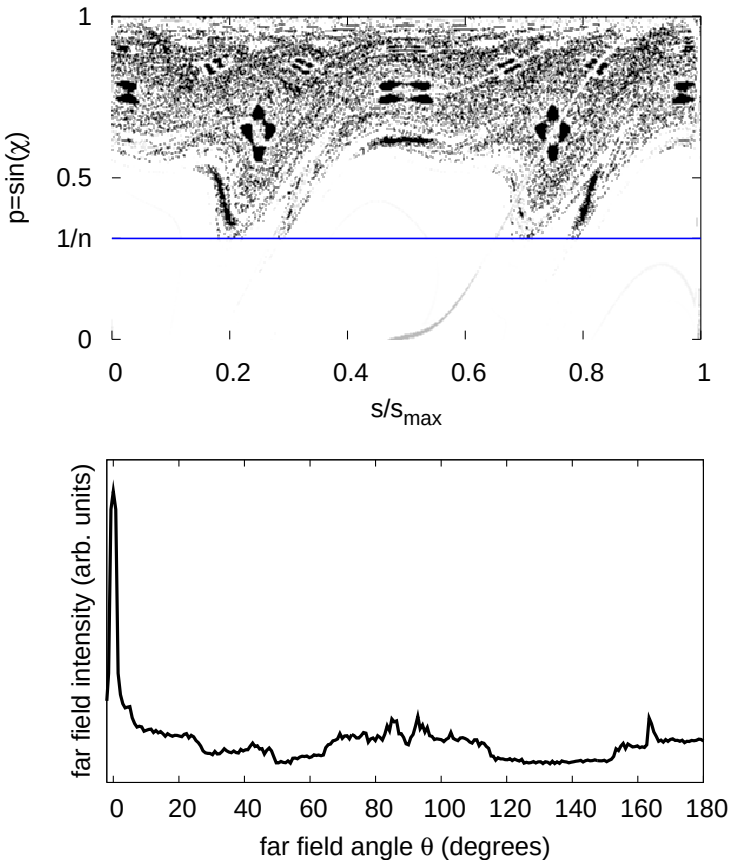

Figure 5.4.: Top panel: Fresnel-weighted unstable manifold for the notched ellipse with $\epsilon = 80/96$, $\delta = 2/96$, $\vartheta = 3/96$. The refractive index is $n = 3.2$, the polarization TM. Bottom panel: the resulting far field pattern.

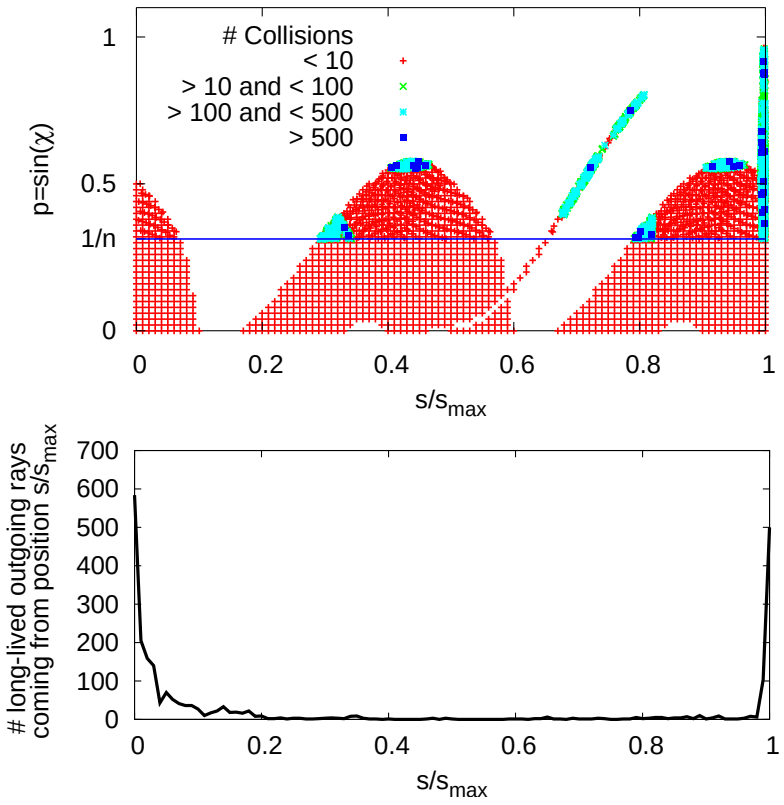

Figure 5.5.: Top panel: phase space positions of the origins of escaping rays. Bottom panel: positions along the cavity boundary of long-lived (> 500 collisions before escaping) escaping rays at the position right before the one they are refracted out at.

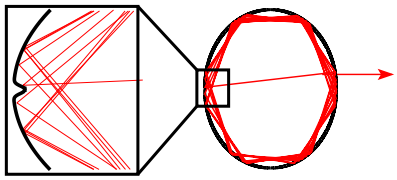

Figure 5.6.: A whispering-gallery-like ray hits the notch and is refracted out of the cavity. The magnification shows to dynamics near the notch.

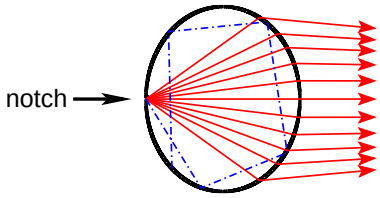

Figure 5.7.: Scattering and collimation: rays are started from the notch position with different outgoing angles. Rays with small outgoing angles are collimated in the far field; this collimation gets worse as the outgoing angle grows. At some point (dashed blue line) the ray no longer escapes, but travels inside the cavity as a whispering-gallery-like ray until it gets scattered once again.

happens to whispering-gallery rays (like the ray marked in green in Fig. 5.2), these rays can travel along the cavity boundary for a long time before finally escaping. Figure 5.6 shows another example of the scattering of a whispering-gallery-like ray by the notch.

So the escaping rays mostly are rays which have been scattered by the notch. They then become parallel rays in the far field, as can be been in Fig. 5.7: there, rays are started at the position of the notch with different outgoing angles, simulating a scattering process. Rays with small outgoing angles become parallel in the far field; this collimation process gets worse for larger outgoing angles, and at some point the outgoing angle is large enough for the ray not being refracted out, but being launched into a whispering-gallery-like mode. Such collimation is known from lenses in geometric optics [BW59]. Directional emission from cavities with point scatterers and collimation according to geometric optics has been studied by Dettmann and coworkers [DMSW08, DMSW09]; however, they only consider circular resonators with high-refractive index scatterers. Such scatterers are difficult to fabricate experimentally, and, as will be shown below, the circular boundary is not optimal for collimation.

In the next section, the collimation of rays in an elliptical resonator will be studied using a geometric optics approach.

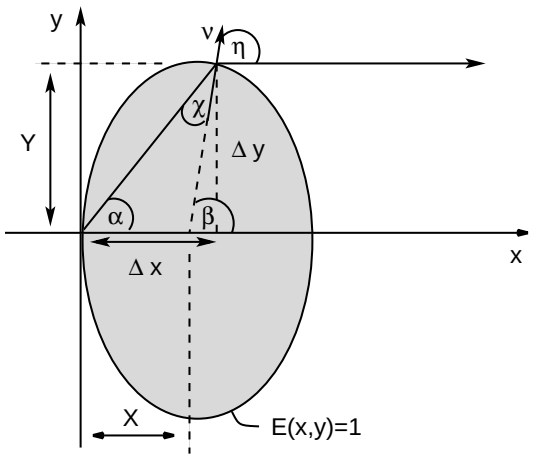

Figure 5.8.: Collimation of light rays in an ellipse. A ray coming from point $(0,0)$ with an angle α is collimated. The parameters X, Y have to be chosen such that rays originating from $(0,0)$ are collimated.

5.4. Collimation of rays scattered by the notch: a "lens model"

5.4.1. Collimation in elliptical resonators

As seen in the previous section, an elliptical cavity can act as a "lens" and collimate rays coming from a fixed position with small angles. In the notched ellipse, this fixed position corresponds to the notch position, which is approximately the $s = 0$ position of the boundary (5.1). The goal of this section is to find the *parameters* of such an ellipse archiving collimation. Figure 5.8 shows collimation of a ray originating $(0,0)$; the parameters of the ellipse now have to be chosen such that this is possible.

The elliptical boundary is given by

$$E(x,y) = \frac{(x+X)^2}{X^2} + \frac{y^2}{Y^2} = 1, \tag{5.2}$$

the normal vector $\boldsymbol{\nu}$ at the position (x,y) on the boundary is given by

$$\boldsymbol{\nu} = \frac{1}{|\nabla E|}\nabla E = \frac{1}{\sqrt{\frac{(x+X)^2}{X^4} + \frac{y^2}{Y^4}}} \begin{pmatrix} (x+X)/X^2 \\ y/Y^2 \end{pmatrix}. \tag{5.3}$$

The following relations can be found from Fig. 5.8:

$$\tan\alpha = \frac{\Delta y}{\Delta x}, \tag{5.4}$$

$$\beta = \eta, \tag{5.5}$$

$$\alpha = \eta - \chi, \tag{5.6}$$

$$\sin\eta = \boldsymbol{\nu} \cdot \begin{pmatrix} 0 \\ 1 \end{pmatrix}; \tag{5.7}$$

the Snell law

$$\sin\eta = n\sin\chi \tag{5.8}$$

holds as well. Equation (5.7) leads to

$$\sin\eta = \frac{y/Y^2}{\sqrt{\frac{(x+X)^2}{X^4}+\frac{y^2}{Y^4}}}. \tag{5.9}$$

Considering collimation only for small angles (rays with larger angles will get reflected back into a whispering-gallery anyway), one can set

$$\tan\alpha \approx \alpha,\ \eta \approx n\chi,\ x \approx X,\ \text{ and } \Delta y = y \ll x. \tag{5.10}$$

One then finds

$$\begin{aligned}\Delta x \approx \frac{\Delta y}{\alpha} = \frac{\Delta y}{\eta-\chi} &= \frac{\Delta y}{\eta\left(1-\frac{1}{n}\right)} \\ &\approx \frac{Y^2\sqrt{\frac{(x+X)^2}{X^4}+\frac{y^2}{Y^4}}}{1-1/n} \approx \frac{1}{1-1/n}\frac{Y^2}{X}.\end{aligned} \tag{5.11}$$

The requirement that rays originating from $(0,0)$ are collimated means that $\Delta x \approx x \approx X$. This leads to

$$\frac{X}{Y} \equiv \epsilon = \frac{1}{\sqrt{2}}\frac{1}{\sqrt{1-1/n}}. \tag{5.12}$$

5.4.2. Collimation for other boundary shapes

The ellipse collimates light scattered by the notch with small outgoing angles. Of course, as rays scattered by the notch emerge with all outgoing angles, it is interesting to ask if there is a shape which collimates light for *all* outgoing angles. To answer this question, one can consider a cavity boundary curve described by $y = f(x)$ and look for a function f such that rays coming from $(0,0)$ are collimated (Fig. 5.9). The following relations can be read off the figure:

$$\tan\alpha = \frac{\Delta y}{x_0} = \frac{f(x_0)}{x_0}, \tag{5.13}$$

$$\tan\beta = -\frac{1}{f'(x_0)} = \tan\eta, \tag{5.14}$$

$$\sin\eta = n\sin\chi, \tag{5.15}$$

$$\alpha = \eta - \chi. \tag{5.16}$$

With $\alpha = \eta - \chi$, one finds

$$\tan\alpha = \tan(\eta-\chi) = \frac{\tan\eta - \tan\chi}{1+\tan\eta\tan\chi}; \tag{5.17}$$

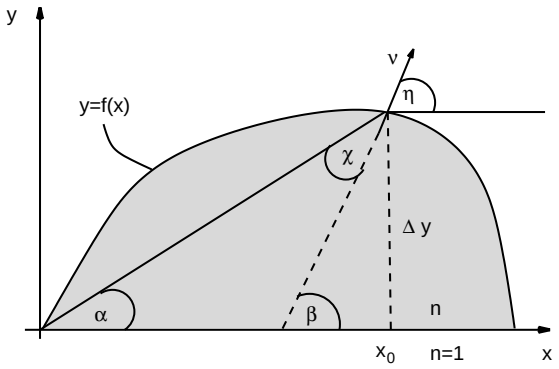

Figure 5.9.: Relations between different parameters in a cavity bounded by the curve $y = f(x)$. The refractive index inside the cavity is n; outside, it is 1. A ray starting at $(0, 0)$ with an angle α is collimated after refracting out of the cavity.

$\tan\chi$ can be calculated from Snell's law:

$$\begin{aligned}\tan\chi &= \frac{\sin\chi}{\sqrt{1-\sin^2\chi}} = \frac{\frac{1}{n}\sin\eta}{\sqrt{1-\frac{1}{n^2}\sin^2\eta}} \\ &= \frac{\tan\eta/n}{\sqrt{1+\tan^2\eta}}\frac{1}{\sqrt{1-\frac{1}{n^2}\left(\frac{\tan^2\eta}{1+\tan^2\eta}\right)}} \\ &\equiv \mathcal{G}(\tan\eta).\end{aligned} \tag{5.18}$$

Combining Eq. (5.18) and Eq. (5.17), using $\tan\eta = -1/f'(x_0)$ and inserting in Eq. (5.13) yields

$$\begin{aligned}\tan\alpha &= \frac{\tan\eta - \mathcal{G}(\tan\eta)}{1+\tan\eta\mathcal{G}(\tan\eta)} = \frac{f(x_0)}{x_0} \\ &\to \frac{-\frac{1}{f'(x_0)} - \mathcal{G}\left(-\frac{1}{f'(x_0)}\right)}{1-\frac{1}{f'(x_0)}\mathcal{G}\left(-\frac{1}{f'(x_0)}\right)} = \frac{f(x_0)}{x_0}.\end{aligned} \tag{5.19}$$

This is a differential equation for the unknown function f and can be solved numerically. Unfortunately, no solution leading to a *closed cavity* exists; the solutions do not have two intersections with the x-axis.

However, a solution leading to a closed cavity exists if Eq. (5.13) does not have to be true for *all* angles α, but instead only for *small* angles. Rays originating from $(0, 0)$ with small angles will then be collimated. In this limit, one has $\tan\eta \approx \sin\eta \approx \eta$ and

orders η^2 and higher can be neglected in Eq. (5.19). This yields

$$\begin{aligned} -\frac{1}{f'(x_0)}\left(1-\frac{1}{n}\right) &= \frac{f(x_0)}{x_0} \\ \rightarrow f'(x_0)f(x_0) &= -x_0\left(1-\frac{1}{n}\right). \end{aligned} \tag{5.20}$$

This differential equation can be solved analytically, for example using separation of variables, which leads to

$$f(x_0) = \sqrt{2c - \left(1-\frac{1}{n}\right)x_0^2} \text{ with an integration constant } c. \tag{5.21}$$

For $c > 0$, this describes an *elliptical* shape, which is closed.

5.5. Dependence of the far field directionality on the system parameters

5.5.1. Axis ratio $\epsilon = X/Y$

As seen in the previous section, far field directionality is archived because the elliptical cavity boundary acts like a lens and collimates the rays scattered by the notch. For any given refractive index n, this works only for one axis ratio $\epsilon = X/Y$ (see Eq. (5.12)). Choosing $n = 3.2$, this optimal axis ratio is

$$\epsilon = \frac{1}{\sqrt{2}}\frac{1}{\sqrt{1-1/n}} \approx 0.83. \tag{5.22}$$

Figure 5.10 shows the far field pattern of notched ellipses with different axis ratios ϵ. Indeed, values near the optimal ϵ lead to the "best" directionality. This is quantified in Fig. 5.11, where the ratio of the intensity emitted into $0 \leq \theta \leq 20$ degrees to the overall emitted intensity is plotted for different ϵ's. The full width at half maximum (FWHM) of the $\theta = 0$ peak is also shown. The notch depth and width are fixed at $\delta = 5/96$ and $\vartheta = 2/96$, respectively.

Indeed, one only finds far field directionality near the optimal ϵ; far away, the far field pattern is almost uniform, as it could be expected from whispering-gallery-rays in an elliptical cavity. Such a far field is also shown for comparison in Fig. 5.10 (blue curve). The main peak at the optimal ϵ is very sharp (≈ 5 degrees). This is significantly less then what can be achieved in the limaçon (≈ 20 degrees) and other systems. A drawback is that the percentage of the overall intensity which is emitted in the main peak is rather small, i.e. below 50 %. While a laser working with an notched elliptical resonator might have excellent output directionality, it probably will not operate too efficiently in terms of pumping versus output power.

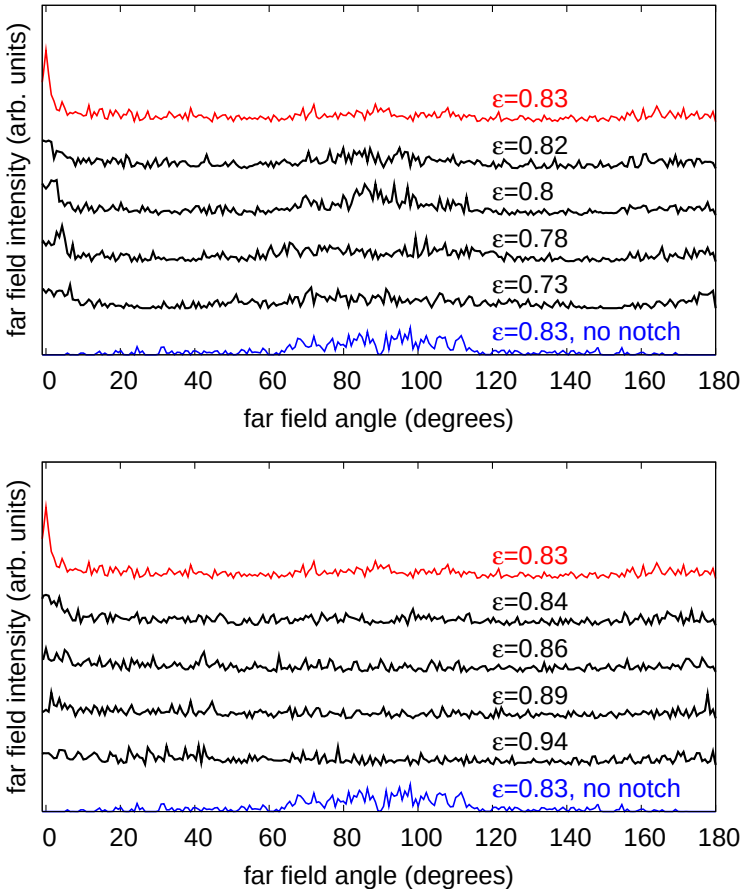

Figure 5.10.: Far field patterns for varying ϵ values and fixed notch depth $\delta = 5/96$ and width $\vartheta = 2/96$. The red curve corresponds to the optimal $\epsilon \approx 0.83$. For comparison, the far field pattern of the ellipse *without* notch (blue curve) is shown as well.

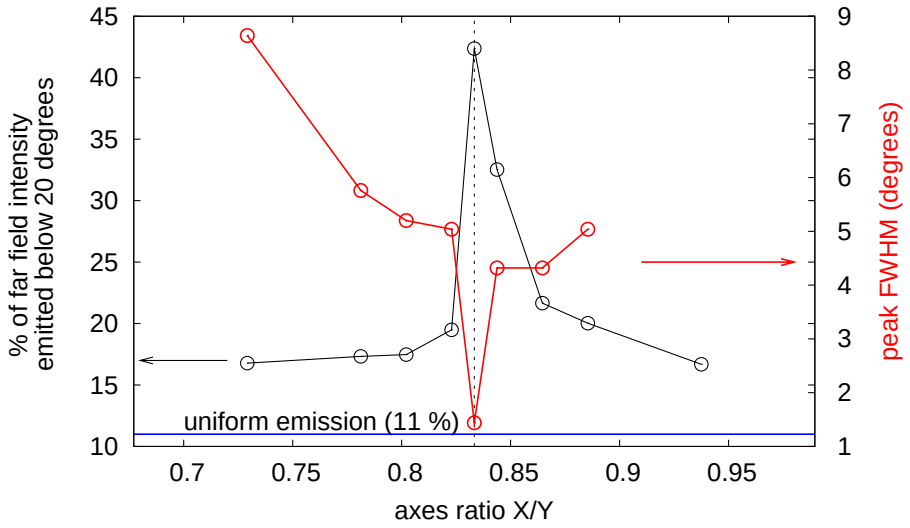

Figure 5.11.: Dependence of the far field directionality and FWHM of the main far field peak in the notched ellipse for various axis ratios ϵ.

5.5.2. Notch depth and width

Figure 5.12 shows the far field pattern for a notched ellipse with the optimal $\epsilon \approx 0.83$ for different notch depths δ and notch widths ϑ.

While too large δ's are unfortunate in term of output unidirectionality (the rays are scattered too far inside the cavity for the lens, which is optimized for scattering at the boundary, to work properly), too small δ's are also not good (the notch is too small to scatter the rays efficiently). There exists a range of $1/96 \leq \delta \leq 5/96$ where the directionality is optimized. The notch width ϑ does not influence the directionality significantly; however, larger ϑ are favorable, probably because having a broader notch enhances the probability of a ray getting scattered by the notch. Such enhanced scattering, on the other hand, leads to faster leakage out of the cavity and thus to a reduced Q factor.

5.5.3. Polarization

Unidirectional emission can not only be achieved for TM, but also for TE polarization, as shown in Fig. 5.13; the divergence angles and the intensity emitted into ± 20 degrees are comparable. This is an advantage of the notched elliptical resonator: other structures proposed for unidirectional emission only work well for TE (e.g. the limaçon, [WH08]) polarization. As only TE or TM polarized emission is possible when using some active materials in experiments, it is useful to have a shape with which both possibilities can be accommodated.

While the percentage of intensity emitted into ± 20 degrees is higher in the TE case, the difference between the two polarizations is very small. The notched elliptical resonator thus exhibits unidirectional light emission in both the TE and the TM cases.

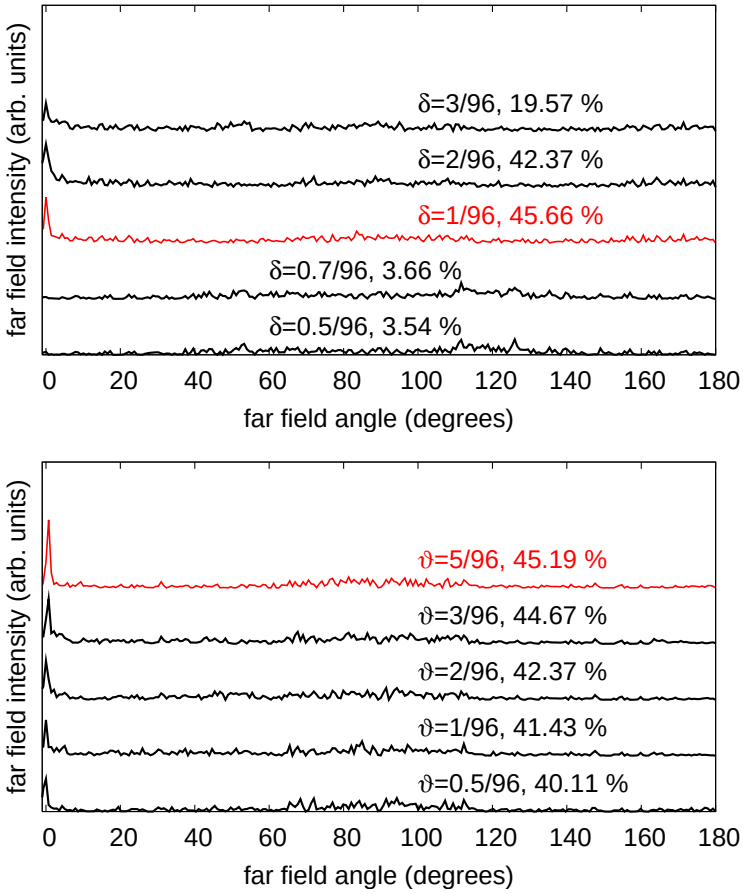

Figure 5.12.: Far fields for the notched ellipse with $\epsilon = 0.83$ for various notch depths δ (with fixed $\vartheta = 2/96$) and notch widths ϑ (with fixed $\delta = 2/96$). The percentage of the intensity emitted into ± 20 degrees is noted; red color indicates the combination yielding the best directionality.

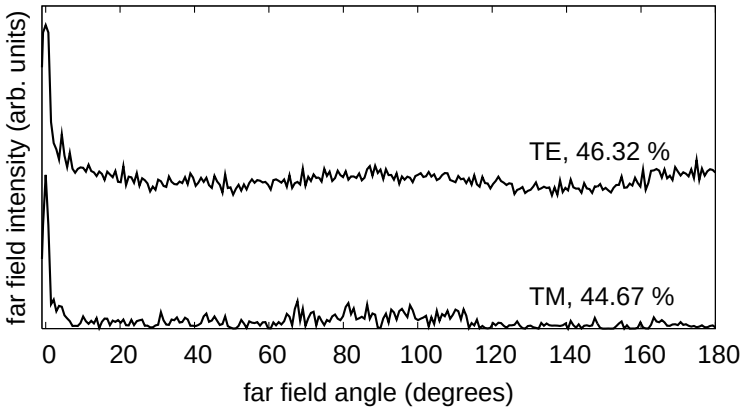

Figure 5.13.: Far fields for the notched ellipse with $\epsilon = 0.83$, notch depth $\delta = 2/96$ and notch width $\vartheta = 3/96$ for TM and TE polarizations. The refractive index is $n = 3.2$. The percentage of the intensity emitted into $\pm$ 20 degrees is noted.

5.5.4. Refractive index

A refractive index of $n = 3.2$ has been used so far in the calculations. This is a refractive index typical for semiconductors (e.g., GaAs has $n \approx 3.3$, GaN $n \approx 3$, AlAs $n \approx 3.2$), which are in fact often used as cavity materials in applications. But there are other materials, e.g. polymers with $n \approx 1.5$, which can also be used; in other applications, despite the use of a semiconductor cavity, one has a refractive index *contrast* between the cavity material and the outside because the cavity is embedded in another material. For example, this is the case in [BRK$^+$08], where a micropillar cavity is embedded in a polymer material. The refractive index contrast is around 2 in this case.

Because of this wide range of refractive indices encountered in applications, it is reasonable to ask if the mechanism presented so far works for refractive indices other than $n = 3.2$. Naively, one could think that it works for *all* refractive indices equally: after all, Eq. (5.12) shows that for any n, an ϵ can be found which optimizes the directionality. But of course, Eq. (5.12) does not tell how good the directional emission of a cavity with this optimal ϵ value actually is. As shown in Fig. 5.14, the directionality indeed varies significantly with the refractive index.

The directionality goes down drastically if n is lowered; at $n = 1.2$, the emission is almost uniform and not very different from the one of the ellipse *without* notch. This is due to the fact that at such a low index, most of the rays hitting the notch actually do so with angles below the critical angle for total internal reflection, and thus are not reflected to the opposite side where collimation can take place, but refracted out right away. This is shown in Fig. 5.14 (b): there, the percentage of the overall emission which comes from transmission of the notch is plotted. While this transmission is only 2.3 % for $n = 4.2$, it goes up to almost 10 % for $n = 2.2$ and $n = 1.2$. Thus, more and more intensity is transmitted at the notch, lowering the emission into $\pm$20 degrees, but also

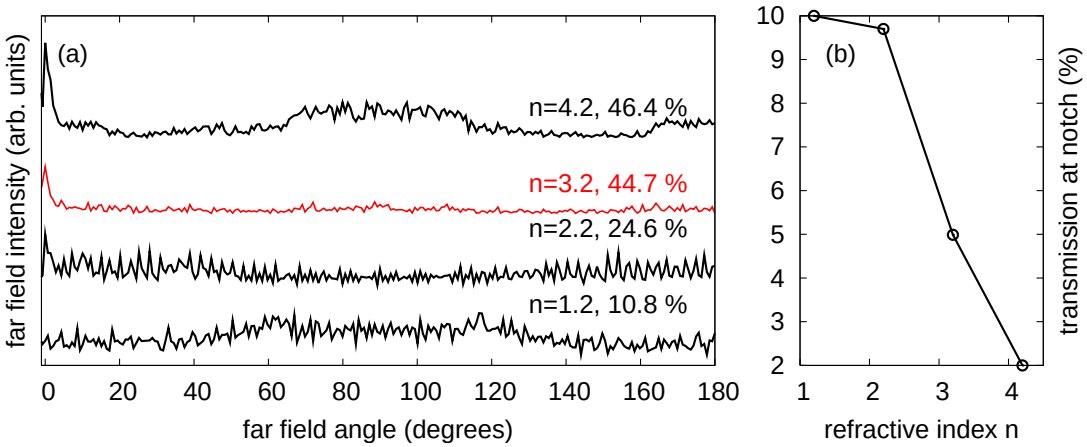

Figure 5.14.: (a) Far field patterns of the notched ellipse with different refractive indices n for $\delta = 2/96$, $\vartheta = 3/96$, and TM polarization. The eccentricity of each ellipse has been optimized with respect to n according to (5.12). The percentage of the intensity emitted into ± 20 degrees is noted. (b) Percentage of the emitted intensity which comes from transmission at the notch for the same refractive indices.

diminishing the number of rays which can participate in the collimation process.

For refractive indices above $n = 3.2$, the directionality improves slightly (even more ray are scattered by the notch without being refracted out), but side peaks arise as well. They are connected to the "bowtie" island (see Fig. 5.2): the bounce points with $p \approx 0$ emit into at ≈ 70 and ≈ 110 degrees. This contribution to the emission is, of course, always present; but at lower refractive indices, other contributions are more important. At $n = 4.2$, most other phase space structures are too far away from the critical line to contribute.

As no materials with $n > 4$ are currently used in applications, one can conclude that unidirectional far field emission in elliptical cavities with a notch can only be achieved for refractive indices typical for semiconductor materials.

5.5.5. Notch shape

The choice of a Gaussian as the notch shape is arbitrary and might be difficult to fabricate experimentally. In this section, two other notch shapes are studied. The first is a Gaussian "double notch", defined by

$$\begin{aligned} x &= \left[\epsilon - \delta\left(e^{-8(\phi-(-\pi+\vartheta/2))^2/\vartheta^2} + e^{-8(\phi-(\pi-\vartheta/2))^2/\vartheta^2}\right)\right]\cos\phi, \\ y &= \sin\phi. \end{aligned} \tag{5.23}$$

This notch is made of two Gaussians with widths $\vartheta/2$ and depths δ. It thus has approximately the same width and depth as the Gaussian notch (Eq. (5.1)), as shown in Fig. 5.15.

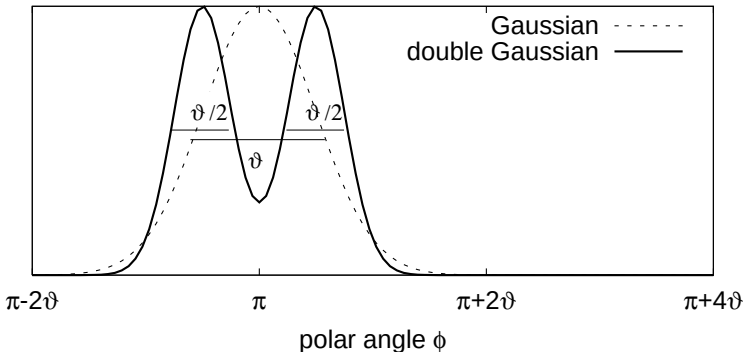

Figure 5.15.: Gaussian (dashed line) and double-Gaussian (solid line) notch shapes.

The second notch is a parabolic notch, which is achieved by cutting a parabola out of the elliptical boundary such that the depth is δ and the overall width is ϑ (see Fig. 5.16). A formula for this piecewise defined boundary can be found by first considering intersections between the elliptical boundary $(x, y) = (\epsilon\cos\phi, \sin\phi)$ and the parabola $(x, y) = (\alpha y^2 + \beta, y)$. Because the notch depth is δ, β is given by $\beta = \epsilon - \delta$, and because the width is ϑ, the intersections happen at the polar angles $\phi_{1,2}$ such that $y = \sin\phi_{1,2} = \pm\vartheta/2$. From these relations, α can be calculated:

$$\begin{aligned} x = \epsilon\cos\phi_{1,2} &= \alpha y^2 + \beta = \alpha\sin^2\phi_{1,2} + \epsilon - \delta \\ \rightarrow \alpha &= -\frac{\epsilon\cos\phi_{1,2} - \epsilon + \delta}{\sin^2\phi_{1,2}} \\ &= -\frac{\epsilon\sqrt{1-\vartheta^2/4} - \epsilon + \delta}{\vartheta^2/4}. \end{aligned} \tag{5.24}$$

In the last step, $\cos\phi_1 = \cos\phi_2 = \cos[\arcsin(\vartheta/2)] = \sqrt{1-\vartheta^2/4}$ has been used. The boundary curve of an elliptical resonator with a parabolic notch is thus given by

$$\begin{aligned} x &= \begin{cases} \left[\epsilon - \delta - \frac{\epsilon\sqrt{1-\vartheta^2/4}-\epsilon+\delta}{\vartheta^2/4}\sin^2\phi\right]\cos\phi, & |\sin\phi| \le \vartheta/2 \text{ and } \cos\phi < 0, \\ \epsilon\cos\phi, & \text{otherwise,} \end{cases} \\ y &= \sin\phi. \end{aligned} \tag{5.25}$$

Figure 5.17 shows the far field patterns of a Gaussian, a double-Gaussian, and a parabolic notch for $\delta = 2/96$, $\vartheta = 3/96$ and $\epsilon = 0.83$. The directionality of the far field pattern is quite insensitive to the precise notch shape, which adds further confirmation to the interpretation of the notch as a point scatterer.

5.5.6. Cavity boundary shape

Only an ellipse collimates rays scattered by the notch. But what happens for other boundary curves whose curvatures are locally very similar to the one of the optimal

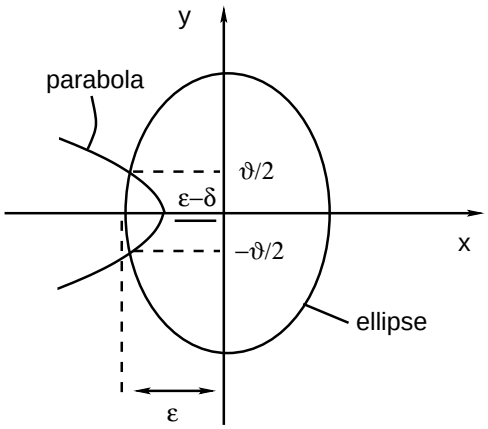

Figure 5.16.: Definition of the boundary curve of an ellipse with a parabolic notch.

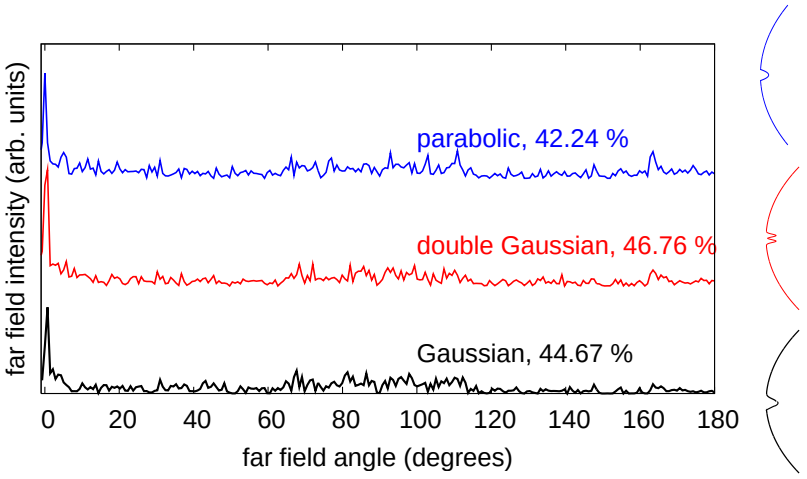

Figure 5.17.: Far field patterns for a notched ellipse with $\epsilon = 0.83$, $\delta = 2/96$, and $\vartheta = 3/96$ for a Gaussian (black curve), a double Gaussian (red curve) and a parabolic notch (red curve). The fraction of intensity emitted into ± 20 degrees is noted. On the right, the notch shapes are shown.

ellipse? As an example, one can look at a notched quadrupole with a certain deformation. Quadrupolar cavities also allow for long-lived rays and directed (although not unidirectional) emission (see, e.g., [NS97]).

The quadrupole is defined by the boundary curve[1]

$$r(\phi) = R(1 - \tilde{\epsilon}\cos(2\phi)), \tag{5.26}$$

with the deformation parameter $\tilde{\epsilon}$ and a length scale parameter R.

In order to find the deformation $\tilde{\epsilon}$ which leads to a curvature similar to the optimal ellipse, one can follow [Nöc97] and view the ellipse as an "approximate quadrupole". The ellipse can be parametrized by the boundary curve

$$r(\phi) = \frac{Y}{\sqrt{1 + e^2\cos^2\phi}}, \tag{5.27}$$

where the eccentricity $e^2 = (Y^2 - X^2)/X^2$ of the ellipse has been introduced. Expansion of the square root in Eq. (5.27) yields

$$r(\phi) \approx Y\left(1 - \frac{e^2}{2}\cos^2\phi\right) = Y\left(1 - \frac{e^2}{2} - \frac{e^2}{4}\cos(2\phi)\right). \tag{5.28}$$

This is the boundary curve describing a quadrupole with deformation parameter $\tilde{\epsilon} = e^2/4$; $\tilde{\epsilon}$ for the optimal notched quadrupole can be estimated to $\tilde{\epsilon} \approx 0.08$. The boundary curve of the notched quadrupole in units of the major half-axis Y is given by

$$\begin{aligned} x &= \left[r(\phi) - \delta\exp(-2(\phi-\pi)^2/\vartheta^2)r(\phi)\right]\cos\phi, \\ y &= r(\phi)\sin\phi, \end{aligned} \tag{5.29}$$

with $r(\phi) = 1 - \tilde{\epsilon}\cos(2\phi) - 2\tilde{\epsilon}$.

Figure 5.18 shows the phase space for the quadrupole and the notched quadrupole at $\tilde{\epsilon} = 0.08$. It can be seen that also in this system, rays traveling along the boundary similar to WGMs until they hit the notch exist; however, the phase space is not changed as drastically as the one of the ellipse. This is due to the fact that the undisturbed quadrupole is already far from being an integrable system at $\tilde{\epsilon} = 0.08$ and the chaotic dynamics does not change drastically. Many islands also persist after "notching" the boundary – and as some of them are localized at the critical line, they contribute to the far field emission.

Figure 5.19 shows the resulting far field patterns as well as the boundary shapes for the optimal ϵ and $\tilde{\epsilon}$. While the boundary shapes are very similar, the notched quadrupole shows little output directionality. It really is essential to shape the cavity boundary elliptically. This is due to the fact that the quadrupolar boundary does not collimate rays as well as the elliptical boundary (see Fig. 5.20).

[1] Usually, the quadrupole is defined by $r(\phi) = R(1 + \tilde{\epsilon}\cos(2\phi))$. The choice of the other sign ensures the same aspect ratio as in the ellipse considered earlier: the major half-axis is oriented along the y axis.

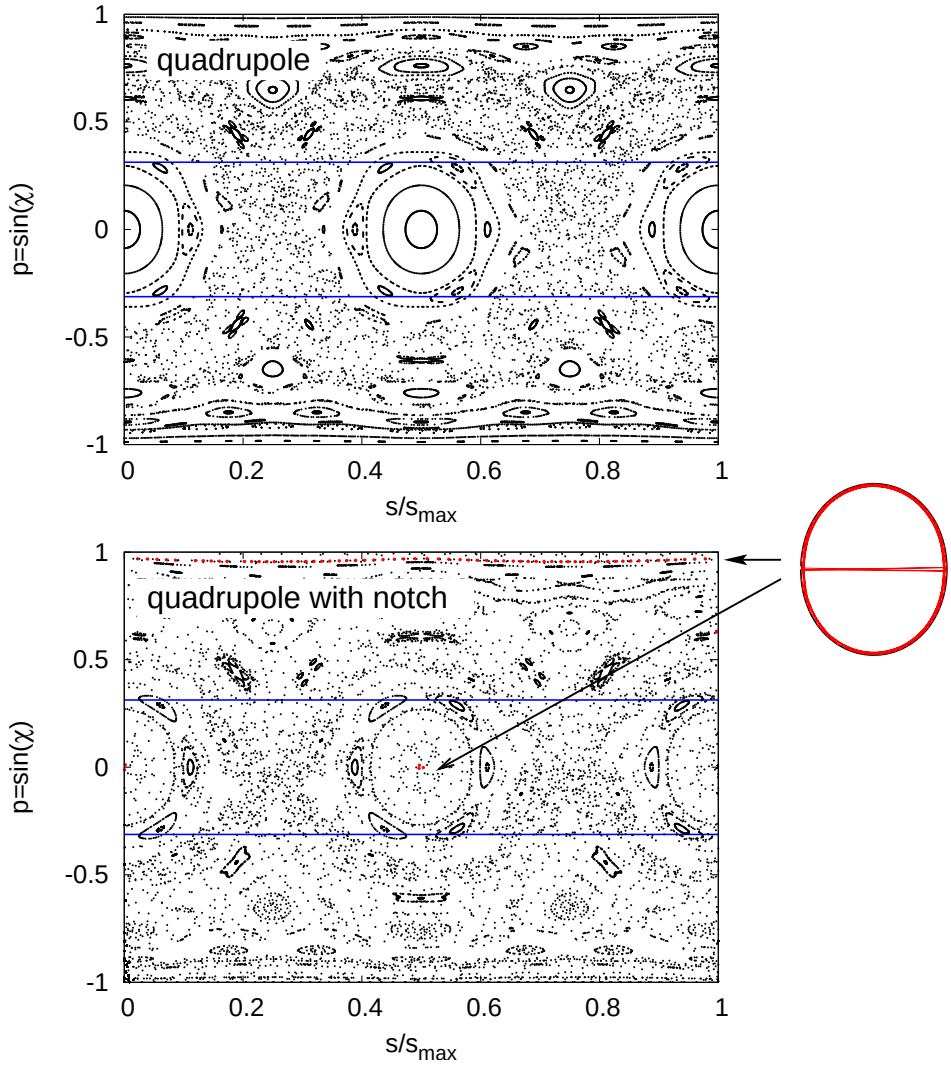

Figure 5.18.: Poincaré surface of section for the quadrupole without notch (top) and the notched quadrupole (bottom) for $\tilde{\epsilon} = 0.08$ and $\delta = 2/96$, $\vartheta = 3/96$. The critical line for total internal reflection for $n = 3.2$ is shown in blue. The points marked red in the bottom panel belong to an orbit which travels WGM-like around the boundary until hitting the notch.

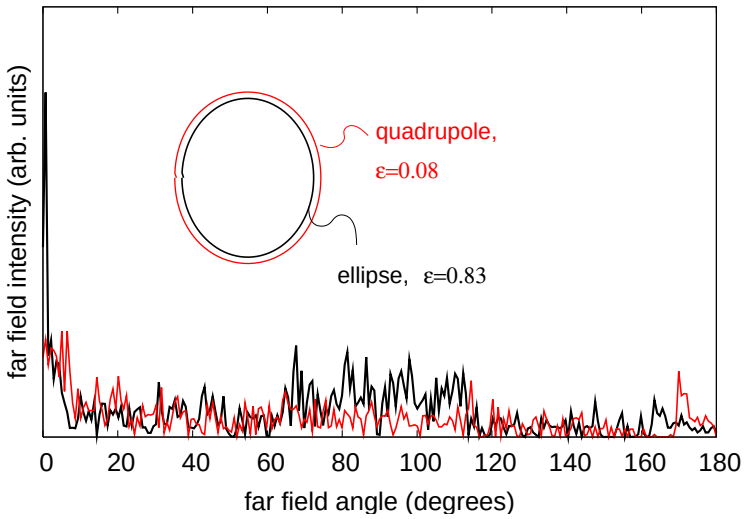

Figure 5.19.: Far field patterns and boundary shapes for the optimal ellipse and quadrupole with notch parameters $\delta = 2/96$ and $\vartheta = 3/96$. The quadrupole shape is slightly enlarged in order to make the comparison easier.

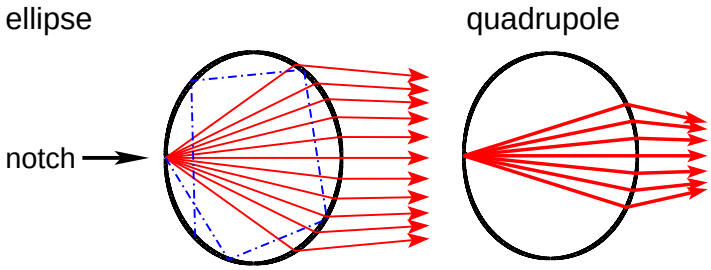

Figure 5.20.: Collimation in the ellipse (left, see Fig. 5.7) and quadrupole (right). Rays originating from the notch are not collimated in the quadrupole even for small angles.

5.6. Comparison with wave calculations

So far, all results have been obtained using a ray model. While the rays can of course resolve an arbitrarily small notch at the boundary, electromagnetic waves can only resolve structures larger than a wavelength. It is thus necessary to check if the results still hold when leaving the ray approximation and solving the wave equation in a notched elliptical cavity directly. This is done here using the boundary element method (BEM) [Wie03] (see also Appendix C for details). Figure 5.21 shows far field patterns for two different modes as well as the mode patterns. The modes are labeled A ($kR = 60.32 - 0.0062i$, $Q = 49\,000$) and B ($kR = 60.59 - 0.055i$, $Q = 5\,500$). While the mode pattern is not very sensitive to the number of boundary elements used for calculation, the Q factor is; the results shown here have been calculated using 4000 boundary elements. Choosing a higher number of boundary elements leads to significantly higher Q factors.

The far field agrees well with the ray simulations; the intensity emitted into ± 20 degrees is between 50 and 60 %, which is a bit larger than the ray simulations predict. This difference can at least in part be attributed to the differences between modes of even and odd parity. Modes with odd parity have higher Q factors, as they have less overlap with the notch (a node is located at the notch position) and thus less leakage out of the cavity at the notch position; they also have less directional emission. Even parity modes, which are more directional, dominate the far field because their Q factors are lower (they have an intensity maximum at the notch position), so that a larger percentage of the light leaking out comes from them. The ray simulation corresponds not to the far field of an *individual* mode, but to and average over all (even and odd) modes (this kind of correspondence has been studied in [SHW+09]). The average ray directionality thus has to be lower than the directionality of a single mode.

5.7. Comparison to experimental results

Elliptical resonators with notches have been fabricated in F. Capasso's group [WYY+10] and used as a cavity for a microlaser. They fabricated GaInAs/AlInAs/InP Quantum Cascade Lasers (QCLs; the working principle is described in [FCS+94]) with an effective refractive index $n \approx 3.2$ and a wavelenght in the material of $\lambda \approx 10\,\mu$m. The minor half-axis X is $X = 80\,\mu$m, the major half axis $Y = 96\,\mu$m. Different notch shapes and sizes were fabricated (see Figs. 5.22 and 5.23), including a double and a parabolic notch; the results shown below are for a parabolic notch with depth $d = 2\,\mu$m and opening angles $o = 3\,\mu$m. The notches are shaped with photo-lithography; the standard accuracy of this method is around $1\,\mu$m.

The light output of a QCL is always TM polarized due to selection rules for the lasing quantum well intersubband transitions. The devices are pumped electrically. The Q-factors are around 1200, which agrees well with the calculated values if material absorption is taken into account. The far fields are measured according to [YFW+08] and also agree well with our theoretical predictions (Fig. 5.24).

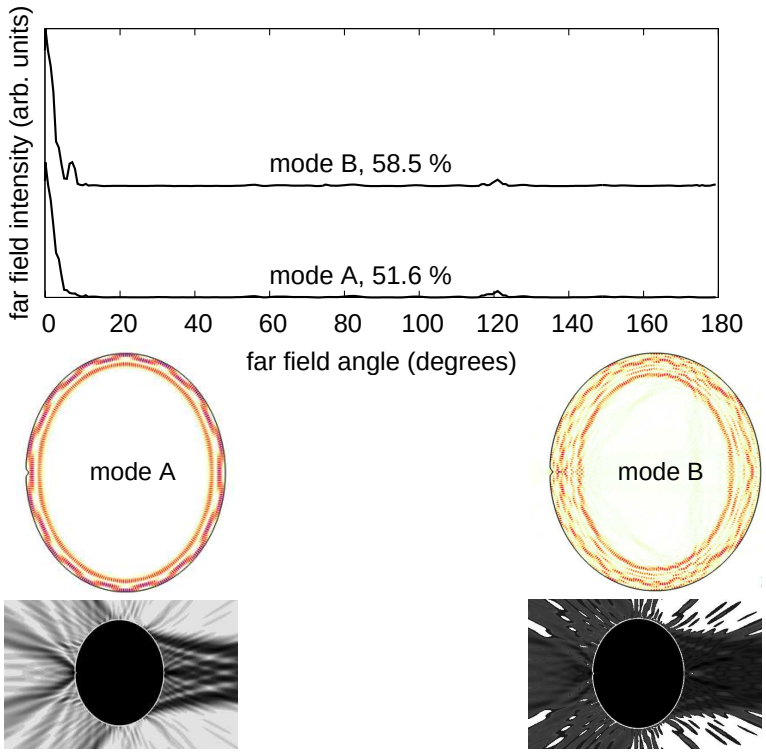

Figure 5.21.: Far field patterns for modes A (high Q) and B (low Q). The mode patterns inside and outside the cavity are also shown.

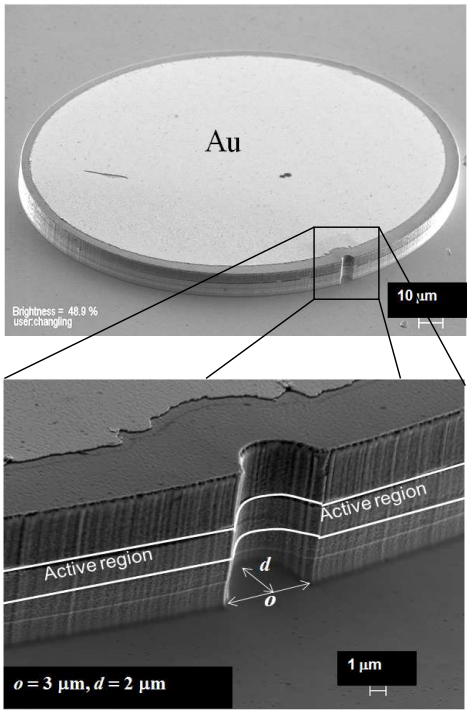

Figure 5.22.: Scanning electron microscope picture of an elliptical cavity with a parabolic notch with $d = 2\,\mu$m and $o = 3\,\mu$m. The top panel shows the resonator as seen from above (with the gold contact as its top plate); the bottom panel shows a magnification around the notch. The notch parameters and indicated as well as the active region (Picture courtesy of Q. J. Wang).

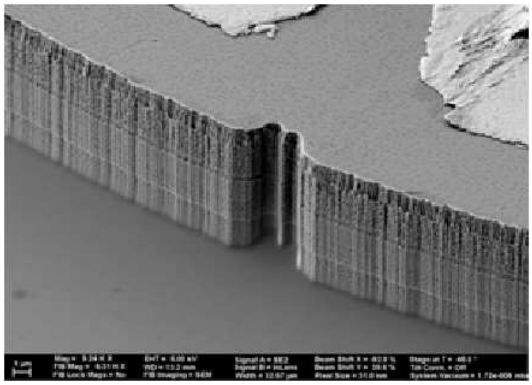

Figure 5.23.: Scanning electron microscope picture of an elliptical resonator with a "double notch" with $d = 2\,\mu$m and $o = 3\,\mu$m (Picture courtesy of Q. J. Wang).

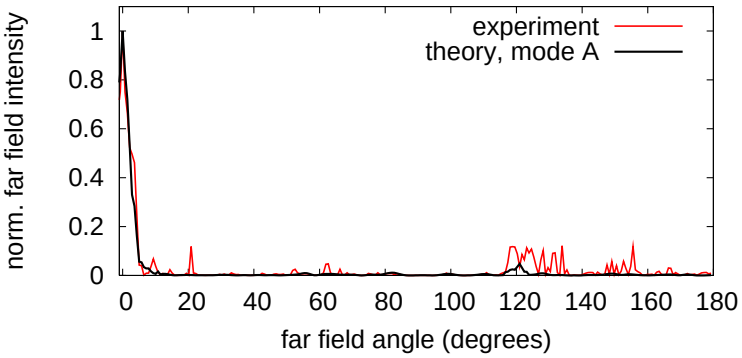

Figure 5.24.: Comparison of the experimental (red curve) and theoretical (black curve) far field patterns for a notched elliptical resonator with $X = 80\,\mu$m, $Y = 96\,\mu$m, $d = 2\,\mu$m, and $o = 3\,\mu$m. The theory curve shows the far field pattern of mode A from above. Both far field patterns are normalized to their maximum value.

6. Extended ray dynamics: including wave corrections in the ray picture

While ray-wave correspondence is very useful for the interpretation of modes and far-field patterns, it fails if the wavelength becomes comparable to the cavity size (λ/R near one), i.e. for low kR. As semiconductor cavities with sizes comparable to the laser emission wavelengths have been build [SGS+10], understanding how and when ray-wave correspondence fails and what other ways of interpreting the wave results are possible becomes more and more important. One idea is to find first-order wave corrections which "extend" the ray dynamics; this can be seen as a "semiclassical" approach: instead of just looking at the classical (ray) limit of a quantum mechanical billiard (dielectric cavity), one considers first-order quantum (wave) corrections to physical quantities.

How does one design this extensions, what are "first-order wave corrections"? If one leaves the ray limit, one no longer deals with rays, but with *beams* which travel, get reflected, and interfere in a cavity; in the limit of narrow beams with wavelengths small compared to the cavity size, one recovers the ray limit. Because one deals with beams, which have a diffractive spreading (i.e. contain partial waves with different incident angles at a point where reflection occurs), the openness of a dielectric cavity is felt much more directly than in the ray picture: at each reflection, a part of the beam can get refracted out, even if the average angle of incidence is above the critical angle for TIR. Wave corrections will thus also mean corrections due to the openness of a dielectric cavity.

One such first-order wave correction has been found experimentally by Goos and Hänchen [GH47]: measuring the reflection of beams on a planar interface, they found that the reflected ray is not reflected at the position of the incident ray, but is shifted along the interface (the shift is now called the Goos-Hänchen shift (GHS)) because of interference of the different reflected partial waves, which accumulate different phases upon reflection; the theory is discussed in more detail in section 6.1.1. This shift can be easily included in a ray picture: one identifies the maximum of the beam as a ray, subjects it to the usual reflection laws at the boundary, and then applies the GHS as a correction. A complementary effect was predicted in [TS02] and measured experimentally in [RTS+02]: when a beam is reflected at an interface, the partial waves with small angles of incidence (which usually exist, even if the average angle of incidence is above the critical angle) get (partially) refracted out of the cavity and are missing in the reflected beam, which thus has an average outgoing angle which is higher than the

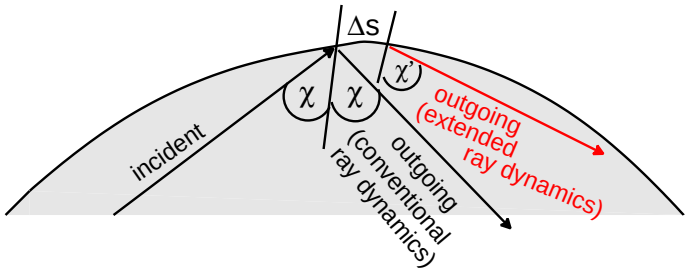

Figure 6.1.: GHS Δs and FF $\Delta p = \sin\chi' - \sin\chi$ as wave corrections to the ray picture. A beam is not reflected at the same position on the boundary, but the outgoing beam is shifted by Δs; the outgoing angle χ' is not the same as the incident angle χ, but the sine is shifted by Δp.

average angle of incidence. This effect, called Fresnel filtering (FF), thus manifests itself as a correction of the outgoing angle of a ray, i.e. as a correction to Snell's law. If one considers both these effects and looks at the dynamics in phase space [SH06], the GHS is a correction of the position s along the cavity boundary, and the FF is a correction of angle χ, i.e., the momentum $p = \sin\chi$. Figure 6.1 shows an illustration of the two effects.

The wave corrections lead to modifications of the phase space: breakup of invariant lines into stable and unstable fixed points (see section 6.4 and [UWH08]), formation of attractors and repellers (see sections 6.5, 6.6 and [AGH08, UW10]) and a momentum shift of phase-space structures (also discussed in section 6.5). Continuing the idea of ray-wave correspondence, one can look at modes for low kR and study how they reflect the modified phase space. Altmann *et al.* [AGH08] have studied the formation of attractors and repellers in the annular cavity with wave corrections, but did not consider modes.

6.1. Wave corrections: Goos-Hänchen shift and Fresnel filtering

6.1.1. Goos-Hänchen shift: analytical results

A simple analytical formula for the GHS is due to Artmann [Art48]. While it can also can be derived from wave optics ([Art48, Art51]; see also section 6.2.1 for another derivation), the simplest approach is to consider a beam consisting of two plane waves being reflected at a planar interface (see Fig. 6.2). The plane waves have slightly different incoming angles χ and χ' (corresponding to $p = \sin\chi$ and $p' = \sin\chi'$), and, upon reflection, gain two slightly different phases ϕ and ϕ'. One can set $p' = p + \Delta p$ and $\phi' = \phi + \Delta\phi$; Δp and $\Delta\phi$ are small numbers. The incoming beam can be written as

$$\psi_{\text{in}}(x) = e^{inkpx} + e^{inkp'x} = e^{inkpx}\left(1 + e^{ink\Delta px}\right), \tag{6.1}$$

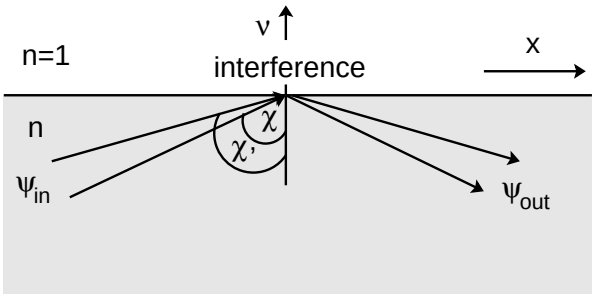

Figure 6.2.: Derivation of the Artmann result for the GHS using an incoming beam consisting of two plane waves. At the interface, they gain different phase shifts, which in turn lead to a lateral displacement.

the outgoing beam as

$$\begin{aligned}\psi_{\text{out}}(x) &= \exp(inkpx + i\phi) + \exp(inkp'x + i\phi') \\ &= \exp(inkpx + i\phi)\left(1 + \exp\left(ink\Delta p\left(x + \frac{1}{nk}\frac{\Delta\phi}{\Delta p}\right)\right)\right) \\ &\approx \exp(inkpx + i\phi)\left(1 + \exp\left(ink\Delta p\left(x + \frac{1}{nk}\frac{\partial\phi}{\partial p}\right)\right)\right) \\ &= \exp(i\phi)\psi_{\text{in}}\left(x + \frac{1}{nk}\frac{\partial\phi}{\partial p}\right).\end{aligned} \tag{6.2}$$

the reflected beam thus has a lateral shift of

$$\Delta s = \frac{1}{nk}\frac{\partial\phi}{\partial p}. \tag{6.3}$$

The phase ϕ is given by the complex Fresnel reflection coefficient, $r = |r|e^{i\phi}$, with

$$\begin{aligned}\phi_{\text{TM}} &= -2\arctan\left(\frac{\sqrt{\sin^2\chi - n^2}}{\cos\chi}\right), \\ \phi_{\text{TE}} &= -2\arctan\left(\frac{\sqrt{\sin^2\chi - n^2}}{n^2\cos\chi}\right).\end{aligned} \tag{6.4}$$

One can thus write Eq. (6.3) as

$$\begin{aligned}\Delta s_{\text{TM}} &= \frac{1}{nk}\frac{1}{\sqrt{\sin^2\chi - 1/n^2}}, \\ \Delta s_{\text{TE}} &= \frac{1}{nk}\frac{1}{n\sqrt{\sin^2\chi - 1/n^2}}.\end{aligned} \tag{6.5}$$

Δs has singularities at $p = \sin\chi = 1/n$ (the critical angle) and also at $p = 1$, both of which are unphysical for a realistic beam. The Artmann result is thus only valid for

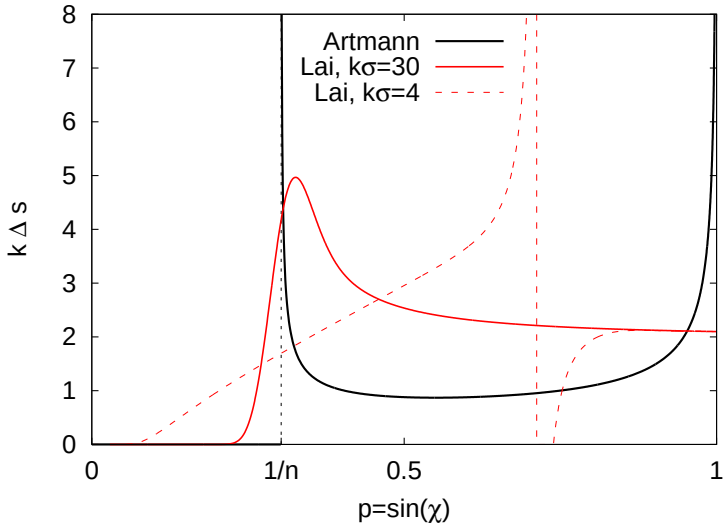

Figure 6.3.: Artmann result (black line) and Lai result for $k\sigma = 30$ (red solid line) and $k\sigma = 4$ (red dashed line). The critical line is marked by the black dashed line. The other parameters are $n = 3.3$, $kR = 8.2$; the polarization is TM.

not-too-high angles of incidence above the critical angle, as the square root in Eq. (6.5) gets complex-valued for $p < 1/n$ and the shift cannot be properly defined.

Lai *et al.* [LCT86] developed an analytical expression for the shift of a Gaussian beam which gets rid of the singularity at $p = 1/n$ and is also valid for angles of incidence below the critical angle. However, their expression is only valid if the beam width σ of the beam is much larger than the wavelength, i.e. in the limit $k\sigma \gg 1$. If one considers minimal-uncertainty beams for small k, one has $k\sigma \approx 1$. This is the limit which will be considered in the following; the Lai result is no longer valid in this limit because it shows unphysical singularities. Figure 6.3 shows both the Artmann result and the Lai result for different σ values.

6.1.2. Fresnel filtering

The Fresnel filtering effect was introduced by Tureci and Stone [TS02] in order to describe deviations of the measured far-field pattern of a quadrupolar cavity from the ray-dynamical predictions. They developed an analytical formula for the far-field emission pattern of a cavity where Gaussian beams are reflected; from it, an analytical expression for the shift in the far-field emission angles (for incidence at the critical angle) can be derived. However, no analytical expressions for the FF itself are given, and none seem to be known. Schomerus and Hentschel [SH06] extracted the FF from wave calculations in a circular cavity; for other investigations, i.e. the formation of periodic orbits in the Spiral cavity [AGH08], for fixed nkR, a constant FF as a function of p is assumed.

6.2. Numerical calculation of GHS and FF

6.2.1. Calculation scheme

As analytical formulas for the GHS suffer from unphysical singularities and so far, none are known for the FF, it is necessary to calculate these corrections numerically as functions of the angle of incidence, depending on the refractive index n, the wavelength (described by the size parameter kR), and the polarization (TM or TE). The numerical scheme is described in the following; the general idea is to calculate the incident and reflected beams and extract the GHS and FF by comparing the average incoming and outgoing reflection positions and angles. Such an approach has been used in [AW07, AW09] and [AMW09] as well, and compared to experimental results for the shifts at planar interfaces (though not in microcavities).

The major approximation here is to treat the interface as planar, thus neglecting the curvature of a cavity boundary. This approximation can be justified because locally, any smooth boundary looks flat; if the radius of curvature is larger than the beam width and the wavelength, it will also look flat to the beam. A generalization to arbitrarily curved boundaries might be desirable if one wants to study $kR \to 1$, but is difficult, as there are no analytical formulas for the Fresnel coefficients at a curved interface. Thus, the following calculations are restricted to the planar-interface situation; as the results agree well with wave results down to $kR \approx 10$ (as will be seen later), this seems reasonable.

The incoming wave function ψ_{in} is modeled as a Gaussian beam:

$$\psi_{\text{in}}(x) = \int_{-1}^{1} \mathrm{d}p\, e^{inkpx} f_{\text{in}}(p), \tag{6.6}$$

with

$$f_{\text{in}}(p) = e^{-n^2k^2(p-p_{\text{in}})^2\sigma^2/4}. \tag{6.7}$$

This describes a Gaussian beam with width σ centered around $x = 0$ (which is chosen as the position where the beam maximum hits the flat interface) and has plane wave components with wave number k whose incoming angles are centered around $p_{\text{in}} = \sin\chi_{\text{in}}$. The width σ can be fixed by choosing a minimal-uncertainty beam where the uncertainties in nkp and x, $nk\Delta p$ and Δx, are of equal size when compared to the typical length scale R of a cavity. The minimal-uncertainty beam is chosen because it best approximates a classical ray and is thus the natural choice in a semiclassical approach. With the uncertainty relation for a Fourier transform, which Eq. (6.6) basically is,

$$nk\Delta p\Delta x = nkR\Delta p\frac{\Delta x}{R} = \frac{1}{2} \tag{6.8}$$

one finds with equal uncertainties $\Delta p = \Delta x/R$

$$\Delta x = \frac{\sqrt{R}}{\sqrt{2nk}}. \tag{6.9}$$

The beam width σ is then given by $\sigma = \sqrt{2}\cdot\Delta x$.

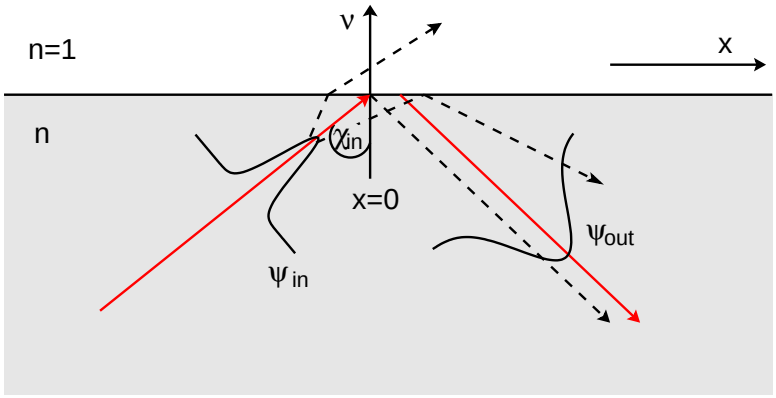

Figure 6.4.: Incoming and outgoing beams. The incoming beam ψ_{in} includes a variety of plane wave components with different incoming angles; the central incoming angle is χ_{in}. Each component gets reflected according to Fresnel's and Snell's laws; the outgoing beam ψ_{out} consists of different angles.

When the beam hits the boundary, each plane wave component gets reflected according to the Fresnel and Snell laws; the wave components with incoming angles below the critical angle for total internal reflection get partially refracted out. The outgoing beam can thus be described as

$$\psi_{\text{out}}(x) = \int_{-1}^{1} \mathrm{d}p\, r(p) e^{inkpx} f_{\text{in}}(p), \tag{6.10}$$

with the complex Fresnel reflection coefficient r applied to each plane wave component. The resulting beam will, in general, no longer be Gaussian. Figure 6.4 illustrates the process. When considering only incoming angles above the critical angle for TIR and a narrow angle distribution, the Fresnel coefficient r can be approximated as

$$r(p) = |r(p)|e^{i\phi(p)} = e^{i\phi(p)} \approx \exp\left(i\phi(p_{\text{in}}) + ip\frac{\partial\,\phi}{\partial\,p}\,|_{p_{\text{in}}}\right), \tag{6.11}$$

which, put into (6.10), leads to

$$\begin{aligned}\psi_{\text{out}}(x) &\approx \int_{-1}^{1} \mathrm{d}p\, e^{inkpx} f_{\text{in}} \exp\left(i\phi(p_{\text{in}}) + ip\frac{\partial\,\phi}{\partial\,p}\,|_{p_{\text{in}}}\right) \\ &= \exp(i\phi(p_{\text{in}})) \int_{-1}^{1} \mathrm{d}p\, \exp\left(inkp\left(x + \frac{1}{nk}\frac{\partial\,\phi}{\partial\,p}\right)\right) \\ &= e^{i\phi(p_{\text{in}})}\psi_{\text{in}}\left(x + \frac{1}{nk}\frac{\partial\,\phi}{\partial\,p}\right).\end{aligned} \tag{6.12}$$

One thus recovers the Artmann result

$$\psi_{\text{out}}(x) = e^{i\phi(p_{\text{in}})}\psi_{\text{in}}(x + \Delta s) \tag{6.13}$$

with

$$\Delta s = \frac{1}{nk}\frac{\partial \phi}{\partial p}. \tag{6.14}$$

In the general case, the GHS is defined as the difference in the "position expectation values" of ψ_{out} and ψ_{in}:

$$\Delta s = \frac{\int_{-\infty}^{\infty} \mathrm{d}x\, x|\psi_{\text{out}}(x)|^2}{\int_{-\infty}^{\infty} \mathrm{d}x\, |\psi_{\text{out}}(x)|^2}, \tag{6.15}$$

as ψ_{in} has a position expectation value of zero by construction. The FF can be calculated using the Fourier transforms $\hat{\psi}_{\text{in}}(p)$, $\hat{\psi}_{\text{out}}(p)$ of ψ_{in} and ψ_{out}:

$$\Delta p = \frac{\int_{-1}^{1} \mathrm{d}p\, p|\hat{\psi}_{\text{out}}|^2}{|\hat{\psi}_{\text{out}}|^2} - p_{\text{in}}, \tag{6.16}$$

as ψ_{in} is centered around p_{in}. Because f_{in} is a Gaussian, the Fourier transform can be calculated, yielding

$$\hat{\psi}_{\text{in}}(p) \sim f_{\text{in}}(p),\ \hat{\psi}_{\text{out}}(p) \sim r(p) f_{\text{in}}(p) \tag{6.17}$$

(the normalization constants do not matter because they cancel each other in (6.16)). The integrals in (6.15) and (6.16) have to be done numerically because of the presence of the reflection coefficient r; the x-integral is done from -50σ to 50σ.

In principle, one could also extract the GHS by comparing the positions of the maxima of ψ_{in} and ψ_{out}; the shift Δs would then be the difference of the positions of the maxima. Lai *et al.* [LCT86] use this definition. But as ψ_{out} need not be Gaussian, this definition might not be straightforward, as ψ_{out} can have different local maxima. An example is shown in Fig. 6.5: The top panel shows the incoming and outgoing wave functions for an incoming angle of $p_{\text{in}} = 0.8$ (above the critical angle for $n = 3.13$) and $kR = 50$. The outgoing wave function is approximately Gaussian, and the expectation value and the maximum give approximately the same result. The bottom panel shows the incoming and outgoing wave functions for $p_{\text{in}} = 0.3$ (just below the critical angle), all other parameters are the same. The outgoing wave function has two maxima; the higher one is shifted to the *left*: defining the GHS as the shift of this maximum would yield a negative GHS. But because of the second maximum and a "tail" in the $x > 0$ region, the GHS extracted by the expectation value is positive.

6.2.2. Dependence on Gaussian beam parameters

For high kR, the p dependence of the GHS and the FF looks similar to the results obtained by Artmann and Lai and also the curves extracted from wave calculations [SH06]. Figure 6.6 shows the GHS and FF for different kR values. For small kR values, the GHS has a very broad maximum above the critical angle and is never zero; the FF also has a broad maximum, and instead of vanishing above the critical angle, it turns negative. This can be understood when looking at the wave function $\hat{\psi}(p)$ in p space (see Fig. 6.7). For low kR, this wave function is very broad. For small p_{in}, the simple picture of the reflection coefficient cutting out the small-p partial waves, resulting in a positive

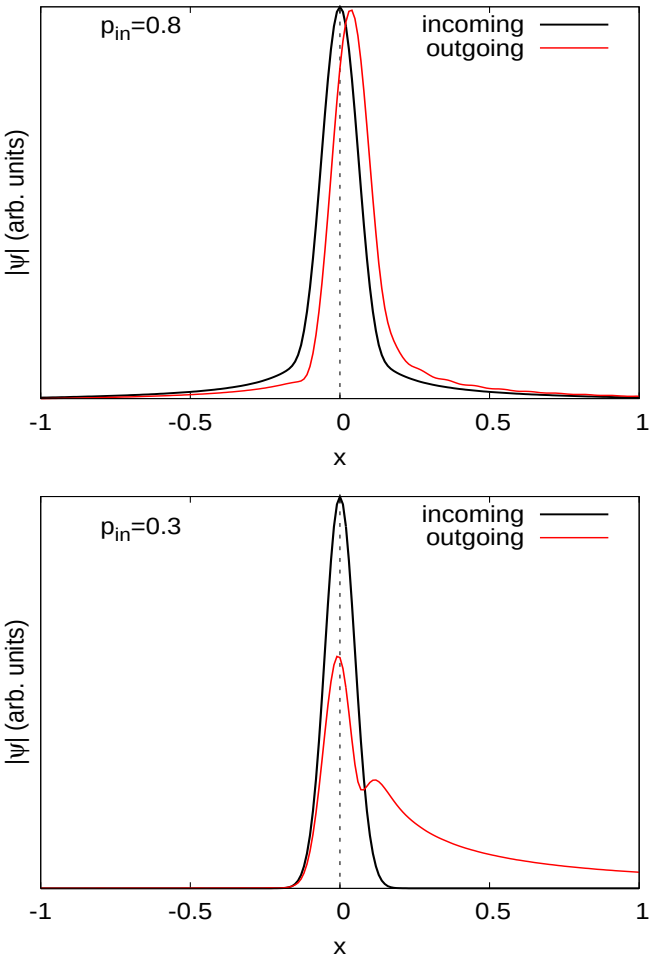

Figure 6.5.: Incoming (black curve) and outgoing (red curve) wave functions for $kR = 50$, TE polarization, $n = 3.13$, and $p_{\text{in}} = 0.8$ (top panel) resp. $p_{\text{in}} = 0.3$ (bottom panel). The outgoing wave function for $p_{\text{in}} = 0.8$ is approximately Gaussian, the outgoing wave function for $p_{\text{in}} = 0.3$ is no longer Gaussian.

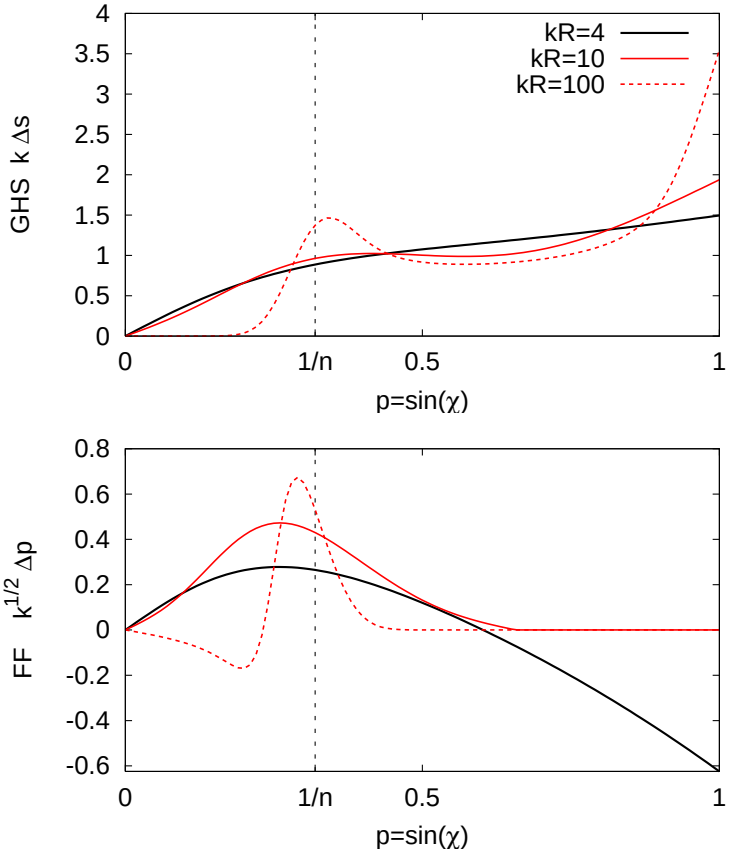

Figure 6.6.: GHS (top panel) and FF (bottom panel) as functions of $\sin\chi$ for $n = 3.13$ and different kR values. The GHS curves have been scaled with k, the FF curves with $\sqrt{k}$ ($R = 1$).

shift, remains true (top panel in Fig. 6.7; p_{in} is just below the critical angle). For larger p_{in}, the reflection coefficients cuts out "intermediate" p values (as it has a minimum at the Brewster angle), but leaves the smaller p values (bottom panel in Fig. 6.7). The resulting shift can be negative. This does not happen for higher kR, as the beams are less broad in this case and thus $|r|$ only has values below one in regions where $\hat{\psi}_{\text{in}} \approx 0$ for angles of incidence above the critical angle. One thus only finds negative FF around the Brewster angle, but not for higher p_{in}; this feature is not present in TM polarization. There, the FF is always positive for high kR.

The GHS approximately scales with $1/kR$ (as can be expected from the Artmann formula (6.5)), the FF, on the other hand, scales approximately as $\sqrt{kR}$, as predicted by Tureci and Stone [TS02].

6.3. The extended billiard mapping

Just like the usual billiard dynamics can be described by a *mapping* $(s_i, p_i) \to (s_{i+1}, p_{i+1})$ [Ber81], the dynamics in a billiard including the GHS and FF corrections can be described using another mapping. If one denotes the billiard mapping by

$$s_{i+1} = f(s_i, p_i),\ p_{i+1} = g(s_i, p_i), \tag{6.18}$$

where the functions f and g depend on the shape of the billiard boundary, the billiard mapping including the corrections is given by

$$\begin{aligned} s'_{i+1} &= f(s_i, p_i),\ p'_{i+1} = g(s_i, p_i), \\ s_{i+1} &= s'_{i+1} + \Delta s(s'_{i+1}, p'_{i+1}),\ p_{i+1} = p'_{i+1} + \Delta p(s'_{i+1}, p'_{i+1}). \end{aligned} \tag{6.19}$$

Thus, starting from (s_i, p_i), first the next intersection (s'_{i+1}, p'_{i+1}) with the boundary is calculated using the billiard dynamics, and then the corrections are applied, leading to the new position (s_{i+1}, p_{i+1}) (see Fig. 6.8). The approximation of calculating the GHS and FF at a planar interface means that one neglects the s'_{i+1} dependence of Δs and Δp in (6.19). If $\hat{J}_B$ is the Jacobian of the billiard dynamics (the linearized mapping),

$$\hat{J}_B = \begin{pmatrix} \frac{\partial f}{\partial s} & \frac{\partial f}{\partial p} \\ \frac{\partial g}{\partial s} & \frac{\partial g}{\partial p} \end{pmatrix}, \tag{6.20}$$

and $\hat{J}_G$ the one of the corrections,

$$\hat{J}_G = \begin{pmatrix} \frac{\partial \Delta s}{\partial s} & \frac{\partial \Delta s}{\partial p} \\ \frac{\partial \Delta p}{\partial s} & \frac{\partial \Delta p}{\partial p} \end{pmatrix} = \begin{pmatrix} 1 & \frac{\partial \Delta s}{\partial p} \\ 0 & 1 + \frac{\partial \Delta p}{\partial p} \end{pmatrix}, \tag{6.21}$$

then the Jacobian of the extended mapping $\hat{J}_E$ is given by $\hat{J}_E = \hat{J}_G \circ \hat{J}_B$. The determinant is given by

$$\det \hat{J}_E = \det \hat{J}_G \det \hat{J}_B = 1 + \frac{\partial \Delta p}{\partial p}, \tag{6.22}$$

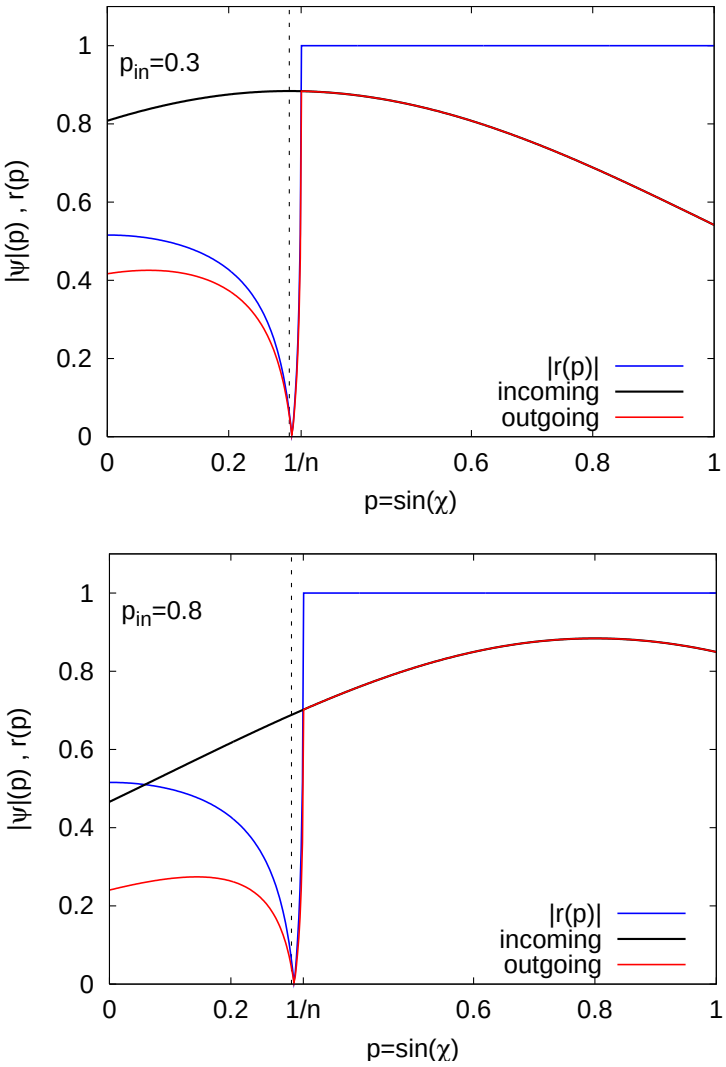

Figure 6.7.: Incoming and outgoing wave functions and reflection coefficient in p space for $kR = 4$, TE polarization, and $n = 3.13$. The top panel shows the case for an angle of incidence $p_{\text{in}} = 0.3$ of the wave packet (corresponding to positive FF), the bottom panel shows $p_{\text{in}} = 0.8$ (corresponding to negative FF).

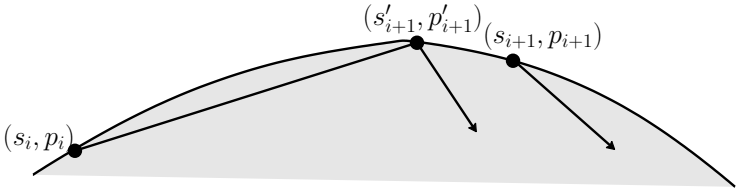

Figure 6.8.: Extended billiard mapping. Starting from (s_i, p_i), the billiard mapping is applied to find (s'_{i+1}, p'_{i+1}); the GHS and FF corrections then yield the new phase space position (s_{i+1}, p_{i+1}).

with $\det \hat{J}_B = 1$, as billiards are Hamiltonian systems. The extended mapping is thus in general not area-preserving, and this is entirely due to the FF; the GHS is a Hamiltonian correction. The trace is given by

$$\operatorname{tr} \hat{J}_E = \operatorname{tr} \hat{J}_B + \frac{\partial \Delta s}{\partial p}\frac{\partial g}{\partial s} + \frac{\partial \Delta p}{\partial p}\frac{\partial g}{\partial s}. \tag{6.23}$$

Using $\det \hat{J}_E$ and $\operatorname{tr} \hat{J}_E$, one can discuss the stability of any given fixed point. The eigenvalues $\lambda_\pm$ of $\hat{J}_E$ are given by

$$\lambda_\pm = \frac{1}{2}\operatorname{tr} \hat{J}_E \pm \sqrt{\frac{1}{4}(\operatorname{tr} \hat{J}_E)^2 - \det \hat{J}_E}. \tag{6.24}$$

The fixed point is stable if $D_{\hat{J}_E} = (\operatorname{tr} \hat{J}_E)^2 - 4\det \hat{J}_E < 0$ (complex $\lambda_\pm$), unstable if $D_{\hat{J}_E} > 0$ (real $\lambda_\pm$) and marginally stable if $D_{\hat{J}_E} = 0$. In first order in Δs, Δp, one finds

$$\begin{aligned} D_{\hat{J}_E} &= (\operatorname{tr} \hat{J}_B)^2 - 4\det \hat{J}_B + 2\operatorname{tr} \hat{J}_B \left[\frac{\partial \Delta s}{\partial s}\frac{\partial g}{\partial s} + \frac{\partial \Delta p}{\partial p}\left(\frac{\partial g}{\partial p} - 4\right)\right] \\ &= D_{\hat{J}_B} + 2\operatorname{tr} \hat{J}_B \left[\frac{\partial \Delta s}{\partial s}\frac{\partial g}{\partial s} + \frac{\partial \Delta p}{\partial p}\left(\frac{\partial g}{\partial p} - 4\right)\right]. \end{aligned} \tag{6.25}$$

As Δs and Δp are small corrections, they only rarely can change a positive $D_{\hat{J}_B}$ into a negative one and vice versa; the stability of a fixed point will thus be the same in the extended billiard dynamics. Only in the marginally stable ($D_{\hat{J}_B} = 0$) case, a fixed point is drastically affected by the wave corrections, and an invariant line can be broken into stable and unstable fixed points (Poincaré-Birkhoff-theorem). An example is discussed in section 6.4 in the elliptical billiard.

If $\partial\Delta p/\partial p < 0$, a stable fixed point will become an attractor in the non-Hamiltonian dynamics; if $\partial\Delta p/\partial p > 0$, it becomes a repeller; the stability is in general not changed. This may comes as a surprise, as one could assume that stable fixed points could only become attractors. Stability of a phase space structure and the type of the dynamics (contracting or expanding) are, however, not related: just like an attractor has a basin of attraction (set of points which converge to the attractor in forward-time evolution) which corresponds to the stable island in the Hamiltonian dynamics, a repeller has a basin of repulsion (set of points which converge to the repeller in *backward-time evolution*) which also corresponds to the stable island in the Hamiltonian dynamics. That both attractors and repellers can be found is an interesting feature of the p dependence of the FF. The "pinball billiards" [AMS09], for example, only show attractors because a constant $\partial\Delta p/\partial p < 0$ is used.

The FF breaks the time-reversal symmetry $(s, p) \to (s, -p)$ present in the billiard system; the partial waves with angles of incidence below the critical angle get refracted out – when reversing the beam, the now incoming beam has a lot less components below the critical angle and does not loose as much intensity. This sometimes creates confusion, as the *wave dynamics* of the system seems to be time-reversal invariant (after all, the Maxwell equations are). This apparent contradiction resolves if one notes that in the

the wave picture, time-reversal invariance is *also* broken due to the outgoing boundary conditions which are usually imposed. If light can not only get out of the cavity, but also come back from infinity, the wave dynamics is time-reversal invariant, and so is the extended ray dynamics.

6.4. GHS and localization of modes in the ellipse

In this section, the effect of the wave corrections on a system whole billiard analog (the ellipse) is integrable is studied. One finds new pairs of stable and unstable periodic orbits, and mode localization along them. Such localization can not be explained from the point of view of the conventional ray dynamics, as the periodic orbits are marginally stable in this case. However, as these orbits turn stable and unstable in the extended ray dynamics, the localization is easily explainable as scarring or localization on stable islands. By calculating mode frequencies for different ellipse eccentricities, it is shown that the localization of modes along periodic orbits happens at avoided resonance crossings.

6.4.1. The open ellipse

In contrast to the elliptical billiard, the dielectric ellipse is not integrable, as the Helmholtz equation only separates for hard-wall boundary conditions [Nöc97]. As the wave corrections GHS and FF only appear because of the openness of a cavity, the extended ray dynamics of the ellipse should reflect this non-integrability.

Figure 6.9 shows the phase space of the ellipse at $e = 0.649$. Far way from the critical line, where the FF is small, the dynamics is approximately Hamiltonian, and some invariant tori persist – thus, WGMs can still be found. In the leaky region, the dynamics is repulsive, but bouncing-ball structures still exist as transients; as rays follow such a line for many bounces, mode localization on these structures can still happen. Because of the corrections, some invariant lines are broken up, giving rise to the stable and unstable period four orbits. This is an effect of the GHS alone [UWH08]. It is consistent with the Poincaré-Birkhoff theorem, where a Hamiltonian correction breaks invariant tori into pairs of stable and unstable periodic orbits.

Figure 6.10 shows emerging Husimi functions for two modes in the $e = 0.649$ ellipse together with the corresponding periodic orbits; the localization can be clearly seen. A similar scenario is valid for the $e = 0.845$ ellipse. There, an additional stable island (corresponding to a "bowtie" orbit) and an unstable periodic orbit appear; there is also localization along them, as shown in Fig. 6.11.

This localization along periodic orbits in the open ellipse would be difficult to understand from a conventional ray-dynamical point of view. Basically, there are two mechanisms which can lead to such localization: scarring [Hel84], which in chaotic systems leads to localization along *unstable* periodic ray trajectories, and localization on *stable* islands (according to the "semiclassical eigenfunction hypothesis" [Per73, Ber77]). Both mechanisms are not applicable here, as in the closed ellipse, the periodic orbits in question are marginally stable and thus neither stable nor unstable. The conventional

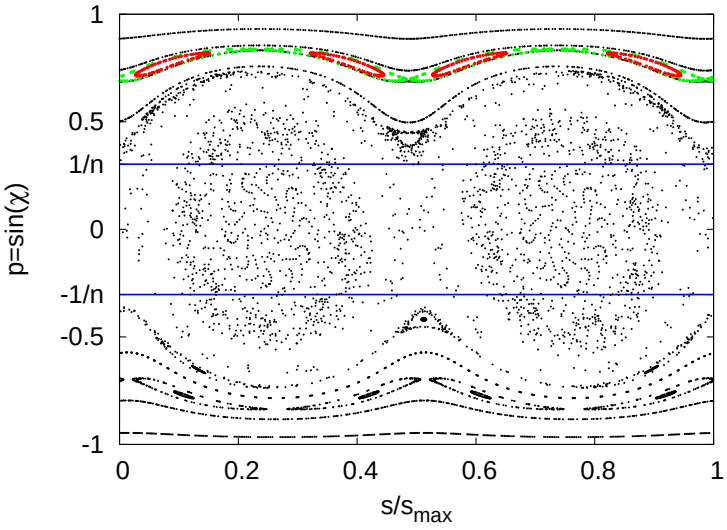

Figure 6.9.: Phase space for the $e = 0.649$ ellipse with wave corrections at $n = 3.3$, TM polarization, and $kR = 8.2$. The red dots mark the stable period-4 islands, the green dots belong to the corresponding unstable trajectory. The blue line marks the critical line for TIR.

ray dynamics thus can not explain this localization, which probably could be expected because it happens at an ARC which also is not present in the closed billiard.

The extended ray dynamics, however, can explain the localization, as it implements corrections which also include the openness of this system.

6.4.2. Scaling with the wavelength

As the GHS is a correction proportional to the wavelength λ (thus scaling with $1/kR$), one could guess that the size of an island formed by this correction also scales with $1/kR$. The size is measured as the phase space area $A = \oint \mathrm{d}s\, p$; it is estimated by overlaying a raster on the island and calculating the area by counting the raster blocks inside. This only gives a rough estimate, as there is uncertainty in the choice of the boundary of the island (one tries to find the outermost boundary, but does not always hit it), as well as deviations depending on the raster parameters. However, the estimate should be enough for studying scaling properties.

Figure 6.12 shows the scaling of the island corresponding to the rectangular orbit at eccentricity $e = 0.649$ (top panel) and the island corresponding to the bowtie mode at $e = 0.845$ (bottom panel) in a double-logarithmic plot. A linear dependence on kR with slope -1 would be expected for scaling with $1/kR$, but while the dependence in both cases is linear, the slope is larger than -1, and different in both cases. At $e = 0.845$, a slope of ≈ -0.7 is found, and at $e = 0.649$, one finds ≈ -0.3. The inset show the shape of the bowtie island for different kR values. In the case if the bowtie island, the first two data points ($kR = 6.5$ and $kR = 13$) have not been used in the fit, as the islands in

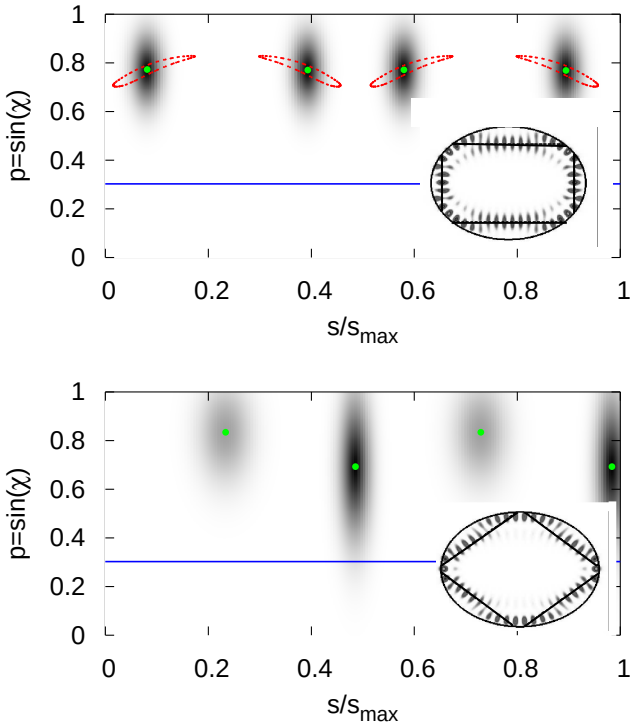

Figure 6.10.: Emerging Husimi functions for modes localizing on stable ("rectangle", top panel) and unstable ("diamond", bottom panel) period-4 orbits in the $e = 0.649$ ellipse. The blue line marks the critical line. The stable and unstable orbit positions are shown as green dots; the stable island is shown in red. The real-space mode patterns are shown in the insets; the periodic orbits are shown as black lines.

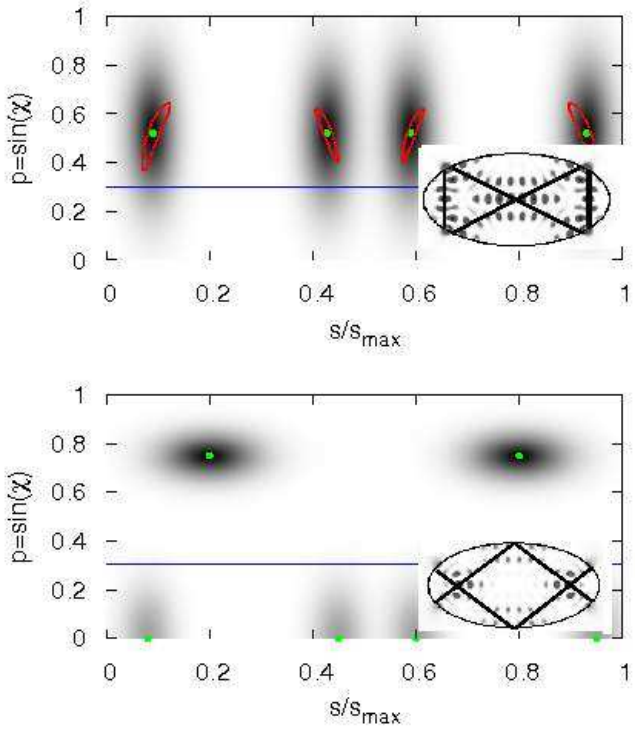

Figure 6.11.: Emerging Husimi functions for modes localizing on stable ("bowtie" top panel) and unstable (bottom panel) periodic orbits in the $e = 0.845$ ellipse. The blue line marks the critical line. The stable and unstable orbit positions are shown as green dots; the stable island is shown in red. The real-space mode patterns are shown in the insets; the periodic orbits are shown as black lines.

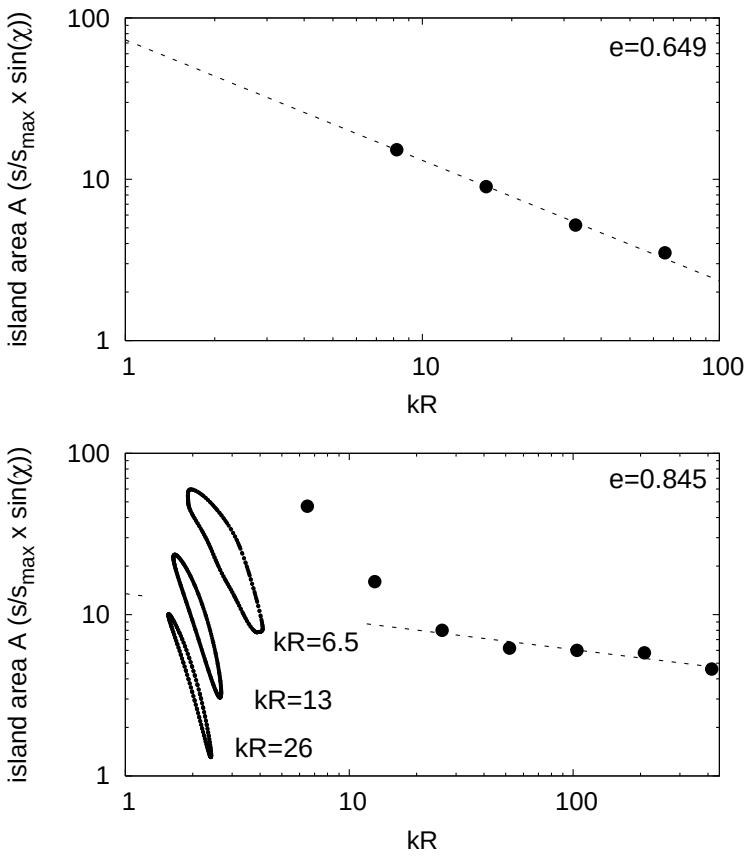

Figure 6.12.: Size of the islands created by the GHS as a function of kR on a double-logarithmic scale. Top panel: stable period-4 island at eccentricity $e = 0.649$, corresponding to the rectangle orbit; the line is a linear fit with slope -0.7. Bottom panel: bowtie orbit at $e = 0.845$ with a linear fit with slope -0.3; the first two data points have not been used in the fit. The insets shows the shape of the bowtie island for different kR values.

this case are very near to the critical line and strongly influenced by it.

Especially in the rectangle case, but also in the bowtie case, the GHS-created islands look "too small" to support the modes. This can be quantified, as the number m of modes fitting into an island of area A can be calculated semiclassically. In EBK quantization, the action I fulfills

$$I = \frac{1}{2\pi} \oint \mathrm{d}s\, p = m\hbar. \tag{6.26}$$

with $p = nk\hbar \sin\chi$ and thus $A = \oint \mathrm{d}s\, p = 2\pi nkI$, one finds

$$m = \frac{I}{\hbar} = \frac{nk\hbar A}{2\pi\hbar} = \frac{nkRA}{2\pi R}. \tag{6.27}$$

From Eq. (6.27) and the estimated island areas, one finds $m \approx 0.04$ for the rectangle island at $kR = 8.2$ and $m \approx 0.1$ for the bowtie island at $kR = 6.5$. As m is smaller

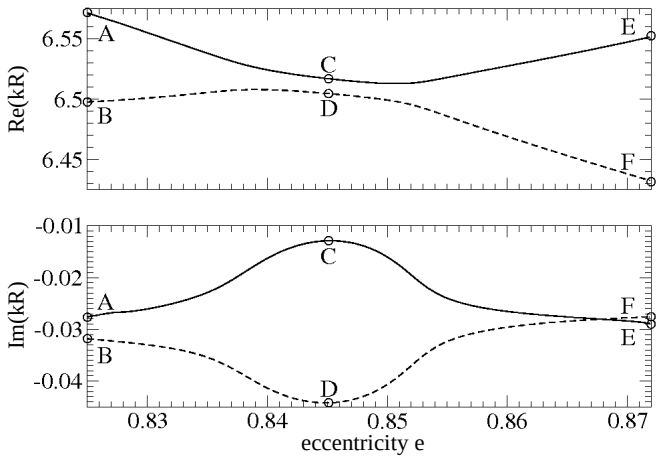

Figure 6.13.: Avoided resonance crossing in the real (top panel) and imaginary (bottom panel) part of kR in the dielectric ellipse at $n = 3.3$.

than one in both cases, one would not expect modes to be able to localize on the island. However, small islands accommodating modes is a well-known phenomenon; typically, it is possible because there are cantori confining the mode, as argued in [WRB05] for a soft-wall billiard or in [SLK+08] for a deformed microcavity. Here, the confinement is not due to cantori, but to *tori*: the unbroken invariant lines of the open ellipse.

6.4.3. Avoided resonance crossings in the dielectric ellipse

The stable islands and unstable periodic orbits are present at different eccentricities e of the ellipse, not just at the ones shown in section 6.4.1 (in particular, the period-4 island seems to be present at all deformations $0 < e \leq 0.85$). However, localization of modes along them only happens at particular e values. If one calculates mode frequencies for a variety of e values around those with localization along periodic orbits, as shown in Figs. 6.13 and 6.14, one finds that this localization happens at an avoided resonance crossing (ARC) between two complex mode frequencies. Integrable systems typically do not show avoided crossings; as their nearest-neighbor level distribution is a Poisson distribution [Stö00], they allow for much more degeneracy of levels, which leads to level crossings, not avoided crossings. ARCs are thus a strong sign for the non-integrability of the open ellipse.

ARCs in microcavities are of interest because they can lead to the formation of long-lived states with directional output [WH06] by coupling a long-lived, non-directional state to a short-lived, directional one. This scenario also happens in the ellipse; an example is shown in Fig. 6.13. The modes corresponding to the points labeled A – F are shown in Figs. 6.15 and 6.16. The hybridized modes A,B and E,F in Fig. 6.15 are of the bouncing-ball type. The modes C and D at the ARC are not of this type, but localizing along periodic orbits which are stable (mode C) or unstable (mode D) in the extended ray dynamics. Mode C has a much higher Q factor than mode D.

In Fig. 6.16, the modes A, B and E, F are of the whispering-gallery type, but the

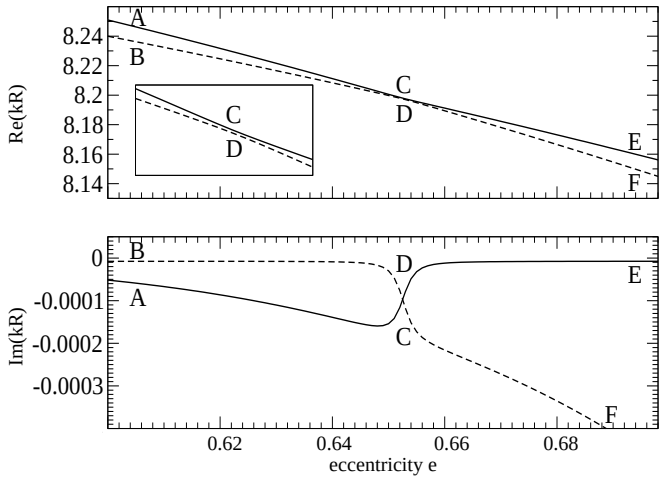

Figure 6.14.: Avoided resonance crossing in the real (top panel) and crossing in the imaginary (bottom panel) part of kR in the dielectric ellipse at $n = 3.3$. The inset of the top panel shows the ARC more clearly.

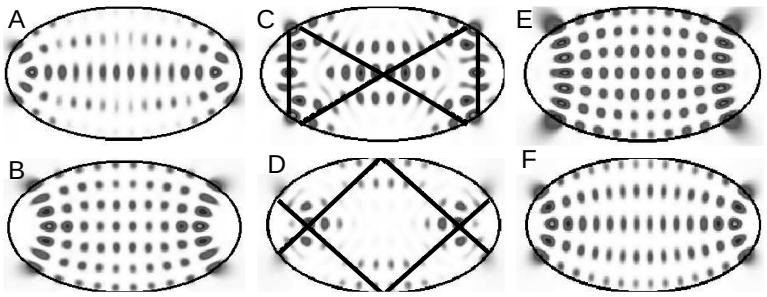

Figure 6.15.: Modes corresponding to the points A – F in Fig. 6.13. While A, B and E, F are bouncing-ball like modes, C and D localize along periodic orbits (red lines), which are stable (C) and unstable (D) in the extended ray dynamics.

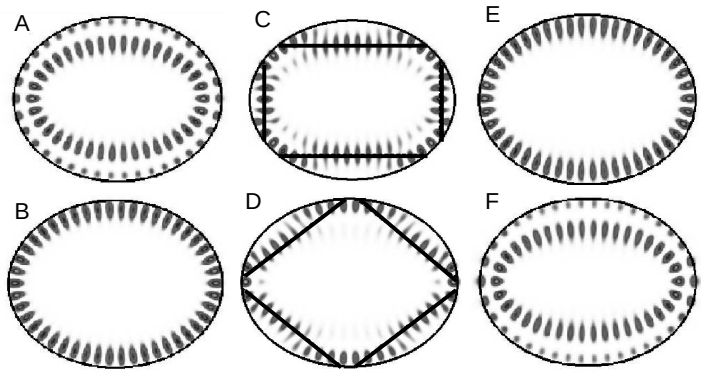

Figure 6.16.: Modes corresponding to the points A – F in Fig. 6.13. While A, B and E, F are whispering-gallery like modes, C and D localize along periodic orbits (red lines), which are stable (C) and unstable (D) in the extended ray dynamics.

modes C and D at the ARC are again localizing along periodic orbits. As the imaginary parts of kR cross in this case (see bottom panel of Fig. 6.14), the modes C and D have similar Q factors.

At an ARC, the two modes whose frequencies come close hybridize; the modes at the ARC then are superpositions of these modes. Such a superposition can lead to a wave function which can be decomposed into a rapidly oscillating part and a weakly varying envelope. The latter defines the localization pattern, which can resemble localization along a short periodic orbit. For example, mode D in Fig. 6.15 resembles the difference of modes B and A: there is no intensity in the center of the cavity, only at the top and bottom parts and near the points of highest curvature of the boundary.

In conclusion, there are two different ways of understanding the formation of modes localized on periodic ray trajectories in the ellipse. One is based only on the wave picture: because of the openness, the ellipse is no longer integrable, ARCs appear, and hybridization of modes leads to the formation of modes localized along periodic ray trajectories. The other way is semiclassical and based on the extended ray dynamics: because of the openness, the extended ray dynamics is no longer integrable; the wave corrections lead to the breakup of invariant lines into pair of stable and unstable periodic orbits, and localization of modes on stable islands and along unstable periodic orbits is possible. The extended ray dynamics thus can give physical insight into the wave dynamics in this case where the conventional ray dynamics could not.

6.5. Shift of phase space structures

In this section, the interplay of the GHS and the boundary curvature of a cavity is studied. It leads to a momentum shift of phase space structures, which is calculated analytically in section 6.5.2 and compared to wave calculations in section 6.5.3. While this shift appears in all cavities with non-vanishing boundary curvature which support

period orbits when introducing the GHS, the special case of the $\epsilon = 0.2$ limaçon is considered as am example; the phase space structure in the case with the wave corrections is introduced in section 6.5.1. In section 6.5.4, the equivalent of the momentum shift in quantum maps is discussed briefly.

6.5.1. Shift of islands in the limaçon

Without the wave corrections, the $\epsilon = 0.2$ limaçon is mostly regular, with only small chaotic regions. When the corrections are included, more chaos appears. Some regular parts persist, in particular the period-3 orbit, which now is a (regular) attractor because of the non-Hamiltonian FF. Figure 6.17 shows the phase space of the $\epsilon = 0.2$ limaçon without (top panel) and with (bottom panel) the wave corrections. The refractive index is $n = 2$, $kR = 14$, and the polarization is TM. Figure 6.18 shows the different types of dynamics present in the system with wave corrections. According to (6.22),

$$\det \hat{E} = 1 + \frac{\partial \Delta p}{\partial p}, \tag{6.28}$$

regions with a positive derivative of the FF Δp are repulsive (phase space volume grows, $\det \hat{E} > 1$), regions with a negative derivative are attractive (phase space volume contracts, $\det \hat{E} < 1$). It is interesting to compare the phase space positions of the period-3 structure with and without the phase space corrections. The period-3 island in the closed limaçon is located right at the critical line; it is thus strongly affected by the GHS and a little less strongly by FF. In Fig. 6.19, the two positions are compared. It is clear that the position of the period-3 attractor in the limaçon with GHS and FF is shifted to higher p values, away from the critical line. The geometrical origin of this shift is discussed in section 6.5.2; it is not due to the FF (which of course also changes the p value of a given structure) alone, but instead, the main contribution arises from the combination of the GHS with a non-vanishing boundary curvature.

6.5.2. Periodic orbit shift

The vertical shift of periodic orbits in phase space can be calculated analytically for the special case of an orbit which stays periodic with the same periodicity and symmetry (as opposed to the "pitchfork"-type bifurcation studied in section 6.6.2, where new orbits with the same periodicity but broken symmetry appear). For example, in the limaçon at $\epsilon = 0.2$ the period-3 and period-4 orbits are of this type, as shown in Fig. 6.20). The rays are "pushed outwards" from the unperturbed orbits. The "outwards pushing" means that the direction vectors without and with the corrections ($\mathbf{v}$ and $\mathbf{v}'$) of the rays are parallel. It should be noted that strictly speaking, such parallelity is not possible if the FF is included, as the incoming and outgoing angles of the perturbed ray still have to be the same if it is parallel to the unperturbed ray. However, if one studies periodic orbits far away from the critical line, where the FF is small, $\mathbf{v}$ and $\mathbf{v}'$ are approximately parallel and the reasoning of this section may still be used.

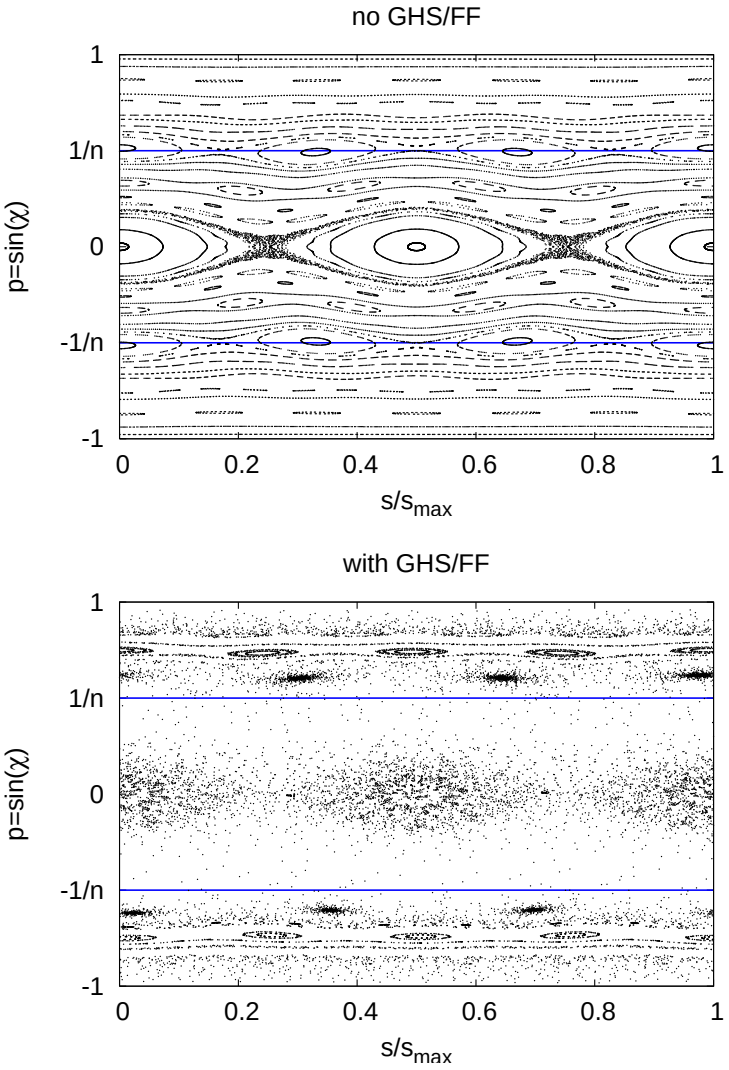

Figure 6.17.: Phase spaces for the $\epsilon = 0.2$ limaçon without (top panel) and with (bottom panel) the wave corrections GHS and FF. The blue line indicates the critical line. The parameters are $n = 2$, $kR = 14$, TM polarization.

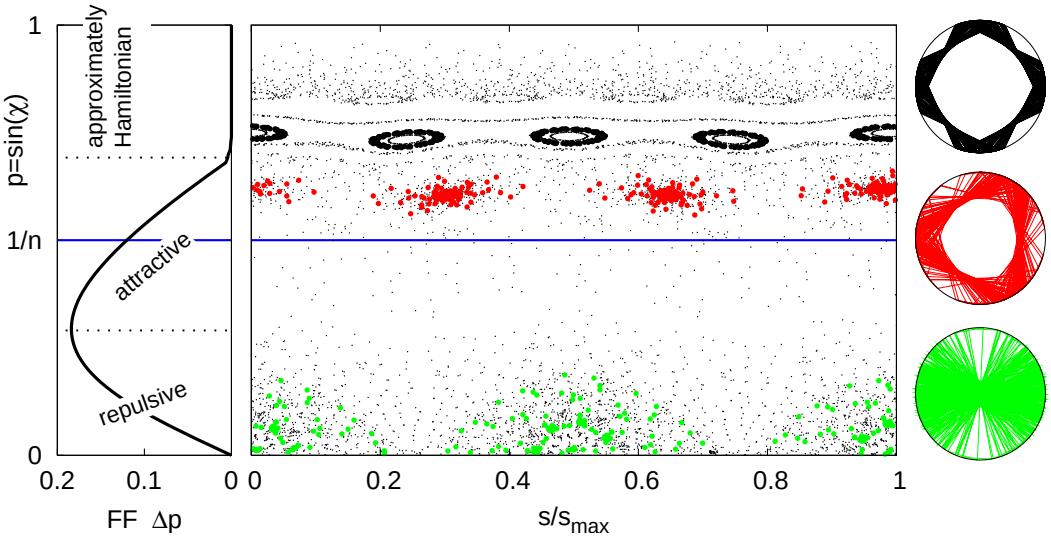

Figure 6.18.: Main panel: Phase space for the $\epsilon = 0.2$ limaçon with wave corrections. Three different types of dynamics present in this system are indicated: near $p = 0$, the dynamics is repulsive (green dots) because of the positive $\partial\Delta p/\partial p$. Above the critical line, the dynamics becomes attractive; the period-3 attractor, which is the strongest one, is indicated in red. For even higher p, the Fresnel filtering is almost zero, which leads to almost Hamiltonian dynamics, as seen for example in the period-4 orbit indicated in black, which is only very weakly attractive. The left panel shows the FF as a function of p.

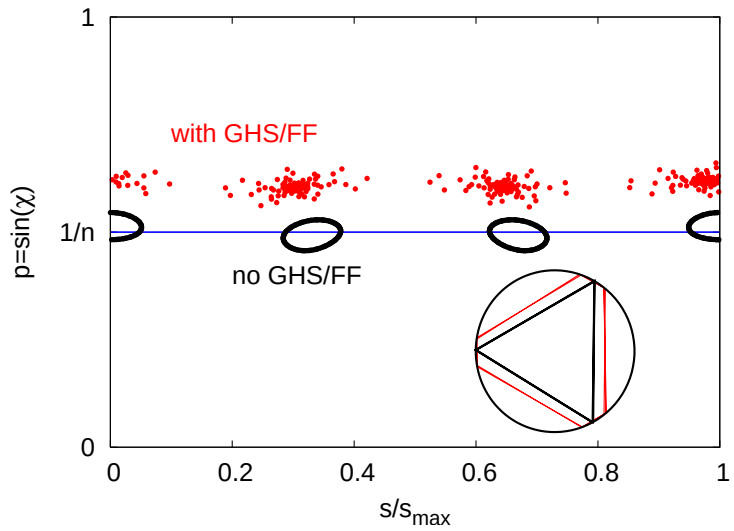

Figure 6.19.: Period-3 island in the limaçon without GHS and FF (black dots) and period-3 attractor (red dots) in the limaçon with GHS and FF. The critical line is indicated by the blue line, and the inset shows the periodic orbits corresponding to the phase space structures.

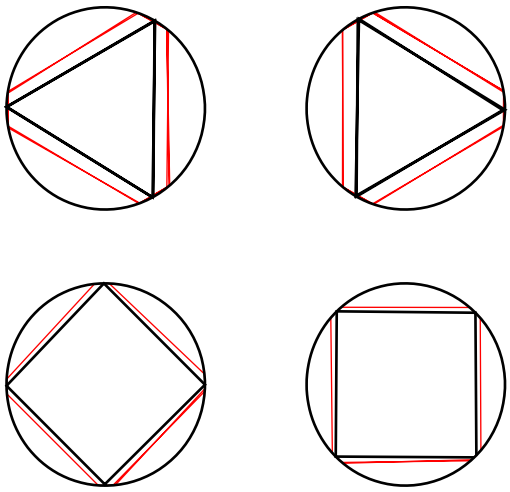

Figure 6.20.: Stable (left column) and unstable (right column) period-3 and period-4 orbits in the closed limaçon at $\epsilon = 0.2$ (black curves) and in the limaçon with $kR = 14$ including GHS and FF corrections (red curves).

Let χ denote the angle of incidence without GHS/FF and χ' the one with them. Using the local tangent vectors $\boldsymbol{\tau}$, $\boldsymbol{\tau}'$ at the bounce points with polar angles ϕ, ϕ' (the corresponding arc lenghts s, s' fulfill $s' - s = \Delta s/2$ with the GHS Δs), and the local normal vectors $\boldsymbol{\nu}$, $\boldsymbol{\nu}'$ (see Fig. 6.21), one finds

$$\begin{aligned} \sin\chi' &= \mathbf{v}' \cdot \boldsymbol{\tau}' = \mathbf{v} \cdot \boldsymbol{\tau}' \quad (\mathbf{v}||\mathbf{v}') \\ &= (\sin\chi\boldsymbol{\tau} - \cos\chi\boldsymbol{\nu}) \cdot \boldsymbol{\tau}'. \end{aligned} \tag{6.29}$$

The vertical shift can then be expressed as

$$\sin\chi' - \sin\chi = \sin\chi\,(\boldsymbol{\tau}\cdot\boldsymbol{\tau}' - 1) - \cos\chi(\boldsymbol{\nu}\cdot\boldsymbol{\tau}'). \tag{6.30}$$

One can clearly see from Eq. (6.30) that the vertical shift is due to the boundary curvature: if the curvature vanishes, $\boldsymbol{\tau} = \boldsymbol{\tau}'$ and $\boldsymbol{\nu} = \boldsymbol{\nu}' \perp \boldsymbol{\tau}'$, so that the right hand side of (6.30) vanishes.

If one sets $\boldsymbol{\tau}' = \boldsymbol{\tau} + \Delta\boldsymbol{\tau}$ and $\boldsymbol{\nu}' = \boldsymbol{\nu} + \Delta\boldsymbol{\nu}$, (6.30) simplifies to

$$\sin\chi' - \sin\chi = \sin\chi\,(\boldsymbol{\tau}\cdot\Delta\boldsymbol{\tau}) - \cos\chi\,(\boldsymbol{\nu}\cdot\Delta\boldsymbol{\tau})\,. \tag{6.31}$$

Using $\kappa\boldsymbol{\nu} = -\mathrm{d}\boldsymbol{\tau}/\mathrm{d}s$ with the curvature κ for the outwards pointing normal, one can approximate

$$\Delta\boldsymbol{\tau} \approx \kappa\frac{\Delta s}{2}\boldsymbol{\nu}, \tag{6.32}$$

which leads to

$$\sin\chi' - \sin\chi \approx \kappa\frac{\Delta s}{2}\cos\chi = \frac{\Delta s}{2\rho}\cos\chi. \tag{6.33}$$

This periodic orbit shift (POS),

$$\Delta p_{\mathrm{POS}} = \frac{\Delta s}{2\rho}\cos\chi, \tag{6.34}$$

thus depends on the ratio of the GHS Δs and the local radius of curvature ρ in this approximation. The curvature κ is in polar coordinates given by

$$\kappa = \frac{|r(\phi)^2 + 2r'(\phi)^2 - r(\phi)r''(\phi)|}{|r(\phi)^2 + r'(\phi)^2|^{3/2}}. \tag{6.35}$$

In the circle with radius R, $\rho = R$, and one finds a POS

$$\sin\chi - \sin\chi' = \frac{\Delta s}{2R}. \tag{6.36}$$

In [HS02] (more in detail in [Hen02]), it was noted that the inclusion of the GHS at a circular boundary can be interpreted as reflection taking place at the boundary with angle of incidence χ, but at an "interface" of larger radius of curvature, with an angle χ' with

$$\chi' = \chi - \frac{\Delta s}{2R}. \tag{6.37}$$

This was used to calculate generalized Fresnel coefficients for reflection at the circular boundary. As the authors did not look at modes and rays in cavities, but just at Gaussian beams reflected only once at the interface, they did not consider momentum shifts of phase space structures. By taking the sine of (6.37), one finds

$$\begin{aligned}\sin\chi' = \sin\left(\chi - \frac{\Delta s}{2R}\right) &= \sin\chi\cos\left(\frac{\Delta s}{2R}\right) + \sin\left(\frac{\Delta s}{2R}\right)\cos\chi \\ &\approx \sin\chi + \frac{\Delta s}{2R}\cos\chi.\end{aligned} \tag{6.38}$$

One thus recovers (6.33) in the limit of small Δs. This expression for the POS can be seen as a generalization of (6.36) for non-circular boundary shapes.

Equation (6.30) can also be evaluated directly, without the help of the approximation (6.32). If the boundary is given by $r = r(\phi)$ in polar coordinates, one can calculate the local normal and tangent vectors at position ϕ:

$$\begin{aligned}\boldsymbol{\tau} &= \frac{1}{\sqrt{r(\phi)^2 + r'(\phi)^2}}\begin{pmatrix} r'(\phi)\cos\phi - r(\phi)\sin\phi \\ r'(\phi)\sin\phi + r(\phi)\cos\phi\end{pmatrix}, \\ \boldsymbol{\nu} &= \frac{1}{\sqrt{r(\phi)^2 + r'(\phi)^2}}\begin{pmatrix} -r'(\phi)\sin\phi - r(\phi)\cos\phi \\ r'(\phi)\cos\phi - r(\phi)\sin\phi\end{pmatrix}.\end{aligned} \tag{6.39}$$

Using (6.39) and addition theorems for the trigonometric functions, one finds

$$\begin{aligned}\boldsymbol{\tau}\cdot\boldsymbol{\tau}' = \frac{1}{\sqrt{r(\phi)^2 + r'(\phi)^2}}\frac{1}{\sqrt{r(\phi')^2 + r'(\phi')^2}}\,&[\cos\Delta\phi\,(r'(\phi)r'(\phi') + r(\phi)r(\phi')) \\ &+ \sin\Delta\phi\,(r(\phi)r'(\phi') - r'(\phi)r(\phi'))]\end{aligned} \tag{6.40}$$

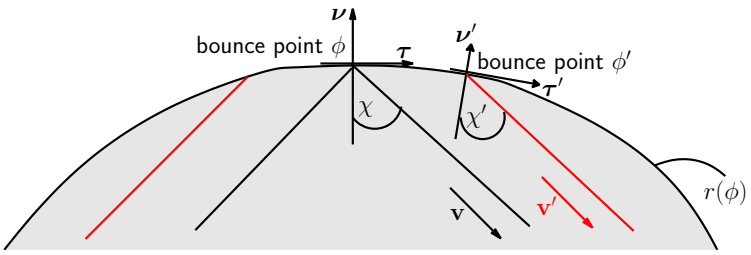

Figure 6.21.: Local tangent and normal vectors at a bounce point of a ray without GHS and FF (black line) and the corresponding ray with them. The unperturbed ray intersects with the boundary at $\phi \mathrel{\hat{=}} s$, the perturbed one at $\phi' \mathrel{\hat{=}} s'$. The GHS fulfills $\Delta s/2 = s' - s$, this corresponds to a shift in the polar angles of $\Delta\phi$.

and

$$\begin{aligned}\boldsymbol{\nu}\cdot\boldsymbol{\tau}' = \frac{1}{\sqrt{r(\phi)^2+r'(\phi)^2}}\frac{1}{\sqrt{r(\phi')^2+r'(\phi')^2}}\big[&\sin\Delta\phi\,(r'(\phi)r'(\phi')+r(\phi)r(\phi'))\\ &-\cos\Delta\phi\,(r(\phi)r'(\phi')-r'(\phi)r(\phi'))\big]\,.\end{aligned} \tag{6.41}$$

By inserting (6.40) and (6.41) into (6.30), the vertical shift $\sin\chi' - \sin\chi$ can be calculated:

$$\begin{aligned}\sin\chi' - \sin\chi = A(\phi,\phi')\Big[&\Big(\sin\chi\left(R(\phi,\phi')\cos\Delta\phi + \tilde{R}(\phi,\phi')\sin\Delta\phi\right)-1\Big)\\ &-\cos\chi\left(R(\phi,\phi')\sin\Delta\phi - \tilde{R}(\phi,\phi')\cos\Delta\phi\right)\Big]\,,\end{aligned} \tag{6.42}$$

with

$$\begin{aligned}A(\phi,\phi') &= \frac{1}{\sqrt{r(\phi)^2+r'(\phi)^2}}\frac{1}{\sqrt{r(\phi')^2+r'(\phi')^2}},\\ R(\phi,\phi') &= r'(\phi)r'(\phi')+r(\phi)r(\phi'),\\ \tilde{R}(\phi,\phi') &= r(\phi)r'(\phi')-r'(\phi)r(\phi').\end{aligned} \tag{6.43}$$

(6.43) and (6.33) give results differing by less than 1 % for typical values of the GHS and the limaçon boundary curve.

Results for the stable and unstable period-3 orbits are shown in Fig. 6.22. The horizontal shift due to the GHS is also indicated, as well as the vertical shift due to the FF. Taken together, these three corrections describe the phase space shift very well. Figure 6.23 shows the shifted stable and unstable period-4 orbits, where the shift is smaller because the GHS is smaller, as one is farther away from the critical line. Also in this case, the analytical formula describes the shift well.

As cavities with $kR \approx 10$ have been studied before, such vertical shifts should also have been seen before when comparing Husimi functions to period orbit positions. This is, in fact, true: in [FYC05], an $\epsilon = 0.15$ stadium-shaped cavity with $n = 3$ was investigated.

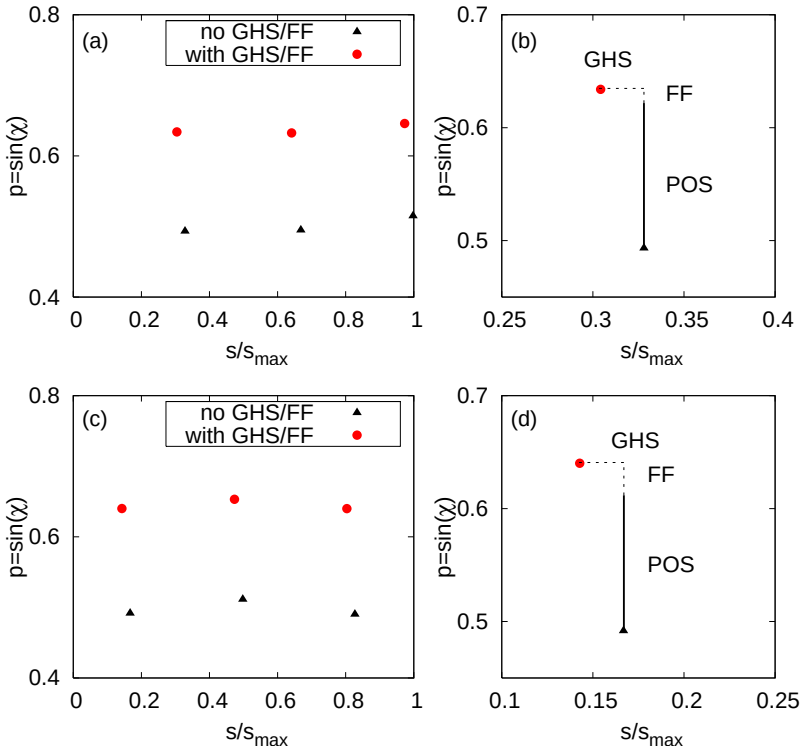

Figure 6.22.: (a) Phase space shifts for the stable period-3 orbit. The bounce points of the orbits with (red circles) and without (black triangles) GHS and FF are shown. The dashed lines indicate the phase space shifts due to GHS and FF; the solid line is the POS calculated according to (6.42). (b) Magnification of (a). (c) Phase-space shifts for the unstable period-3 orbit. (d) Magnification of (c).

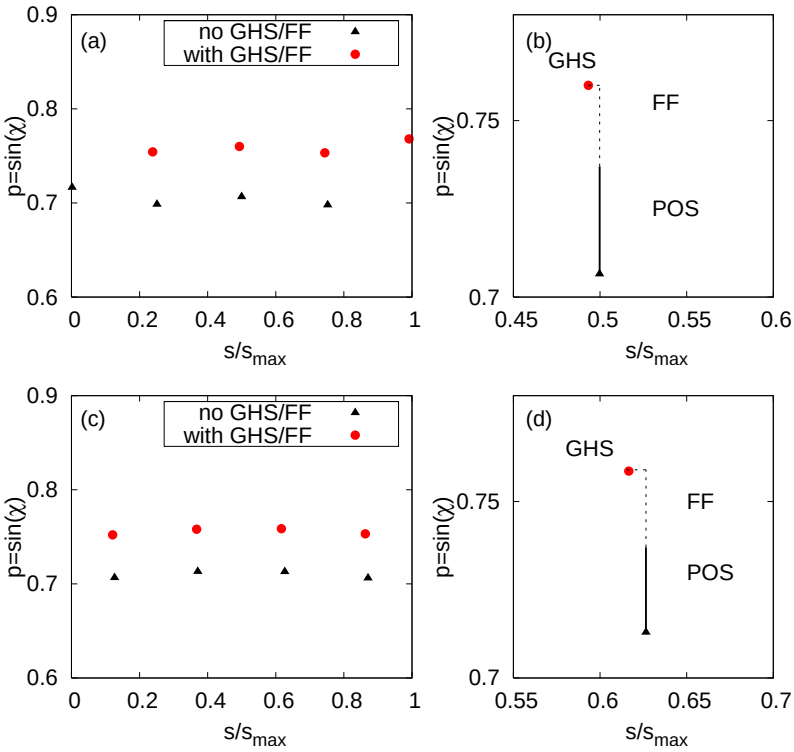

Figure 6.23.: (a) Phase space shifts for the stable period-4 orbit. The bounce points of the orbits with (red circles) and without (black triangles) GHS and FF are shown. The dashed lines indicate the phase space shifts due to GHS and FF; the solid line is the POS calculated according to (6.42). (b) Magnification of (a). (c) Phase-space shifts for the unstable period-4 orbit. (d) Magnification of (c).

At $kR \approx 3.3$, Husimi functions for modes localizing on a rectangular and a diamond-shaped unstable period orbit are shown. The rectangular one hits the boundary only at the half-circle parts, thus $\rho = r$ with the half-circle radius $r \approx 0.9\,\mu$m; with $p \approx 0.7$ one can estimate a periodic orbit shift of $\Delta p \approx 0.08$. The shift between the maxima of the Husimi function and the periodic orbit position is ≈ 0.1; the estimate is thus quite good. In the case of the diamond orbit, there are two different types of bounce points: the first type is located on the straight-line part of the stadium boundary, which has $\kappa = 0$ and thus yields no periodic orbit shift, as can be seen when comparing again Husimi maxima with the periodic orbit in phase space. The second type is located on the half-circle. Here, one also can estimate $\Delta p \approx 0.1$ from the Husimi function and $\Delta p \approx 0.08$ as the POS. The agreement is good again. A similar analysis can be applied to the $\epsilon = 1.1$ stadium with $n = 1.5$ from [FC07]; there, evaluation of the Husimi distribution yields $\Delta p \approx 0.05$, which agrees well with the POS $\Delta p \approx 0.04$.

Another interesting case is the one of a negative-index cavity. As the GHS is negative there [WUS+10a], one finds a negative POS. As an example, one can consider the unstable period-4 orbit in the $\epsilon = 0.43$ limaçon with positive and negative refractive index ($|n| = 1.5$). The results are shown in Fig. 6.24. The agreement is not as good as in the previous cases, which can be expected, as the approximation of parallel rays for the orbit without GHS and FF and the one with these corrections is not valid here. This effect is more pronounced for the negative-index case, which is due to the fact that the period-4 orbit in this belongs to the leaky region, as the shift is negative. The FF is more pronounced there (it is almost zero for the positive-index case), which leads to non-parallelity of the rays with and without corrections. However, the calculated POS still agrees qualitatively with the shift seen in phase space.

6.5.3. Localization of modes on shifted islands

Because phase space structure are shifted to higher p values by the POS (in conventional, positive-index cavities), modes localizing on them are farther away from the critical line as modes localizing on the original structures. In the case of the period-3 attractor, a mode localizing on the original island would be located right at the critical line, whereas a mode localizing on the period-3 attractor would be above the critical line, and thus would be longer-lived. The POS could thus, in principle, lead to modes localizing on certain phase space structures which have a high Q-factor than it could be expected from ray dynamics alone.

The picture, however, is not that simple because when considering the wave corrections, one no longer deals with rays but with beams; the corrections thus change the Fresnel coefficients. In [HS02], such deviations from the Fresnel laws have been studied. The authors show that the deviations, which are due to the non-vanishing curvature of the boundary, can be explained by taking into account the Goos-Hänchen effect at a planar interface; the resulting reflection coefficients show a "broadening" with $|r| < 1$ even above the critical angle. While no analytical formulas exist for such corrected Fresnel laws, the reflection coefficients can be calculated numerically by reflecting a wave packet

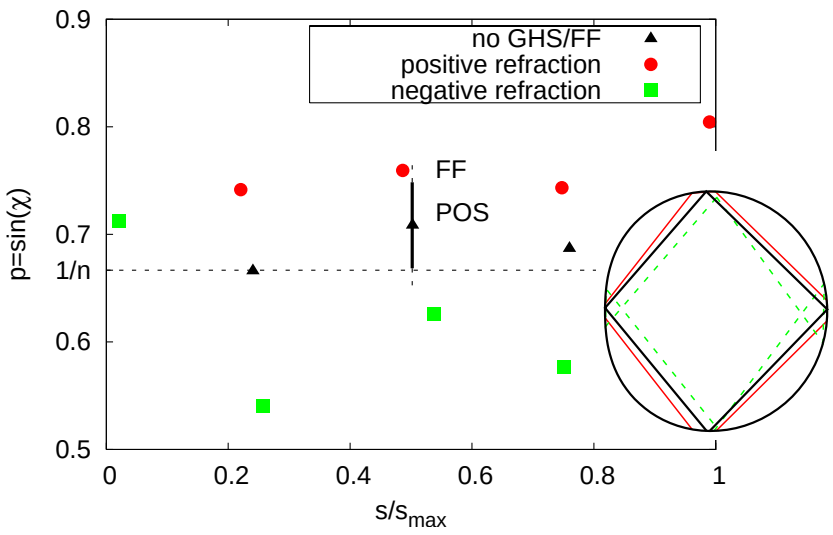

Figure 6.24.: Periodic orbit shifts of the period-4 orbit (black triangles) in the $\epsilon = 0.43$ limaçon with positive (red circles) and negative (green squares) refractive index $|n| = 1.5$. The POS is shown as the solid black line, the FF as the dashed black line. On the right, the orbits are depicted in real space.

at the interface:

$$\psi_{\text{in}}(x) = \int_{-1}^{1} \mathrm{d}p\, e^{inkpx} f_{\text{in}}(p) \rightarrow \psi_{\text{out}}(x) = \int_{-1}^{1} \mathrm{d}p\, e^{inkpx} f_{\text{in}}(p) r(p), \tag{6.44}$$

and calculating the reflection coefficient of the wave packet as

$$|\tilde{r}|^2 = \frac{\int_{-\infty}^{\infty} \mathrm{d}x |\psi_{\text{out}}(x)|^2}{\int_{-\infty}^{\infty} \mathrm{d}x |\psi_{\text{in}}(x)|^2}. \tag{6.45}$$

r is the Fresnel coefficient for a ray at a planar interface, and the wave packets are defined as in section 6.2.1. Evaluation of Eq. (6.45) for all incoming angles yields the modified reflection coefficient $|\tilde{r}|$. Figure 6.25 shows how the shifted period-3 structure relates to this new reflection coefficient. It can be seen that even when accounting for the deviations, the period-3 attractor is still localized in a region with approximate total internal reflection ($|\tilde{r}| \approx 90\%$).

One can thus find long-lived modes localizing on the period-3 attractor, and, as it turns out, also on the corresponding unstable period-3 orbit. Figure 6.26 shows Husimi functions and modes patterns (calculated with the BEM) of such modes. The filled dots indicate the orbits in the case with wave corrections, the open circles indicate the orbits in the case without wave corrections. The agreement with the shift is good, which can also be seen in the mode pattern itself. The Q factors are 682 (mode localizing on the stable orbit) and 460 (mode localizing on the unstable orbit).

Are these Q factors "high"? Certainly not by the standards for laser applications, where typically $Q = 10^4$ can be achieved. But they are high compared to what can be

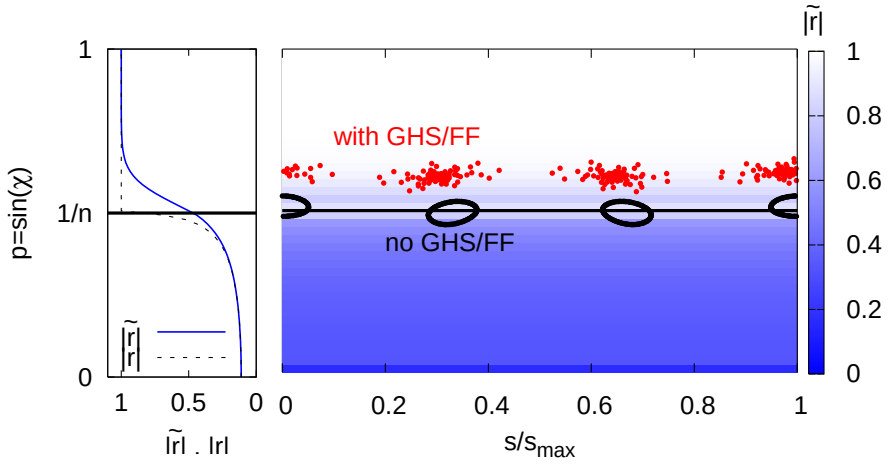

Figure 6.25.: Main panel: period-3 island and attractor as given in Fig. 6.19. The color scale corresponds to the value of the modified reflection coefficient $|\tilde{r}|$. On the left, the Fresnel reflection coefficient $|r|$ (dashed line) and modified reflection coefficient $|\tilde{r}|$ (solid line) for $kR = 14$.

expected from the ray dynamics without corrections alone. Following [HS02], one can calculate the Q factor from the reflection probability $\tilde{R}$ of a given ray in a circular cavity with radius R_c (direct tunneling into the leaky region). Reflections happen with a rate

$$\gamma_r = \frac{c}{2nR_c \cos\chi}, \tag{6.46}$$

which can be related to the intensity decay rate γ_I by

$$|R|^{t\gamma_r} = e^{-t\gamma_I} \rightarrow \gamma_I = -\gamma_r \ln|R| = -\frac{c \ln|R|}{2nR_c \cos\chi}. \tag{6.47}$$

$|R|$ is the absolute value of the reflection coefficient. γ_I in turn is related to the Q factor via

$$Q = \frac{c\mathrm{Re}(k)}{\gamma_I} = -\frac{2n\cos\chi \mathrm{Re}(kR_c)}{\ln|R|}. \tag{6.48}$$

With $n = 2$, $p = 0.5$ ($|\tilde{r}| \approx 0.5$ at this point), one finds $Q \approx 72$, which is almost ten times lower than the Q factors for the modes localizing on the period-3 attractor. As the period-3 attractor in the extended ray dynamics is located at $p \approx 0.6$, one can estimate the Q factor in the extended ray dynamics as $Q \approx 225$, which also is lower than the Q factors of the modes localizing on the period-3 orbits, but closer to the actual order of magnitude. The deviation may be due to the fact that one does, in fact, not deal with a circular boundary here. So, the modes localizing on "shifted" phase space structures are "high" by comparison. The period-4 stable and unstable orbits also experience a shift; there are also modes localizing on them. An example is shown in Fig. 6.27. The

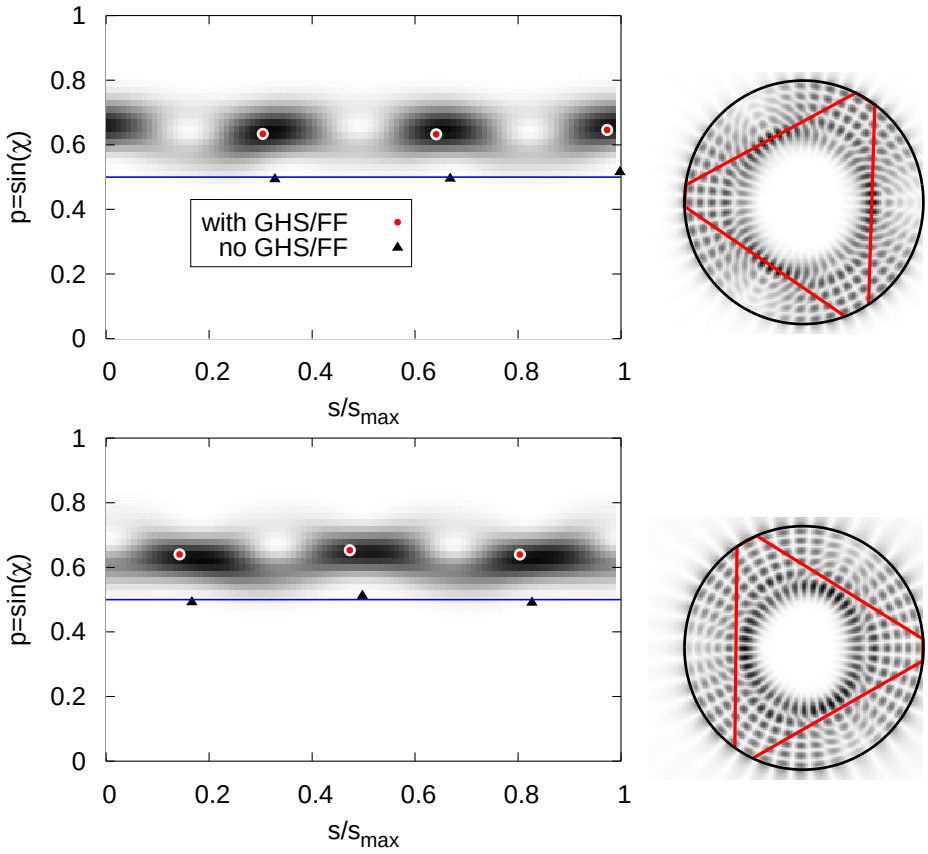

Figure 6.26.: Outgoing Husimi distributions for a mode with $kR = 13.9 - 0.01i$ localizing on the stable period-3 orbit (top panel) and a mode with $kR = 13.9 - 0.015i$ localizing on the unstable period-3 orbit (bottom panel). The stable and unstable orbits are indicated with red filled dots; black triangles are the corresponding orbits without wave corrections. On the right, the mode patterns are shown.

agreement is again good, but harder to see than in the period-3 case because the shift is smaller.

6.5.4. "Periodic orbit shift" in quantum maps

Even though the POS has been derived for billiards, it also arises in maps which are amended by a correction Δs. The typical example of a map is the Chirikov standard map [Chi79], which can be written as

$$\begin{aligned} p_{j+1} &= p_j + K \sin q_j, \\ q_{j+1} &= q_j + p_{j+1}. \end{aligned} \tag{6.49}$$

The constant K can be varied from zero to infinity, which leads to a KAM transition from regular behaviour ($K = 0$) to chaotic dynamics ($K \approx 1$). For $K = 0$, the standard map is very similar the motion of a particle with mass one in a circular billiard, as $p = \text{const}$.

Introducing a correction $\Delta s = \Delta s(p_j)$ to the standard map, one finds the "extended standard map"

$$\begin{aligned} p_{j+1} &= p_j + K \sin q_j, \\ q_{j+1} &= q_j + p_{j+1} + \Delta s(p_{j+1}). \end{aligned} \tag{6.50}$$

It can be already guessed from Eq. (6.50) that Δs can act as a correction not only of q, but of p: it can be rewritten as

$$\begin{aligned} \tilde{p}_{j+1} &= p_j + K \sin q_j + \Delta s(p_j), \\ q_{j+1} &= q_j + \tilde{p}_{j+1} \end{aligned} \tag{6.51}$$

by defining an amended new momentum $\tilde{p}_{j+1} = p_{j+1} + \Delta s(p_j)$. This only works because of the simplicity of the q_{j+1} equation; the mapping can not be rewritten this easily in a billiard mapping.

The standard map can be quantised by introducing a Hamiltonian, $H(q, p) = T(p) + V(q)$, such that

$$\begin{aligned} p_{j+1} &= p_j - \frac{\partial V}{\partial q}\Big|_{q_j}, \\ q_{j+1} &= q_j + \frac{\partial T}{\partial p}\Big|_{p_{j+1}}; \end{aligned} \tag{6.52}$$

one can choose $T(p) = p^2/(2m)$ and $V(q) = K \cos q$. The time evolution operator of the quantum standard map is then given by

$$\hat{U} = \exp(-i\hat{H}t/\hbar), \tag{6.53}$$

with $\hat{H}$ the Hamiltonian operator corresponding to the classical Hamiltonian fulfilling (6.52). The extended standard map can be quantized in the same way, using

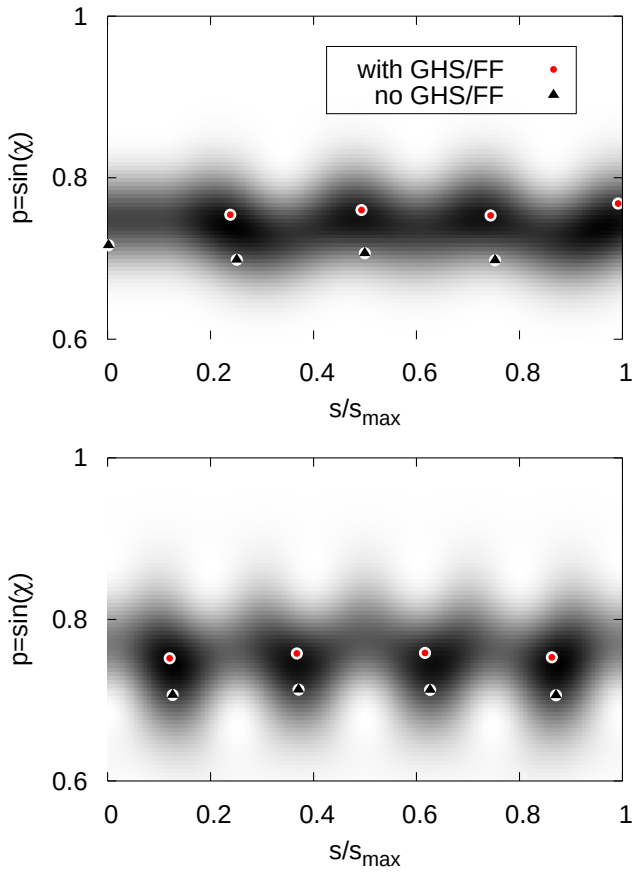

Figure 6.27.: Outgoing Husimi distributions for a mode with $kR = 14-0.0003i$ localizing on the stable period-4 orbit (top panel) and a mode with $kR = 14-0.0001i$ localizing on the unstable period-4 orbit (bottom panel). The stable and unstable orbits are indicated with red filled dots; black triangles are the corresponding orbits without wave corrections.

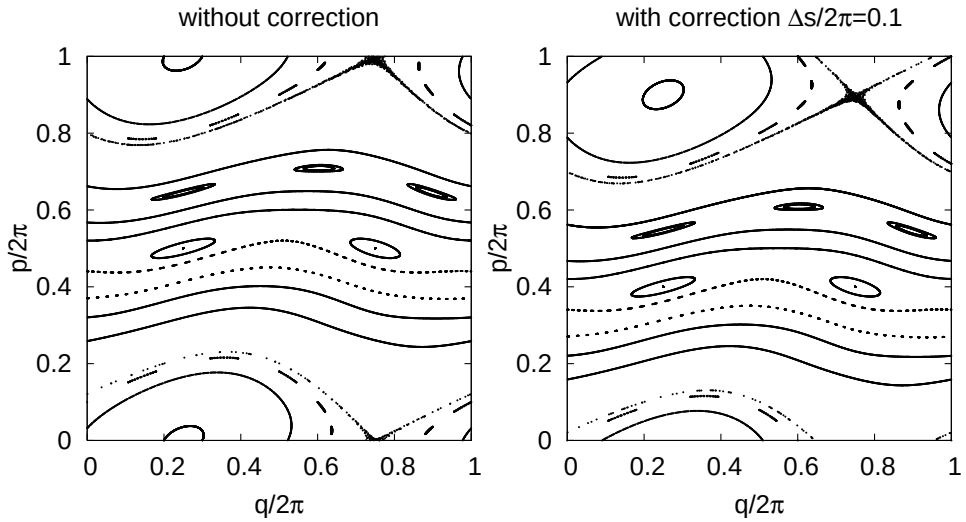

Figure 6.28.: Chirikov standard map for $K = 0.5$ without (left panel) and with (right panel) a constant correction $\Delta s = 0.1 \cdot 2\pi$.

$T'(p) = T(p) + \Phi(p)$, such that

$$\begin{aligned} q_{j+1} &= q_j + \frac{\partial T'}{\partial p}\Big|_{p_j} \\ &= q_j + \frac{\partial T'}{\partial p}\Big|_{p_{j+1}} + \Delta s(p_{j+1}). \end{aligned} \tag{6.54}$$

Δs is thus given by $\Delta s = \partial\Phi/\partial p$, in complete analogy to the Artmann result (6.14), where Δs also is given as the p-derivative of a function ϕ (in this case, the electromagnetic reflection coefficient phase). In the special case $\Delta s = \text{const}$ (not depending on p), Eq. (6.53) can be written as

$$\hat{U}_{\text{ext}} = \exp(-iT'(p)/\hbar)\exp(-iV(q)/\hbar) = \exp(-ip\Delta s/\hbar)\exp(-iT(p)/\hbar)\exp(-iV(q)/\hbar). \tag{6.55}$$

Splitting the exponentials is possible because $T(p), V(q)$ commute, as well as p and $T(p)$. The map of the extended standard map is thus given by

$$\hat{U}_{\text{ext}} = \exp(-ip\Delta s/\hbar)\hat{U}, \tag{6.56}$$

with $\hat{U}$ the map of the usual standard map. It is thus give by applying the usual standard map, and then adding the translation operator $\exp(-ip\Delta s/\hbar)$. It is thus clear also from the quantum version why the correction Δs leads to a shift in the momentum direction of phase space. Figure 6.28 shows an example of the phase space of the standard map with and without a constant correction $\Delta s = 0.1 \cdot 2\pi$ at $K = 0.5$. Here, the whole phase space structure shifts (down in this case), not just the periodic orbits.

In the standard map, one finds $\Delta p_{\text{POS}} = \Delta s$ by comparing Eqs. (6.50) and (6.51). This is the case because of the simple dependence of q_{j+1} on p_{j+1}. As the billiard mapping

can be written down explicitly in the circle, one can try to extract the POS from it in a similar way. The extended mapping is given as

$$\begin{aligned} p_{j+1} &= p_j, \\ q_{j+1} &= q_j + 2\rho \arccos p_{j+1} + \Delta s; \end{aligned} \tag{6.57}$$

(ρ is the circle radius), rewriting it as

$$\begin{aligned} \tilde{p}_{j+1} &= p_j + \Delta p_{\mathrm{POS}}, \\ q_{j+1} &= q_j + 2\rho \arccos \tilde{p}_{j+1} \end{aligned} \tag{6.58}$$

by defining a new momentum $\tilde{p} = p + \Delta p_{\mathrm{POS}}$. One can insert the equation for $\tilde{p}_{j+1}$ in the one for q_{j+1}, which yields

$$q_{j+1} = q_j + 2\rho \arccos(p_j + \Delta p_{\mathrm{POS}}) \approx 2\rho \arccos p_j + \frac{2\rho \Delta p_{\mathrm{POS}}}{\sqrt{1-p_j^2}}. \tag{6.59}$$

In the last step, $\arccos(p_j + \Delta p_{\mathrm{POS}})$ has been Taylor expanded, as Δp_{POS} is supposed to be a small correction. Comparing to Eq. (6.57), and using $p_j = \sin \chi_j$, one finds

$$\Delta p_{\mathrm{POS}} = \Delta s \frac{\sqrt{1-p_j^2}}{2\rho} = \Delta s \frac{\cos \chi_j}{2\rho}, \tag{6.60}$$

in complete agreement with Eq. (6.34).

6.6. Effects of Fresnel filtering

While the effects of the GHS have been studied in the previous sections, this section investigates the effects of the FF. In section 6.6.1, a feature of chaotic systems at small kR values is studied: in this case, a chaotic attractor is formed which closely resembles the Fresnel-weighted unstable manifold of the chaotic repeller of the *closed* system. In section 6.6.2 it is shown that the FF can lead to the formation of periodic orbits which are different for clockwise and counterclockwise travelling rays; this is a consequence of the time-reversal invariance breaking due to the FF.

In the last sections, the effect of the wave corrections on *regular* structures has been investigated. Here, their effect on chaotic structures is studied. As example systems, the limaçon at a higher deformation ($\epsilon = 0.43$, the "standard" value for directional emission) and a "deformed limaçon" [SFL$^+$09, SGS$^+$10], which also has been fabricated as a microdisk resonator.

6.6.1. Far field patterns, the chaotic saddle, and attractors

In small ($5 < kR < 10$) cavities [SGS$^+$10], a crossover from directional to bi-directional emission and back has been observed. One could guess that these deviations from the

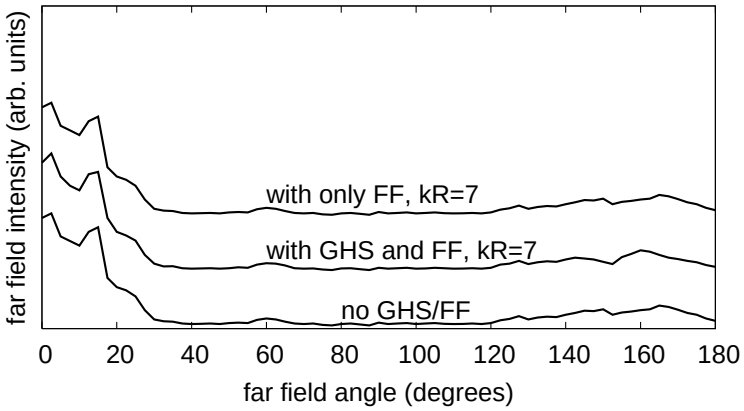

Figure 6.29.: Far field patterns for the $\epsilon = 0.43$ limaçon without the wave corrections, with only the FF included ($kR = 7$) and with both GHS and FF included. The refractive index is $n = 3.3$.

ray-dynamical prediction [WH08] are due to the wave corrections. This assumption is not correct, as Fig. 6.29 shows: including the corrections does not lead to significant changes in the far-field patterns, let alone bi-directional emission. As the wave corrections typically affect the phase space structure drastically, it is surprising that they do not seem to affect the far field patterns significantly – and more so, why including only the FF does not seem to change the far field pattern at all. Some insight into this is gained by comparing the phase space *with* only the FF with the chaotic saddle *without* the wave corrections, as shown in Fig. 6.30. They have almost the same structure, which of course leads to similar far field patterns. Sometimes, structures like the chaotic saddle have also been referred to as "attractors", as they lead basically to the same result as an attractor would: if you wait long enough, all intensity will be localized on it. However, it is important to recognize that chaotic saddles arise from Hamiltonian dynamics; there are no attractors in this case, and the localization of intensity is due to the fact that intensity leaks out of the cavity over time. The ray dynamics itself stays Hamiltonian. If, on the other hand, the FF is included, the ray dynamics becomes non-Hamiltonian, and attractors can form. Essentially, one has two different approaches leading to similar phase space structures: first, the ray dynamics is Hamiltonian, but the intensity of a ray varies, leading to the chaotic saddle; the openness is contained in the reflection coefficients. Second, the ray dynamics in non-Hamiltonian, but the intensity of a ray stays constant, leading to the formation of attractors. In this case, the openness is contained in the non-Hamiltonian corrections.

That these two approaches lead to similar results is not that surprising given that the actual calculations done are very similar. When calculating the chaotic saddle, one starts with a uniform distribution of rays in phase space, and notes the intensity retained; when calculating attractors within the extended ray dynamics, one starts with a Gaussian distribution of rays centered around each phase space point and notes where they are scattered to. I.e., one basically calculates a "local chaotic saddle" before starting

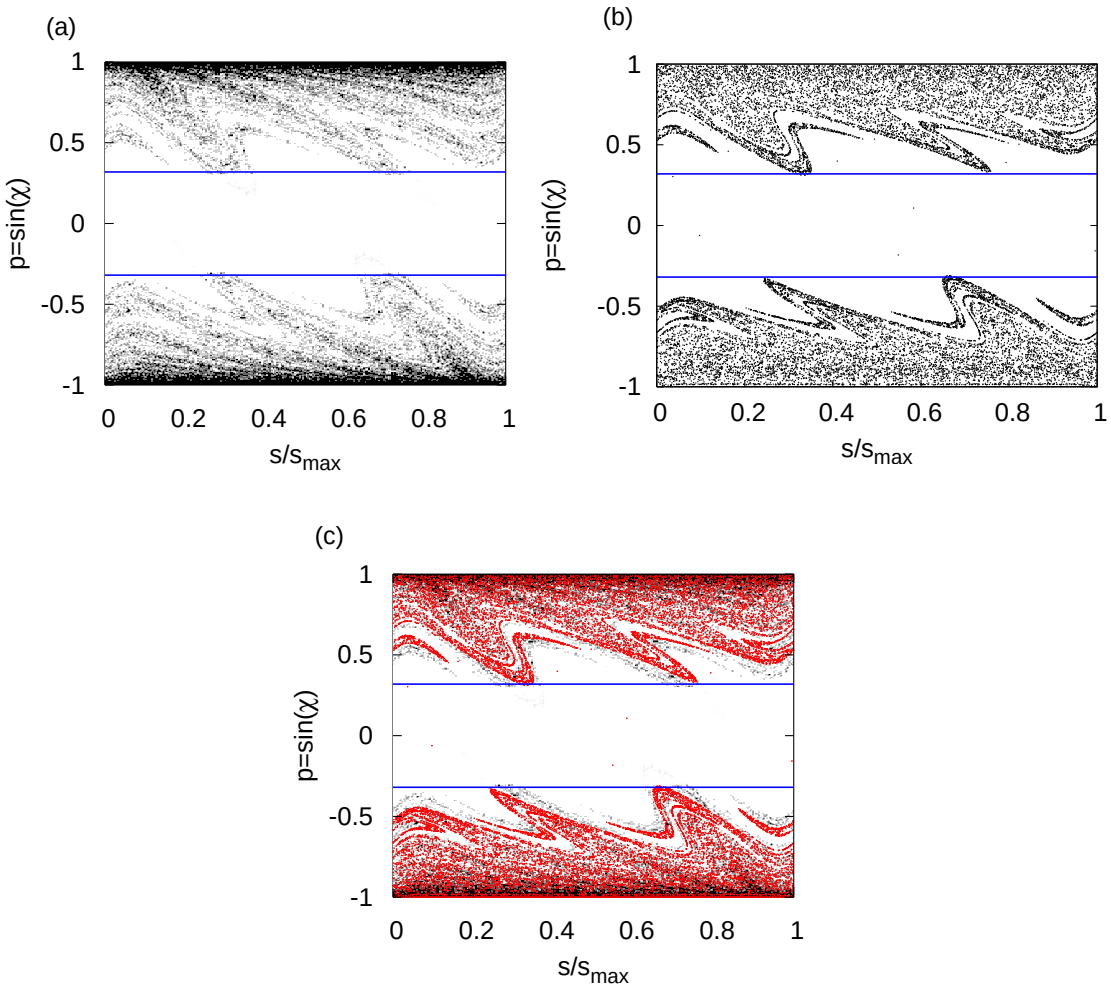

Figure 6.30.: (a) Chaotic saddle of the limaçon, calculated using the conventional ray dynamics. (b) Phase space structure of the limaçon with FF ($kR = 7$). (c) Overlay of (a) and (b). The chaotic attractor of (b) clearly has the same structure as the chaotic saddle in (a). The blue lines mark the critical lines for $n = 3.3$.

the ray dynamics.

6.6.2. Chiral symmetry breaking

As noted in [AGH08], the FF as a time-reversal symmetry breaking wave correction, can lead to asymmetry between clockwise (CW) and counterclockwise (CCW) travelling rays, as a CW ray turns into a CCW ray upon time reversal. These effects will be studied in the case of a cavity with the shape of a "deformed limaçon", which also has been studied experimentally [SGS+10].

The deformed limaçon is defined by the boundary curve

$$r(\phi) = R(1 + \epsilon \cos\phi)(1 - \epsilon_1 \cos(2\phi)) + d; \tag{6.61}$$

in addition to the dipolar limaçon deformation, its boundary also contains a (weaker) quadrupolar deformation. The Poincaé SOS of the deformed limaçon for the typical experimental parameters

$$R = 890 \text{ nm}, \epsilon = 0.28, \epsilon_1 = 0.06, d = 60 \text{ nm}, \tag{6.62}$$

calculated using the conventional ray dynamics (i.e. no GHS/FF corrections are included), is shown in Fig. 6.31. While the phase space is mostly chaotic for these parameters, it contains more regular structures than the usual limaçon at a similar deformation. The period 3 and 4 orbits are unstable, but bifurcations of them are stable (see Fig. 6.31); these orbits are interesting because they lie in the region of total internal reflection, but not far away from the critical line, and thus can influence output directionality.

Figure 6.32 shows the situation for $kR = 7$. It should be noted that while the calculations in this section include both wave corrections, the breaking of the symmetry between CW and CCW rays is an effect of the FF alone, and the formation of pairs of CW and CCW pseudo-orbits can also be observed if only the FF correction is included into the extended ray dynamics. One interesting aspect of this asymmetry between CW and CCW rays is that in this case, it leads to directional emission which does not happen in the case without FF. In the following, modes localizing on the period-3 orbits will be considered; light thus can leak out even if the periodic orbits are above the critical line. Figure 6.33 shows the situation for the symmetric period-3 orbit. Most light is emitted from positions 2 and 3, as the angles of incidence there are nearer to the critical line. A CW ray will emit light from position 2 in the backward and from position 3 in the forward direction, while a CCW ray emits light from position 2 in the forward and from position 3 in the backward direction. A mode localizing on the symmetric period-3 orbit is thus expected to have bi-directional emission.

In the symmetry-broken case, the situation is different, as Fig. 6.34 shows. In the CW case, the emission is predominantly from position 2, as the angle of incidence there is considerably smaller that at positions 1 or 3. The emission is into the backward direction. In the CCW case, the emission is predominantly from position 3, and again in the backward direction. The time-reversal symmetry breaking, which translates itself

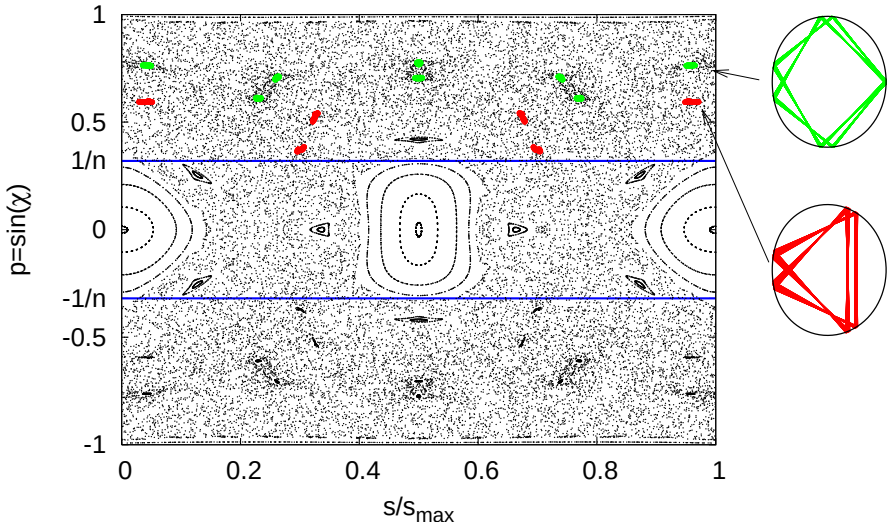

Figure 6.31.: Poincaré SOS for the deformed limaçon with parameters as defined in (6.62), calculated using the conventional ray dynamics. The blue lines mark the critical lines for $n = 3.13$. Stable islands formed by bifurcations of the period-3 (red) and period-4 (green) orbits are indicated.

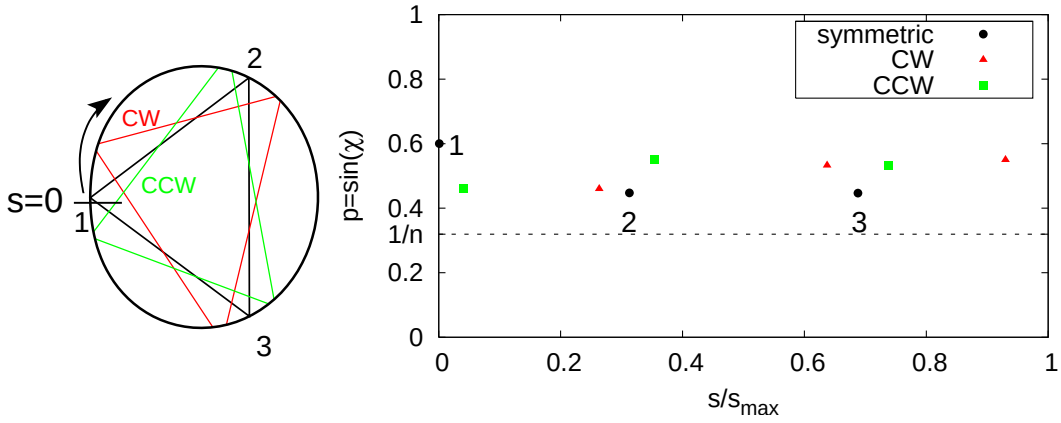

Figure 6.32.: Symmetric and asymmetric period-3 orbits in the deformed limaçon at $kR = 7$ with TE polarization. The black line is the symmetric period-3 orbit without GHS and FF which is the same for CW and CCW travelling rays. The red and green curves show the asymmetric CW and CCW travelling rays, respectively. The orbits are shown in real (left panel) and phase space (right panel). The three bounce points are labeled 1, 2 and 3.

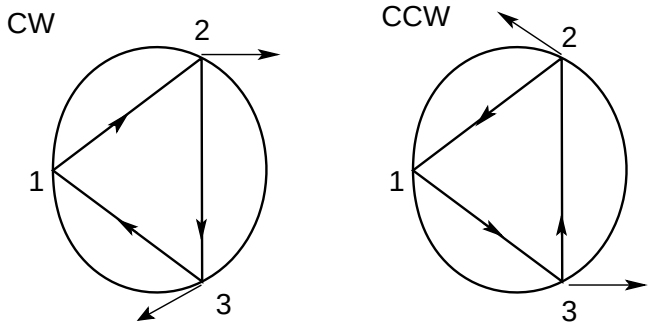

Figure 6.33.: Expected light emission pattern from the symmetric period-3 orbit. Both CW and CCW rays emit in the backward and forward directions.

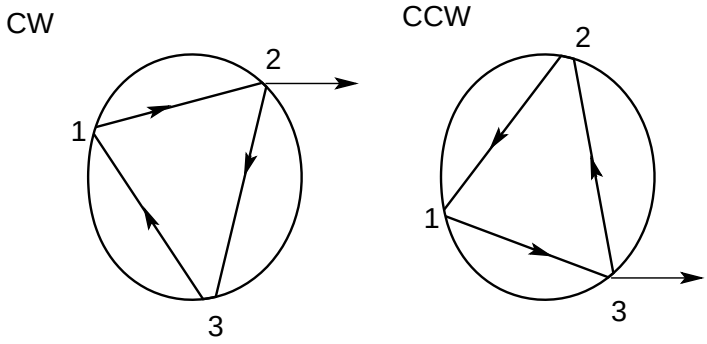

Figure 6.34.: Expected light emission pattern from CW and CCW rays for the asymmetric period-3 orbits. Both CW and CCW rays emit in the backward direction.

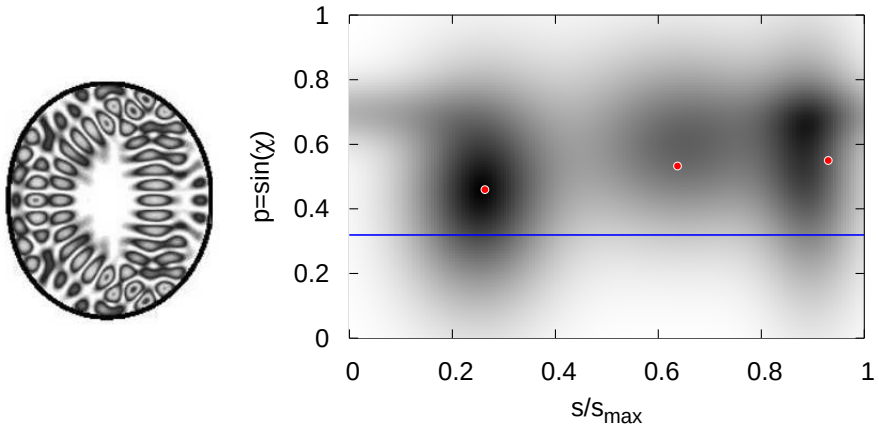

Figure 6.35.: Husimi distribution for a mode with $kR = 11 - 0.03i$ localized an the period-3 orbit. The red dots mark the bounce positions of the CW pseudo-orbit, the blue line the critical line. On the left, the mode pattern in real space is shown.

into an asymmetry between the bounce points 2 and 3, leads to directional emission in this case.

The asymmetry between CW and CCW rays can easily be seen in the Husimi functions in this case, and even the pseudo-orbits can be extracted from the maxima of the Husimi distributions [SGS+10]. An exemplary Husimi function is shown in Fig. 6.35; the agreement with the bounce points of the CW pseudo-orbit is quite good.

Another interesting feature visible in Fig. 6.32 is that the FF leads to a shift of the periodic (pseudo-) orbit bounce points along the boundary. Just as it has been shown in section 6.5 that the GHS leads to a periodic orbit shift Δp_{POS} in the momentum direction of phase space, the FF also leads to a periodic orbit shift Δs_{POS} in the position direction. Unfortunately, this shift can not be calculated analytically as easily, as both the direction vector of the trajectory and the angle of incidence at the corresponding bounce point change; an approach similar to the one in section 6.5.2 is not possible.

7. Measuring the Goos-Hänchen shift in microwave cavities

So far, microdisk cavities, which support modes with frequencies from the mid-infrared to ultraviolet ranges, have been discussed. As all relevant quantities only depend on the size parameter kR, they also apply to larger cavities and modes with longer wavelengths. One example are microwave cavities: with sizes of several 10 cm, they support modes with frequencies in the GHz range, corresponding to size parameters of the order of $kR \approx 100$. In particular, the effects of wave corrections, which have been discussed in chapter 6, can also be observed in dielectric microwave cavities. One advantage of such systems is that the full wavefunction inside the cavity can be easily measured; so far, equivalent measurements are not possible in microresonators. In this chapter, a setup for the experimental observation of the Goos-Hänchen effect in a microwave billiard is introduced. Section 7.1.1 introduces microwave cavities in general, whereas section 7.1.2 discusses the measurement technique which allows the extraction of the full wave function. The experimental setup is introduced in section 7.2.1 and results are shown in section 7.3.

All experiments discussed in this section have been performed by the author in collaboration with the group of Prof. Hans-Jürgen Stöckmann at the university of Marburg.

7.1. Microwave billiard experiments

7.1.1. Microwave billiards

Microwave billiards (open and closed) have been used as model systems for quantum chaos for a long time. The first experiments were reported in [SS90]; similar results are found in [Sri91], [SS92], and [GHL$^+$92]. The first two references also feature wavefunction measurements in addition to resonance frequencies. Measurements including the phase of the wave function are discussed in [SSS95].

Microwave resonators are typically several tens of centimeters in diameter and several millimeter high; they are thus nearly two-dimensional. In fact, if one considers frequencies below $\nu_{\max} = c/(2h)$ (c is the speed of light in the resonator, and h its height), no modes can propagate in the z direction, as $h < \lambda/2$ with the wavelength λ. For h in the mm range, $\nu_{\max}$ is around 20 GHz; such frequencies can be easily excited with microwave antennas. Dirichlet boundary conditions are realized by metallic (often brass or aluminium; in order to maximize the reflection, superconducting cavities, often made of niobium, can be used) boundaries. If one wants to study dielectric cavities, Teflon

is commonly used as a material. It has low absorption for microwaves in the relevant frequency range and a refractive index $n = 1.44$.

The main idea of measurements in microwave cavities comes from scattering theory. There, the amplitudes b_j of the outgoing waves are connected to the amplitudes of the incoming waves a_ℓ by a scattering matrix $S_{j\ell}$:

$$b_j = \sum_\ell S_{j\ell} a_\ell. \tag{7.1}$$

This scattering matrix is related to the Green function of the billiard,

$$\begin{aligned} S_{j\ell} &= \delta_{j\ell} - i\gamma G(\mathbf{r}_j, \mathbf{r}_\ell, k) \\ &= \delta_{j\ell} - i\gamma \sum_{\text{resonances } k_n} \frac{\psi(\mathbf{r}_j)\psi(\mathbf{r}_\ell)}{k^2 - k_n^2}. \end{aligned} \tag{7.2}$$

k is the wave number one is measuring at, k_n are the complex wave numbers of the resonances of the cavity, and $\psi(\mathbf{r}_i)$ are the wave functions at the positions $\mathbf{r}_i$. γ is a coupling constant related to the geometry of the antenna used for measuring wave functions; it can be obtained by measuring the transmission amplitude between the antennas at positions $\mathbf{r}_j$ and $\mathbf{r}_\ell$ directly, without scattering by the billiard.

Reflection measurements (measuring S_{jj}) yield the modulus $|\psi(\mathbf{r}_j)|$ at the position $\mathbf{r}_j$ of the measuring antenna. If one wants to measure the phase of ψ as well, an additional transmission experiment has to be performed; how the full scattering matrix is measured is described in the next section. Equation (7.2) holds for resonances which do not overlap strongly in frequency.

If one now excites incoming waves with an antenna at a fixed position $\mathbf{r}_\ell$ and measures reflected and transmitted waves with a movable antenna which is moved to different positions $\mathbf{r}_j$, a spatially resolved wave function can be measured.

7.1.2. Vectorial network analysis

By using a vector network analyzer (VNA; the Marburg group uses an Agilent 8720ES VNA), the full scattering matrix $S_{j\ell}$ can be measured. The principle is shown in Fig. 7.1. Each of the two channels has a reference signal; both the input signal and signal after scattering are measured with respect to this reference, which enhances accuracy. On channel one, the signal a_1 is used as input. The reflected signal $S_{11}a_1$ is measured as well. On channel two, the transmitted part of a_1, $S_{21}a_1$, is measured, but in addition, another measurement with input signal a_2 and reflected part $S_{22}a_2$ is done. The transmitted part of a_2, $S_{12}a_2$, is measured on channel one. Thus, by doing both reflection and transmission experiments on the two channels, all a_ℓ, b_j are measured, and the full scattering matrix $S_{j\ell}$ can be extracted. Figure 7.2 shows an exemplary measured reflection (top panel) and transmission spectrum.

Systematic errors due to phase or frequency changes upon reflection, transmission, or directly at the connection between cable and port or cable and antenna, as well as errors due to leaking can be corrected by using a calibration procedure before starting

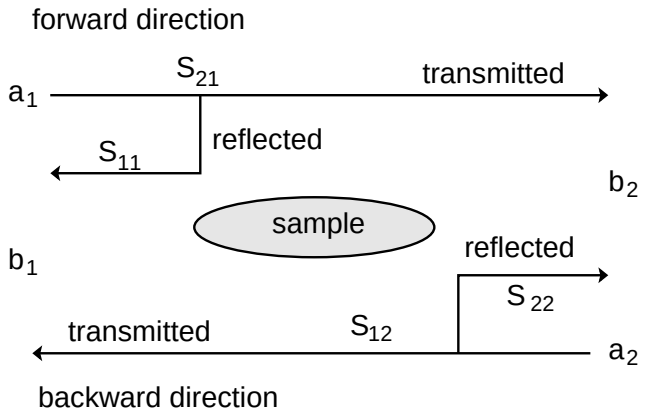

Figure 7.1.: Principle of the VNA. There are two channels; each of them can transmit an input signal and measure an output signal after scattering with the sample. a_1, a_2 are in input signals and b_1, b_2 the measured signals.

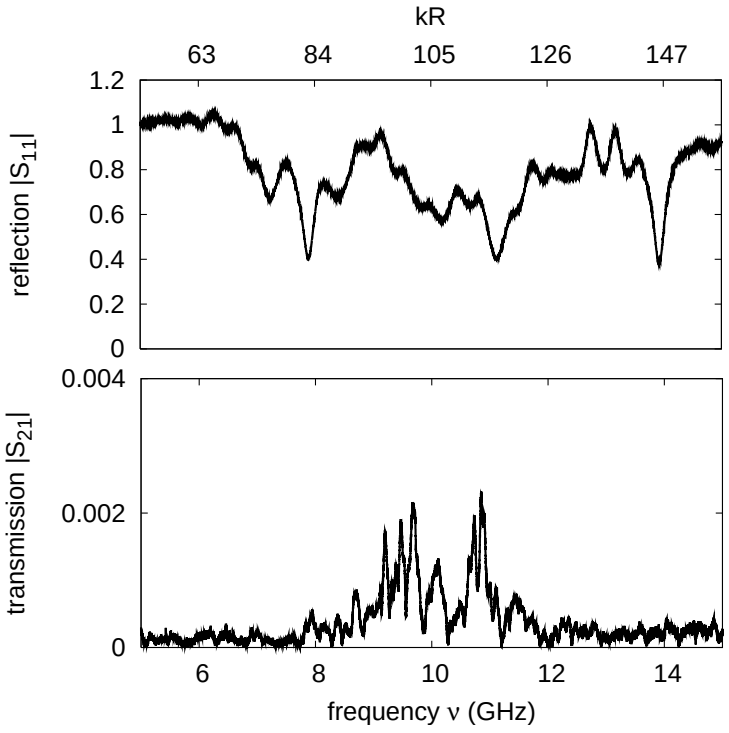

Figure 7.2.: Measured reflection (top panel) and transmission (bottom panel) spectra. The sum of their squares does not equal unity because of absorption in the system. Resonances can be seen as dips in $|S_{11}|$. The bottom x axis shows the frequency ν, the top x axis shows kR.

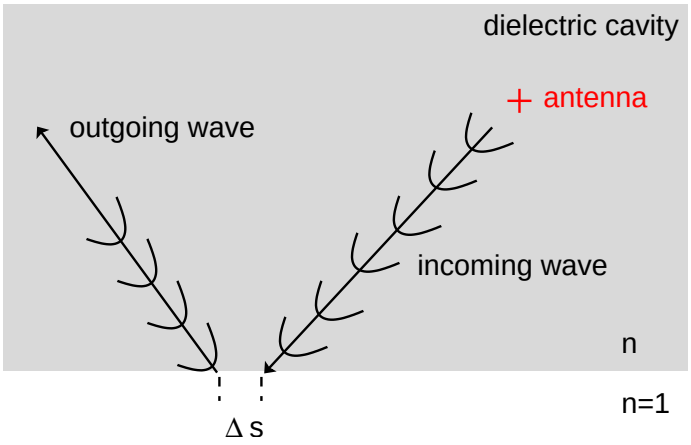

Figure 7.3.: Principal idea for GHS measurements in a rectangular microwave cavity. The antenna creates a wave packet which is reflected at the bottom cavity boundary; the GHS Δs is the shift between the incoming and outgoing wave packets.

measurements. In this case, measurements are performed while connecting different gauged standards to the VNA. Details of the setup and the calibration process can, e.g., be found in [Bar01]. The computer control of the setup and data acquisition are described in [Kuh98].

7.2. Measurements of the Goos-Hänchen shift

7.2.1. Basic idea for measurements

The most simple way of measuring the GHS in a microwave cavity is depicted in Fig. 7.3. The cavity is rectangular in this case; reflection thus happens at a planar interface. An antenna excites a wave packet, which travels to the bottom part and is reflected. The GHS Δs can directly be extracted as the shift between incoming and outgoing waves.

Figure 7.4 shows the idea of GHS extraction from measured data in more detail. It is possible to extract Poynting vectors $\mathbf{S}_{\text{in}}$ and $\mathbf{S}_{\text{out}}$ of the incoming and outgoing wave functions at each point $\mathbf{r} = (x, y)$ in space from the measured wave functions. As wave packets with a clear propagation direction should be generated, averaging these over the full measured wave functions yields average Poynting vectors $\langle \mathbf{S}_{\text{in}} \rangle$, $\langle \mathbf{S}_{\text{out}} \rangle$ which are representative of the wave function. They are given by

$$\langle \mathbf{S}_{\text{in (out)}} \rangle = \frac{1}{N_x N_y} \sum_{i=1}^{N_x} \sum_{j=1}^{N_y} \mathbf{S}_{\text{in (out)}}(x_i, y_j), \tag{7.3}$$

where the x_i, y_j are the positions on which $\mathbf{S}_{\text{in (out)}}$ values have been measured. $N_{x(y)}$ is the number of $x(y)$ positions measured.

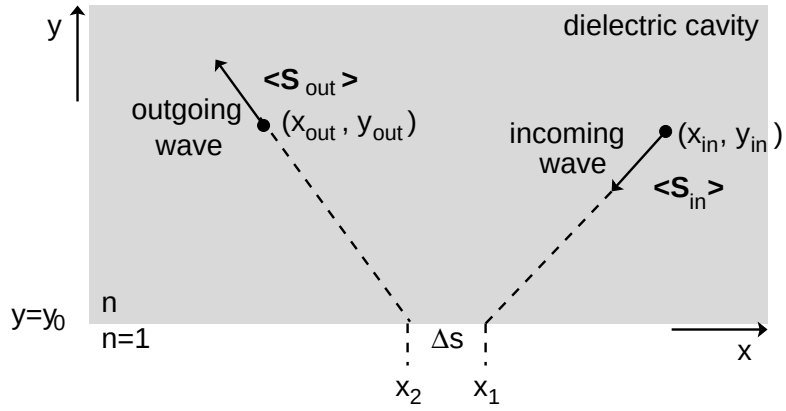

Figure 7.4.: Extraction of the GHS Δs from the measured incoming and outgoing wave functions. $\langle \mathbf{S}_{\text{in}} \rangle$ and $\langle \mathbf{S}_{\text{out}} \rangle$ are averaged Poynting vectors of the incoming and outgoing waves and $(x_{\text{in}}, y_{\text{in}})$ and $(x_{\text{out}}, y_{\text{out}})$ position averages. x_1 and x_2 are intersections of the straight lines defined by the Poynting vectors and averaged positions with $y = y_0$.

The average Poynting vectors define the propagation direction of the incoming and outgoing waves. Together with the position $\mathbf{r}_{\text{in}} = (x_{\text{in}}, y_{\text{in}})$ on the incoming wave ($\mathbf{r}_{\text{in}}$ is the average over all positions at which the incoming wave is measured), $\langle \mathbf{S}_{\text{in}} \rangle$ defines a straight line

$$\begin{pmatrix} x \\ y \end{pmatrix} = \begin{pmatrix} x_{\text{in}} \\ y_{\text{in}} \end{pmatrix} + t \, \langle \mathbf{S}_{\text{in}} \rangle. \tag{7.4}$$

The intersection of this straight line with $y = y_0$ yields the position x_1 where the incoming wave hits the cavity boundary. Analogously, the position x_2 where the outgoing wave starts at the boundary can be calculated by intersecting the straight line

$$\begin{pmatrix} x \\ y \end{pmatrix} = \begin{pmatrix} x_{\text{out}} \\ y_{\text{out}} \end{pmatrix} + t \, \langle \mathbf{S}_{\text{out}} \rangle \tag{7.5}$$

with $y = y_0$. The GHS is then given by $\Delta s = x_2 - x_1$.

7.2.2. Beam generation

The theory for the GHS described in section 6.1 only applies to Gaussian beams. Microwave antennas, however, only produce spherical waves. One thus needs to generate beams from these spherical waves. The generation of *plane waves* can be easily done because the superposition of N spherical waves with wave number k and centers (x_j, y_j) on a straight line creates a wave function

$$\psi(x, y) = \sum_{j=-N/2}^{j=N/2} \frac{\exp\left[ik\sqrt{(x - x_j)^2 + (y - y_j)^2}\right]}{\sqrt{(x - x_j)^2 + (y - y_j)^2}} \tag{7.6}$$

which approaches a plane wave if N goes to infinity. Examples for different N values are shown in Fig. 7.5 for $k = 5\ \mathrm{cm}^{-1}$ and spherical wave centers (x_j, y_j) with $x_j = x_0 + jd/\sqrt{2}$, $y_j = y_0 - jd/\sqrt{2}$ with $d = 0.5$ cm and $x_0 = 40$ cm, $y_0 = 5$ cm. In this case, the resulting plane wave travels with a propagation direction of ~ 45 degrees to the bottom left. $N = 20$ seems to yield a sufficiently plane wave front, which also can be seen in the measured wave fronts in Fig. 7.14 and Poynting vectors in Fig. 7.15 in section 7.3.1, even though the cross-section at $x = 30$, $y = 3.75$ shown in the bottom panel of Fig. 7.5 does not look completely like a plane wave. In an experiment, the different spherical waves generated by the antennas will not all have the same phases even if the same antenna is used to generate them; random phase fluctuations can occur because the antenna is not connected in precisely the same way, which leads to a different capacity and thus a different phase. However, this does not perturb the formation of a plane wave much, as Fig. 7.6 shows. There, Eq. (7.6) has been used with the same parameters as in Fig. 7.5, but each term in the j-sum has been multiplied with a phase factor $\exp(i\rho_j)$, where ρ_j is a random number between zero and 2π (the phases in the experiment typically will not vary this much, but the "worst case" is studied here). The resulting wave for $N = 20$ still is to a good approximation plane; even random phase fluctuations do not destroy this property.

The propagation direction of a plane wave generated from spherical waves can be influenced by adding a phase factor to each spherical wave. In this case, the phases are not random, but functions of the position j of the individual spherical wave in the array:

$$\psi(x,y) = \sum_{j=-N/2}^{j=N/2} \frac{\exp\left[ik\sqrt{(x-x_j)^2+(y-y_j)^2} + i\phi(j)\right]}{\sqrt{(x-x_j)^2+(y-y_j)^2}}. \tag{7.7}$$

Figure 7.7 shows plane waves with different phase functions $\phi(j)$ and their propagation directions. By varying $\phi(j)$, one can thus achieve propagation directions which lead to reflection under different angles of incidence. I.e., $\phi(j) = j$ leads to reflection with an angle below the critical angle $\chi_{\mathrm{cr}} \approx 44$ degrees for Teflon with $n = 1.44$, $\phi(j) = -j$ leads to reflection with an angle above the critical angle, and for $\phi(j) = 0$ the reflection happens close to the critical angle. Unfortunately, there is no analytical formula for the relation of $\phi(j)$ and the resulting propagation direction; the choice of the $\phi(j)$ functions therefore remains somewhat arbitrary.

A plane wave, however, does not experience the GHS upon reflection, as the GH effect is a consequence of the *interference* of partial waves with different angles of incidence. Creating a plane wave thus does not suffice if one wants to measure the GHS. But by superimposing *two* plane waves generated according to Eq. (7.7) with different $\phi(j)$ functions corresponding to a small difference in their propagation directions leads to a beam just like the one assumed in the derivation of the Artmann result (see section 6.1.1):

$$\psi(x,y) = \psi_1(x,y) + \psi_2(x,y) \approx \exp\left(ikp_1x\right) + \exp\left(ikp_2x\right), \tag{7.8}$$

with $p_m = \sin\chi_m \sim S_{m,x}$, where $S_{m,x}$ is the x component of the Poynting vector of

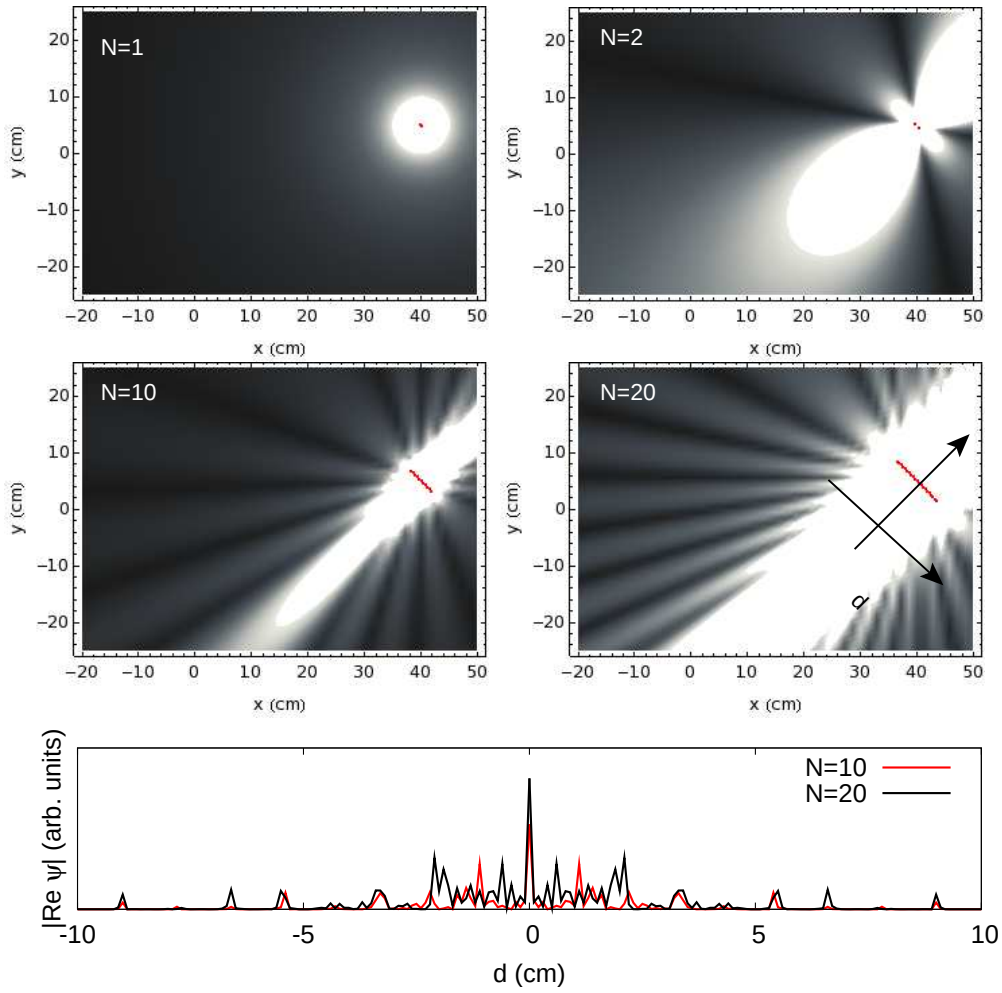

Figure 7.5.: Illustration of the generation of a plane wave-like beam from spherical waves. The number of spherical waves contributing varies from $N = 1$ to $N = 20$. The red dots mark the antenna positions. The bottom panel shows a cross-section of the $N = 10$ (red line) and $N = 20$ (black line) beams at $x = 30$, $y = 3.75$.

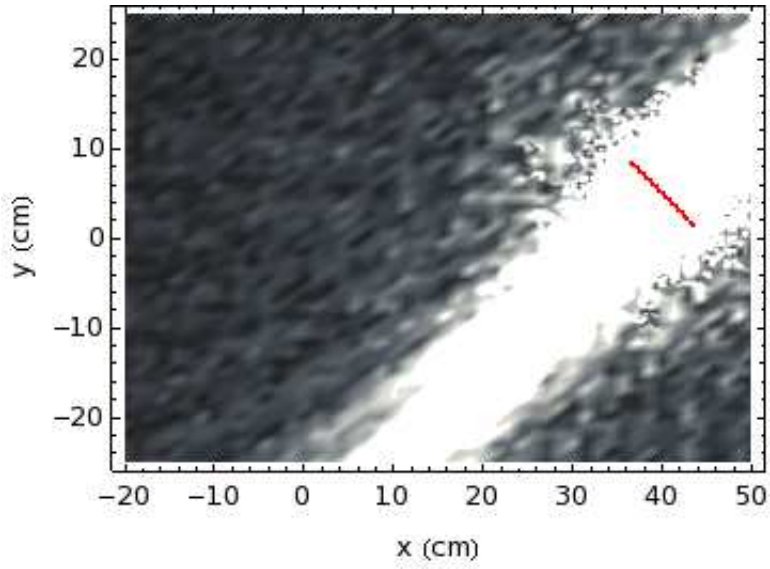

Figure 7.6.: Plane wave generated from $N = 20$ spherical waves with random phase factors. The parameters are the same as in Fig. 7.5.

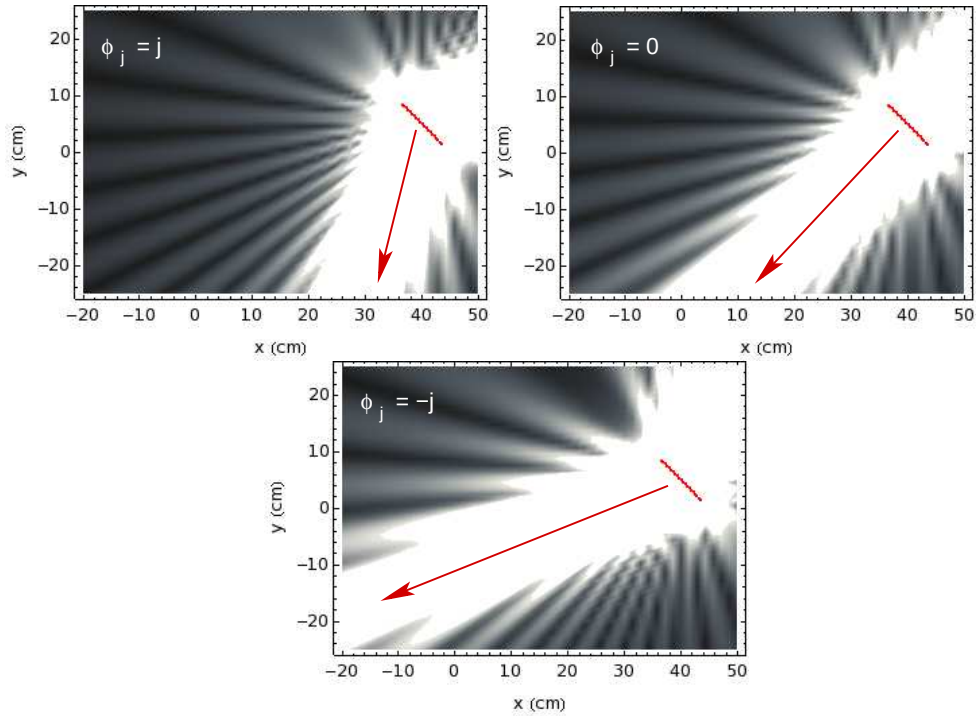

Figure 7.7.: Plane waves with generated according to Eq. (7.7) with different phase functions $\phi(j)$. The number of spherical waves is $N = 20$, the other parameters are as in Fig. 7.5.

partial wave m (with $m = 1, 2$). If p_1 and p_2 are similar, the Artmann result

$$\Delta s_{\mathrm{TM}} = \frac{1}{nkp} \frac{1}{\sqrt{\sin^2 \chi - 1/n^2}} \tag{7.9}$$

can be used to predict the GHS.

As both partial waves of the beam (7.8) are calculated using the same spherical wave components ψ_j,

$$\psi_1 = \sum_{j=-N/2}^{N/2} \psi_j e^{i\phi_1(j)},\ \psi_2 = \sum_{j=-N/2}^{N/2} \psi_j e^{i\phi_2(j)}, \tag{7.10}$$

the sum is just given by

$$\psi = \psi_1 + \psi_2 = \sum_{j=-N/2}^{N/2} \psi_j \left(e^{i\phi_1(j)} + e^{i\phi_2(j)} \right). \tag{7.11}$$

It is also possible to create a Gaussian beam from many plane waves generated by Eq. (7.7):

$$\begin{aligned} \psi &= \int_{-1}^{1} \mathrm{d}p\, f_{\mathrm{in}}(p) e^{inkpx} \\ &= \int_{-1}^{1} \mathrm{d}p\, f_{\mathrm{in}}(p) \sum_{j=-N/2}^{N/2} \psi_j e^{i\phi_j}. \end{aligned} \tag{7.12}$$

The p integration in Eq. (7.12) has to be done numerically, i.e. has to be approximated as a sum over different p values p_m, each corresponding to a phase function $\phi_m(j)$:

$$\psi \approx \sum_{j=-N/2}^{N/2} \psi_j \sum_m \Delta p_m f_{\mathrm{in}}(p_m) e^{i\phi_m(j)}, \tag{7.13}$$

with $\Delta p_m = p_{m+1} - p_m$. As there is no analytical formula relation the phase function ϕ_j to the propagation direction (and thus to p), finding the required ϕ_m function is tedious. In this thesis, only beams consisting of two plane waves will be considered.

7.2.3. Experimental setup

Figure 7.8 shows the cavity used in the experiments. It is a Teflon plate with dimensions 50 cm (length) × 100 cm (width) × 0.5 cm (height); modes with frequencies up to $\nu_{\mathrm{max}} = 30$ GHz can thus be treated as two-dimensional. All boundaries except the bottom one, where the reflection of the beams happens, are clad with a carbon-based material (ROHACELL from the company Röhm GmbH) which absorbs microwaves, as to reduce noise created by multiple reflections. As the plate is glued to an aluminium plate and pressed to another plate from below in the experiments, bending of the plate is

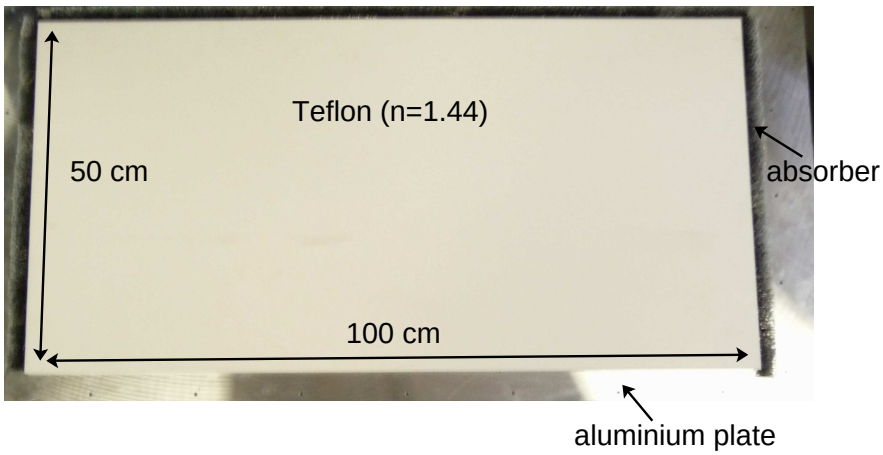

Figure 7.8.: Photograph of the rectangular Teflon billiard used in the experiments. All boundaries except the one the reflection happens at are clad with an absorbing material. The billiard is glued to an aluminium plate.

no issue. The experimental setup is shown in Fig. 7.9. The billiard is pressed from below to the table on which the wave functions are measured. The fixed antenna (connected to one port of the VNA) creates the spherical waves; the wave function is measured with the movable antenna (connected to the other port of the VNA). It is moved by means of three step motors, which are controlled by a computer. Figure 7.10 shows the movable antenna in more detail. The top plate of the table underneath which the billiard is placed is made of aluminium and has holes in it which are arranged on a rectangular grid with distances of 5 mm. Wave function measurements can only be done at the hole positions: the movable antenna holder moves to the position of a hole and then downwards, so that the antenna is sunk into the hole. If the measurement at this position is finished, the antenna holder moves up again and then to the position at which one wishes to measure next. This of course limits the spatial resolution of wave function measurements, which can not be better than the hole distance, but on the other hand, it greatly enhances the precision with which the movable antenna can be placed on the table.

As microwave cables are expensive, it is not possible to place about 20 antennas on the table and measure the spherical waves they generate simultaneously – it also would not be possible to connect them all to the VNA. Hence, only one fixed antenna is placed on the table, the wavefunction is measured, and the antenna is moved to another position. When wave functions at enough different positions are measured, they are superimposed, and the plane wave is generated. Additional phase factors can also be added when doing this superposition. The plane wave is thus given by

$$\psi(\mathbf{r}) = \sum_{\text{antennas } j} \psi_j(\mathbf{r}) e^{i\phi(j)}, \tag{7.14}$$

where ψ_j is the wave function measured by antenna j and $\phi(j)$ is a phase function designed to ensure propagation in the right direction, as described in section 7.2.2. Figure 7.11 shows the positions of the fixed antennas on the hole raster. In the experiments,

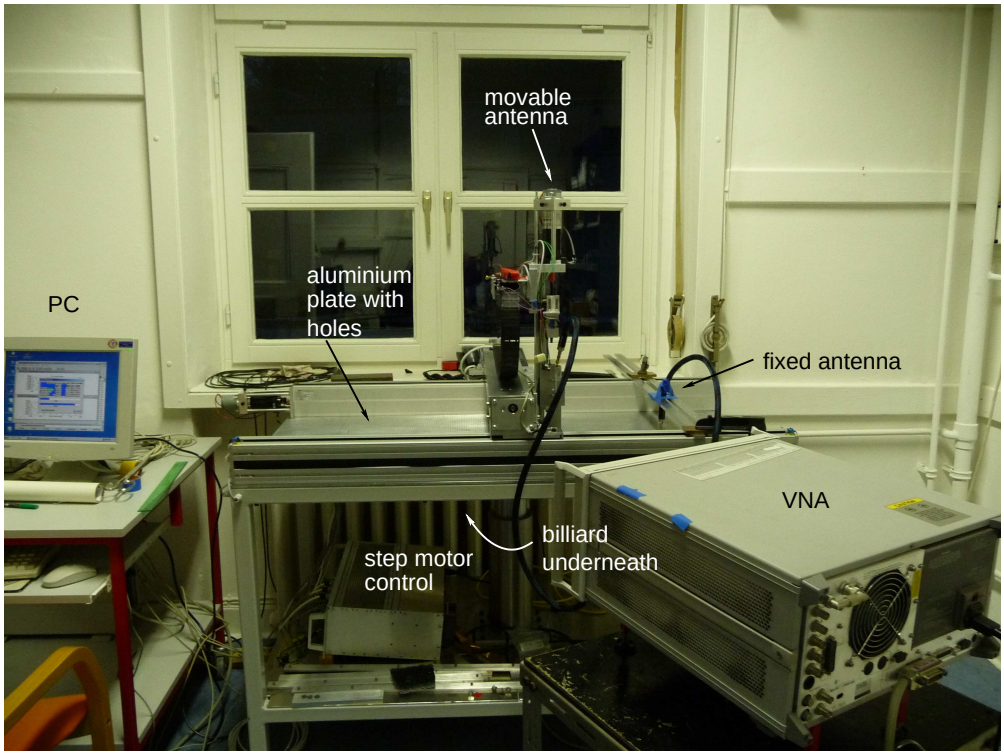

Figure 7.9.: Photograph of the experimental setup. Wave function measurements are made with an antenna which can be moved on a table with three step motors (controlling movement in three dimensions). The movable antenna, as well as the fixed antenna generating the spherical waves, are connected to a VNA. The antenna movement and data acquisition is controlled by a PC.

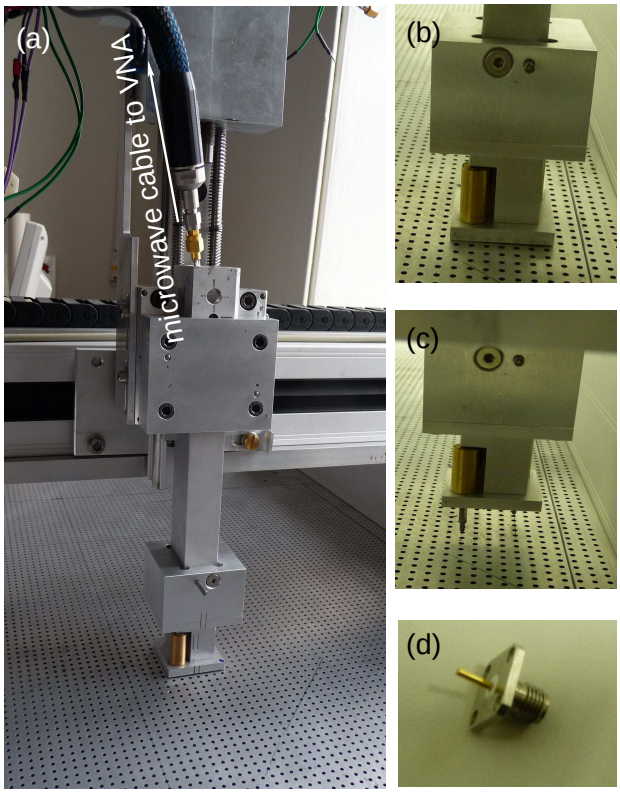

Figure 7.10.: (a) Photograph of the movable antenna holder. (b) Close-up photograph of the movable antenna while measuring (antenna is sunk into a hole). (c) Close-up photograph of the movable antenna after measuring (antenna is now above the table). (d) Photograph of the microwave antenna itself.

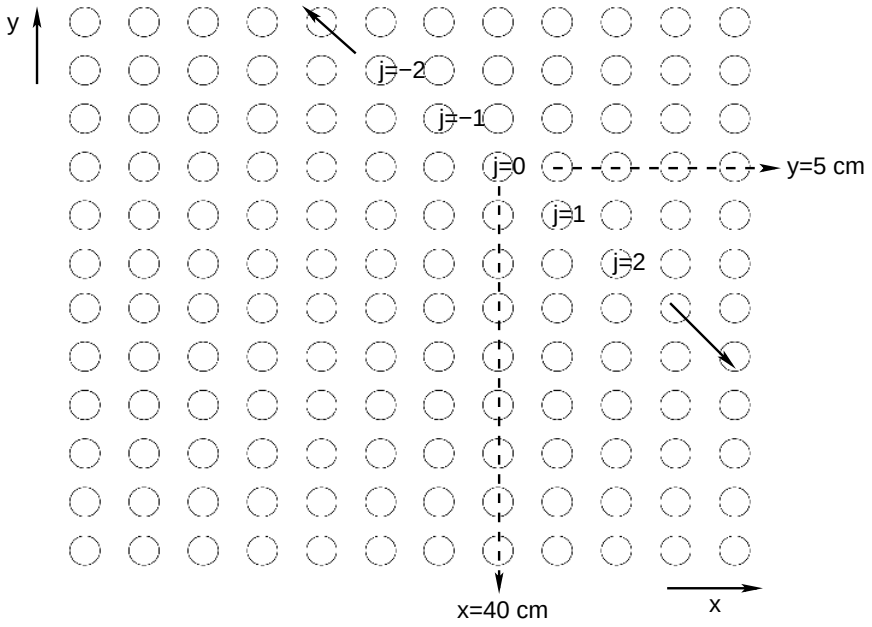

Figure 7.11.: Positioning of the fixed antennas on the hole raster on the measuring table.

18 antenna positions were used.

Measuring the wave function at a point in space takes about 2 minutes. If one would like to measure it on the whole billiard, this would take about 48 days for one antenna position. Measuring 10 positions would take more than a year; this is not feasible. Therefore, wave functions are only measured in parts of the billiard, as shown in Fig. 7.12. These parts are such that the incoming and outgoing wave functions and their Poynting vectors can be extracted. In addition, the wave function at the interface is measured. One measurement now takes about 36 hours, and the 18 antenna positions are measured in about a month.

7.3. Results

7.3.1. Generation of a single plane wave

Figure 7.13 shows wave functions $\mathrm{Re}(\psi)$ calculated from the measured data according to Eq. (7.14) with $\phi_j = 0$ at $\nu = 15$ GHz, corresponding to $kR = 157.5$. The boundary of the Teflon billiard is shown, as well as the position of the $j = 0$ antenna in the middle of the antenna array. It is already clear from Fig. 7.13 that both the incoming and the outgoing waves have nearly plane wave fronts and travel at an angle of approximately 45 degrees to the billiard boundary.

As it is difficult to see details of the wave functions in the different measured parts of the billiard, they are shown individually in Fig. 7.14. From Fig. 7.14, the width of the generated plane waves can be estimated. The incoming wave has a width of ≈ 3 cm, which is much smaller than the ≈ 9 cm one would expect from an 18-antenna antenna

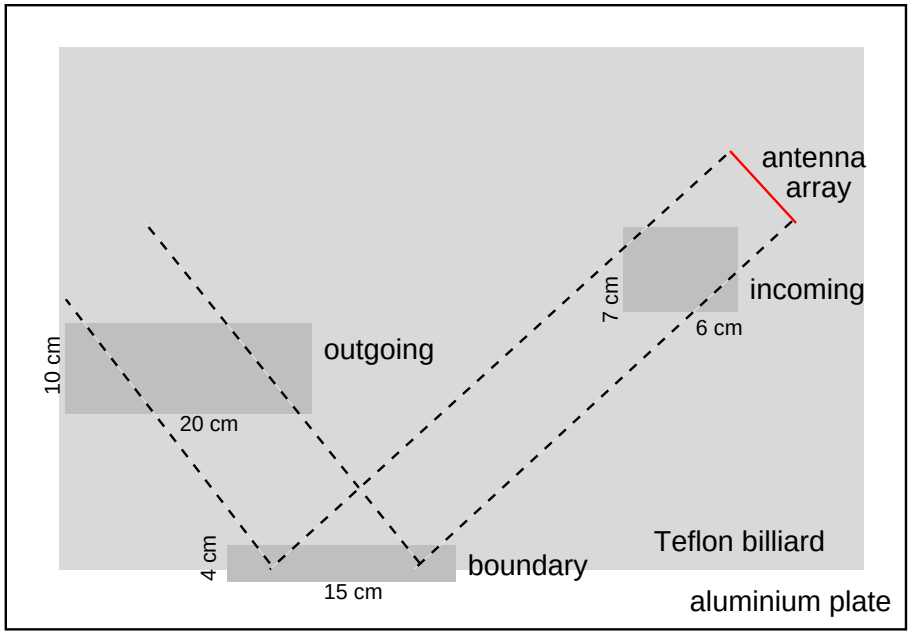

Figure 7.12.: Definition of the parts of the billiard (dark grey) in which the wave functions are measured for all antennas in the antenna array. Incoming and outgoing wave functions as well as the wave function at the interface, where reflection happens, can be extracted. The measured parts are not shown to scale.

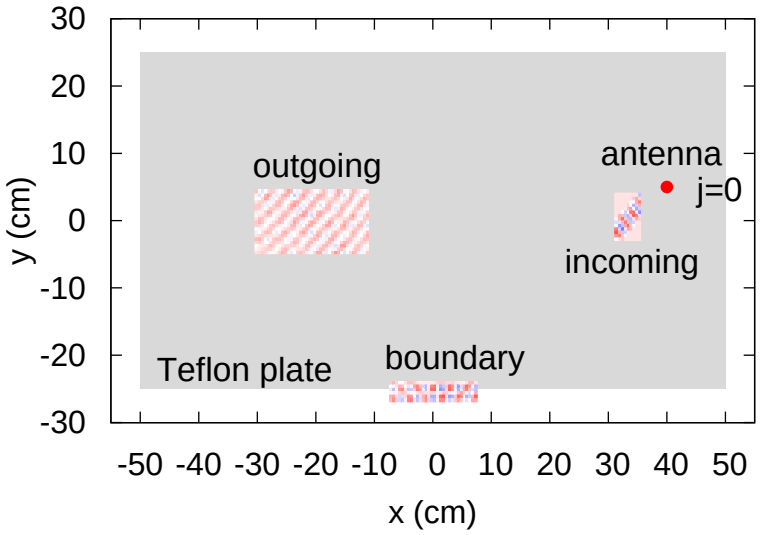

Figure 7.13.: Wave functions $\mathrm{Re}(\psi)$ on the measured parts of the billiard at $\nu = 15$ GHz. The billiard is shown as the gray region; the position of the middle ($j = 0$) antenna in the antenna array is shown as well.

array. The outgoing wave, while less sharply defined, has approximately the same width (≈ 4 cm). The spatial resolution of 5 mm, which is given by the hole raster on the table, is clearly sufficient to see the structure of the incoming and outgoing waves. The wave function on the boundary looks less well defined; with an extension of only 3 cm in the y direction, the defined measuring area probably is too small to allow for a distinction of the incoming and outgoing waves and the penetration of the wave into the region outside the billiard boundary. The penetration depth is approximately one wavelength, $\lambda \approx 2$ cm in the case of the Teflon material with $\nu = 15$ GHz, which explains why much intensity is found outside the billiard. Measuring the wave function much farther outside the material would, however, not have been possible because the table ends approximately 4 cm away from the bottom of the billiard and some space is required for the movable antenna to fit in. For GHS extraction as described in section 7.2.1, however, only the incoming and outgoing wave functions are required, and the fact that the size of the measured boundary wave function is too small is not relevant.

Figure 7.15 shows the Poynting vectors extracted for the three measured parts of the billiard. The positions $\mathbf{r}_{\mathrm{in}}$ and $\mathbf{r}_{\mathrm{out}}$ are taken as the middle point of the regions marked by the dashed lines in Fig. 7.14; they are given by

$$\mathbf{r}_{\mathrm{in}} = \begin{pmatrix} 33.5\ \mathrm{cm} \\ 1.0\ \mathrm{cm} \end{pmatrix}, \quad \mathbf{r}_{\mathrm{out}} = \begin{pmatrix} -19.0\ \mathrm{cm} \\ 0.0\ \mathrm{cm} \end{pmatrix} \tag{7.15}$$

for the Poynting vectors in this figure. As could already be expected from the plane wave

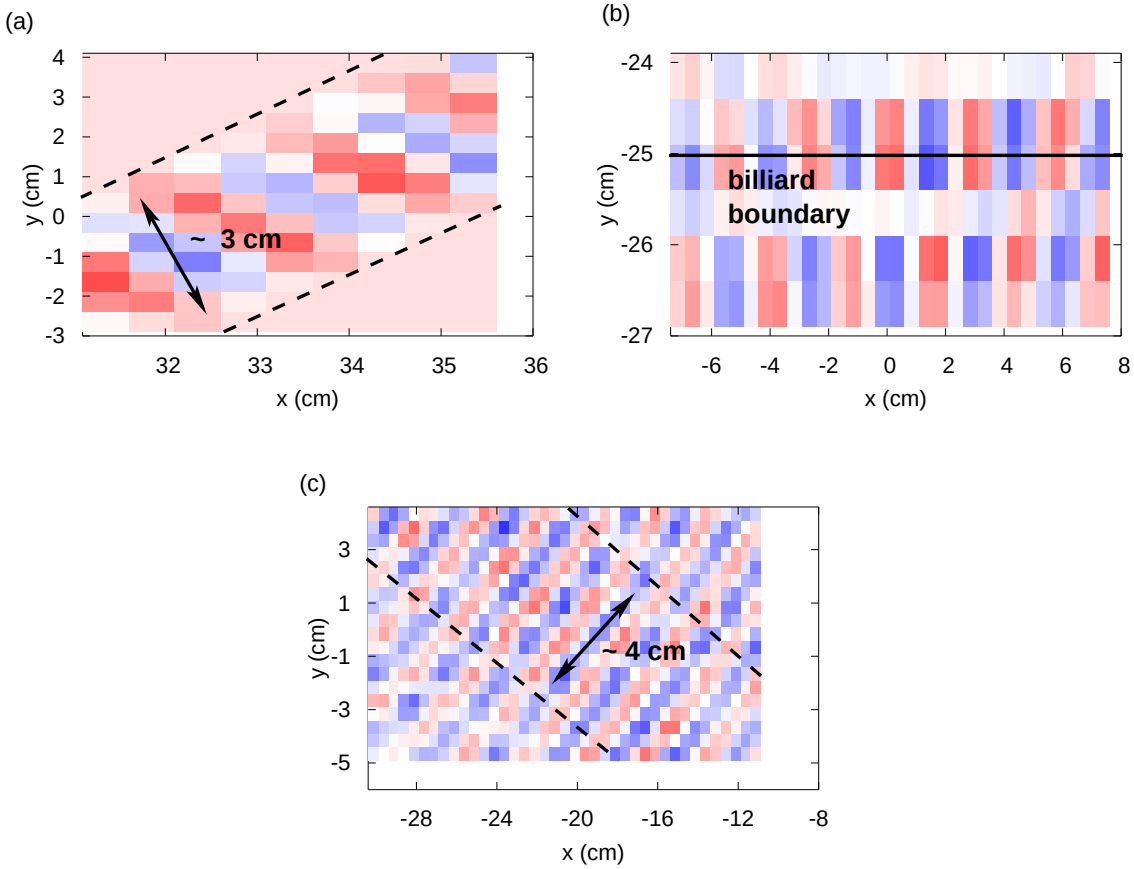

Figure 7.14.: Wave functions Re(ψ) in the three measured parts of the billiard. (a) incoming wave function, (b) wave function of billiard boundary, (c) outgoing wave function. The width of the incoming and outgoing wave functions is noted.

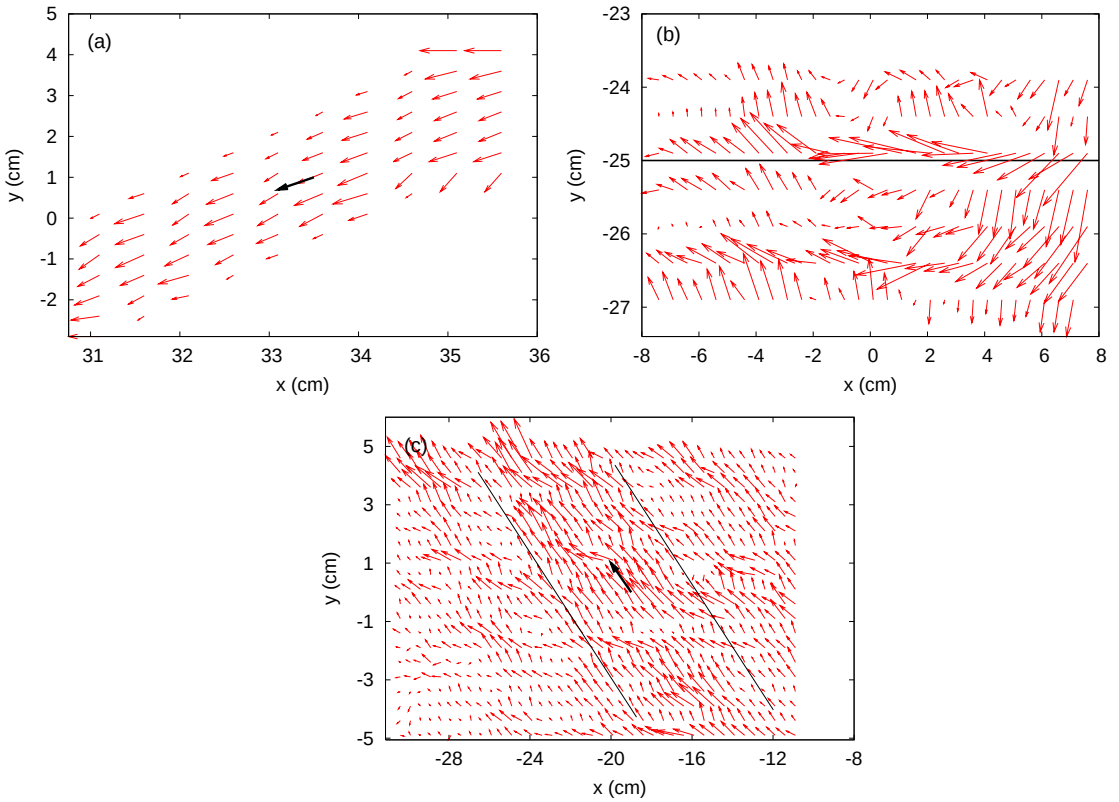

Figure 7.15.: Poynting vectors (red arrows) for the (a) incoming wave, (b) wave function on the billiard boundary, and (c) outgoing wave. In (a) and (c), the average Poynting vector at $\mathbf{r}_{\text{in (out)}}$ is shown as well (black arrow). The black line in (b) marks the billiard boundary. The averaging in (c) has been done over the region marked by the black lines. The Poynting vectors are scaled differently in the three figures.

fronts of the incoming and outgoing waves, their respective Poynting vectors show a clear propagation direction. The incoming angle calculated from the averaged Poynting vector is $\chi \approx 47$ degrees, the respective outgoing angle is $\chi \approx 45$ degrees, which further supports the claim that, in fact, a plane wave travelling at an angle of 45 degrees has been created. The Poynting vectors of the wave function at the boundary, perhaps surprisingly given that so little could be seen in the wave function itself, reveal that, in fact, there are incoming and outgoing parts of the wave at the boundary. A part is reflected at the boundary, but another part penetrates outside the billiard. The penetration depth seems to be a bit larger than the wavelength of 2 cm.

The generation of plane waves with one propagation direction thus works, at least for high ν values ($\nu \geq 10$ GHz; below that value, the wave fronts are less well defined and the extraction of Poynting vectors is thus not possible with high accuracy).

7.3.2. Superposition of two plane waves and GHS extraction

Two plane waves generated according to the scheme discussed in the previous section can now be superimposed. The GHS of the resulting beam can be extracted and compared to the Artmann result.

Table 7.1 shows the different phase functions $\phi_1(j)$, $\phi_2(j)$ used in this section and the angle of incidence χ of the beam constructed with them according to Eq. (7.11). The choice of the $\phi(j)$ is of course somewhat arbitrary; here, they are chosen such that the j dependence is simple, the difference between $\phi_1(j)$ and $\phi_2(j)$ is small (as this is the approximation in the Artmann result), and such that a range of angles of incidence results.

Figure 7.16 shows Poynting vectors at $\nu = 15$ GHz for the incoming (top panel) and outgoing (bottom panel) waves for $\phi_1(j) = 0$ and $\phi_2(j) = -j/4$, corresponding to an incoming angle of $\chi = 47.6$ degrees. The propagation direction is still well defined.

The extracted GHS for the incoming angles given in Table 7.1 is shown in Fig. 7.17 for $\nu = 10$ GHz and $\nu = 15$ GHz together with the Artmann result (7.11). The error shown as the error bar is given by the errors in $\langle \mathbf{S} \rangle_{\text{in (out)}}$, which in turn are, as $\langle \mathbf{S} \rangle_{\text{in (out)}}$ is an average value, given by the standard deviation. The error $\delta\Delta s$ in Δs is then given by error propagation:

$$\begin{aligned} \delta\Delta s = &\left|\frac{\partial\,\Delta s}{\partial\,\langle S_{\text{in}}\rangle_x}\right| \delta\langle S_{\text{in}}\rangle_x + \left|\frac{\partial\,\Delta s}{\partial\,\langle S_{\text{in}}\rangle_y}\right| \delta\langle S_{\text{in}}\rangle_y \\ &+ \left|\frac{\partial\,\Delta s}{\partial\,\langle S_{\text{out}}\rangle_x}\right| \delta\langle S_{\text{out}}\rangle_x + \left|\frac{\partial\,\Delta s}{\partial\,\langle S_{\text{out}}\rangle_y}\right| \delta\langle S_{\text{out}}\rangle_y. \end{aligned} \tag{7.16}$$

The errors are all approximately $\delta\Delta s/\Delta s \approx 20$ % (incoming angles above the critical angle) and $\delta\Delta s/\Delta s \approx 50$ % (incoming angles below critical angle). As the GHS below the critical angle is small, relatively larger errors are expected. Overall, the errors are quite large, which is mostly due to the uncertainties in the average Poynting vectors

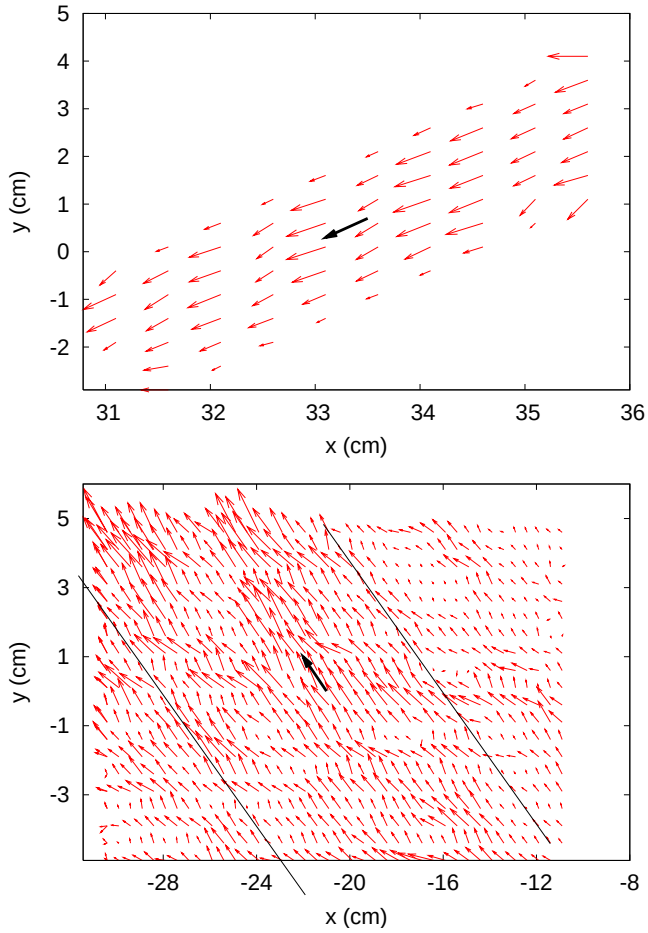

Figure 7.16.: Poynting vectors for the incoming (top panel) and outgoing (bottom panel) waves for $\nu = 15$ GHz, $\phi_1(j) = 0$ and $\phi_2(j) = -j/4$. The thick black arrows are the average Poynting vectors.

$\phi_1(j)$	$\phi_2(j)$	χ (degrees)
$8j/9$	j	22.5
$2j/3$	$3j/4$	27.9
$j/2$	$j/3$	35.1
0	$j/4$	41.4
$j/10$	0	44.9
0	$-j/4$	47.6
$-j/2$	$-j/3$	55.9
$-8j/9$	$-j$	68.9

Table 7.1.: Phase functions $\phi_{1,2}(j)$ and the resulting incoming angles χ in degrees as extracted from the experimental data.

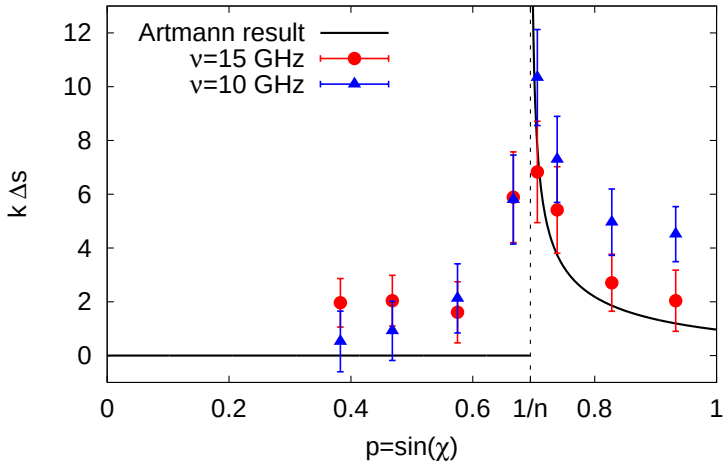

Figure 7.17.: GHS $k\Delta s$ as extracted from the measured data for $\nu = 15$ GHz (red dots) and $\nu = 10$ GHz (blue triangles). The black solid line is the Artmann result, the black dashed line marks the critical angle for $n = 1.44$.

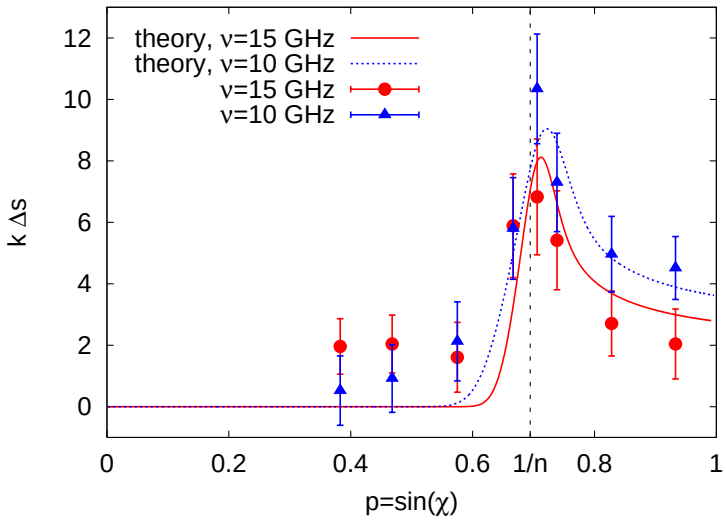

Figure 7.18.: GHS $k\Delta s$ extracted from the measured data at $\nu = 15$ GHz (red dots) and $\nu = 10$ GHz (blue triangles). For comparison, the calculated GHS for a Gaussian wave packet with the corresponding frequency is shown as well (red solid and blue dotted curves).

– and even a small change in the propagation direction can lead to a larger change in the GHS. But overall, the main features of the Artmann result (zero GHS below the critical angle, maximum GHS at the critical angle, approximately constant GHS above the critical angle, independence on k) can be seen quite well in the data. Especially at $\nu = 10$ GHz, the agreement above the critical angle is not so good, and the GHS is systematically higher than the Artmann result predicts.

The deviations at and above the critical angle can be explained as being due to deviations from the Artmann form of the incoming wave. The individual waves are not completely plane waves, as they have a width fixed by the width of the antenna array. If one approximates them as Gaussian, the resulting GHS Δs can be calculated numerically, as shown in section 6.2. In contrast to the calculations there, no minimal-uncertainty beam is used, but the width is given by the experimentally extracted beam width $\sigma \approx 3$ cm. Figure 7.18 shows the results together with the experimental data for $\nu = 10$ GHz and $\nu = 15$ GHz. The deviations above the critical angle are explained very well by a Gaussian beam profile. This is not surprising, as it has been shown by Lai *et al.* [LCT86] that the precise form of the beam envelope does not influence the GHS much: a rectangle profile (which is approximately the form our beams have, as can be seen in the bottom panel of Fig. 7.5) results in a GHS which is very similar to the one of a Gaussian profile.

For comparison, one can also extract a GHS Δs from the pure generated "plane waves" without superimposing them according to Eq. (7.11). After all, the generated "plane wave" beams only have a width of a couple of wavelengths are thus not really good plane waves; they could also show a GHS. The phase functions $\phi(j)$ used in this case

$\phi(j)$	χ (degrees)
j	20.6
$8j/9$	27.5
$j/4$	33.6
$j/6$	38.8
$j/8$	41.5
0	46.1
$-j/4$	53.4
$-j$	69.0

Table 7.2.: Phase functions $\phi(j)$ and resulting incoming angles χ for the GHS extraction from the generated "plane waves".

are shown in Table 7.2 together with the resulting incoming angles χ.

The resulting GHS $k\Delta s$ is shown in Fig. 7.19 for $\nu = 15$ GHz. While the extracted GHS is not zero, it fits neither to the Artmann result nor to the result of a Gaussian beam calculation, which is probably due to the fact that the beam profile (see Fig. 7.5) is too different from a Gaussian profile in this case, and approximately only one propagation direction instead of many is present in the beam. The results for $\nu = 10$ GHz are quite similar.

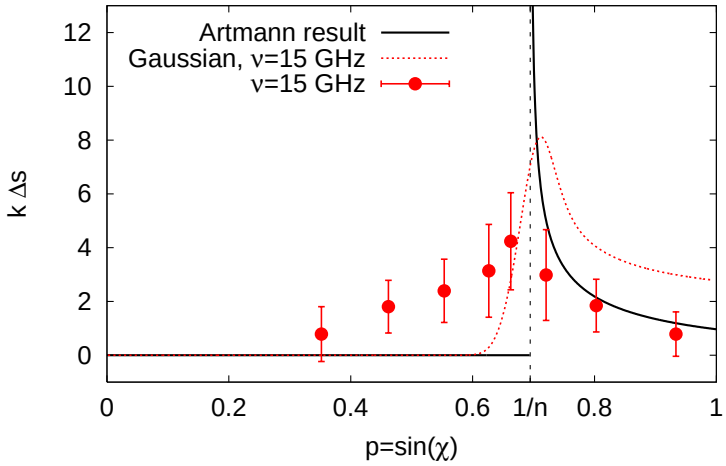

Figure 7.19.: GHS $k\Delta s$ as extracted from the generated "plane wave" beams without superposition of two beams for $\nu = 15$ GHz (red dots). The black solid line shows the Artmann result, the red dashed lines the result of a Gaussian beam calculation of the GHS for $\nu = 15$ GHz.

Summary

In this work, ray and extended ray models were investigated in special optical microcavities, namely deformed microdisk cavities; such cavities were introduced in chapter 2. As the dynamics of light rays which stay inside the cavity is equivalent to the dynamics of a classical particle in a billiard, billiard systems and their nonlinear dynamics were discussed in chapter 3. Optical modes in microdisk cavities and ray-wave correspondence were reviewed in chapter 4.

In chapter 5, a successful ray model was presented for a microdisk cavity with elliptical cross-section and a wavelength-scale "notch" at the cavity boundary; this boundary shape supports long-lived optical modes with highly unidirectional far field emission. That this is the case can be understood from the ray model alone: whispering-gallery-like rays, which travel along the boundary for a long time, eventually hit the notch. It scatters them to the opposite cavity boundary, which for certain choices of the eccentricity of the ellipse, acts like a lens and collimates the rays in the far field. This combination of a smooth boundary, allowing long-lived whispering-gallery-like rays, scattering, and collimation leads to the long mode life-times and the directed emission. Chapter 5 also dealt with optimization of the directionality depending on parameters like cavity shape, refractive index, and notch size and shape. Elliptical cavities with notch have been fabricated by collaborators at Harvard university and used as resonators for quantum cascade lasers; this work compared their experimental result to the author's own ray and mode calculations, finding good agreement between them.

Chapter 6 introduced an extended ray model, which includes first-order wave corrections, the so-called Goos-Hänchen shift (GHS) and the Fresnel filtering (FF) effect. Both corrections manifest themselves as phase-space shifts; the GHS is a shift in the s direction, the FF a shift in p direction. Using Gaussian beams, both corrections were calculated and the inclusion in the ray dynamics of a cavity was discussed. Inclusion of them was shown to lead to a variety of phase-space modifications: new stable islands and unstable periodic orbits can be created, attractors and repellers can form, periodic orbits can experience a phase-space shift compared to their counterparts in the conventional ray dynamics, and there may be asymmetries between clockwise and counter-clockwise travelling rays. The discussion of these effects and the comparison of results of the extended ray dynamics with mode calculations was the main part of chapter 6.

Chapter 7 described the setup and results of experiments performed by the author during a stay at the university of Marburg. The aim was to measure the GHS in a microwave cavity; measurements in optical microcavities are difficult, because measuring electrical field distributions with a high spatial resolution is non-trivial in this case. As the results for the GHS scale with λ/R (λ being the wavelength and R a typical cavity length scale), such measurements can also be performed in microwave cavities (where

the wavelengths are larger as in the optical microcavity case, but the cavity sizes are larger as well; in this case, high-resolution field measurements can be easily managed. In chapter 7, the experimental setup was described, the generation of suitable beams and the extraction of the GHS from the experimental data discussed, and the results were compared to numerical calculations of the GHS. Overall, the agreement between measured GHS values and numerical calculations was quite good.

A. Numerical calculation of billiard dynamics

A.1. Billiard dynamics for arbitrary boundary shapes

For a general billiard boundary curve $r(\phi)$, the mapping $(s,p) \to (s',p')$ can not be calculated analytically. Instead, the dynamics has to be calculated numerically. Starting with initial values $(\phi,\chi) \leftrightarrow (s,p)$, the real space position $(x_0,y_0) = \mathbf{r}_0 = (r(\phi)\cos\phi, r(\phi)\sin\phi)$ can be calculated. The local tangent $\boldsymbol{\tau}$ and (outwards pointing) normal vector $\boldsymbol{\nu}$ a given by

$$\begin{aligned} \boldsymbol{\tau} &= \frac{1}{|\mathrm{d}\mathbf{r}/\mathrm{d}\phi|}\frac{\mathrm{d}\mathbf{r}}{\mathrm{d}\phi} = \frac{1}{\sqrt{r^2(\phi)+r'^2(\phi)}}\begin{pmatrix} -\sin\phi\, r(\phi) + \cos\phi\, r'(\phi) \\ \cos\phi\, r(\phi) + \sin\phi\, r'(\phi) \end{pmatrix}, \\ \boldsymbol{\nu} &= \begin{pmatrix} -\tau_y \\ \tau_x \end{pmatrix}, \\ &\text{with } r'(\phi) = \frac{\mathrm{d}r}{\mathrm{d}\phi}. \end{aligned} \tag{A.1}$$

$\boldsymbol{\tau}$ and $\boldsymbol{\nu}$ then are normalized and orthogonal. The arc length is given by

$$s(\phi) = \int_{-\pi}^{\phi} \mathrm{d}\phi' \left|\frac{\mathrm{d}\,\mathbf{r}}{\mathrm{d}\,\phi'}\right| = \int_{-\pi}^{\phi} \mathrm{d}\phi' \sqrt{r^2(\phi')+r'^2(\phi')}. \tag{A.2}$$

Here, the polar angle ϕ lies between $-\pi$ and π. Definition of ϕ such that it is between 0 and 2π is, of course, also possible; however, values between $-\pi$ and π are numerically convenient, as this is the output range of `arctan` implementations which are needed in the calculations (see Eq. (A.4)).

One can then define a direction vector ("velocity") for the ray or particle travelling in the billiard:

$$\mathbf{v} = v_0\left[\sin\chi\boldsymbol{\tau} - \cos\chi\boldsymbol{\nu}\right]; \tag{A.3}$$

v_0 can be set as unity. In order to find the position where the billiard boundary will be hit the next time, one has to find intersections between the boundary curve $r(\phi)$ and the straight line $(x(t),y(t)) = (x_0,y_0) + t\mathbf{v}$; the parameter t is the elapsed time. One thus has to solve the equation

$$F(t) \equiv \sqrt{x(t)^2+y(t)^2} - r\left(\arctan\frac{y(t)}{x(t)}\right) = 0. \tag{A.4}$$

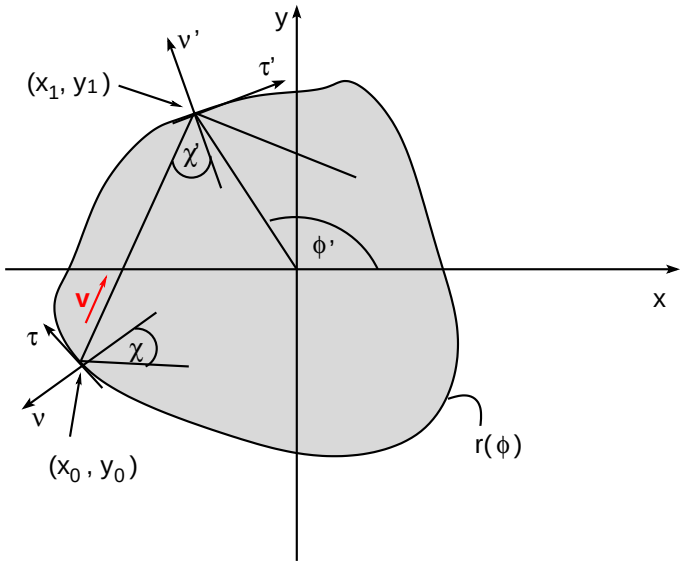

Figure A.1.: Calculating the billiard mapping $(s, p) \to (s', p')$.

This can be done using Newton's method, which here needs a reasonable starting value, as $t = 0$ is always a possible solution ((x_0, y_0) is on the billiard boundary by definition) which has to be avoided. A good starting value is found by calculating $F(ih)$ for integers i and a step size h until a sign change of F between i_n and i_{n+1} is found, and taking $t_0 = (i_{n+1} + i_n)h/2$. The step size h has to be chosen smaller if the boundary has regions with high curvature or is non-convex; for other cavities with area one, $h = 10^{-5}R$ seems to be sufficient, if R is the typical billiard length scale. In billiards with regions of high curvature, $h = 10^{-5}\rho$ with the local radius of curvature ρ is used. The resulting t_0 is taken as a starting point for Newton's method, which yields a solution t_s of (A.4). The new position on the boundary is then $(x_1, y_1) = (x_0, y_0) + t_s\mathbf{v}$. With

$$\tan\phi' = \frac{y_1}{x_1}, \sin\chi' = \mathbf{v} \cdot \boldsymbol{\tau}' \tag{A.5}$$

(where $\boldsymbol{\tau}'$ is the tangent vector at the position (x_1, y_1)), ϕ' and χ' (and correspondingly s' and p') are found. Figure A.1 illustrates the procedure.

A.2. Calculation of far field patterns

In order to calculate far field patterns, one has to find the intensity emitted into θ when starting from the phase space position (s, p). Starting from this point with the intensity $I = 1$, the billiard mapping is applied, leading to (s', p') (corresponding to a polar angle ϕ and an angle of incidence χ). If χ' is below the critical angle for total internal reflection, Snell's law is applied, leading to an angle of refraction η via $\sin\eta = n\sin\chi$. The direction $\mathbf{v}'$ of the refracted ray is then given by

$$\mathbf{v}' = \sin\eta\boldsymbol{\tau} + \cos\eta\boldsymbol{\nu}. \tag{A.6}$$

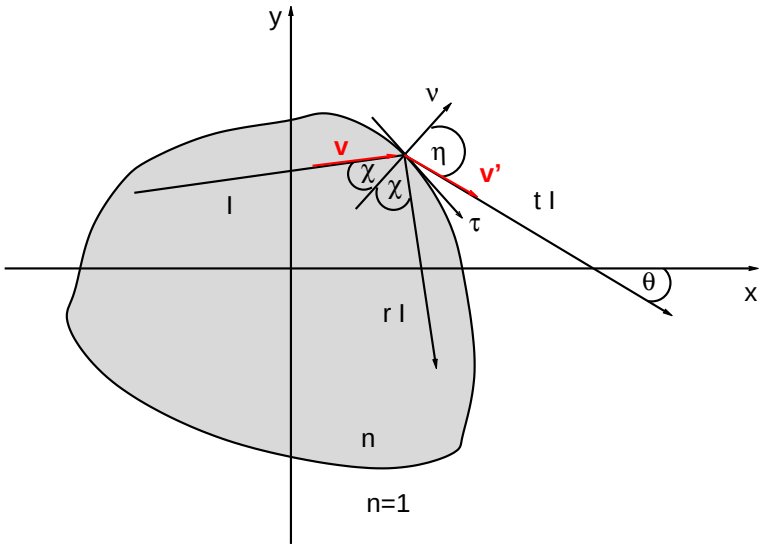

Figure A.2.: Calculation of far field patterns from ray dynamics.

(see Fig. A.2). The far field angle can be calculated as

$$\tan\theta = \frac{v'_y}{v'_x}. \tag{A.7}$$

The intensity of the refracted ray is given by $I = |t|^2 I$ and the intensity of the reflected ray, which stays inside the cavity, is given by $|r|^2 I$. r is the complex Fresnel reflection coefficient.

$$r(\chi) = \begin{cases} \frac{\sin(\eta-\chi)}{\sin(\eta+\chi)}, & \text{(TM polarization)}, \\ \frac{\tan(\eta-\chi)}{\tan(\eta+\chi)}, & \text{(TE polarization)}. \end{cases} \tag{A.8}$$

η is given by the Snell law, and $|t|^2 = 1-|r|^2$. This procedure is iterated until a maximum number of collisions with the boundary has occurred or the intensity inside the cavity has sunk below a threshold value.

One measure of directionality is given by the intensity emitted into the angle region $\pm\Delta$, i.e.

$$I_{\pm\Delta} = \frac{\int_{-\Delta}^{\Delta} \mathrm{d}\theta\, I(\theta)}{\int_{-\pi}^{\pi} \mathrm{d}\theta\, I(\theta)} \tag{A.9}$$

where $I(\theta)$ is the intensity emitted in the θ direction. Another directionality measure, which is sometimes called U_3, is given by

$$U_3 = \frac{\int_{-\pi}^{\pi} \mathrm{d}\theta\, \cos\theta\, I(\theta)}{\int_{-\pi}^{\pi} \mathrm{d}\theta\, I(\theta)}. \tag{A.10}$$

A.3. Implementation: billiard classes

The numerical calculation of billiard dynamics and far field patterns is done using a collection of C++ classes, all derived from an abstract base class, which implement the different boundary curves. In this section, the structure of such a boundary class is described as well as selected of its functions. The classes proving functions for the calculation of the wave corrections and for far field calculations are discussed as well.

The `Boundary` class is an abstract base class from which the different specific boundary classes (like `Limacon` implementing the limaçon shape) are derived. Any boundary shape which can be described by a curve $r(\phi)$ in polar coordinates can be easily implemented. The boundary classes provide functions describing the boundary itself (`BoundaryCurve` being the boundary curve $r(\phi)$ itself, `TangentVector` the local tangent vector $\boldsymbol{\tau}$, etc.), and also procedures for the calculation of the billiard mapping: `ConvertToCartesian` finds the real space position (x_0, y_0) and the velocity $\mathbf{v}$ from the phase space coordinates ϕ and χ, `StartFinder` find a starting value for Newton's method, which is implemented in `NumtCalc` (the `Ellipse` class has an analytical calculation of the intersection instead), and so on. The `GoosHaenchenShift` procedure applies the wave corrections (Goos-Hänchen shift and Fresnel filtering) to ϕ and χ. As the boundary classes only implement the billiard dynamics, no refractive index has to be provided; if the extended ray dynamics including GHS and FF corrections is calculated, a refractive index is of course implicated by the choice of a GHS/FF data set. The following listing shows the contents of the `Boundary.h` file; all virtual member functions have to be implemented in the derived boundary classes which define a special boundary.

```
#ifndef Boundary__H
#define Boundary__H

class Boundary
{
public:
        // boundary curve and first derivative
        virtual double BoundaryCurve(double phi1)=0;
        virtual double dBoundaryCurve(double phi1)=0;

        // tangent and normal vectors, arc length
           calculation
        virtual void TangentVector(double phi1, double *
           tx1, double *ty1)=0;
        virtual void NormalVector(double phi1, double *
           nx1, double *ny1)=0;
        virtual double ArcLenght(double phi1)=0;

        // finding of intersections with boundary, new
           position, new incoming angles
        virtual double F(double t1, double x1, double y1,
            double vx1, double vy1)=0;
```

```
        virtual double dF(double t1, double x1, double y1
            , double vx1, double vy1)=0;

        virtual void ConvertToCartesian(double phi1,
            double theta1, double *rho1, double *x1, double
             *y1, double *vx1, double *vy1)=0;
        virtual double tCalc(double x1,double y1,double
            rho1,double phi1)=0;
        virtual double NumtCalc(double x1, double y1,
            double vx1, double vy1)=0;
        virtual void newPosition(double x1,double y1,
            double vx1,double vy1,double *x2,double *y2)=0;
        virtual void newVelocity(double theta1,double
            rho1, double phi1,double *vx1, double *vy1)=0;
        virtual double newTheta(double vx1,double vy1,
            double tx1, double ty1)=0;

        // Newton's method and starting value finder for
            it
        virtual double StartFinder(double x1, double y1,
            double vx1, double vy1)=0;
        virtual double Newton(double ts, double x1,
            double y1, double vx1, double vy1)=0;

        // application of GHS/FF and calculation of polar
             angle from arc length
        virtual double GoosHaenchenPhi(double *phi1,
            double *s1, double ss, int s_len)=0;
        virtual void GoosHaenchenShift(double phi1,
            double theta1, double xi1[], double yi1[],
            double yi2[], int N1, double ys1[], double ys2
            [],double *arc2, double *theta2)=0;

        // step size for Newton's method
        static double const h_newton=1e-5;
        static double const h_SF=1e-7;
};

#include "Boundary.cpp"
#endif
```

Methods for the numerical calculation of the GHS and FF corrections are found in the `GHSInterpolation` class, which also provides the analytical GHS formulas of Artmann and Lai. `GHSInterpolation` also provides methods for reading the GHS/FF values from given data files and writing them to arrays which can be used for interpolation.

New boundary classes can be written easily by changing the template (`Template.cpp` and `Template.h`). After choosing a name (which should be descriptive) for the new class,

one changes the constructor by introducing the parameter(s) describing the boundary shape (i.e., deformation parameter(s) if the shape is a deformed circle), if there are any. The boundary curve has to be provided to the `BoundaryCurve` and `dBoundaryCurve` methods; the derivative $\mathrm{d}r/\mathrm{d}\phi$ provided by `dBoundaryCurve` can be calculated numerically if necessary.

For example, the constructor of the `Limacon` class implementing the limaçon boundary curve looks like this:

```
Limacon::Limacon(double e_parameter)
{
        epsilon=e_parameter;
}
```

and the `BoundaryCurve` method looks like this:

```
double Limacon::BoundaryCurve(double phi1)
{
        double r1;

        r1=1.0+epsilon*cos(phi1);
        return(r1);
}
```

The `dBoundaryCurve` method can be implemented using an analytical expression (which is actually used in the `Limacon` class),

```
double Limacon::dBoundaryCurve(double phi1)
{
        double r1;

        r1=-epsilon*sin(phi1);
        return(r1);
}
```

as well as using a numerical calculation of the derivative

```
double Limacon::dBoundaryCurve(double phi1)
{
        double r1;
        double const h1=1e-10;

        r1=(BoundaryCurve(phi1+h1)-BoundaryCurve(phi1-h1)
           )/(2.0*h1);
        return(r1);
}
```

Apart from `BoundaryCurve` and `dBoundaryCurve`, no other methods in `Template.cpp` have to be changed.

The boundary curves implemented are shown in Table A.1. As the boundary curves $r(\phi)$ for the ellipse with a double or parabolic notch are quite complex, they are not

displayed in the table; they are given in section 5.5.5. The `RoundedSquare` and `RoundedHexagon` classes define "rounded" versions of billiards (the square and the hexagon) whose boundaries are given by polygons. For low deformation parameters n and s, the polygon edges are rounded; they become less round, and the boundary curves approximate the square and hexagon billiards better, if $n, s \to \infty$.

The methods for calculating far field patterns are provided by the `FarField` class, which takes an object of the `Boundary` class and a refractive index as input. It provides reflection coefficients (`reflectionTM` and `reflectionTE`) as well as methods for calculating the far field emission angle θ (`FindFarFieldAngle`) and the intensity emitted into $\pm\Delta$ degrees (`CalculateIntensityDegrees`, Δ has to be provided as input) as well as the directionality measure U_3 (`CalculateU3`). Far fields can then be calculated using both the conventional and the extended ray dynamics.

class name	**boundary curve** $r(\phi)$
`Ellipse`	$1/\sqrt{\frac{\sin^2\phi}{a^2}+\frac{\cos^2\phi}{b^2}}$
`Limacon`	$1+\epsilon\cos\phi$
`DeformedLimacon`	$R(1+\epsilon\cos\phi)(1-\epsilon_1\cos(2\phi))+d$
`Quadrupol`	$1+\epsilon\cos(2\phi)$
`Multipol`	$1+\epsilon\cos(m\phi)$
`ThreePointedEgg`	$1+\alpha\cos(3\phi)$
`RoundedSquare`	$1/\sqrt[n]{\cos^n\phi+\sin^n\phi}$
`RoundedHexagon`	$\sqrt[s]{2/\left[\left(\cos\phi-\frac{\sin\phi}{\sqrt{3}}\right)^s+\left(\frac{2\sin\phi}{\sqrt{3}}\right)^s+\left(\cos\phi+\frac{\sin\phi}{\sqrt{3}}\right)^s\right]}$
`EllipseNotch`	$\sqrt{\sin^2\phi+\left(\epsilon\cos\phi-\delta\exp(-2(\phi-\pi)^2/\vartheta^2)\cos\phi\right)^2}$
`EllipseDoubleNotch`	see Eq. (5.23)
`EllipseParabolicNotch`	see Eq. (5.25)
`QuadrupolNotch`	$\sqrt{r_0^2\sin^2\phi+\left(r_0\cos\phi-\delta r_0\exp(-2(\phi-\pi)^2/\theta^2)\cos\phi\right)^2}$ with $r_0=1.0-\epsilon\cos(2\phi)$.

Table A.1.: Class names and boundary curves $r(\phi)$ of the boundary curves already implemented.

B. Derivation of the Helmholtz equation

B.1. Derivation of the mode equations

The Maxwell equations (in SI units) without free charges and currents are given by

$$\nabla \cdot \mathbf{D} = 0, \tag{B.1}$$
$$\nabla \cdot \mathbf{B} = 0, \tag{B.2}$$
$$\nabla \times \mathbf{E} = -\frac{\partial \mathbf{B}}{\partial t}, \tag{B.3}$$
$$\nabla \times \mathbf{H} = \frac{\partial \mathbf{D}}{\partial t}. \tag{B.4}$$

c is the speed of light in vacuum. The electric field $\mathbf{E}$, the magnetic field $\mathbf{H}$, the electric displacement $\mathbf{D}$, and the magnetic flux $\mathbf{B}$ are, in linear isotropic media, related by

$$\mathbf{D} = \epsilon_0 \epsilon_r \mathbf{E},\ \mathbf{B} = \mu_0 \mu_r \mathbf{H} \tag{B.5}$$

with the electric susceptibility ϵ_r and the magnetic permeability μ_r of the material. The refractive index is then given by $n^2 = \epsilon_r \mu_r$. The cavity modes are solutions with a harmonic time dependence $e^{i\omega t}$, Eqs. (B.1)–(B.4) simplify to

$$\nabla \cdot \epsilon_0 \epsilon_r \mathbf{E} = 0, \tag{B.6}$$
$$\nabla \cdot \mathbf{H} = 0, \tag{B.7}$$
$$\nabla \times \mathbf{E} = i\omega \mu_0 \mu_r \mathbf{H} \tag{B.8}$$
$$\nabla \times \mathbf{H} = -i\omega \epsilon_0 \epsilon_r \mathbf{E}. \tag{B.9}$$

For microcavities, the refractive index usually is piecewise constant with respect to space, i.e. it has one value n_2 inside the cavity and another value n_1 outside of it. The cavity geometry is then given solely by the function $n(\mathbf{r})$. For $\mathbf{r}$ not on the cavity boundary, ϵ_r and μ_r are thus constants. By calculating $\nabla \times$ (B.8) and $\nabla \times$ (B.9), one finds with $c^2 = 1/\epsilon_0 \mu_0$:

$$\begin{aligned} \nabla \times \nabla \times \mathbf{E} &= -\nabla(\nabla \cdot \mathbf{E}) - \Delta \mathbf{E} \\ &= -\Delta \mathbf{E} \,(\text{ as } \nabla \cdot \mathbf{E} = 0 \text{ with (B.6)}) \\ &= i\omega\mu \nabla \times \mathbf{H} \\ &= \frac{\omega^2 \epsilon_r \mu_r}{c^2} \mathbf{E}, \ (\text{with (B.9)}) \end{aligned} \tag{B.10}$$

e. g.,

$$\Delta\mathbf{E} = -n^2(\mathbf{r})\frac{\omega^2}{c^2}\mathbf{E}. \tag{B.11}$$

Analogously, one finds

$$\Delta\mathbf{H} = -n^2(\mathbf{r})\frac{\omega^2}{c^2}\mathbf{H}. \tag{B.12}$$

At the cavity boundary with local normal vector $\boldsymbol{\nu}(\mathbf{r})$, the continuity relations

$$\begin{aligned} &\boldsymbol{\nu}(\mathbf{r}) \cdot \left(n_1^2\mathbf{E}_1(\mathbf{r}) - n_2^2\mathbf{E}_2(\mathbf{r})\right) = 0,\ \boldsymbol{\nu}(\mathbf{r}) \cdot (\mathbf{H}_1(\mathbf{r}) - \mathbf{H}_2(\mathbf{r})) = 0, \\ &\boldsymbol{\nu}(\mathbf{r}) \times (\mathbf{E}_1(\mathbf{r}) - \mathbf{E}_2(\mathbf{r})) = 0,\ \boldsymbol{\nu}(\mathbf{r}) \times (\mathbf{H}_1(\mathbf{r}) - \mathbf{H}_2(\mathbf{r})) = 0, \end{aligned} \tag{B.13}$$

hold, meaning that the tangential components of $\mathbf{E}$ and $\mathbf{H}$ are continuous across the boundary, as well as the normal component of $\mathbf{H}$. Equations (B.11) and (B.12), together with the relations (B.13), define the optical modes.

B.2. Reduction of Maxwell's equations in cylindrical geometry

When dealing with microdisks, one is only interested in the fields in the disk $(x-y)$ plane; the dependence of the fields on z is not interesting. This means that the two-dimensional disk can be viewed as an infinite cylinder: if the z dependence is not important, one can assume about is whatever is most convenient. In such a cylindrical geometry, the (x, y) and z components can be regarded as decoupled. Because of the translational symmetry along z, the propagation in z direction is given by a plane wave ansatz $\sim e^{-ik_z z}$, and the fields can be separated as

$$\mathbf{E}(x, y, z) = \mathbf{E}(x, y)e^{-ik_z z},\ \mathbf{H}(x, y, z) = \mathbf{H}(x, y)e^{-ik_z z}. \tag{B.14}$$

Inserting this ansatz into the mode equations (B.11) and (B.12) yields

$$\begin{aligned} \left(\Delta_\perp + n_{\text{eff}}^2 k^2\right)\mathbf{E}(x, y) = 0, \\ \left(\Delta_\perp + n_{\text{eff}}^2 k^2\right)\mathbf{H}(x, y) = 0. \end{aligned} \tag{B.15}$$

Here, the vacuum wave number $k = \omega/c$ and the effective refractive index $n_{\text{eff}}^2 = n^2 - k_z^2$ have been introduced as well as $\nabla_\perp = \nabla - (\partial_z)\mathbf{e}_z$.

In order to simplify things even further, one can decompose the fields in components parallel and perpendicular to z:

$$\begin{aligned} \mathbf{E}(x, y) = E_z(x, y)\mathbf{e}_z + \mathbf{E}_\perp(x, y), \\ \mathbf{H}(x, y) = H_z(x, y)\mathbf{e}_z + \mathbf{H}_\perp(x, y). \end{aligned} \tag{B.16}$$

Inserting this ansatz into the Maxwell equations (B.6)–(B.9), one finds

$$\nabla_\perp \cdot \mathbf{E}_\perp = ik_z E_z \tag{B.17}$$

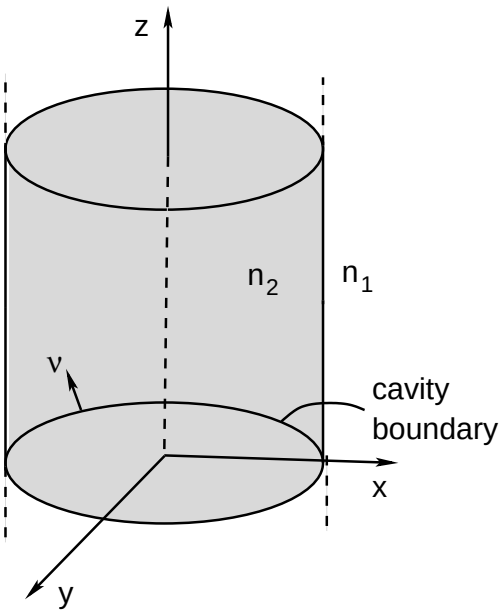

Figure B.1.: Geometry with cylindrical symmetry for microdisk cavities. The disk plane is the (x, y)-plane; $\boldsymbol{\nu}$ is a local normal vector to the cavity boundary. The refractive index inside the disk is n_2, the refractive index outside n_1.

and

$$\begin{aligned} i\omega\mu_0\mu_r\mathbf{H} &= \nabla \times (\mathbf{E}_\perp + E_z\mathbf{e}_z) \\ &= (\nabla_\perp \times \mathbf{E}_\perp) + [ik_z\mathbf{E}_\perp \times \mathbf{e}_z + (\nabla_\perp E_z) \times \mathbf{e}_z]\,. \end{aligned} \tag{B.18}$$

These relations, split up in z and $\perp$ components, lead to

$$\nabla_\perp \cdot \mathbf{E}_\perp = ik_z E_z, \tag{B.19}$$

$$i\omega\mu_0\mu_r H_z = (\nabla_\perp \times \mathbf{E}_\perp)_z\,, \tag{B.20}$$

$$i\omega\mu_0\mu_r\mathbf{H}_\perp = (ik_z\mathbf{E}_\perp + \nabla_\perp E_z) \times \mathbf{e}_z. \tag{B.21}$$

Similar relations follow from the equations for the magnetic field $\mathbf{H}$:

$$\nabla_\perp \cdot \mathbf{H}_\perp = ik_z H_z, \tag{B.22}$$

$$-i\omega\epsilon_0\epsilon_r E_z = (\nabla_\perp \times \mathbf{H}_\perp)_z\,, \tag{B.23}$$

$$-i\omega\epsilon_0\epsilon_r\mathbf{E}_\perp = (ik_z\mathbf{H}_\perp + \nabla_\perp E_z) \times \mathbf{e}_z. \tag{B.24}$$

When Eq. (B.24) is used to eliminate $\mathbf{H}_\perp$ from Eq. (B.21), one can find a relation between $\mathbf{E}_\perp$ and E_z and H_z:

$$\mathbf{E}_\perp = \frac{i}{n_{\text{eff}}^2}\left(k_z\nabla_\perp E_z - k\mathbf{e}_z \times \nabla_\perp H_z\right). \tag{B.25}$$

Analogously, one can find a relation between $\mathbf{H}_\perp$ and E_z, H_z by eliminating $\mathbf{E}_\perp$ from Eq. (B.24) by means of Eq. (B.21):

$$\mathbf{H}_\perp = \frac{i}{n_{\text{eff}}^2}\left(k_z\nabla_\perp H_z + kn^2\mathbf{e}_z \times \nabla_\perp E_z\right). \tag{B.26}$$

It is thus sufficient to solve Eqs. (B.15) for E_z and H_z, i.e. the scalar wave equations

$$\left(\Delta_\perp + n_{\text{eff}}^2 k^2\right) E_z = 0,\ \left(\Delta_\perp + n_{\text{eff}}^2 k^2\right) H_z = 0, \tag{B.27}$$

as the other field components then can be calculated from E_z, H_z. As one typically deals either with TM polarization ($H_z = 0$ for all x, y) or TE polarization ($E_z = 0$ for all x, y), one only has to solve one scalar wave equation, the Helmholtz equation

$$\left(\Delta_{x,y} + n_{\text{eff}}(x,y)^2 k^2\right) \psi(x,y) = 0 \tag{B.28}$$

for a piecewise constant refractive index n_{eff} and a scalar function ψ with $\psi = E_z$ (TM) or $\psi = H_z$ (TE). In this case, the continuity relations (B.13) simplify to

$$\begin{aligned} &\psi_1 = \psi_2,\ \partial_\nu \psi_1 = \partial_\nu \psi_2 \text{ (TM)}, \\ &\psi_1 = \psi_2,\ \frac{\partial_\nu \psi_1}{n_1^2} = \frac{\partial_\nu \psi_2}{n_2^2} \text{ (TE)}, \end{aligned} \tag{B.29}$$

with $\partial_\nu \psi = \boldsymbol{\nu} \cdot \nabla_{x,y} \psi$.

While the Helmholtz equation (B.28) is valid not only for cavities made of positive-index material, but for negative-index cavities as well, the continuity relations (B.29) have to be modified in the negative-index case [WUS+10a].

C. Boundary element method

The boundary element method (BEM) [Wie03] is a Green function-based method for calculating resonances of two-dimensional dielectric cavities with spatially homogeneous index of refraction. Resonances can be calculated for cavities of arbitrary shape, which may be coupled. The refractive index may be complex, which can be used to include the effects of a medium with gain or loss in a simple way.

The main idea is to map the two-dimensional Helmholtz equation to a (one-dimensional) integral equation which can then be solved numerically.

C.1. Derivation of boundary integral equations

Figure C.1 shows an exemplary system whose resonances can be studied using the BEM. It consists of $J-1$ cavities with refractive indices n_j, interiors Ω_j and boundaries $\Gamma_j = \partial\Omega_j$ (which do not have to be simply connected). Each boundary can be parametrized using an arc length s, and on each boundary, a normal vector $\boldsymbol{\nu}$ can be defined at each boundary point. The region outside the cavities is Ω_J, bounded by a circle at infinity $\partial\Omega_J = I_\infty$. Inside each region Ω_j, the Helmholtz equation holds:

$$\left(\Delta + n_j^2 k^2\right)\psi(\mathbf{r}) = 0. \tag{C.1}$$

A solution of this equation yields both the cavity resonance wavenumbers k and the corresponding wavefunctions ψ. At each cavity boundary Γ_j, the following boundary conditions (quantities with index "in" are inside the region Ω_j, quantities with index "out" are outside) hold:

$$\begin{aligned} &\psi_{\text{in}} = \psi_{\text{out}} \text{ (both TM and TE polarization)}, \\ &\partial_\nu\psi_{\text{in}} = \partial_\nu\psi_{\text{out}} \text{ (TM)}, \\ &\partial_\nu\psi_{\text{in}}/n_{\text{in}}^2 = \partial_\nu\psi_{\text{out}}/n_{\text{out}}^2 \text{ (TE)}. \end{aligned} \tag{C.2}$$

$\partial_\nu = \boldsymbol{\nu}\cdot\nabla_{\mathbf{r}}$ is the normal derivative. As modes are often calculated for the simulation of cavities for lasers, where only light comes out of the cavity, but no light comes in, one can choose *outgoing-wave* conditions at infinity:

$$\psi(r\to\infty) \sim h(\theta,k)\frac{e^{ikr}}{\sqrt{r}}. \tag{C.3}$$

Even though the Helmholtz equation (C.1) is invariant under time reversal, the outgoing-wave condition (C.3) is *not*, and thus introduces solutions which also violate time-reversal invariance.

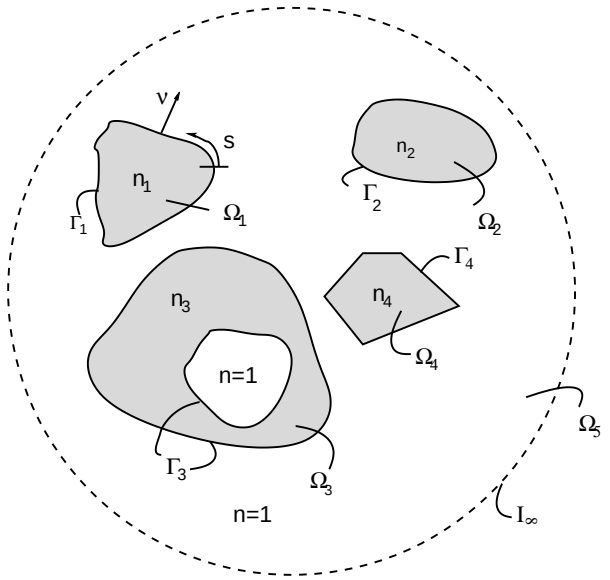

Figure C.1.: An exemplary system to be studied using the BEM, consisting of $J-1$ arbitrarily shaped cavities with different refractive indices n_j.

The Green's function is the solution of

$$\left(\Delta + n_j^2 k^2\right) G(\mathbf{r}, \mathbf{r}', k) = \delta(\mathbf{r} - \mathbf{r}'). \tag{C.4}$$

The Green's function is just the Green's function of an outgoing wave in a medium with constant index of refraction (i.e., basically the free space solution) and known analytically:

$$G(\mathbf{r}, \mathbf{r}', k) = G_0(\mathbf{r}, \mathbf{r}', k) = -\frac{i}{4} H_0^{(1)}(n_j k|\mathbf{r} - \mathbf{r}'|), \tag{C.5}$$

with the zeroth-order Hankel function of the first kind $H_0^{(1)}$. Calculating

$$\psi(\mathbf{r}) \times (\text{C.1}) - G_0(\mathbf{r}, \mathbf{r}', k) \times (\text{C.4}), \tag{C.6}$$

one finds

$$\begin{aligned} \psi(\mathbf{r})\delta(\mathbf{r} - \mathbf{r}') &= \psi(\mathbf{r})\nabla^2 G_0(\mathbf{r}, \mathbf{r}', k) - G_0(\mathbf{r}, \mathbf{r}', k)\nabla^2\psi(\mathbf{r}) \\ &= \nabla \cdot \left(\psi(\mathbf{r})\nabla G_0(\mathbf{r}, \mathbf{r}', k) - G_0(\mathbf{r}, \mathbf{r}', k)\nabla\psi(\mathbf{r})\right). \end{aligned} \tag{C.7}$$

Integration over the region Ω_j and applying Green's theorem yields

$$\psi(\mathbf{r}') = \oint_{\Gamma_j} \mathrm{d}s \left[\psi(\mathbf{r}(s))\partial_\nu G_0(\mathbf{r}(s), \mathbf{r}', k) - G_0(\mathbf{r}(s), \mathbf{r}', k)\partial_\nu\psi(\mathbf{r}(s))\right], \tag{C.8}$$

where s is the arc length around the boundary Γ_j. The normal derivative of the Green's function $\partial_\nu G_0(\mathbf{r}(s), \mathbf{r}', k)$ can be calculated analytically using properties of the Hankel functions [GR65]:

$$\partial_\nu G_0(\mathbf{r}(s), \mathbf{r}', k) = \frac{i n_j k}{4} \cos\alpha \, H_1^{(1)}(n_j k|\mathbf{r}(s) - \mathbf{r}'|) \tag{C.9}$$

with

$$\cos\alpha = \boldsymbol{\nu}(\mathbf{r}) \cdot \frac{\mathbf{r}-\mathbf{r}'}{|\mathbf{r}-\mathbf{r}'|}. \tag{C.10}$$

The limit $\mathbf{r}' \to \Gamma_j$ in Eq. (C.8) can be performed. The integral has then to be calculated as a Cauchy principal value integral, yielding

$$\psi(\mathbf{r}') = 2\mathcal{P} \oint_{\Gamma_j} \mathrm{d}s \left[(\psi(\mathbf{r}(s))\partial_\nu G_0(s,\mathbf{r}',k) - G_0(s,\mathbf{r}',k)\partial_\nu\psi(\mathbf{r}(s))\right]. \tag{C.11}$$

It can be shown [Wie03] that the circle at infinity I_∞ does not give a contribution. Apart from that, there is an equation like (C.11) of each region Ω_j. Equation (C.11) can be rewritten as

$$\oint_{\Gamma_j} \mathrm{d}s \left[B(s',s,k)\phi(s) + C(s',s,k)\psi(s)\right] = 0, \tag{C.12}$$

with the integral kernels

$$\begin{aligned} B(s',s,k) &= \begin{cases} -2G_0(\mathbf{r}(s),\mathbf{r}(s'),k), & \text{TM polarization,} \\ -2n_j^2 G_0(\mathbf{r}(s),\mathbf{r}(s'),k), & \text{TE polarization.} \end{cases} \\ C(s',s,k) &= 2\partial_\nu G_0(\mathbf{r}(s),\mathbf{r}(s'),k) - \delta(\mathbf{r}(s)-\mathbf{r}(s')) \end{aligned} \tag{C.13}$$

and

$$\psi(s) = \psi(\mathbf{r}(s)), \phi(s) = \begin{cases} \partial_\nu\psi(\mathbf{r}(s)), & \text{TM polarization,} \\ \partial_\nu\psi(\mathbf{r}(s))/n_j^2, & \text{TE polarization.} \end{cases} \tag{C.14}$$

The boundary conditions, i.e. the fact that ψ and ϕ have to be continuous across each boundary Γ_j, are then build in: each equation has two contributions, one from *inside* the region Ω_j and one from *outside* the region Ω_j (both contributions are calculated on the shared boundary Γ_j); they have the same ψ, ϕ, but different B and C (because the refractive index n_j enters the integral operators via the Green's function). Solution of Eq. (C.12) yields the wavefunction on the boundary Γ_j and the resonance wavenumber k; the full wave function can be calculated using Eq. (C.8).

C.2. Numerical solution of the boundary integral equations

C.2.1. Discretization

The boundary is discretized into small boundary elements (BEs) with lengths Δs_i, such that the length is smaller than the wavelength $\lambda = 2\pi/(n_j k)$ inside the region Ω_j, and also smaller than the local radius of curvature. Typically, one chooses $\Delta s_i/\lambda \approx 1/10$. Then, the wavefunction ψ, its normal derivative ϕ, and the local normal vector $\boldsymbol{\nu}$ can be considered constant on a BE. The BEs do not have to have equal lengths; in fact, it is reasonable to optimize the length distribution such that regions of high curvature are

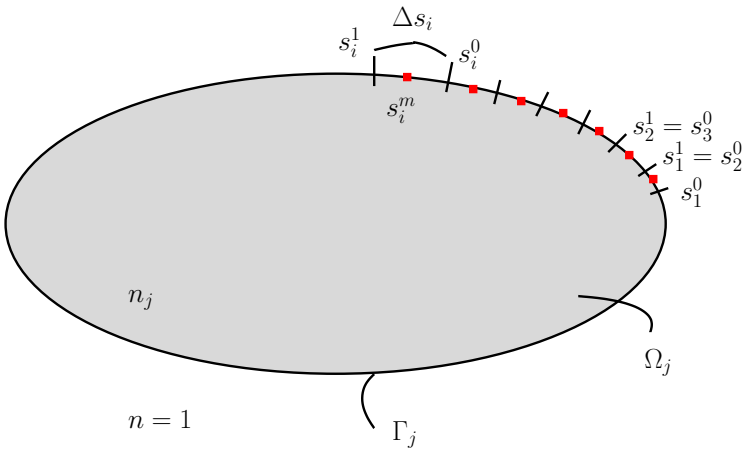

Figure C.2.: Illustration of a discretization of the boundary of a cavity. The BEs have starting points s_i^0, end points s_i^1, mid points s_i^m, and lengths Δs_i.

divided into more BEs of smaller length and regions of low curvature into correspondingly less BEs. Figure C.2 illustrates such a discretization. The BEs have starting points s_i^0, end points s_i^1, and mid points s_i^m. The boundary is divided into N_j BEs. Using this discretization, the boundary integral equations (C.12) can be written as

$$\sum_{l=1}^{N_j} (B_{il}\phi_l + C_{il}\psi_l) = 0, \tag{C.15}$$

with

$$\begin{aligned} B_{il} &= \int_{s_l^0}^{s_l^1} \mathrm{d}s\, B(s_i, s), \\ C_{il} &= \int_{s_l^0}^{s_l^1} \mathrm{d}s\, C(s_i, s), \\ \psi_l &= \psi(s_l^m),\ \phi_l = \phi(s_l^m). \end{aligned} \tag{C.16}$$

Because the integral operators are nearly singular, one has to calculate the diagonal elements B_{ll}, C_{ll} separately. This can be done by using the expansion of the Hankel functions for small arguments:

$$\begin{aligned} B_{ll} &\approx \frac{\Delta s_l}{\pi}\left[1 - \ln\left(\frac{n_j k \Delta s_l}{4}\right) + i\frac{\pi}{2} - \gamma\right], \\ C_{ll} &\approx -1 + \frac{\kappa_l \Delta s_l}{2\pi}. \end{aligned} \tag{C.17}$$

κ_l is the curvature at the midpoint s_l^m and $\gamma = 0.577215\ldots$ is Euler's constant.

Equation (C.15) can be written in matrix form:

$$\begin{pmatrix} B_{il}^1 & C_{il}^1 \\ B_{il}^2 & C_{il}^2 \\ \vdots & \vdots \\ B_{il}^J & C_{il}^J \end{pmatrix} \cdot \begin{pmatrix} \phi_l^1 \\ \phi_l^2 \\ \vdots \\ \phi_l^J \\ \psi_l^1 \\ \psi_l^2 \\ \vdots \\ \psi_l^J \end{pmatrix} = 0, \tag{C.18}$$

where B_{il}^j, C_{il}^j are the integral kernels in region Ω_j and ϕ_l^j, ψ_l^j the respective wavefunctions on the boundary Γ_j.

For the special (and most common) case of only one cavity, Eq. (C.18) reads

$$\begin{pmatrix} B_{il}^{\text{inside}} & C_{il}^{\text{inside}} \\ B_{il}^{\text{outside}} & C_{il}^{\text{outside}} \end{pmatrix} \cdot \begin{pmatrix} \phi_l \\ \psi_l \end{pmatrix} = 0. \tag{C.19}$$

Denoting the matrix of the integral operators appearing in Eq. (C.18) as $\hat{M}(k)$ and the vector of the wavefunctions and their normal derivatives by $(\phi, \psi)^t$, (C.18) reads

$$\hat{M}(k) \cdot \begin{pmatrix} \phi \\ \psi \end{pmatrix} = 0. \tag{C.20}$$

This equation has to be solved for both the parameter k and the vector $(\phi, \psi)^t$. This can be viewed as a singular value or eigenvalue problem: One has to find the parameter k such that $\hat{M}(k)$ has a singular value (or eigenvalue) of zero, and then find the corresponding singular or eigenvector.

C.2.2. Computing resonances and wave functions

The first step to the solution of the boundary integral equations is to find the resonance wavenumber k_{res}, i.e., a k value for which $\hat{M}(k)$ has an eigen- or singular value of zero. The matrix itself is calculated by calculating the B_{il} and C_{il} blocks; the necessary integration over the BEs can be done using a simple integration procedure like Numerical Recipe's `qromb` (Romberg integration) [PFTV92]. Hankel functions for complex arguments are provided by the free `slatec` library (`zbesh` routine).

In order for $\hat{M}(k)$ to have a zero singular- or eigenvalue, $\det\hat{M}(k)$ has to be zero. This equation can be solved using Newton's method, which iteratively improves the approximate solutions to $\det\hat{M}(k) = 0$ as

$$k_{j+1} = k_j - \frac{\det\hat{M}(k_j)}{\partial[\det\hat{M}(k_j)]/\partial k}. \tag{C.21}$$

Because calculating determinants, particularly small determinants, is hard to do accurately numerically, one can use the identity

$$\ln \det \hat{M} = \mathrm{tr} \ln \hat{M} \rightarrow \det \hat{M} = \exp(\mathrm{tr} \ln \hat{M}), \tag{C.22}$$

which yields

$$\begin{aligned} \frac{\partial \det \hat{M}}{\partial k} &= \exp(\mathrm{tr} \ln \hat{M}) \mathrm{tr} \left(\frac{\partial \ln \hat{M}}{\partial k} \right) \\ &= \det \hat{M} \mathrm{tr} \left(\hat{M}^{-1} \cdot \partial \hat{M} / \partial k \right), \end{aligned} \tag{C.23}$$

which, put into (C.21), leads to

$$k_{j+1} = k_j - \frac{1}{\mathrm{tr} \left(\hat{M}^{-1} \cdot \partial \hat{M} / \partial k \right)}. \tag{C.24}$$

The inverse matrix $\hat{M}^{-1}$ and the matrix product can be efficiently calculated using BLAS routines (`zgetri`/`zgetrf` and `zgemm`).

After k_{res} has been found with sufficient accuracy, the vector $(\phi, \psi)^t$ fulfilling (C.20) with $k = k_{\mathrm{res}}$ has to be calculated. This can be done either by finding the left singular vector to the singular value zero of $\hat{M}(k_{\mathrm{res}})$ (e.g., using the `zgesvd` routine from LAPACK) or the eigenvector corresponding to the eigenvalue zero of $\hat{M}(k_{\mathrm{res}})$ (e.g., using the `zheevd` routine). Eigenvector calculation is typically a bit faster, the singular value decomposition, on the other hand, is typically numerically more stable. After the wavefunction on the boundary is known, the full wavefunction in the region Ω_j is calculated according to

$$\begin{aligned} \psi(\mathbf{r}') = &\sum_{l=1}^{N_j} \psi_l \int_{s_l^0}^{s_l^1} \mathrm{d}s \, \partial_\nu G_0(\mathbf{r}(s), \mathbf{r}', k_{\mathrm{res}}) \\ &- \sum_{l=1}^{N_j} \phi_l \int_{s_l^0}^{s_l^1} \mathrm{d}s \, G_0(\mathbf{r}(s), \mathbf{r}', k_{\mathrm{res}}). \end{aligned} \tag{C.25}$$

Far field patterns can be calculated by adding up intensities on a circle

$$\mathbf{R}(\theta) = \begin{pmatrix} R_0 \cos\theta \\ R_0 \sin\theta \end{pmatrix} \tag{C.26}$$

far away from the cavities; typically, one chooses $R_0 \approx 1000$ times the radius of the region containing the cavities. The far field is then given by

$$I(\theta) = |\psi(\mathbf{R}(\theta))|^2. \tag{C.27}$$

C.2.3. More accurate Q-factor calculation

For long-lived modes with high Q factors, the accurate calculation of

$$Q = -\frac{\mathrm{Re}(k_{\mathrm{res}})}{2\mathrm{Im}(k_{\mathrm{res}})} \tag{C.28}$$

using the BEM can be difficult because the imaginary part of k_{res} is very small; even small numerical errors can thus change Q drastically or even lead to the unphysical result of a negative Q value (positive imaginary part of k_{res}). Zou *et al.* [ZYX+09] developed a method which can improve the accuracy of Q factors calculated by the BEM significantly.

As the imaginary part of the wavenumber k defines a lifetime of the cavity mode (and subsequently the energy inside the cavity and the energy flow to the exterior) via $\tau = -\mathrm{Im}(k)/2c$, the energy decay can be described as

$$I(t) = I_0 \exp(-t/\tau) = I_0 \exp\left[t\mathrm{Re}(k)/(\mathrm{Im}(k)\mathrm{Re}(k)/2c)\right] = I_0 \exp(-Qt/\mathrm{Re}(\omega)), \tag{C.29}$$

with the frequency $\omega = ck$. This implies

$$Q = -\mathrm{Re}(\omega)\frac{I(t)}{\mathrm{d}\ I/\mathrm{d}\ t}. \tag{C.30}$$

The energy decay can be calculated using the energy balance of the electromagnetic field [Jac75]:

$$\frac{\mathrm{d}\, I}{\mathrm{d}\, t} = \oint_A \mathrm{d}\mathbf{A} \cdot \mathbf{S}, \tag{C.31}$$

where $\mathbf{S}$ is the Poynting vector $\mathbf{S} = \mathbf{E} \times \mathbf{H}$ and the right-hand side is the energy flow through a surface A surrounding the cavity. Combining equations (C.30) and (C.31) yields

$$Q = k^2 \frac{\int_{\Omega_j} \mathrm{d}\, V n_j^2 |\psi|^2}{\oint_A \mathrm{d}s\, \mathrm{Im}(\psi^* \partial_\nu \psi)}, \tag{C.32}$$

where $S = \mathrm{Im}(\psi^* \partial_\nu \psi)$, which holds for two-dimensional cavities, has been used.

Even if the error in the imaginary part of k_{res} obtained by the BEM is relatively large, the *overall* error in k_{res} is small, and the extracted wave function ψ is quite insensitive to small changes in k_{res} and thus also accurate. Therefore, the Q factor calculated using Eq. (C.32) can be more accurate than the one calculated just using k_{res}.

C.3. Husimi functions

It is often useful to project the calculated mode wave functions to the Poincaré surface of section; this can be done by means of the Husimi distribution. Fortunately, it can be easily calculated from the wave function and its normal derivative on the cavity boundaries, which are calculated anyway if one uses the BEM to find modes.

The incoming and emergent Husimi functions inside the cavity region Ω_j are given by [HSS03]:

$$H_j^{\text{inc/em}}(s,p) = \frac{n_j \text{Re}(k_{\text{res},j})}{2\pi} \left| -\mathcal{F}_j h_j(s,p) \pm \frac{i}{k_{\text{res},j}\mathcal{F}_j} h_j'(s,p) \right|^2, \tag{C.33}$$

with[1]

$$\begin{aligned} h_j(s,p) &= \int_0^{s_{\max}} \mathrm{d}\, s' \psi_j(s') \xi(s,s',p), \\ h_j'(s,p) &= \int_0^{s_{\max}} \mathrm{d}\, s' \partial_\nu \psi_j(s') \xi(s,s',p), \\ \mathcal{F}_j &= \sqrt{n_j \sqrt{1-p^2}}, \\ \xi(s,s',p) &= \frac{1}{\sqrt[4]{\sigma\pi}} \sum_{l=-\infty}^{\infty} e^{-i n_j k_{\text{res},j} p (s' + l s_{\max})} e^{-(s'-s+l s_{\max})^2/2\sigma^2}. \end{aligned} \tag{C.34}$$

One has the freedom to choose the width of the minimal-uncertainty wave packet ξ; here, $\sigma^2 = s_{\max}/n_j k_{\text{res},j}$ is chosen. The l-sum in Eq. (C.33) which ensures the correct periodicity of ξ is, of course, numerically only taken from $-N$ to N. $N = 1$ is mostly sufficient; another (yet arbitrary) choice is $N = 1 + 20\sigma/s_{\max}$.

Using the discretization of section C.2.1, one finds

$$\begin{aligned} h_j(s,p) &\approx \sum_{l=1}^{N_j} \psi_l \int_{s_l^0}^{s_l^1} \mathrm{d}s'\, \xi(s,s',p), \\ h_j'(s,p) &\approx \sum_{l=1}^{N_j} \phi_l \int_{s_l^0}^{s_l^1} \mathrm{d}s'\, \xi(s,s',p); \end{aligned} \tag{C.35}$$

the Husimi functions (C.33) can thus be calculated directly from the wavefunction on the boundary as found from the BEM.

C.4. Boundary element method for negative-index cavities

In [WUS+10a], the boundary element method has been generalized in order to described cavities made of negative-index metamaterials (NIMs), i.e. materials where both the electric permeability ϵ and the magnetic permittivity μ are negative. The Helmholtz equation (C.1) remains unchanged, but for $\mu_{\text{in}} < 0$ inside the cavity and $\mu_{\text{out}} > 0$

[1] Note that [HSS03] has a typo in the ξ equation: there, the first exponential is written as $\exp(-ik_{\text{res}} \dots)$ without the refractive index n_j, which is wrong.

outside, the boundary conditions read

$$\begin{aligned}
&\psi_{\text{in}} = \psi_{\text{out}} \text{ (both TE and TM polarization)},\\
&\frac{1}{\mu_{\text{in}}}\partial_\nu\psi_{\text{in}} = \frac{1}{\mu_{\text{out}}}\partial_\nu\psi_{\text{out}} \text{ (TM)},\\
&\frac{1}{\epsilon_{\text{in}}}\partial_\nu\psi_{\text{in}} = \frac{1}{\epsilon_{\text{out}}}\partial_\nu\psi_{\text{out}} \text{ (TE)}.
\end{aligned} \tag{C.36}$$

If $\mu = -1$ inside the cavity and $\mu = 1$ outside, the only change in the boundary conditions compared to (C.2) is a sign in the condition for $\partial_\nu\psi$; this can be implemented easily by setting $\phi = -\partial_\nu\psi$ (TM) or $\phi = -\partial_\nu\psi/n_j^2$ (TE) at each boundary dividing a positive-index from a negative-index region. The B integral kernel also gets a sign change in the same cases.

However, this is not the only change necessary. In order to ensure a positive Q factor (energy decay in the passive cavity), one has to include frequency-dispersion of the refractive index. When introducing dispersion, the electromagnetic energy density (in cgs units) reads

$$W = \frac{1}{8\pi}\left(\mathbf{E}^2\frac{\partial(\epsilon\omega)}{\partial\omega} + \mathbf{H}^2\frac{\partial(\mu\omega)}{\partial\omega}\right), \tag{C.37}$$

which is only positive (and thus physical) if

$$\frac{\partial(\epsilon\omega)}{\partial\omega}, \frac{\partial(\mu\omega)}{\partial\omega} > 0. \tag{C.38}$$

The frequency dispersion in a NIM has to fulfill (C.38). A simple possibility is found by expanding ϵ and μ around a resonance frequency ω_r (typically, ω_r is near the frequency of the cavity resonance one wants to calculate), which leads to

$$\begin{aligned}
\epsilon &\approx \epsilon(\omega_r)\left(1 + \alpha_\epsilon\frac{\omega_r - \omega}{\omega_r}\right),\\
\mu &\approx \mu(\omega_r)\left(1 + \alpha_\mu\frac{\omega_r - \omega}{\omega_r}\right)
\end{aligned} \tag{C.39}$$

with dimensionless constants α_ϵ, α_μ which have to be larger than one in order to fulfill (C.38). The refractive index n_j changes according to

$$n_j = \sqrt{\epsilon\mu} \approx n_j(\omega_r)\left(1 + \frac{\alpha_\epsilon + \alpha_\mu}{2}\frac{\omega_r - \omega}{\omega_r}\right). \tag{C.40}$$

When implementing the BEM for NIMs, one has to update the refractive index in each step of Newton's method when calculating resonances, depending on k_j; when calculating wavefunctions or Husimi functions, one has to use the wavenumber-dependent refractive index $n_j(k_{\text{res}})$ as well. ω_r can be chosen as the frequency corresponding to the starting value of Newton's method.

Bibliography

[AGH08] E. G. Altmann, G. del Magno, M. Hentschel. *Non-Hamiltonian dynamics in optical microcavities resulting from wave-inspired corrections to geometric optics.* Eur. Phys. Lett. **84**, 10008 (2008)

[AKF+05] A. M. Armani, R. P. Kulkarni, S. E. Fraser, R. C. Flagan, K. J. Vahala. *Label-Free, Single-Molecule Detection with Optical Microcavities.* Science **317**, 783 (2005)

[Alt09] E. Altmann. *Emission from dielectric cavities in terms of invariant sets of the chaotic ray dynamics.* Phys. Rev. A **79**, 013830 (2009)

[Ami97] E. Y. Amiran. *Integrable smooth planar billiards and evolutes.* New York J. Math. **3**, 32 (1997)

[AMS09] A. Arroyo, R. Markarian, D. P. Sanders. *Bifurcations of periodic and chaotic attractors in pinball billiards with focusing boundaries.* Nonlinearity **22**, 1499 (2009)

[AMW09] A. Aiello, M. Merano, J. P. Woerdman. *Duality between spatial and angular shift in optical reflection.* Phys. Rev. A **80**, 061801(R) (2009)

[And58] P. W. Anderson. *Absence of Diffusion in Certain Random Lattices.* Phys. Rev. **109**, 1492 (1958)

[AR04] V. M. Apalkov, M. E. Raikh. *Directional emission from a microdisk with a linear defect.* Phys. Rev. B **70**, 195317 (2004)

[Arn63] V. I. Arnol'd. *Proof of a theorem of A. N. Kolmogorov on the invariance of quasi-periodic motions under small perturbations of the Hamiltonian.* Russ. Math. Surv. **18**, 9 (1963)

[Art48] K. Artmann. *Berechnung der Seitenversetzung des totalreflektierten Strahles.* Ann. Phys. **2**, 87 (1948)

[Art51] K. Artmann. *Brechung und Reflexion einer seitlich begrenzten (Licht-) Welle an der ebenen Trennfläche zweier Medien in Nähe des Grenzwinkels der Totalreflexion.* Ann. Phys. **8**, 270 (1951)

[AW07] A. Aiello, J. P. Woerdman. *The reflection of a Maxwell-Gaussian beam by a planar surface.* arXiv:0710.1643v2 (2007)

[AW09] A. Aiello, J. P. Woerdman. *Theory of angular Goos-Hänchen shift near Brewster incidence.* arXiv:0903.3730v2 (2009)

[Bar01] M. Barth. *Mikrowellen-Experimente zu Leveldynamik und Wirbelbildung.* Ph.D. thesis, Philipps-Universität Marburg (2001)

[BBD+10] S. Bittner, E. Bogomolny, B. Dietz, M. Miski-Oglu, P. Oria Iriarte, A. Richter, F. Schäfer. *Experimental test of a trace formula for two-dimensional dielectric resonators.* Phys. Rev. E **81**, 066215 (2010)

[BBSN06a] S. V. Boriskina, T. M. Benson, P. Sewell, A. I. Nosich. *Q Factor and Emission Pattern Control of the WG Modes in Notched Microdisk Resonators.* J. Sel. Top. Quant. Electron. **12**, 52 (2006)

[BBSN06b] S. V. Boriskina, T. M. Benson, P. D. Sewell, A. I. Nosich. *Directional Emission, Increased Free Spectral Range, and Mode Q-Factors in 2-D Wavelenght-Scale Optical Microcavity Structures.* J. Sel. Top. Quant. Electron. **12**, 1175 (2006)

[BDM+09] S. Bittner, B. Dietz, M. Miski-Oglu, P. Oria Iriarte, A. Richter, F. Schäfer. *Experimental test of a two-dimensional approximation for optical microcavities.* Phys. Rev. A **80**, 023825 (2009)

[BDS08] E. Bogomolny, R. Dubertrand, C. Schmit. *Trace formula for dielectric cavities: General properties.* Phys. Rev. E **78**, 056202 (2008)

[Ber77] M. V. Berry. *Regular and irregular semiclassical wavefunctions.* J. Phys. A: Math. Gen **10**, 2083 (1977)

[Ber81] M. V. Berry. *Regularity and chaos in classical mechanics, illustrated by three deformations of a circular 'billiard'.* Eur. Phys. J. **2**, 91 (1981)

[BIL+00] I. Braun, G. Ihlein, F. Laeri, J. U. Nöckel, G. Schulz-Ekloff, F. Schüth, U. Vietze, Ö. Weiss, D. Wöhrle. *Hexagonal microlasers based on organic dyes in nanoporous crystals.* Appl. Phys. B: Lasers Opt. **70**, 335 (2000)

[Bir13] G. D. Birkhoff. *Proof of Poincaré's geometric theorem.* Trans. Am. Math. Soc. **14**, 333 (1913)

[Bir26] G. D. Birkhoff. *An extension of Poincaré's last geometric theorem.* Act. Math. **47**, 297 (1926)

[Bir27] G. D. Birkhoff. *On the periodic motions of dynamical systems.* Act. Math. **50**, 359 (1927)

[BKL+09] A. Bäcker, R. Ketzmerick, S. Löck, J. Wiersig, M. Hentschel. *Quality factors and dynamical tunneling in annular microcavities.* Phys. Rev. A **79**, 063804 (2009)

[BKM05] A. Bäcker, R. Ketzmerick, A. G. Monastra. *Flooding of Chaotic Eigenstates into Regular Phase Space Islands.* Phys. Rev. Lett. **94**, 054102 (2005)

[BKM07] A. Bäcker, R. Ketzmerick, A. G. Monastra. *Universality in the flooding of regular islands by chaotic states.* Phys. Rev. E **75**, 066204 (2007)

[BRK+08] C. Böckler, S. Reitzenstein, C. Kistner, R. Debusmann, A. Löffler, T. Kida, S. Höfling, A. Forchel, L. Grenouillet, J. Claudon, J. M. Gérard. *Electrically driven high-Q quantum dot-micropillar cavities.* Appl. Phys. Lett. **92**, 091107 (2008)

[BW59] M. Born, E. Wolf. *Principles of Optics* (Cambridge University Press, 1959)

[CCF+10] R. J. Collins, P. J. Clarke, V. Fernández, K. J. Gordon, M. N. Makhonin, J. A. Timpson, A. Tahraoui, M. Hopkinson, A. M. Fox, M. S. Skolnick, G. S. Buller. *Quantum key distribution system in standard telecommunications fiber using a short wavelength single photon source.* J. Appl. Phys. **102**, 073102 (2010)

[Chi79] B. V. Chirikov. *A universal instability of many-dimensional oscillator systems.* Phys. Rep. **52**, 263 (1979)

[CLB+93] L. Collot, V. Lefèvre-Seguin, M. Brune, J. M. Raimond, S. Haroche. *Very High-Q Whispering-Gallery Mode Resonances Observed on Fused Silica Microspheres.* Europhys. Lett. **23**, 327 (1993)

[CPC93] B. Crespi, G. Perez, S.-J. Chang. *Quantum Poincaré sections for two-dimensional billiards.* Phys. Rev. E **47**, 986 (1993)

[CTS+03] G. D. Chern, H. E. Tureci, A. D. Stone, R. K. Chang, M. Kneissl, N. M. Johnson. *Unidirectional lasing from InGaN multiple-quantum-well spiral-shaped micropillars.* Appl. Phys. Lett. **83**, 1710 (2003)

[DB01] H. R. Dullin, A. Bäcker. *About ergodicity in the family of limaçon billiards.* Nonlinearity **14**, 1673 (2001)

[DGH+00] C. Dembowski, H.-D. Gräf, A. Heine, R. Hofferbert, H. Rehfeld, A. Richter. *First Experimental Evidence for Chaos-Assisted Tunneling in a Microwave Annular Billiard.* Phys. Rev. Lett. **84**, 867 (2000)

[DH81] M. J. Davis, E. J. Heller. *Quantum dynamical tunneling in bound states.* J. Chem. Phys. **75**, 246 (1981)

[DJ88] F. De Martini, G. R. Jacobovitz. *Anomalous spontaneous-stimulated-decay phase transition and zero-threshold laser action in a microscopic cavity.* Phys. Rev. Lett. **60**, 1711 (1988)

[DLMM01] V. Doya, O. Legrand, F. Mortessagne, C. Miniatura. *Light Scarring in an Optical Fiber.* Phys. Rev. Lett. **88**, 014102 (2001)

[DMSW08] C. P. Dettmann, G. V. Morozov, M. Sieber, H. Waalkens. *Directional emission from an optical microdisk resonator with a point scatterer.* Eur. Phys. Lett. **82**, 34002 (2008)

[DMSW09] C. P. Dettmann, G. V. Morozov, M. Sieber, H. Waalkens. *Unidirectional Emission from Circular Dielectric Microresonators with a Point Scatterer.* Phys. Rev. A **80**, 063813 (2009)

[Ein17] A. Einstein. *Zum Quantensatz von Sommerfeld und Epstein.* Verh. DPG **19**, 82 (1917)

[FC07] W. Fang, H. Cao. *Wave interference effect on polymer microstadium laser.* Appl. Phys. Lett. **91**, 041108 (2007)

[FCPN05] W. Fang, H. Cao, V. Podolskiy, E. Narimanov. *Dynamical localization in microdisk lasers.* Opt. Express **13**, 5641 (2005)

[FCS+94] J. Faist, F. Capasso, D. L. Sivco, C. Sirtori, A. L. Hutchinson, A. Y. Cho. *Quantum Cascade Laser.* Science **264**, 553 (1994)

[FGP82] S. Fishman, D. R. Grempel, R. E. Prange. *Chaos, Quantum Recurrences, and Anderson Localization.* Phys. Rev. Lett. **49**, 509 (1982)

[FS97] K. M. Frahm, D. L. Shepelyansky. *Quantum Localization in Rough Billiards.* Phys. Rev. Lett. **78**, 1440 (1997)

[FSVY97] S. V. Frolov, M. Shkunov, Z. V. Vardeny, K. Yoshino. *Ring microlasers from conducting polymers.* Phys. Rev. B **56**, R4363 (1997)

[FYC05] W. Fang, A. Yamilov, H. Cao. *Analysis of high-quality modes in open chaotic microcavities.* Phys. Rev. A **72**, 023815 (2005)

[Gas98] P. Gaspard. *Chaos, scattering and statistical mechanics* (Cambridge University Press, 1998)

[GBM+96] J. M. Gérard, D. Barrier, J. Y. Marzin, R. Kuszelewicz, L. Manin, E. Costard, V. Thierry-Mieg, T. Rivera. *Quantum boxes as active probes for photonic microstructures: The pillar microcavity case.* Appl. Phys. Lett. **69**, 449 (1996)

[GCN+98] C. Gmachl, F. Capasso, E. E. Narimanov, J. U. Nöckel, A. D. Stone, J. Faist, D. L. Sivco, A. Y. Cho. *High-Power Directional Emission from Microlasers with Chaotic Resonators.* Science **280**, 1556 (1998)

[GH47] F. Goos, H. Hänchen. *Ein neuer und fundamentaler Versuch zur Totalreflexion.* Ann. Phys. **1**, 333 (1947)

[GHL+92] H.-D. Gräf, H. L. Harney, H. Lengeler, C. H. Lewenkopf, C. Rangacharyulu, A. Richter, P. Schardt, H. A. Weidenmüller. *Distribution of eigenmodes in a superconducting stadium billiard with chaotic dynamics.* Phys. Rev. Lett. **69**, 1296 (1992)

[GNP+08] M. Ghulinyan, D. Navarro-Urrios, A. Pitanti, A. Lui, G. Pucker, L. Pavesi. *Whispering-gallery modes and light emission from a Si-nanocrystal-based single microdisk resonator.* Opt. Express **17**, 13218 (2008)

[GR65] I. S. Gradshteyn, I. M. Ryzhik. *Table of Integrals, Series, and Products* (New York (Academic), 1965)

[Gut71] M. C. Gutzwiller. *Periodic Orbits and Classical Quantization Conditions.* J. Math. Phys. **12**, 343 (1971)

[GWLJ07] C. Gies, J. Wiersig, M. Lorke, F. Jahnke. *Semiconductor model for quantum-dot-based microcavity lasers.* Phys. Rev. A **75**, 013803 (2007)

[Haa10] F. Haake. *Quantum Signatures of Chaos (3rd edition)* (Springer, 2010)

[Hel84] E. J. Heller. *Bound-State Eigenfunctions of Classically Chaotic Hamiltonian Systems: Scars of Periodic Orbits.* Phys. Rev. Lett. **53**, 1515 (1984)

[Hen02] M. Hentschel. *Mesoscopic wave phenomena in electronic and optical ring structures.* Ph.D. thesis, Technische Universität Dresden (2002)

[HK09] M. Hentschel, T.-Y. Kwon. *Designing and understanding directional emission from spiral microlasers.* Opt. Lett. **34**, 163 (2009)

[HKOS02] L. Hufnagel, R. Ketzmerick, M.-F. Otto, H. Schanz. *Eigenstates Ignoring Regular and Chaotic Phase-Space Structures.* Phys. Rev. Lett. **89**, 154101 (2002)

[HN97] G. Hackenbroich, J. U. Nöckel. *Dynamical tunneling in optical cavities.* Europhys. Lett. **39**, 371 (1997)

[HR02] M. Hentschel, K. Richter. *Quantum chaos in optical systems: The annular billiard.* Phys. Rev. E **66**, 056207 (2002)

[HS02] M. Hentschel, H. Schomerus. *Fresnel laws at curved dielectric interfaces of microresonators.* Phys. Rev. E **65**, 045603(R) (2002)

[HSI05] T. Harayama, S. Sunada, K. S. Ikeda. *Theory of two-dimensional microcavity lasers.* Phys. Rev. A **72**, 013803 (2005)

[HSS03] M. Hentschel, H. Schomerus, R. Schubert. *Husimi functions ar dielectric interfaces: Inside-outside duality for optical systems and beyond.* Europhys. Lett. **62**, 636 (2003)

[Hus40] K. Husimi. *Some formal properties of the density matrix.* Proc. Phys.-Math. Soc. Japan **22**, 264 (1940)

[IGYM01] V. S. Ilchenko, M. L. Gorodetsky, X. S. Yao, L. Maleki. *Microtorus: a high-finesse microcavity with whispering-gallery modes.* Opt. Lett. **26**, 256 (2001)

[IKK88] K. Iga, F. Koyama, S. Kinoshita. *Surface emitting semiconductor lasers.* IEEE J. Quant. Electron. **24**, 1845 (1988)

[Jac75] J. D. Jackson. *Classical electrodynamics (second edition)* (John Wiley and Sons, New York, 1975)

[KJD+95] M. Kuwata-Gonokami, R. H. Jordan, A. Dodabalapur, H. E. Katz, M. L. Schilling, R. E. Slusher, S. Ozawa. *Polymer microdisk and microring lasers.* Opt. Lett. **20**, 2093 (1995)

[KKPV06] T. J. Kippenberg, J. Kalkman, A. Polman, K. J. Vahala. *Demonstration of an erbium-doped microdisk laser on a silicon chip.* Phys. Rev. A **74**, 051802(R) (2006)

[Kol54] A. N. Kolmogorov. *On conservation of conditionally periodic motions for a small change in Hamilton's function.* Dokl. Akad. Nauk SSSR **98**, 527 (1954)

[Kuh98] U. Kuhl. *Mikrowellenuntersuchungen an eindimensionalen Streusystemen und in zweidimensionalen Kavitäten.* Ph.D. thesis, Philipps-Universität Marburg (1998)

[Laz73] V. F. Lazutkin. *The existence of caustics for a billiard problem in a convex domain.* Math. USSR Izv. **7**, 185 (1973)

[LCT86] H. M. Lai, F. C. Cheng, W. K. Tang. *Goos-Hänchen effect around and off the critical angle.* J. Opt. Soc. Am. A **3**, 550 (1986)

[LLC+02] S. B. Lee, J. H. Lee, J. S. Chang, H. J. Moon, S. W. Kim, K. An. *Observation of Scarred Modes in Asymmetrically Deformed Microcylinder Lasers.* Phys. Rev. Lett. **88**, 033903 (2002)

[LLHZ06] M. Lebental, J. S. Lauret, R. Hierle, J. Zyss. *Highly directional stadium-shaped polymer microlasers.* Appl. Phys. Lett. **88**, 031108 (2006)

[Löc09] S. Löck. *Dynamical tunneling in systems with a mixed phase space.* Ph.D. thesis, Technische Universität Dresden (2009)

[LRK+04] S.-Y. Lee, J.-W. Ryu, T.-Y. Kwon, S. Rim, C.-M. Kim. *Scarred resonances and steady probability distribution in a chaotic microcavity.* Phys. Rev. A **72**, 061801(R) (2004)

[LRR+04] S.-Y. Lee, S. Rim, J.-W. Ryu, T.-Y. Kwon, M. Choi, C.-M. Kim. *Quasiscarred Resonances in a Spiral-Shaped Microcavity.* Phys. Rev. Lett. **93**, 164102 (2004)

[Mar93] R. Markarian. *New ergodic billiards: exact results.* Nonlinearity **6**, 819 (1993)

[Mic09] C. P. Michael. *Optical Material Characterization Using Microdisk Cavities.* Ph.D. thesis, California Institute of Technology (2009)

[MIM+00] P. Michler, A. Imamoğlu, M. D. Mason, P. J. Carson, G. F. Strouse, S. K. Buratto. *Quantum correlation among photons from a single quantum dot at room temperature.* Nature **406**, 968 (2000)

[MLS+92] S. L. McCall, A. F. J. Levi, R. E. Slusher, S. J. Pearton, R. A. Logan. *Whispering-gallery mode microdisk lasers.* Appl. Phys. Lett. **60**, 289 (1992)

[Mos66] J. Moser. *On the theory of quasiperiodic motions.* SIAM Review **8**, 145 (1966)

[Nöc97] J. U. Nöckel. *Resonances in Nonintegrable Open Systems.* Ph.D. thesis, Yale University (1997)

[Nol08] W. Nolting. *Grundkurs Theoretische Physik 5/1: Quantenmechanik – Grundlagen (seventh edition)* (Springer, 2008)

[NS95] J. U. Nöckel, A. D. Stone. *Chaotic Light: A Theory of Asymmetric Resonant Cavities.* In: R. Chang, A. Campillo (Editors), *Optical Processes in Mircocavities (Advanced Series in Applied Physics vol 3)* (World Scientific, 1995)

[NS97] J. U. Nöckel, A. D. Stone. *Ray and wave chaos in asymmetric resonant optical cavities.* Nature **385**, 45 (1997)

[NSC94] J. U. Nöckel, A. D. Stone, R. K. Chang. *Q-spoiling and directionality in deformed ring cavities.* Opt. Lett. **19**, 1693 (1994)

[Per73] I. C. Percival. *Regular and irregular spectra.* J. Phys. B: At. Mol. Phys. **6**, L229 (1973)

[PFTV92] W. H. Press, B. P. Flannery, A. A. Teukolsky, W. T. Vetterling. *Numerical Recipes in C (second edition)* (Cambridge University Press, 1992)

[PLS+99] O. Painter, R. K. Lee, A. Scherer, A. Yariv, J. D. O'Brien, P. D. Dapkus, I. Kim. *Two-Dimensional Photonic Band-Gap Defect Mode Laser.* Science **284**, 1819 (1999)

[PN05] V. A. Podolskiy, E. E. Narimanov. *Chaos-assisted tunneling in dielectric microcavities.* Opt. Lett. **30**, 474 (2005)

[Poi12] H. Poincaré. *Sur un théorème de géométrie.* Rend. Circ. Math. Palermo **33**, 375 (1912)

[Ray85] L. Rayleigh. *On waves propagated along the plane surface of an elastic solid.* Proc. Lond. Math. Soc. **17**, 4 (1885)

[Ray07] L. Rayleigh. *On the dynamical theory of gratings.* Proc. Roy. Soc. A **79**, 399 (1907)

[RC94] P. R. Rice, H. J. Carmichael. *Photon statistics of a cavity-QED laser: A comment on the laser-phase-transition analogy.* Phys. Rev. A **50**, 4318 (1994)

[Rob83] M. Robnik. *Classical dynamics of a family of billiards with analytic boundaries.* J. Phys. A: Math. Gen. **16**, 3971 (1983)

[RS02] K. Richter, M. Sieber. *Semiclassical Theory of Chaotic Quantum Transport.* Phys. Rev. Lett. **89**, 206801 (2002)

[RSL+04] J. P. Reithmaier, G. Sęk, A. Löffler, C. Hofmann, S. Kuhn, S. Reitzenstein, L. V. Keldysh, V. D. Kulakovskii, T. L. Reinecke, A. Forchel. *Strong coupling in a single quantum dot-semiconductor microcavity system.* Nature **432**, 197 (2004)

[RTS+02] N. B. Rex, H. E. Tureci, H. G. L. Schwefel, R. K. Chang, A. D. Stone. *Fresnel Filtering in Lasing Emission from Scarred Modes of Wave-Chaotic Optical Resonators.* Phys. Rev. Lett. **88**, 094192 (2002)

[SFL+09] Q. Song, W. Fang, B. Liu, S.-T. Ho, G. S. Solomon, H. Cao. *Chaotic microcavity laser with high quality factor and unidirectional output.* Phys. Rev. A **80**, 041807(R) (2009)

[SGS+10] Q. H. Song, L. Ge, A. D. Stone, H. Cao, J. Wiersig, J.-B. Shim, J. Unterhinninghofen, W. Fang, G. S. Solomon. *Directional laser emission from a wavelenght-scale wave-chaotic microcavity.* Phys. Rev. Lett. **105**, 103902 (2010)

[SH06] H. Schomerus, M. Hentschel. *Correcting Ray Optics at Curved Dielectric Microresonator Interfaces: Phase-Space Unification of Fresnel Filtering and the Goos-Hänchen Shift.* Phys. Rev. Lett. **96**, 243903 (2006)

[SH07] S. Shinohara, T. Harayama. *Signature of ray chaos in quasibound wave functions for a stadium-shaped dielectric cavity.* Phys. Rev. E **75**, 036216 (2007)

[SHF+10] S. Shinohara, T. Harayama, T. Fukushima, M. Hentschel, T. Sasaki, E. E. Narimanov. *Chaos-Assisted Directional Light Emission from Microcavity Lasers.* Phys. Rev. Lett. **104**, 163902 (2010)

[SHKC02] S. Suzuki, Y. Hatakeyama, Y. Kokubun, S. T. Chu. *Precise Control of Wavelength Channel Spacing of Microring Resonator Add-Drop Filter Array.* J. Lightw. Technol. **20**, 745 (2002)

[SHW+09] S. Shinohara, M. Hentschel, J. Wiersig, T. Sasaki, T. Harayama. *Ray-wave correspondence in limaçon-shaped semiconductor microcavities.* Phys. Rev. A **80**, 031801(R) (2009)

[SLK+08] J.-B. Shim, S.-B. Lee, S. W. Kim, S.-Y. Lee, J. Yang, S. Moon, J.-H. Lee, K. An. *Uncertainty-Limited Turnstile Transport in Deformed Microcavities.* Phys. Rev. Lett. **100**, 174102 (2008)

[Sri91] S. Sridhar. *Experimental Observation of Scarred Eigenfunctions of Chaotic Microwave Cavities.* Phys. Rev. Lett. **67**, 785 (1991)

[SS90] H.-J. Stöckmann, J. Stein. *"Quantum" chaos in billiards studied by microwave absorption.* Phys. Rev. Lett. **64**, 2215 (1990)

[SS92] J. Stein, H.-J. Stöckmann. *Experimental Determination of Billiard wave Functions.* Phys. Rev. Lett. **68**, 2867 (1992)

[SSS95] J. Stein, H.-J. Stöckmann, U. Stoffregen. *Microwave Studies of Billiard Green Functions and Propagators.* Phys. Rev. Lett. **75**, 53 (1995)

[Stö00] H.-J. Stöckmann. *Quantum chaos: an introduction* (Cambridge University Press, 2000)

[Szá92] D. Szász. *On the K-property of some planar hyperbolic billiards.* Comm. Math. Phys. **145**, 595 (1992)

[TG06] T. Tél, M. Gruiz. *Chaotic Dynamics: An Introduction based on Classical Mechanics* (Cambridge University Press, 2006)

[TH00] A. Taflove, S. C. Hagness. *Computational Electrodynamics: the Finite-Difference Time-Domain Method* (Artech House (London), 2000)

[TKJVC09] M. Tomes, K. K. J. Vahala, T. Carmon. *Direct imaging of tunneling from a potential well.* Opt. Express **17**, 19160 (2009)

[TS02] H. E. Tureci, A. D. Stone. *Deviation from Snell's law for beams transmitted near the critical angle: application to microcavity lasers.* Opt. Lett. **27**, 7 (2002)

[TSC06] H. E. Türeci, A. D. Stone, B. Collier. *Self-consistent multimode lasing theory for complex or random lasing media.* Phys. Rev. A **74**, 043822 (2006)

[TSG07] H. E. Türeci, A. D. Stone, L. Ge. *Theory of the spatial structure of nonlinear lasing modes.* Phys. Rev. A **76**, 013813 (2007)

[TSG+09] H. E. Türeci, A. D. Stone, L. Ge, S. Rotter, R. J. Tandy. *Ab initio self-consistent laser theory and random lasers.* Nonlinearity **22**, C1 (2009)

[TSS05] H. E. Türeci, H. G. L. Schwefel, A. D. Stone. *Modes of wave-chaotic dielectric resonators.* Prog. Opt. **47**, 75 (2005)

[TU94] S. Tomsovic, D. Ullmo. *Chaos-assisted tunneling.* Phys. Rev. E **50**, 145 (1994)

[TV07] A. Tulek, Z. V. Vardeny. *Unidirectional laser emission from π-conjugated polymer microcavities with broken symmetry.* Appl. Phys. Lett. **90**, 161106 (2007)

[UGA+07] S. M. Ulrich, C. Gies, S. Ates, J. Wiersig, S. Reitzenstein, C. Hofmann, A. Löffler, A. Forchel, F. Jahnke, P. Michler. *Photon Statistics of Semiconductor Microcavity Lasers.* Phys. Rev. Lett. **98**, 043906 (2007)

[UW10] J. Unterhinninghofen, J. Wiersig. *Interplay of Goos-Hänchen shift and boundary curvature in deformed microdisks.* Phys. Rev. E **82**, 026202 (2010)

[UWH08] J. Unterhinninghofen, J. Wiersig, M. Hentschel. *Goos-Hänchen shift and localization of optical modes in deformed microcavities.* Phys. Rev. E **78**, 016201 (2008)

[Ves68] V. G. Veselago. *The electrodynamics of substances with simultaneously negative values of ϵ and μ.* Sov. Phys. Usp. **10**, 509 (1968)

[vF80] P. M. van den Berg, J. T. Fokkema. *The Rayleigh hypothesis in the theory of diffraction by a perturbation in a plane surface.* Radio Sci. **15**, 723 (1980)

[WGJ+09] J. Wiersig, C. Gies, F. Jahnke, M. Aßmann, T. Berstermann, M. Bayer, C. Kistner, S. Reitzenstein, C. Schneider, S. Höfling, A. Forchel, C. Kruse, J. Kalden, D. Hommel. *Direct observation of correlations between individual photon emission events of a microcavity laser.* Nature **460**, 245 (2009)

[WH06] J. Wiersig, M. Hentschel. *Unidirectional light emission from high-Q modes in optical microcavities.* Phys. Rev. A **73**, 031802(R) (2006)

[WH08] J. Wiersig, M. Hentschel. *Combining Directional Light Output and Ultralow Loss in Deformed Microdisks.* Phys. Rev. Lett. **100**, 033901 (2008)

[Wie03] J. Wiersig. *Boundary element method for resonances in dielectric microcavities.* J. Opt. A: Pure Appl. Opt. **5**, 53 (2003)

[Woj86] M. Wojtkowski. *Principles for the design of billiards with nonvanishing Lyapunov exponents.* Comm. Math. Phys. **105**, 391 (1986)

[WRB05] B. Weingartner, S. Rotter, J. Burgdörfer. *Simulation of electron transport through a quantum dot with soft walls.* Phys. Rev. B **72**, 115342 (2005)

[WRM+93] D. Weiss, K. Richter, A. Menschig, R. Bergmann, H. Schweizer, K. von Klitzing, G. Weimann. *Quantized periodic orbits in large antidot arrays.* Phys. Rev. Lett. **70**, 4118 (1993)

[WUS+10a] J. Wiersig, J. Unterhinninghofen, H. Schomerus, U. Peschel, M. Hentschel. *Electromagnetic modes in cavities made of negative-index metamaterials.* Phys. Rev. A **81**, 023809 (2010)

[WUS+10b] J. Wiersig, J. Unterhinninghofen, Q. Song, H. Cao, M. Hentschel, S. Shinohara. *Review on unidirectional light emission from ultralow-loss modes in deformed microdisks.* In: O. Kwon, B. Lee, K. An (Editors), *Trends in nano- and micro-cavities* (Bentham Science Publishers Ltd., 2010)

[WYD+09] Q. J. Wang, C. Yan, L. Diehl, M. Hentschel, J. Wiersig, N. Yu, C. Pflügel, M. A. Belkin, T. Edamura, M. Yamanishi, H. Kan, F. Capasso. *Deformed microcavity quantum cascade lasers with directional emission.* New J. Phys. **11**, 125018 (2009)

[WYY+10] Q. J. Wang, C. Yang, N. Yu, J. Unterhinninghofen, J. Wiersig, C. Pflügel, L. Diehl, T. Edamura, M. Yamanishi, H. Kan, F. Capasso. *Whispering gallery mode resonators for highly directional laser action.* PNAS **107**, 22407 (2010)

[XZL+10] Y.-F. Xiao, C.-L. Zou, Y. Li, C.-H. Dong, Z.-F. Han, Q. Gong. *Asymmetric resonant cavities and their applications in optics and photonics: a review.* Front. Optoelectron. China **Online First**, 1 (2010)

[Yee66] K. Yee. *Numerical solution of initial boundary value problems involving Maxwell's equations in isotropic media.* IEEE Trans. Ant. Prop. **14**, 302 (1966)

[YFW+08] N. Yu, J. Fan, Q. J. Wang, C. Pflügel, L. Diehl, T. Edamura, M. Yamanishi, H. Kan, F. Capasso. *Small-divergence semiconductor lasers by plasmonic collimation.* Nature Photon. **2**, 564 (2008)

[YKK09] C.-H. Yi, M.-W. Kim, C.-M. Kim. *Lasing characteristics of a Limaçon-shaped microcavity laser.* Appl. Phys. Lett. **95**, 141107 (2009)

[YML+06] J. Yang, S. Moon, S.-B. Lee, J.-H. Lee, K. An, J.-B. Shim, H.-W. Lee, S.-W. Kim. *Development of a deformation-tunable quadrupolar microcavity.* Rev. Sci. Instrum. **77**, 083103 (2006)

[YWD+09] C. Yan, Q. J. Wang, L. Diehl, M. Hentschel, J. Wiersig, N. Yu, C. Pflügel, F. Capasso, M. A. Belkin, T. Edamura, M. Yamanishi, H. Kan. *Directional emission and universal far-field behaviour from semiconductor lasers with limaçon-shaped microcavity.* Appl. Phys. Lett. **94**, 251101 (2009)

[ZYX+09] C.-L. Zou, Y. Yang, Y.-F. Xiao, C.-H. Dong, Z.-F. Han, G.-C. Guo. *Accurately calculating high quality factor of whispering-gallery modes with boundary element method.* J. Opt. Soc. Am. B **26**, 2050 (2009)

Acknowledgements

First, I would like to thank Prof. Dr. Jan Wiersig for giving me the opportunity for writing this thesis, for always having time for my questions, and for many helpful discussions and suggestions. I also thank Dr. Martina Hentschel, my unofficial co-adviser, for helpful discussions and much encouragement.

The DFG research group 760, "Scattering Systems with Complex Dynamics", has not only supported me financially; it also provided the opportunity of doing experiments in Prof. Dr. Hans-Jürgen Stöckmann's group at the University of Marburg, which I have visited twice. I especially thank Prof. Dr. Ulrich Kuhl for making the setup and data acquisition as easy as possible even for theoreticians as well as many helpful suggestions and ideas; Prof. Stöckmann for the hospitality and stimulating discussions; and Alexander Potzuweit, Sonja Barkhofen, Tobias Weich, and Stefan Gehler for being nice office- and lab mates during my stay.

On many conferences and workshops, it has been great to hang out and discuss everything from quantum chaos to climbing especially with members from Prof. Roland Ketzmerik's group in Dresden. In particular, Dr. Steffen Löck, Lars Bittrich, Dr. Waltraut Wustmann, Martin Richter, and Matthias Michler have always been good to meet.

Prof. Dr. Frank Jahnke has welcomed me in his group when I started my thesis in Bremen, and thanks to him and the companionship of Sandra Ritter, Dr. Micheal Lorke, Dr. Christopher Gies, and Dr. Jan Seebeck in particular, I have never felt isolated even though I belonged to a distinct subgroup.

Without Silvia Simon and Dr. Gerald Kasner, the transition to Magdeburg could not possibly have been this smooth; I thank them for kind explanations of the local culture, history, and sometimes even language. I thank Mrs. Simon in particular for explaining the university forms to me, reminding me of forgotten ones, and telling me what's really important regarding the thesis defense (bring nice cookies). The coffee rounds (or "group meetings") with them and the other members of the Wiersig group, Dr. Jeong-Bo Shim and the A-team (Alexander Leymann, Alexander Förster and Alexander Eberspächer) will be missed. Alexander Eberspächer also kindly read my manuscript; his remarks certainly helped improve it.

During my Bremen time, my friend Sandra Ritter was always open for going for coffee or tea and discussions. My friends Vivien Voßebürger, Anne Stegmann and Daniel Kitzmann also always had open ears for complaints about weird numerical problems, bad conference talks, thesis writing, and everything else.

My parents always have supported me (and googled my publications). In particular I thank my father for being especially interested in the limaçon cavity.

Stefan Falk just has been there – through two moves across Germany, always listening, always encouraging... thanks a lot.